UNIVERSITÄTSKLINIKUM HAMBURG EPPENDORF

Zentrum für Molekulare Neurobiologie Hamburg
Institute for Synaptic Neuroscience

Prof. Dr. Thomas G. Oertner

All-optical investigation of the role of CaMKII in long-term plasticity in the hippocampus and the development of a method for ultrastructural analysis of synapses

Dissertation

With the aim of achieving a doctoral degree (Dr. rer. nat.) at the Faculty of Mathematics, Informatics and Natural Sciences of the University of Hamburg

Submitted by

Rui Wang

Hamburg, Germany
December, 2024

The following evaluators recommend the admission of the dissertation:

Thesis:

Prof. Dr. Thomas Oertner
Institut für Synaptische Neurowissenschaft
Zentrum für molekulare Neurobiologie Hamburg
Universitätsklinikum Hamburg-Eppendorf

Prof. Dr. Matthias Kneussel
Institut für Molekulare Neurogenetik
Zentrum für molekulare Neurowissenschaft Hamburg
Universitätsklinikum Hamburg-Eppendorf

Oral defense:

Prof. Dr. Thomas Oertner
Institut für Synaptische Neurowissenschaft
Zentrum für molekulare Neurobiologie Hamburg
Universitätsklinikum Hamburg-Eppendorf

Prof. Dr. Ileana Hanganu-Opatz
Institut für Entwicklungsneurowissenschaften
Zentrum für molekulare Neurobiologie Hamburg
Universitätsklinikum Hamburg-Eppendorf

Prof. Dr. Markus Glatzel
Zentrum für Diagnostik
Institut für Neuropathologie
Universitätsklinikum Hamburg-Eppendorf

Date of oral defense: 7 April 2025

Contents

Summary

Dynamic changes in synaptic efficacy and structure, termed synaptic plasticity, are a major mechanism of information storage in the brain. Calcium–calmodulin-dependent protein kinase II (CaMKII) is one of the most important memory molecules that, through its autophosphorylation feature, transforms transient activation due to synaptic activity-related increases in calcium into longer-lasting changes in synaptic strength. Whether CaMKII is essential to induce and/or to maintain synaptic plasticity remains controversial. I took advantage of optogenetic tools to investigate the role of CaMKII in synaptic plasticity by inducing plasticity and manipulating relevant signaling pathways at the same time. Specifically, I induced spike-timing-dependent plasticity (STDP) at Schaffer collateral synapses in rat hippocampal slice cultures by optogenetic stimulation of two neuronal populations expressing spectrally separated channelrhodopsins. The all-optical protocol induced timing-dependent long-term potentiation (tLTP), increasing synaptic strength both acutely and more interestingly, chronically. Optical inhibition of CaMKII during tLTP induction complete blocked acute tLTP, but interestingly, chronic tLTP did still emerge. Optical activation of CaMKII, on the other hand, accomplished by photoactivatable CaMKII, induced acute functional, structural and ultrastructural alterations at synapses. Structural plasticity often developed in a spatially clustered manner. However, these CaMKII-activation-induced synaptic alterations did not last for more than one day. Together, these data suggest that activity-dependent potentiation of synaptic inputs has two phases: CaMKII is necessary and sufficient for the induction of early LTP. A second, CaMKII-independent mechanism, possibly through the persistent activity of protein kinase Mζ (PKMζ), is responsible for the selective strengthening of inputs days later.

Although significant progress has been made in understanding the mechanism of information storage at the synaptic level, our knowledge of the mechanisms of long-term synaptic information storage and the ultrastructural anatomical features of synaptic plasticity is still rudimentary. For this reason, I developed a genetic labeling method that allows the visualization of synapses of interest under electron microscopy (EM) in a robust and versatile manner. I use two organelle-targeted peroxidases, dAPEX2-NES and SYP-HRP, and the Cre/LoxP system, which together allow specific labeling of optogenetically manipulated synapses at the EM level. Optimizing transfection, stimulation, fixation and image analysis, I have established a pipeline for the ultrastructural analysis of synapses after optogenetic stimulation.

Zusammenfassung

Dynamischen Veränderungen in synaptischer Wirksamkeit und Struktur, bekannt als synaptische Plastizität, stellen einen wesentlichen Mechanismus der Informationsspeicherung im Gehirn dar. Calcium-Calmodulin-abhängige Proteinkinase II (CaMKII) ist eines der wichtigsten Gedächtnismoleküle, das durch seine Autophosphorylierung temporäre Aktivierungen aufgrund synaptisch-aktivitätsbedingter Calcium-Erhöhungen in länger anhaltende Veränderungen der synaptischen Stärke umwandelt. Ob CaMKII unerlässlich ist, um synaptische Plastizität zu induzieren und/oder aufrechtzuerhalten, bleibt umstritten. Ich habe optogenetische Werkzeuge genutzt, um die Rolle von CaMKII in der synaptischen Plastizität zu untersuchen, indem ich Plastizität induzierte und gleichzeitig relevante Signalwege manipulierte. Insbesondere induzierte ich spike-timing-abhängige Plastizität (STDP) an Schaffer-Kollateralsynapsen in Ratten-Hippocampus-Schnittkulturen durch optogenetische Stimulation zweier neuronaler Populationen, die spektral getrennte Channelrhodopsine exprimieren. Das vollständig optische Protokoll induzierte timing-abhängige Langzeitpotenzierung (tLTP), die die synaptische Stärke sowohl akut als auch chronisch erhöhte. Optische Deaktivierung von CaMKII während der tLTP-Induktion blockierte die akute tLTP vollständig, während chronisches tLTP nicht betroffen war. Andererseits war die direkte optische Aktivierung von CaMKII, erreicht durch die Verwendung einer photoaktivierbaren CaMKII, ausreichend, um akute funktionale, strukturelle und ultrastrukturelle Veränderungen der Synapsen zu induzieren. Strukturelle Plastizität trat häufig in Clustern von Synapsen auf. Diese durch CaMKII-Aktivierung induzierten Veränderungen der Synapsen hielten jedoch nicht länger als einen Tag an. Zusammen deuten diese Daten darauf hin, dass die aktivitätsabhängige Potenzierung synaptischer Verbindungen zwei Phasen aufweist: CaMKII ist notwendig und hinreichend für die Induktion der frühen LTP. Ein zweiter, CaMKII-unabhängiger Mechanismus, möglicherweise durch die anhaltende Aktivität der Proteinkinase Mζ (PKMζ), ist für die selektive Verstärkung der Verbindungen einige Tage später verantwortlich.

Obwohl bedeutende Fortschritte im Verständnis der Mechanismen der Informationsspeicherung auf synaptischer Ebene erzielt wurden, ist unser Wissen über den Mechanismus der langfristigen Speicherung synaptischer Ereignisse und die ultrastrukturellen anatomischen Merkmale der synaptischen Plastizität, die letztlich die Plastizitätsmaschinerie ermöglichen, noch rudimentär. Aus diesem Grund habe ich eine genetische Markierungsmethode entwickelt, die die Visualisierung interessierender Synapsen unter dem Elektronenmikroskop (EM) auf eine robuste und vielseitige Weise ermöglicht. Ich verwende zwei an Organellen gebundenen Peroxidasen, dAPEX2-NES und SYP-HRP, sowie das Cre/LoxP-System, die zusammen eine spezifische Markierung optogenetisch manipulierter Synapsen im EM erlauben. Durch die Optimierung von Transfektion, Stimulation, Fixierung und Bildanalyse konnte ich eine Pipeline für die ultrastrukturelle Analyse von Synapsen nach optogenetischer Stimulation etablieren.

1. Introduction

1.1 The hippocampus

The hippocampus is one of the most well-studied brain regions, known for its critical role in memory formation, learning and spatial navigation. The intra-hippocampal anatomical connectivity (Fig. 1) starts from the dentate gyrus (DG) region, which receives cortical inputs mainly from the entorhinal cortex (EC) perforant pathway. DG granule cells (GCs) project via mossy fibers to CA3, and CA3 pyramidal neurons (PNs) send projections to CA1, forming the Schaffer collateral (SC) synapses. Together, these excitatory connections form the hippocampal unidirectional trisynaptic loop. Finally, CA1 projects back to the EC via the subiculum. In addition, recurrent connections are made between neurons from areas CA3 and CA1. While neurons from different regions of the hippocampus have different physiological properties, in this study I focused on the CA3-CA1 SC circuit.

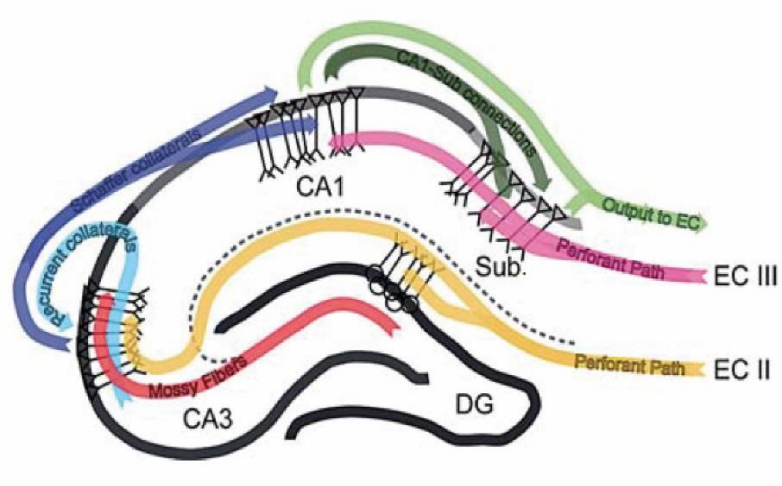

Figure 1: Intra-hippocampal connectivity.

EC layer II sends the primary input to DG GCs, where mossy fibers project from the DG to CA3 PNs dendrites. CA3 PN axons project to CA1 PNs, which send signals out of the hippocampus back to the EC. Apart from the unidirectional trisynaptic loop, recurrent collateral loops exist in CA3 and CA1. Image from (Witter et al., 2017)

1.2 Hippocampal Organotypic Slice Cultures

This PhD project investigates the molecular mechanism of synaptic plasticity in the hippocampus (SC synapses) by using organotypic hippocampal slice cultures as an experimental model. Using organotypic hippocampal slice cultures allows the study of hippocampus synaptic plasticity in a controlled environment. The slice can be cultured *in vitro* for months and the neurons typically recover from the altered physical state caused by the cutting of the tissue within two weeks (Gähwiler et al., 1997). Microglia cells also recover their basal activity state after 13 days in vitro (Laprell et al., 2021). This provides us with a sufficiently long time-window to study early and late long-term synaptic plasticity. As the word 'organotypic' implies, the cultured tissue has similar postnatal developmental and physical characteristics to the native hippocampus, with regard to neuronal electrophysiological properties, morphology, spine shape and size (De Simoni et al., 2003; Stoppini et al., 1991), synapse ultrastructure (Fiala et al., 2003, Stoppini et al., 1991), spontaneous activity (Mohajerani & Cherubini, 2005), structural plasticity features (Harvey & Svoboda, 2007, Noguchi et al., 2019) and neurogenesis (Raineteau et al., 2004). Importantly, intra-hippocampal connectivity pathways are reasonably well preserved, although the connection probability between CA3 and CA1 PCs is higher than *in vivo*. Also, while long-range modulatory inputs are removed by the slice cutting procedure, local release of modulatory factors is intact. For example, endogenous brain-derived neurotrophic factor (BDNF) levels in slice culture are sufficient to promote tropomyosin receptor kinase B-dependent long-term synaptic plasticity (Harward et al., 2016). Thus, preserving the physiological properties of these basic hippocampal cells allows the maintenance of higher order hippocampal functions such as spontaneous recurrent network activity (Garaschuk et al., 1998; Mohajerani & Cherubini, 2005) and multiple forms of synaptic plasticity. As a great practical advantage, the accessibility of the slice culture allows for convenient genetic manipulations and read-out methods to be performed. The organotypic hippocampal slice culture is therefore an appropriate model to study synaptic plasticity *ex vivo.*

1.3 Hippocampal Synaptic plasticity

In this subchapter I will focus on discussing the characteristics of excitatory synaptic plasticity in the CA3-CA1 SC circuit which I use as my experimental model.

1.3.1 Memory and long-term synaptic plasticity in the hippocampus

Research on the correlation between hippocampal function and memory formation started with the case study of patient Henry Molaison in 1957. It was reported that the patient lost the ability to form declarative memories after surgery to treat epilepsy in which his hippocampus was removed (Scoville & Milner, 1957), suggesting that memory formation is a function of the hippocampus. In 1971, O'Keefe and Dostrovsky discovered place cells in the hippocampus (O'Keefe & Dostrovsky, 1971). In their study, they recorded the activity of hippocampal neurons in freely moving rats and found that neuronal activity represented the spatial location of the animal. Today it is widely accepted that memory is based on the dynamic change of synaptic strength, a process also known as synaptic plasticity. The long-term stability of increased synaptic transmission is called long-term potentiation (LTP). Bliss & Lømo discovered LTP in the hippocampal DG *in vivo*, induced by prior synaptic activity (Bliss & Lømo, 1973). *In vitro*, LTP could be induced in CA1 by tetanic stimulation in hippocampal slices (Schwartzkroin & Wester, 1975) (Fig. 2). In 1983, Richard Morris showed that specific blockade of N-methyl-D-aspartate (NMDA) receptors in the hippocampus impaired spatial learning in animals and, importantly, the induction of LTP, without affecting non-hippocampal memory or the baseline transmission properties (Morris et al., 1986). By performing inhibitory avoidance behavioral tests and *in vivo* electrophysiological recordings, Whitlock and colleagues showed in 2006 that the aversive stimulus that induces memory encoding also promotes the development of hippocampal LTP (Whitlock et al., 2006). This is remarkable because as early as 1921, the memory engram hypothesis proposed by Semon suggested that memory formation leads to the activation of a specific group of neuronal cells, resulting in a long-lasting physical change in these neurons – the memory trace (Semon, 1921), and in the following decades this hypothesis was confirmed by electrophysiology in the hippocampus. Together, these findings demonstrate that the hippocampus is one of the hubs of memory formation and hippocampal synaptic plasticity is an important physiological basis of memory. In general, synaptic long-term plasticity can be divided into long-term potentiation (LTP) and long-term depression (LTD). LTP is believed to

support memory formation while the weakening of synaptic strength (LTD) erases memory and maintains synaptic balance (Bear, 1999). Together, LTP and LTD enable the bidirectional control of synaptic strength.

The occurrence of hippocampal LTP *in vitro* (Schwartzkroin & Wester, 1975) provides a convenient way to study its molecular mechanisms. However, the technical limitations of electrophysiological recordings limit the study of LTP timescale to only several hours. The development of long-term synaptic plasticity involves three stages: plasticity induction, expression, and maintenance (Bliss & Collingridge, 1993). Understanding the mechanism of plasticity maintenance is a challenging task, as acute slice preparations cannot be maintained in a healthy state for very long.

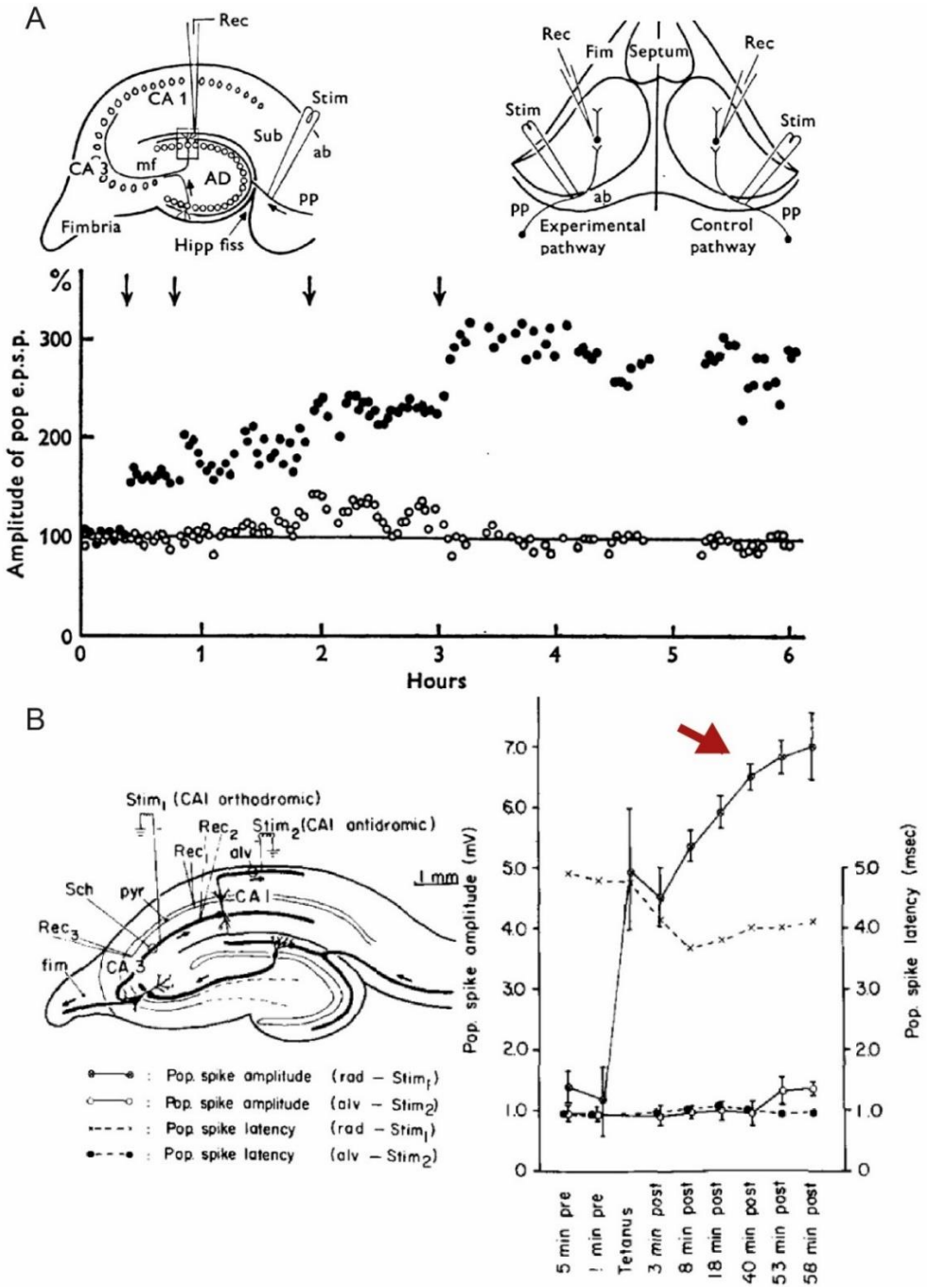

Figure 2: The discovery of long-term synaptic plasticity in the hippocampus

A. In 1973 Bliss and Lømo performed the first experiment demonstrating LTP in vivo in the hippocampus. Upper: placing of stimulation and recording electrodes in the hippocampus (left) and the control pathway in the ipsilateral hemisphere (right). Lower: 10 seconds of electical stimulation (15 Hz) was delivered at the perforant path, indicated by the arrows. A long-lasting increase of the population postsynaptic potential amplitude at the stimulated pathway (close circles) but not the control pathway (open circles) was observed. B. In 1975, Schwartzkroin and Wester showed the induction protocols necessary for inducing LTP in vitro in hippocampal slices. 7.5 seconds of electrical stimulation (33 Hz) in CA1 radiatum, but not in the alveus (left, stim1), induced a long-lasting increase of postsynaptic population spike amplitude in CA1 (right, red arrow). Images adapted from Bliss & Lømo, 1973, and Schwartzkroin & Wester, 1975.

1.3.2 Synaptic glutamate receptors

Synaptic communication of excitatory synapses is typically initiated by the exocytosis of presynaptic vesicles containing neurotransmitters, including glutamate, which is the most common excitatory synapse transmitter (Fonnum, 1984). The presynaptic action potential (AP) triggers the release of glutamate. Glutamate reaches the postsynaptic membrane by diffusion across the synaptic cleft and binds to glutamate receptors in the postsynaptic membrane. The main ionotropic glutamate receptors that mediate excitatory synaptic transmission are α-amino-3-hydroxy-5-methyl-4-isoxazolepropionic acid (AMPA) and N-methyl-D-aspartate (NMDA) receptors (Dingledine et al., 1999). Both are permeable to Na^+ and K^+. Binding of glutamate activates AMPA receptors and an influx of Na^+ depolarizes the postsynaptic membrane. The mechanism of NMDA receptors activation is more complex. At the resting membrane potential, NMDA receptors are largely blocked by Mg^{2+} which is only released during depolarization of the postsynaptic membrane. Activated NMDA receptors allow Na^+ and, importantly, Ca^{2+} influx. These two features, namely the requirement for both pre- and postsynaptic activation and the activation-induced conductance of Ca^{2+}, make NMDA receptors critical for multiple forms of synaptic plasticity (coincidence detection).

1.3.3 Basic properties of hippocampal long-term synaptic plasticity

NMDA receptor-dependent LTP of CA1 synapses is one of the best characterized forms of plasticity. As previously mentioned, the activation of NMDA receptors requires glutamate (and co-agonist glycine or D-serine) binding and the removal of the Mg^{2+} block by postsynaptic depolarization. These features make NMDA receptors the primary coincidence detectors of pre- and postsynaptic activation. The NMDA receptor-dependent synaptic plasticity of CA1 synapses thus has three characteristics (Fig. 3): (1) Input-specific: only those synapses that directly receive repetitive presynaptic stimulation will experience input strengthening, while their non-activated neighboring synapses will not. This can be explained by the localized of Ca^{2+} influx through NMDA receptors. (2) Cooperative: plasticity can only be induced if a sufficiently large number of presynaptic fibers are activated simultaneously. This is due to the necessity of depolarization for NMDA receptor activation. (3) Associative: if synapses on the same cell are activated by weak, sub-threshold stimuli, but their activation is paired with a strong, LTP-inducing stimulus at another set of synapses, LTP can still be induced (Malenka, 2003).

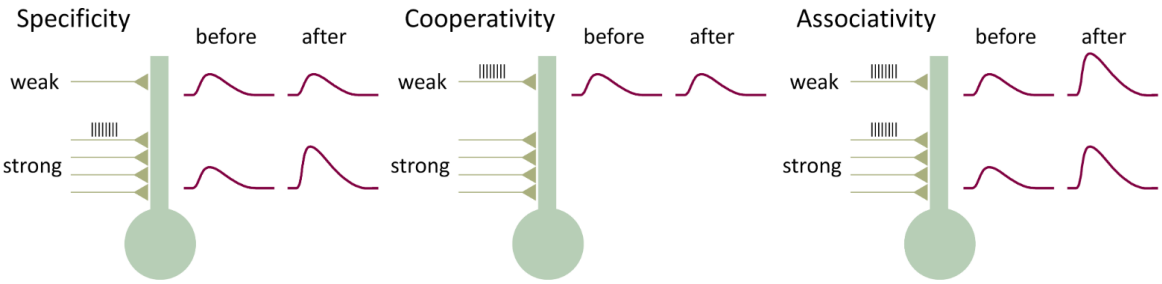

Figure 3: Basic properties of long-term potentiation

The key features of synaptic potentiation in hippocampus. Image from textbook "Cellular Neurophysiology", Stony Brook University Library. Image created by David McKinnon.

The key ion in NMDA-dependent plasticity is Ca^{2+}. During the plasticity induction phase, Ca^{2+} floods into spines through activated NMDA receptors and acts as an intracellular second messenger to initiate the process of plasticity expression (Bliss & Collingridge, 1993).

1.3.4 The bidirectional synaptic strength modification and STDP

Specific patterns of neuronal activity can induce NMDA receptor-dependent LTP and LTD in hippocampal area CA1 (Malenka, 1994). Conventionally, high frequency stimulations (HFS, e.g 100 Hz, 1 second, Berretta et al., 1991) induces LTP and prolonged low frequency stimulation (LFS, e.g 1 Hz, 15 minutes, Dudek & Bear, 1992; Mulkey & Malenka, 1992) induces LTD. HFS allows a sufficiently strong summation of EPSPs that depolarizes the postsynaptic membrane, whereas prolonged LFS induces a mild but sustained depolarization of the postsynaptic membrane (Lüscher & Malenka, 2012). As a result, HFS leads to a strong Ca^{2+} influx, whereas LFS induces a modest but prolonged Ca^{2+} influx (Malenka & Bear, 2004; S. N. Yang et al., 1999). Strong Ca^{2+} influx tends to activate protein kinases and leads to LTP, while modest Ca^{2+} influx results in preferential activation of phosphatases and leads to LTD (Fig. 4).

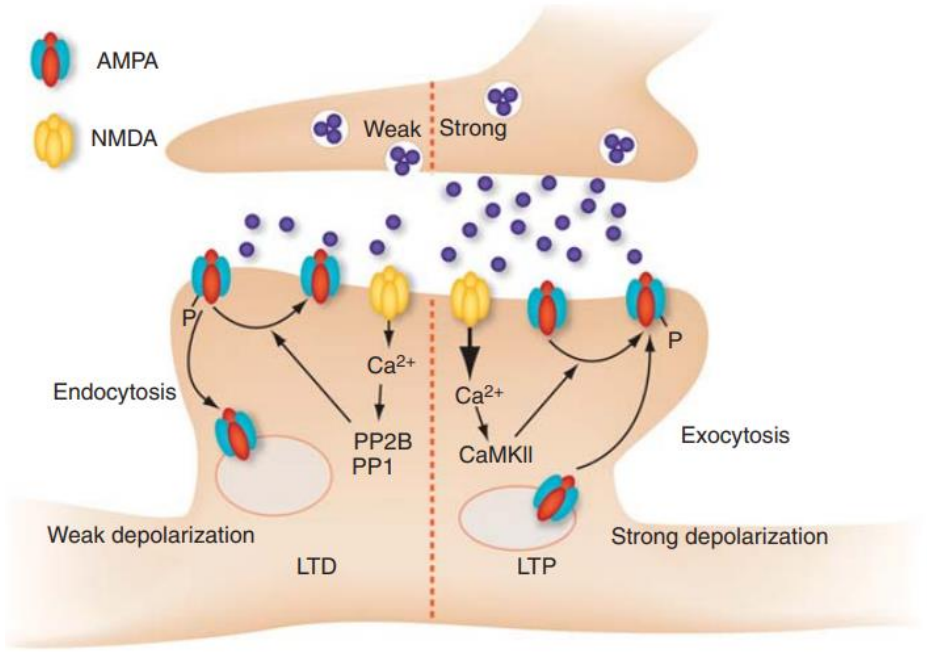

Figure 4: Expression mechanisms of NMDA-dependent LTP and LTD

Weak depolarization (left) initiated by weak activity of pre-synapses results in a modest activation of NMDA receptors and leads to a modest Ca^{2+} influx. This mild elevation of Ca^{2+} preferentially activates protein phosphatases, which causes endocytosis of AMPA receptors. Strong depolarization (right) initiated by strong activity of pre-synapses triggers strong Ca^{2+} influx that further results in AMPA receptors exocytosis in part due to CaMKII activity. Image from Lüscher & Malenka, 2012.

These induction protocols allow the investigation of molecular mechanisms involved in LTP or LTD and provide candidate models for characterizing the synaptic basis of memory (Bliss & Collingridge, 1993; Siegelbaum & Kandel, 1991). One can, however, hardly imagine regular HFS or LFS spiking patterns happening *in vivo* (Softky & Koch, 1993). A more physiological plasticity induction protocol has been characterized more recently, where LTP/LTD can be induced by pairing the pre- and postsynaptic cells with appropriate timing, termed spike-timing-dependent plasticity (STDP, Caporale & Dan, 2008; Dan & Poo, 2006).

The learning rule proposed by Hebb in 1949 (Hebb, 1949) is often summarized as "fire together, wire together" (Shatz, 1992), meaning that if pre- and postsynaptic activation arrives simultaneously, that synaptic connection will strengthen. However, in 1983, an *in vivo* characterization of precise temporal requirements for the induction of synaptic plasticity in EC-DG connections revealed that the synaptic strength strongly depends on the order of pre- and postsynaptic stimuli (+/- 20ms) (Levy & Steward, 1983). This phenomenon was further demonstrated by experiments performed in the hippocampus (Debanne et al.,

1998; Magee & Johnston, 1997) and cortex (Markram et al., 1997). Furthermore, a narrow temporal window for the time-dependent induction of LTP/LTD (tLTP/tLTD) between excitatory cells (Fig. 5A, B) was characterized *in vitro* (Bi & Poo, 1998) and *in vivo* (Zhang et al., 1998).

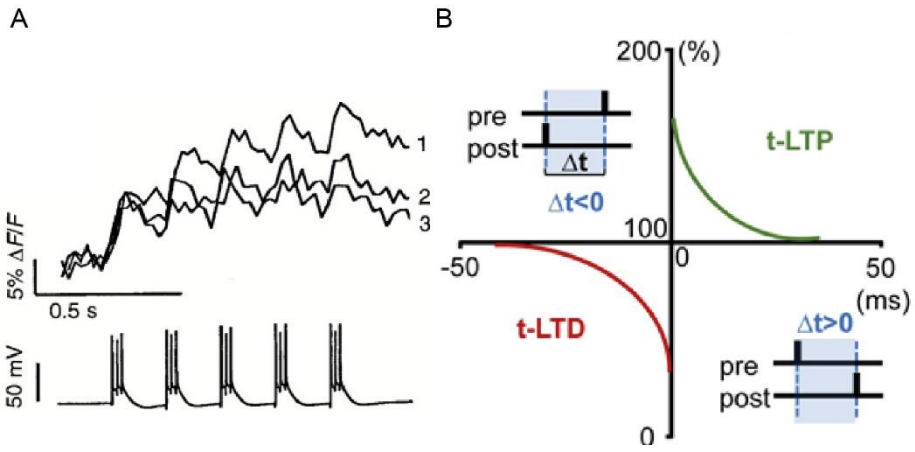

Figure 5: induction of STDP

A. (Upper) Increase in Ca^{2+} concentration at paired neuron's dendritic tree, induced by pairing the trains of subthreshold EPSPs and action potentials. The pairing protocol increased dendritic Ca^{2+} concentration. (Lower) Somatic voltage shows the pairing of both action potential and subthreshold EPSP trains. Images from Magee & Johnston, 1997. B. STDP in hippocampus CA3-CA1 follows the classical spike timing pairing. Image from Andrade-Talavera et al., 2023.

Previously in the lab, long-lasting synaptic changes (at least 3 days in the hippocampus) in the form of tLTP and tLTD were induced all-optically (Fig. 6) using a similar temporal window as in Fig. 5B (Anisimova et al., 2022). This was accomplished by using an optogenetic method based on channelrhodopsin tools to spike the pre- and postsynaptic neurons and the STDP protocol characterized by Magee & Johnston (Magee & Johnston, 1997) and Wittenberg & Wang (Wittenberg & Wang, 2006). The CA3 presynaptic neurons expressing ChrimsonR were activated by red lights versus the CA1 postsynaptic neurons expressing CheRiff were activated by violet lights (Fig. 6A). The acutely induced tLTP and tLTD (Fig. 6B, C) can be detected as input strength potentiation after 3 days (Fig. 6D, E).

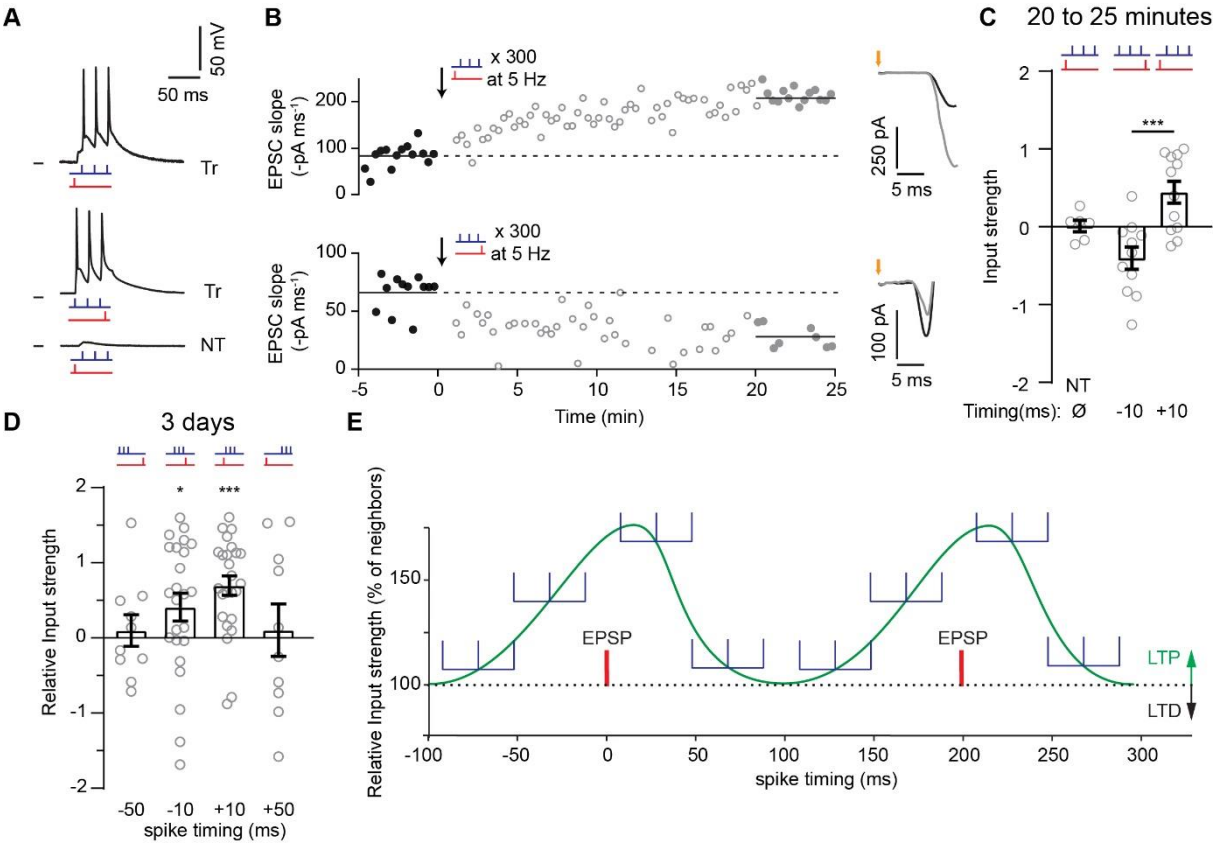

Figure 6: all-optical induction of STDP

Images adapted from Anisimova et al., 2022. A. All-optical STDP induction protocol. Current-clamp recordings from CA1 neurons during causal, anti-causal and control pairing (from top to bottom, tLTP induction, tLTD induction and control, respectively, Tr: CheRiff transfected, NT: non-transfected). Pre-synaptic cells are activated by red flashes (EPSPs), and the post-synaptic patched neuron is activated by theta-burst violet flashes (bAPs). Black ticks at left indicate −70 mV B. Representative experiments. Causal pairing induced tLTP (top), and anti-causal pairing induced tLTD (bottom). C. Normalized change in EPSC slope 20–25 min after oSTDP induction as in B (NT, n = 6; causal, n = 12; anti-causal, n = 11) ∗∗∗P = 0.0003, On-way ANOVA followed by Sidak's multiple comparisons. D. Normalized input strength of CheRiff-CA1 neurons 3 days after 300 pairings of single presynaptic and 3 postsynaptic spikes at 5 Hz. During anticausal pairing the last postsynaptic spike occurred −50 or −10 ms before the EPSP. During causal pairing the first postsynaptic spike occurred +10 or + 50 ms after the EPSP. n = 10; 24; 25; 10 (left to right). ∗P < 0.05, ∗∗∗P < 0.001. One-way ANOVA followed by Dunnett's multiple comparisions. E. Mean input strength (data from E) as a function of timing between EPSPs (red) and postsynaptic spike bursts (violet, at mean) at 5 Hz repetition frequency. Two complete cycles are illustrated.

The mechanisms and temporal window necessary for STDP are different in different CNS regions and cell types. In general, in the hippocampus STDP is NMDA-dependent (Nishiyama et al., 2000) and under experimental conditions the depolarization of the postsynaptic membrane is due to the back-propagation action potentials (bAP) of postsynaptic neuronal activation (Magee & Johnston, 1997). Similar to HFS-LTP and LFS-LTD,

pre-post timing leads to a strong Ca^{2+} entry and post-pre timing induces a milder Ca^{2+} entry (Koester & Sakmann, 1998).

Compared to HFS- and LFS-induced LTP/LTD, STDP emphasizes the critical role of causality in determining the alteration of synaptic strength, as implied by Hebb's original postulate (Caporale & Dan, 2008). Computationally, the STDP learning rule filters out delayed input signals (considered noise) which do not contribute to neuronal firing. It also improves resource efficiency by reducing energy and material consumption at synapses that do not reliably induce postsynaptic action potentials.

1.3.5 Molecular mechanism of hippocampal synaptic plasticity

While different neuronal activity patterns initiate the induction of synaptic plasticity by triggering Ca^{2+} influx, the amplitude and frequency of postsynaptic calcium influx determine whether plasticity shifts toward LTP or LTD (Artola et al., 1990). This calcium-based theory of plasticity was coined 'the calcium hypothesis' (J. Lisman, 1989) at its time, and has since been extensively validated. Ca^{2+} binds to calmodulin (CaM) and forms the Ca^{2+}/CaM complex with very fast kinetics, allowing rapid dynamic buffering of intracellular Ca^{2+} concentration as well as the activation of downstream signaling. A critical kinase activated by the Ca^{2+}/CaM is CaMKII. CaMKII activation facilitates synaptic plasticity through its autophosphorylation feature, which maintains the kinase in an active state independent of calcium/calmodulin. This prolonged activity allows for the sustained phosphorylation of key postsynaptic density proteins, such as AMPA receptors.

In addition to CaMKII activation, changes in Ca^{2+} concentration also trigger the activation of other important signaling pathways, such as cAMP-dependent protein kinase A (PKA), protein kinase C (PKC), mitogen-activated protein kinases, protein phosphatases, including calcineurin (CaN) and protein phosphatase 1 (PP1) (Bliss & Collingridge, 1993; J. Lisman, 1989; J. Lisman et al., 2002; Malenka & Nicoll, 1999; Mulkey et al., 1993, 1994; Sweatt, 2004). Activation of these enzymes mediates several synaptic plasticity expression events, including the exocytosis and endocytosis of AMPA receptors and changes in AMPA and NMDA receptor conductance and open probability (Carroll et al., 2001; Malinow & Malenka, 2002). These processes also influence the rapid morphological changes in the

synapses, for example, spine head growth or shrinkage (Matsuzaki et al., 2004; Q. Zhou et al., 2004), termed structural LTP and LTD (sLTP/sLTD).

Additionally, according to the synaptic tagging and capture hypothesis, synaptic activity triggers the expression of synaptic 'tags' which guide the 'capture' of plasticity-relevant proteins during the late phase of synaptic plasticity (Frey & Morris, 1997). In parallel, retrograde signaling pathways, including nitric oxide (NO) and BDNF, are activated and alter presynaptic properties, such as vesicle release probability (Castillo, 2012; Zakharenko et al., 2003). Maintenance of the late phase of synaptic plasticity (days) typically requires protein synthesis, initiated by PKA, PKMζ, extracellular signal–regulated kinase (ERK), CaMKIV, and other signaling molecules (Citri & Malenka, 2008; Sacktor, 2008; G. M. Thomas & Huganir, 2004). This is regulated by the activation or expression of transcription factors, for example, c-Fos, one of the most studied immediate-early genes (G. M. Thomas & Huganir, 2004). The synthesis of the new proteins that are critical for plasticity maintenance is either produced by nuclear transcription and translation (Sacktor, 2008) or by translation existing mRNAs at the synaptic site (Sutton & Schuman, 2006). These newly produced proteins support the changes that are necessary for synaptic potentiation, such as AMPA receptor stabilization and anchoring (Carroll et al., 2001; Malinow & Malenka, 2002; Sacktor, 2008), the formation of CaMKII/GluN2B stable binding (Barcomb et al., 2016; K. U. Bayer et al., 2006) and the structural remodeling of the synapse (J. E. Lisman & Zhabotinsky, 2001; Lüscher et al., 2000).

Initiated by Ca^{2+} influx, many molecules that support synaptic plasticity respond rapidly to external stimuli and translocate to activated dendritic spines. Further, activated downstream messenger molecules spread along the dendritic tree, neighboring spines, and the nucleus. The temporal and spatial regulation of plasticity-relevant signaling pathways is highly organized (Fig. 7). The typical size of a dendritic spine head is around 0.01 to 1 μm^3, while the spine neck that connects to the dendrite is relatively narrow (diameter ~0.1 μm) and long (0.1 to 1 μm) (Harris & Stevens, 1989). The narrow spine neck creates a diffusion barrier between the spine head and dendrite that reduces the diffusional exchange rate of second messengers (Müller & Connor, 1991). This compartmentalized machinery provides the structural basis for temporal and spatial regulation of signaling pathways and further ensures the coordination of downstream cellular processes in different dendritic microdomains (Yasuda, 2017).

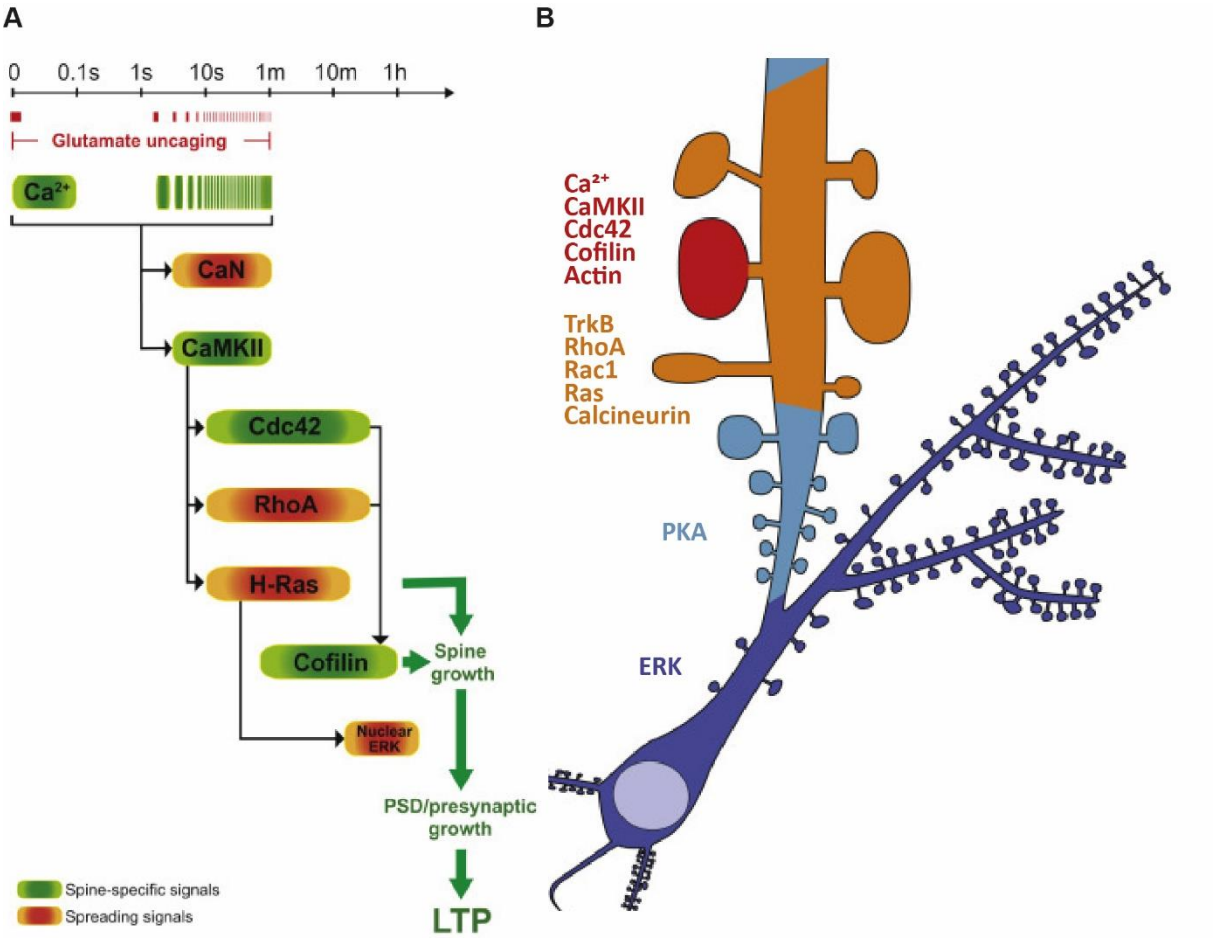

Figure 7: Temporal and spatial regulation of intracellular signaling.

A. Timeline of spine-specific signaling (green) and other spreading signaling (red) when LTP was induced in single spines using glutamate uncaging. B. Spatial distribution of potentiation-related signaling that starts at the stimulated spines (red), spreads to neighboring spines and dendrites (orange and cyan), and that reaches the nucleus (violet). Images adapted from Nishiyama & Yasuda, 2015; Yasuda, 2017

1.4 CaMKII

As briefly mentioned above, CaMKII is one of the most critical signaling factors in synaptic plasticity. Early studies revealed that CaMKII expression in the hippocampus becomes abundant by the second postnatal week, accounting for about 2% of the total protein and about 10% of the PSD protein. Such expression levels are comparable to those of cytoskeletal proteins (Burgin et al., 1990; Kennedy et al., 1983; Sheng & Hoogenraad, 2007) suggesting that CaMKII is important for synaptic functions and structure. In the following sections, I will discuss the mechanisms involved in CaMKII regulation of synaptic plasticity. There are four CaMKII isoforms: -α, -β, -γ and CaMKIIδ. In the CNS, CaMKII holoenzymes consist primarily of -α and -β subunits (Bennett et al., 1983). In the following sections, I will mainly discuss the properties of CaMKIIα.

1.4.1 CaMKII structure and activation regulations

CaMKII, activated by Ca^{2+}/calmodulin (CaM), functions as a serine/threonine protein kinase and assembles into a dodecameric complex (Rellos et al., 2010). The unique structure of CaMKII facilitates its function in modulating synaptic physiology and strength. CaMKII operates as a holoenzyme comprising a kinase domain, a regulatory domain, and an association domain (Chao et al., 2011; Hudmon & Schulman, 2002) (Fig. 8A). The regulatory domain contains two key phosphorylation sites: T286 and T305/T306. Under basal Ca^{2+} conditions, CaMKII is locked at the inactivated form: the regulator domain binds to the kinase domain by T286 and kinase domain T site interaction, blocking the entry to the kinase domain substrate binding site (S site). During Ca^{2+} influx triggered by synaptic activity, Ca^{2+}/CaM binds to the regulatory domain and subsequently activates the kinase domain S site, enabling the catalytic activity of CaMKII. In addition, the kinase domain T site and regulatory domain T286 are exposed, enabling the formation of reciprocally activating complexes, such as the CaMKII/GluN2B complex and T286 autophosphorylation. Such autophosphorylation further allows the Ca^{2+}/CaM-independent partial activation of CaMKII, termed the autonomous state (Hanson et al., 1989; J. Lisman et al., 2002) (Fig. 8B). Furthermore, T286 phosphorylation enhances the CaMKII affinity to Ca^{2+}/CaM by 1000 fold, in a process called 'CaM trapping': when the Ca^{2+} levels fall, Ca^{2+}/CaM remains bound to CaMKII for an extended period of time (Meyer et al., 1992). Such a significant increase in affinity is due to the different dissociation time between Ca^{2+}/CaM from phosphorylated

CaMKII (minutes) and from non-phosphorylated CaMKII (about 1 sec) (Chang et al., 2017, 2019).

On the other hand, the T305/306 site is located closer to the central hub and autophosphorylation at this location is, contrary to the T286 site, inhibitory. When Ca^{2+}/CaM dissociates from the kinase phosphorylated at T286, the autophosphorylation occurs at T305 /T306. These sites are within the CaM binding domain, thus preventing rebinding of Ca^{2+}/CaM, even if the phosphorylation of T305/T306 does not directly inhibit the CaMKII kinase activity (Hanson & Schulman, 1992). Phosphorylation sites T286 and T305/306 play distinct roles on gating synaptic LTP versus LTD (Cook et al., 2021).

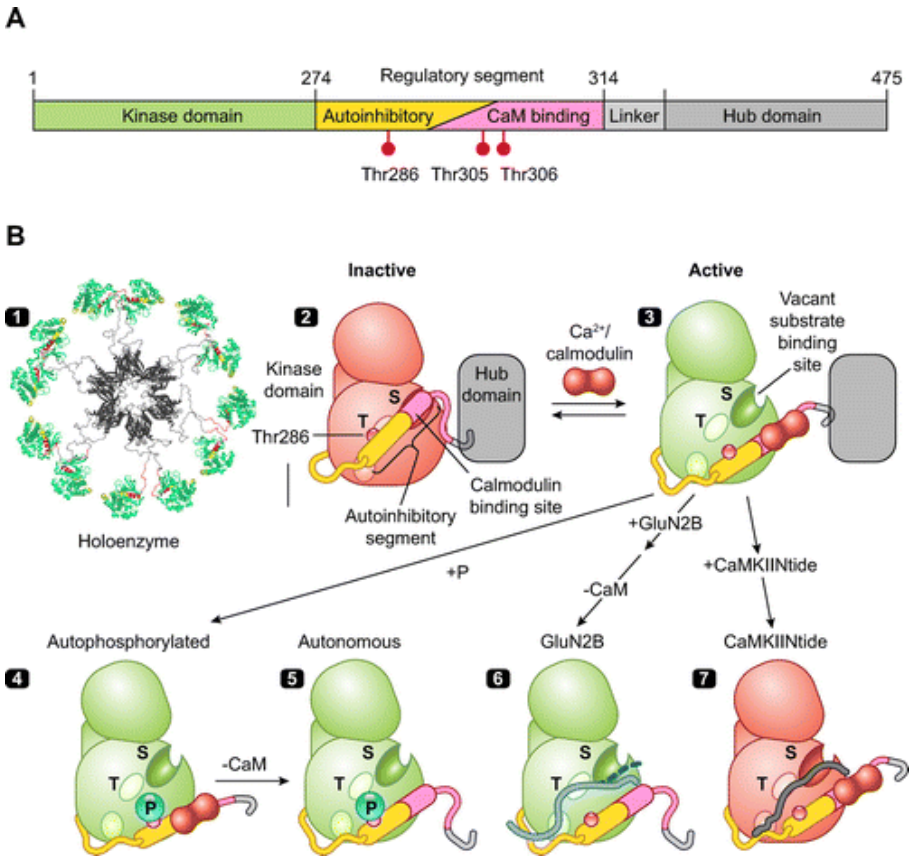

Figure 8: The structure and basic regulatory mechanism of CaMKII.

A. The domain structure. The 12 CaMKII isoforms are bounded by the association domain (hub domain), forming the donut shape holoenzyme structure. The regulatory domain regulates CaMKII activity by phosphorylation on T286 and T305/T306, upon the stimulation of Ca^{2+}/CaM binding. The kinase domain, which is autoinhibited at resting Ca^{2+} level, is released by the regulatory domain at elevated levels of Ca^{2+}. B. (1) The structure of CaMKII holoenzyme. (2-3) The regulation of CaMKII activation/inhibition upon Ca^{2+}/CaM binding. (4-6) CaMKII can be persistently activated by either autophosphorylation of T286 or by the NMDA receptor subunit GluN2B binding even when Ca^{2+} returns to the baseline level. (7) The application of a regulatory domain-competitive CaMKII inhibitor deactivates CaMKII. Image from Nicoll & Schulman, 2023.

1.4.2 CaMKII in memory and synaptic plasticity

Pharmacological or genetic blockade of postsynaptic CaMKII activity impairs LTP induction (Giese et al., 1998a; Incontro et al., 2018; Malenka et al., 1989; Malinow et al., 1989; Xiao et al., 2023) and memory formation (Giese et al., 1998b; Silva et al., 1992; Yamagata et al., 2009). On the other hand, acute application or transfection of activated CaMKII induces a 2 to 3-fold enhancement of AMPA EPSCs without effects on NMDA currents, meaning that CaMKII activation mimics behavior of HFS-induced LTP (Incontro et al., 2018; Jourdain et al., 2003; Shirke & Malinow, 1997). Further LTP induction is impaired by prior CaMKII activation, as LTP is already saturated (Lledo et al., 1995; Pettit et al., 1994). However, the role of CaMKII in LTP maintenance is still under debate (Sacktor & Fenton, 2018). In the following sections, I will discuss the molecular mechanisms of CaMKII-related changes in synaptic plasticity at different stages and examine the tools available for CaMKII manipulation.

1.4.2.1 Frequency decoder

As discussed above, the amplitude and frequency of postsynaptic Ca^{2+} events determines whether plasticity shifts towards LTP or LTD (Artola et al., 1990). CaMKII acts as a primary frequency decoder of Ca^{2+} influx. This property was first observed *in vitro*: kinase activity assays showed that CaMKII activation was modulated by the amplitude and duration of spikes in Ca^{2+} concentration (De Koninck & Schulman, 1998). By performing live-imaging of CaMKII activity using Camuiα (a CaMKII activity sensor, see discussion in 1.4.4) while uncaging glutamate at different frequencies, Chang and co-authors showed that at the single-spine level, CaMKII serves as a leaky integrator of Ca^{2+} pulses (Chang et al., 2017). This frequency-sensing function depends on T286 autophosphorylation and CaM trapping. As illustrated in Fig. 9, when high frequency stimulation is delivered, high frequency Ca^{2+} transients lead to Ca^{2+}/CaM accumulation near CaMKII, which increases the probability of Ca^{2+}/CaM binding and inter-subunit T286 autophosphorylation. CaM trapping is triggered by autophosphorylated subunits, and therefore the probability of next Ca^{2+}/CaM binding before next Ca^{2+} pulse is enhanced, enabling Ca^{2+} signal integration. When the stimulation is delivered at low frequency, or when the T286 autophosphorylation is dysfunctional (e.g. T286A mutation), CaMKII is inactivated during the pulse interval driven by Ca^{2+}/CaM dissociation. Taken together, the structure and function of CaMKII allows integration of

activity during different frequencies of stimulations and different CaMKII activation patterns have the potential of changing the sign of synaptic plasticity.

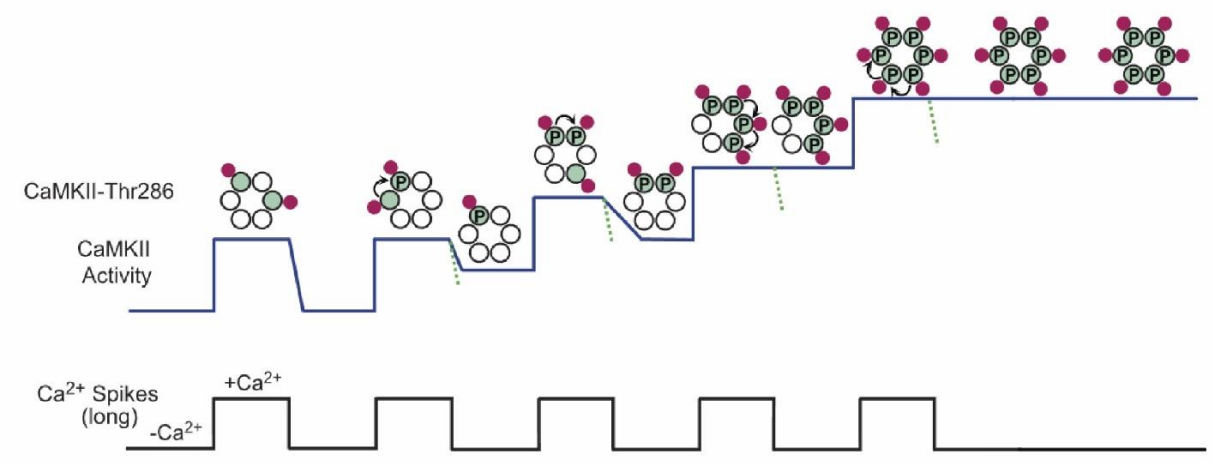

Figure 9: CaMKII integration of Ca2+ pulses.

Blue line: CaMKII activity integration. Black line: Intracellular Ca2+ level. Red circles: Ca2+/CaM binding to CaMKII. Green/white circles: activated/inactivated subunits. Image adapted from Nicoll & Schulman, 2023.

1.4.2.2 Activity-triggered translocation of CaMKII

Like other kinases, CaMKII is a slow enzyme, which means that tethering CaMKII near the substrates is critical for achieving efficient catalytic activity. Chemical LTP stimulation induces rapid translocation and accumulation of CaMKII to the PSD in a spine-specific manner (Fig. 10), and this rapid cluster of CaMKII persists for 30 minutes to several hours (Lee & Yasuda, 2009; Otmakhov et al., 2004; Shen & Meyer, 1999; Zhang et al., 2008). Conversely, chemical LTD stimulation selectively induces CaMKII translocation to inhibitory spines (Cook et al., 2021; Marsden et al., 2010).

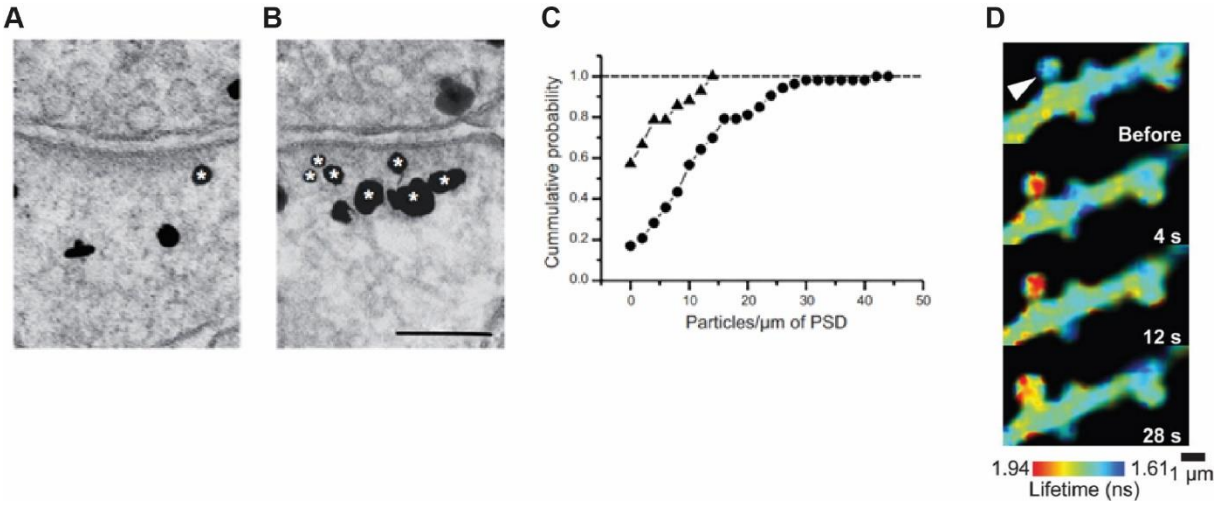

Figure 10: LTP induction induced CaMKII accumulation at PSD.

A-B. Under electron microscopy (EM), compared to the control condition (A), after cLTP induction (B), there is an increased proportion of PSD-associated CaMKII (white asterisks). Scale bar: 100 nm. C. Cumulative distribution of PSD-associated CaMKII, under control conditions (triangles) or cLTP (dots) conditions. Image adapted from Otmakhov et al., 2004. D. High-frequency glutamate uncaging triggers CaMKII accumulation in single spines. Image adapted from Lee et al., 2009.

1.4.2.3 CaMKII-NMDA receptor interactions: The CaMKII-GluN2B complex

The rapid and sustained translocation of CaMKII is driven by its interaction with CaMKII-associated proteins (CAMKAPs). An important CAMKAP is the GluN2B NMDA receptor subunit. As mentioned above (1.4.1, Fig. 8), similar to T286 phosphorylation, CaMKII binding GluN2B locks CaMKII in the activated state and facilitates its catalytic activity. This interaction acts as a long-term molecular memory mechanism during synaptic plasticity (Bayer et al., 2001). Many studies have shown that disruption of CaMKII-GluN2B complex formation also impairs LTP, spine stabilization and spatial learning (Barria & Malinow, 2005; Incontro et al., 2018; Y. Zhou et al., 2007), while rescue of CaMKII-GluN2B binding ability also rescues LTP (Tullis et al., 2023). The CaMKII-GluN2B complex is rather stable, as it is not only independent of sustained Ca^{2+}/CaM binding, but it is also protected from phosphatases (Mullasseril et al., 2007). Due to these properties, it is thought to be the underlying mechanism for synaptic plasticity maintenance. In addition, CaMKII-GluN2B binding stabilizes CaMKII anchoring at the PSD, which enables its proximity not only to the source of external Ca^{2+} (NMDA receptors), but also to the downstream factors involved in LTP formation, such as AMPA receptors.

1.4.2.4 CaMKII-AMPA receptor interactions

As discussed in 1.3.5, the regulation of AMPA receptor conductance and the trafficking of AMPA receptors to the PSD are involved in the expression of LTP. CaMKII is able to gate single AMPA receptor conductance by phosphorylating the GluA1 subunit at site S831 (Derkach et al., 1999; Kristensen et al., 2011). However, LTP did not appear to be impaired in S831A knock-in mice, suggesting that CaMKII-mediated AMPA receptor conductance gating is not necessary for LTP (Lee et al., 2003, 2010). The dominant mechanism is CaMKII-mediated trafficking of AMPA receptors to the PSD. Using a photoactivatable CaMKII (see discussion in 1.4.4), it was shown that the activation of CaMKII itself triggers rapid insertion of AMPA receptors into activated spines (Shibata et al., 2021). This insertion is based on exocytosis of AMPA receptor-containing vehicles to the plasma membrane. Activated CaMKII mediates exocytosis mainly by regulating the Rho GTPase family, the RAS-ERK signaling pathway, transmembrane AMPAR regulatory proteins, vesicle fusion machinery proteins (e.g., syntaxin-3), and the actin motor myosin V (Herring & Nicoll, 2016). In addition, inserted AMPA receptors are stabilized at the PSD by immobilization. CaMKII phosphorylates stargazin, a member of the transmembrane AMPA receptor regulatory protein (TARP) family. Stargazin phosphorylation promotes the interaction between AMPA receptors and postsynaptic density protein 95 (PSD-95), thereby driving the translocation of AMPA receptors from extrasynaptic sites into the synapse. This phosphorylation event also reduces the mobility of AMPA receptors within the synaptic membrane region (Bats et al., 2007; Opazo et al., 2010).

1.4.3 CaMKII for plasticity maintenance and late memory

As I addressed earlier, it is generally agreed that CaMKII activation is critical for LTP induction, while its role in plasticity maintenance is debated. Live imaging of CaMKII activity showed that it is activated for only a few seconds to up to a minute, suggesting that CaMKII activation is only critical during the plasticity induction phase (Chang et al., 2017). In addition, using an optogenetic CaMKII activity inhibitor, paAIP2 (see discussion 1.4.4), it was shown that blocking CaMKII activation after plasticity induction does not impair LTP and fear memory (Murakoshi et al., 2017). On the other hand, some studies have reported that CaMKII activity, especially CaMKII-GluN2B interaction, is important for the maintenance of basal level synaptic strength (Barcomb et al., 2016; Sanhueza et al., 2011; Tao et al., 2021).

In addition, by using pharmacological inhibitors and optogenetic tools, it was found that inhibition of CaMKII after LTP induction erases LTP, suggesting that continuous CaMKII activity is necessary for LTP maintenance (Sanhueza et al., 2007, 2011; Tao et al., 2021). These discrepancies may be due to the insufficient specificity and efficacy of pharmacological inhibitors, as well as the limitations of current methods to follow neuronal physiological properties over extended periods of time.

1.4.4 Approaches to investigate CaMKII

In this subchapter I will briefly discuss the tools designed for CaMKII activity manipulation and readout that can be conveniently used in organotypic slice cultures.

1.4.4.1 Pharmacological inhibitors

To investigate the role of CaMKII in neuronal physiology, an intuitive strategy is to block CaMKII activity with inhibitors and monitor the putative changes in neuronal transmission or plasticity. The available pharmacological CaMKII inhibitors can be classified into three main groups: (1) CaM-competitive inhibitors; (2) peptide inhibitors; (3) ATP-competitive inhibitors (Brown & Bayer, 2024).

(1) The CaM-competitive inhibitors include KN62 and KN93 (Sumi et al., 1991; Tokumitsu et al., 1990). They function by inhibiting both the CaMKII enzymatic activity and CaMKII/GluN2B binding. Early work using these inhibitors showed that long-term functional and structural plasticity is impaired when CaMKII activity is blocked (Bortolotto & Collingridge, 1998; Harvey et al., 2008; Lee et al., 2009). However, in addition to that of CaMKII, these inhibitors interfere with the activity of CaMKIV, PKC, voltage-gated Ca^{2+} channels, and voltage-gated K^{+} channels (Rezazadeh et al., 2006).

(2) Peptide inhibitors are the most widely used inhibitors for studying the role of CaMKII in synaptic plasticity. They are based on two different inhibiting strategies. One class imitates CaMKII substrates and includes autocamide-3 and AIP (Ishida et al., 1998; Ji et al., 2003). The other strategy relies on mimicking the peptide domain that is close to the regulatory domain T site. These inhibitors include CN21 and CN27 (Buard et al., 2010; J. Lee et al., 2022). They all bind to the T and S sites, blocking both enzymatic and CaMKII/GluN2B interactions (Brown & Bayer, 2024). A major drawback of peptide inhibitors is that they have weak membrane penetration (Wang et al., 2022). However, by myristoylation or by fusing

them with a TAT sequence, cell penetration can be greatly improved (Buard et al., 2010; Wu et al., 2009).

(3) ATP-competitive inhibitors have been developed more recently. They work by occupying the CaMKII ATP binding pocket, thus the kinase activity is blocked without effects on the interaction of CaMKII and GluN2B (Barcomb et al., 2013). This type of inhibitor has been used to dissect the CaMKII enzymatic function and CaMKII/GluN2B binding function (Tullis et al., 2023).

1.4.4.2 Optical manipulations of CaMKII activity

Similar to the experimental advantages brought by channelrhodopsins, optogenetic tools that can manipulate CaMKII activity enable high temporal and spatial accuracy, which is crucial for examining CaMKII's role in different phases of synaptic plasticity.

1.4.4.2.1 Photoactivatable CaMKII activity inhibitor: paAIP2

Photoactivatable AIP2 (paAIP2) is a light-inducible CaMKII activity inhibitor, comprised of the fusion between a light-sensitive domain (light-oxygen-voltage domain 2, LOV2) and AIP2, an improved version of AIP (Fig. 11) (Murakoshi et al., 2017). Light illumination in the violet-blue range activates paAIP2 by undocking the Jα helix, thereby exposing AIP2 and enabling the CaMKII inhibition. The Jα helix spontaneously reverses to the closed conformation without light illumination and deactivates paAIP2. The application of paAIP2 enables the control of CaMKII activity with a high spatial and temporal accuracy, meaning that paAIP2 can be used to dissect the kinetics of CaMKII requirement for synaptic physiology. For example, it was found that paAIP2 activation blocked synaptic plasticity and memory, as expected, but did not reverse established LTP (Murakoshi et al., 2017).

1.4.4.2.2 Photoactivatable CaMKII: paCaMKII

In contrast to paAIP2, violet-blue light triggers CaMKII activation in paCaMKII-expressing cells. The paCaMKII molecule consists of the fusion between LOV2 and the regulatory domain of CaMKII. Upon illumination, the activated paCaMKII functions similarly to CaMKII activated by Ca^{2+}/CaM (Fig. 11) (Shibata et al., 2021). Using paCaMKII, it was found that without elevation of intracellular Ca^{2+}, acute CaMKII activation triggers functional and structural LTP by recruiting AMPA receptors to the CaMKII-activated spines, a process also dependent on Cdc42 signaling (Shibata et al., 2021). There are two potential concerns of

using paCaMKII: (1) In addition to the formation of holoenzymes, paCaMKII monomers can potentially form dimers. (2) Overexpression of CaMKII itself could have potential effects on CaMKII enzymatic properties, thereby altering synaptic physiology and memory. However, expression of paCaMKII is typically much lower than endogenous CaMKII isoforms (Shibata et al., 2021).

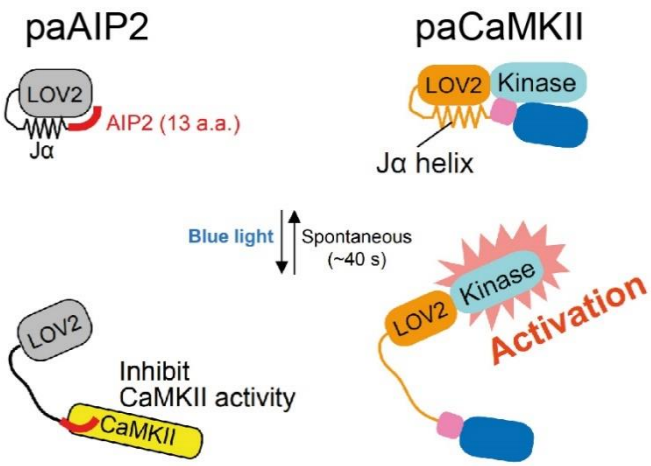

Figure 11: paAIP2 and paCaMKII.

Left: structure of paAIP2. Upon light illumination, AIP2 (red) is released and deactivates CaMKII. Right: structure of paCaMKII. Upon light illumination, the autoinhibition of CaMKII through its regulatory domain (blue) is released and CaMKII is activated. Murakoshi et al., 2017 and Shibata et al., 2021.

1.4.4.3 Sensors

As discussed above, both the activation and movement of CaMKII are critical for the development of synaptic plasticity. In order to monitor the activation of CaMKII, sensors based on fluorescence resonance energy transfer (FRET)/fluorescence lifetime (FLIM) have been developed. These mainly rely on the conformational changes of the holoenzyme induced by CaMKII activation. Camuiα is one of the early FRET-based sensors. It consists of a FRET pair of fluorescent proteins connected by CaMKII regulatory domain. When activated, it changes conformation which alters FRET efficiency (Takao et al., 2005). Using Camuiα and its variants, it has been demonstrated that while CaMKII autophosphorylation is essential for the optimal integration of Ca^{2+} signals during the induction phase of LTP, it is not required for LTP maintenance (Chang et al., 2017). Another type of FRET sensor that reports CaMKII activity is FRESCA, with its design based on substrate phosphorylation of PKC activity (Ardestani et al., 2019). More recently, CaMKAR has been developed, which also directly senses CaMKII activity based on substrate phosphorylation (Gaido et al., 2023). The CaMKII activity sensing generates changes in the fluorescence intensity of a circularly-permutated GFP. Finally, to monitor CaMKII location dynamically, GFP-tagged CaMKII (Shen & Meyer,

1999), photoactivatable/photoswitchable GFP-tagged CaMKII (Lee et al., 2009; Zhang et al., 2008) and FinGR intrabodies against endogenous CaMKII (Cook et al., 2021) have been used. Together, these tools allow direct readout of CaMKII localization and activity in living neurons.

1.5 Synaptic structure, function and plasticity

Dendritic spines are small, protruding structures that extend laterally from dendrites. As discussed briefly in 1.3.5, a typical spine comprises a bulbous head connected to the dendrite by a narrow neck, supported by scaffold proteins such as actin. Synapses, the connection between presynaptic boutons and postsynaptic spines, have been considered the site of memory and information storage. The structural and molecular remodeling of spines has been proposed to be one of the most critical mechanisms underlying these processes. Several types of imaging methods that are able to uncover synaptic structure have been developed. In this chapter, I will mainly discuss findings using live two-photon imaging and EM imaging methods.

1.5.1 Synaptic structural plasticity

In 2001, Matsuzaki and co-authors measured the AMPA current of each individual spine upon glutamate uncaging. They found a linear correlation between spine head volume and AMPA current (Fig. 12), suggesting that spine structure is tightly correlated with its function (Kasai et al., 2003; Matsuzaki et al., 2001). These results observed with live imaging are consistent with earlier EM imaging findings. Using nano-gold labeling of AMPA receptors, Nusser and co-authors demonstrated a positive correlation between AMPA receptor concentration and spine head volume (Nusser et al., 1998). Later, in 2004, it was found that in single spines high frequency (100 Hz for 1 s) glutamate uncaging induces long-lasting and input-specific functional (increased AMPA currents) and structural LTP (spine head volume enlargements, lasting over 100 min), and that changes in function and structure are again linearly correlated (Matsuzaki et al., 2004). Moreover, large spines are largely resistant to LTP while small spines are more plastic, suggesting that large spines are possibly the physical traces of long-term memory at the individual synapse level. Such a finding demonstrates that heterogeneity in spine volume may represent their heterogeneous roles in information encoding and storage. Furthermore, it has been shown that *in vivo*, memory formation is

associated with both new spine formation and spine head enlargement (Hofer et al., 2009; Holtmaat et al., 2006; G. Yang et al., 2009). Spine volume is also closely related to organelles distribution, as larger spines tend to contain more smooth endoplasmic reticulum (SER), mitochondria and polyribosomes (MacAskill & Kittler, 2010; Ostroff et al., 2002; Spacek & Harris, 1997). The PSD, characterized by the electron dense region located at the spine membrane, is a protein-dense stretch of membrane composed of neurotransmitter receptors, scaffolding proteins and diverse signaling molecules. Not only is the PSD size (or volume) tightly correlated with spine volume, but PSD enlargement is also observed during LTP induction and memory formation(Arellano et al., 2007; K. Harris & Stevens, 1989; D. Meyer et al., 2014; Woods et al., 2011). However, PSD changes in individual spines upon plasticity induction remains inconclusive (Borczyk et al., 2019; Bosch et al., 2014, 2014; K. M. Harris et al., 2024; D. Meyer et al., 2014; Śliwińska et al., 2020; Sun et al., 2021).

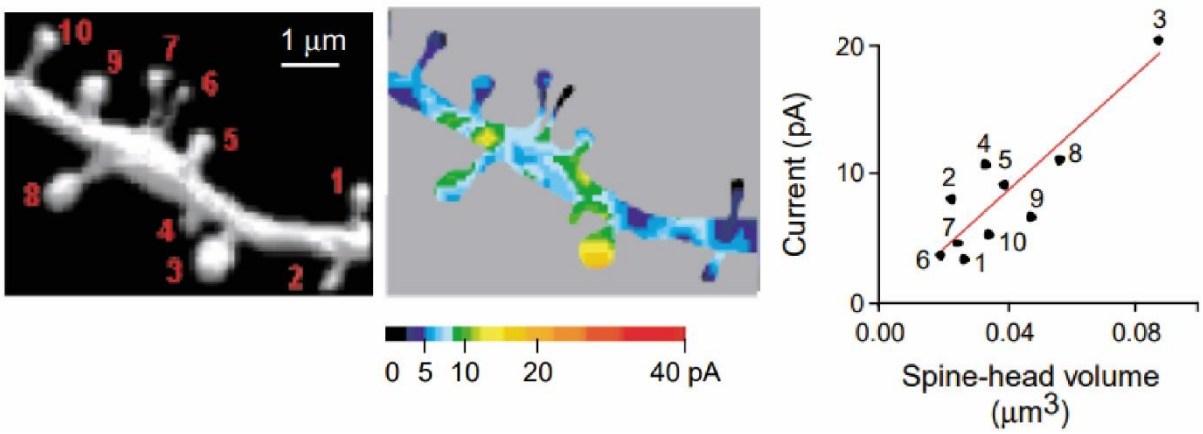

Figure 12: Spine structure and function.

Fluorescence image of a dendrite with spines in a CA1 pyramidal neuron (rat hippocampal slice) (Left) and the current responses recorded upon glutamate uncaging (middle). (Right) The correlation between spine volume and glutamate-evoked current, indicating the expression of functional AMPA receptors. Numbers on the plot refer to the spines on the left image. Images from Kasai et al., 2003.

1.5.2 Tracking synaptic structure with two-photon laser scanning microscopy

Spontaneous neuronal activity and synaptic changes are pervasive properties of the nervous system (Blankenship & Feller, 2010). The disruption of spontaneous neuronal activities in hippocampus leads to neuronal system functional also behavioral deficits (Smedler et al., 2022) and synapse morphological changes particularly in the CA1 region (Sando et al., 2017). Theoretical studies suggest that spontaneous activity is critical to

maintain a broad distribution of synaptic strengths. Synaptic diversity enhances robustness of neuronal network, which is a critical feature of the neural system (Eggl et al., 2023; Stepanyants et al., 2002). This feature is well preserved in organotypic hippocampus slice cultures (Garaschuk et al., 1998), but not in acute brain slices, which are largely silent.

Synaptic plasticity does not occur in isolation, but is a network phenomenon, meaning that the dynamics of populations of synapses encode information. Therefore, it is desirable to monitor synapse dynamics at a relatively large scale, which allows observing how changes at individual synapses contribute to broader network dynamics, such as synchronization, oscillations, and network reorganization (Harvey & Svoboda, 2007; Kasai et al., 2010). Furthermore, tracking synaptic dynamics over a long period of time offers the opportunity to capture the difference between early and late phases of synaptic plasticity, providing insights into the time course of learning-related synaptic changes and how these changes are stabilized or reversed, which is critical for understanding long-term memory formation and maintenance. Large-scale, chronic imaging of synaptic structure is therefore desirable, and two-photon laser scanning microscopy (2PLSM, 2P imaging) is practical for achieving this goal.

Starting from traditional confocal microscopy techniques, the development of 2PLSM evolved quickly in the last decades. The concept of two-photon absorption/excitation was first described by Maria Göppert Mayer (Göppert-Mayer, 1931). Much later, by combining two-photon excitation with a laser scanner, 2PLSM was finally developed by Winfried Denk, James Strickler, and Watt W. Webb (Denk et al., 1990). Two-photon excitation is localized to the laser focus, preventing out-of-focus fluorescence and allowing for efficient wide-field detection without pinhole. In addition, by using long wavelength excitation photons (near-infrared), scattering and absorption of photons in biological tissue is significantly reduced, resulting in deeper optical penetration, less phototoxicity, and less bleaching. Essentially, by using a pulsed laser and beam focusing, 2PLSM achieves high temporal and spatial accuracy and minimal background noise. These advantages make 2PLSM ideal for chronic, repetitive imaging of organotypic hippocampal slice cultures.

1.5.3 Approaches to studying the plasticity of synaptic ultrastructure

Electron microscopy (EM) is a powerful tool for studying the ultrastructural components of synaptic plasticity, however identifying the specific synapse of interest

remains challenging. Attempts have been made to identify specific cells/structures of interest and in this chapter, I will discuss the advantages and limitations of these methods and whether they are suitable for investigating plasticity-induced synapse ultrastructural changes over time.

1.5.3.1 Theta-burst stimulation and control pathway

Brief theta-burst stimulation (TBS) can induce long-lasting LTP in the CA1 region of the hippocampus (Cao & Harris, 2012). Using a dual electrode approach, one can induce LTP in a subset of inputs (LTP circuit) while a simple stimulation of nearby axons provides the non-LTP control within the same slice (Fig. 13). Using this approach, structural changes due to synaptic plasticity have been discovered (discussed in more detail in 3.3.5). However, when considering the 'LTP' circuit, many synapses are potentiated simultaneously, potentially inducing homeostatic plasticity (i.e., depression) at non-stimulated synapses.

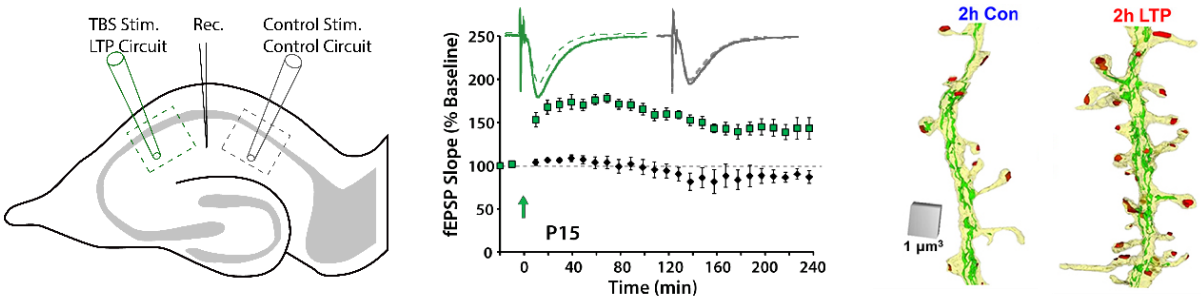

Figure 13: TBS-LTP and control pathway

Arrangement of stimulation electrodes (TBS and control) and recording electrode in hippocampal slice, *stratum radiatum* region. Squares represent the sampling of LTP and control samples for EM experiments. Middle: fEPSP slope shows that LTP was induced in the TBS circuit but not in the control. Right: Reconstruction from two circuits, two plasticity conditions, same hippocampal slice. Figure adapted from Cao & Harris, 2012; Harris, 2020

1.5.3.2 Genetic labeling methods

To identify the specific synapses of interest, a straightforward strategy is to label these synapses under EM. However, unlike LM, it is not possible to use multicolor fluorescent reporters because only gray-scale contrasts are visible under EM (Fig. 14). Cell-specific labelling for EM can be achieved by genetic transfection methods, inducing local DAB polymerization, which then reacts with osmium tetroxide to produce an electron-dense precipitate, or by attaching EM-visible nanoparticles to labeled structures. For the study of

synaptic ultrastructural plasticity in the hippocampus, the desired labeling strategy should be able to label synaptic structures globally and be easily combined with the expression of optogenetic tools. Antibody staining, which relies on secondary antibodies that can provide the electron-dense signal deposition (typically HRP or nanogold secondary antibodies), requires mild fixation of the tissue to preserve the antigenicity of the epitopes, with the trade-off of relatively poor ultrastructural preservation. Another issue is poor antibody penetration in tissue. Together, these caveats make antibody staining not suitable for 3D analysis of synaptic ultrastructure in tissue.

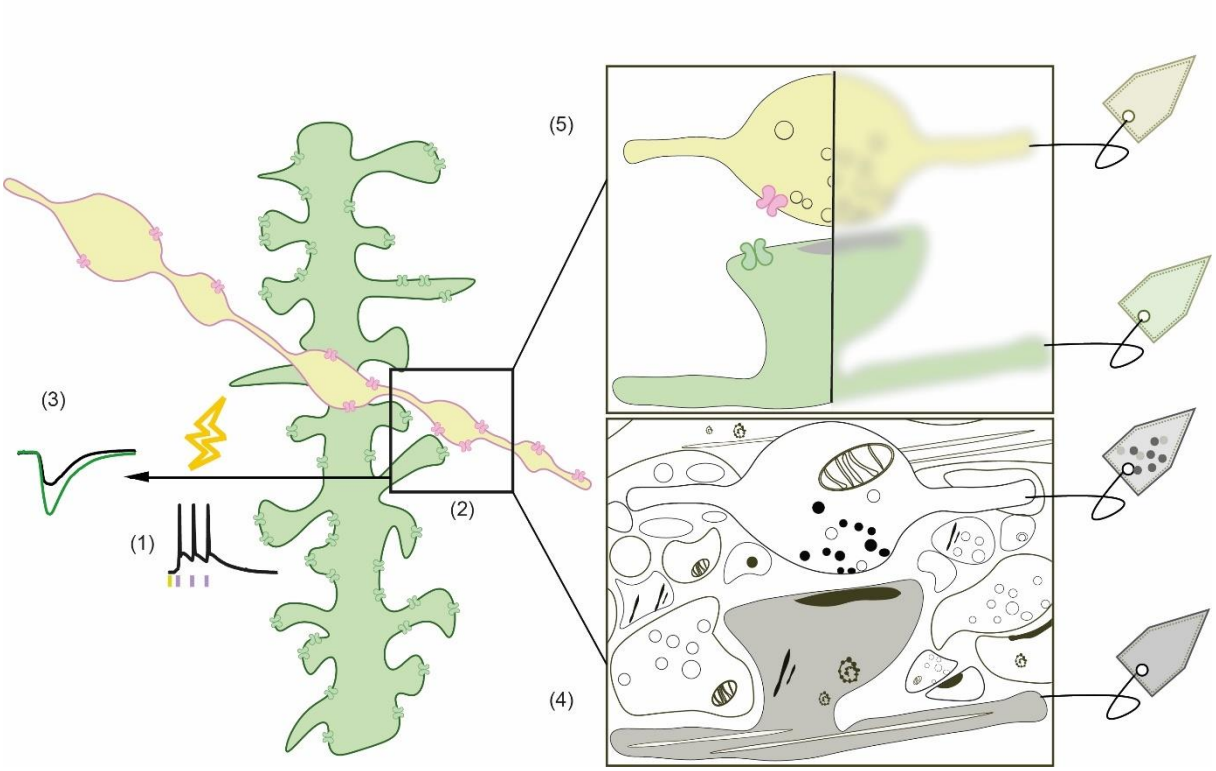

Figure 14: Identifying synapses of interest under LM or EM.

Using optogenetic tools based all-optical approach (1), STDP can be induced at synapses that connect two neurons expressing channelrhodopsins with distinct activation spectra (2), which persists for days (3). Co-expression of channelrhodopsins with pre- or post-synaptic specific tags allows localization of potentiated synapses in TEM (4). Compared to LM (5), EM offers higher resolution and unbiased imaging for ultrastructural analysis of synapses after optogenetic stimulation.

Peroxidase tags

Peroxidases are oxidoreductases that use hydroperoxide as the electron acceptor. This DAB-osmium tetroxide reaction locally produces an electron-dense precipitate, allowing EM studies of cells of interest. Engineering of peroxidases has enabled their localization to intracellular structures, e.g. synaptic vesicles, ER membrane, mitochondrial membrane or

matrix. Many studies used horseradish peroxidase (HRP) labeling, which provides very high signal sensitivity. The major drawback of HRP labeling is that this enzyme is inactive in the cell cytosol (Hopkins et al., 2000), which severely limits the application of HRP for genetic labeling. More recently, mutant ascorbate peroxidases (APEX) have been developed. The activity of APEX is present also in the cytosol (Martell et al., 2012), but APEX is not as sensitive as HRP. Several variants of APEX have been developed, such as APEX2 (Lam et al., 2015) and dAPEX2 (Zhang et al., 2019) which present higher signal sensitivity. By linking the peroxidase sequences to subcellular structure-specific genes, these peroxidases can tag many organelle compartments (enzyme-catalyzed proximity labeling).

Photocatalytic protein Tag

Illumination of EM-labeled photocatalytic proteins initiates intersystem crossing, locally generating singlet oxygen and enabling the DAB-osmium tetroxide reaction. These proteins are fluorescent which facilitates correlative imaging by light- and electron microscopy (CLEM method, discussed in 1.5.3.3). Based on this strategy, tools such as ReAsH (Lysova et al., 2018) and miniSOG (Shu et al., 2011) have been developed. However, the photooxidation step has to be performed very carefully ensuring perfect timing control, delicate supply of DAB, oxygen, local light illumination at low temperature and in a dark environment. In addition, possible fixation methods are very limited in order to avoid autofluorescence. Taken together, these considerations limit the application of photocatalytic protein tagging.

Nano-compartments Tag

More recently, a genetically encoded barcode labeling system called EMcapsulin (Sigmund et al., 2019, 2023) has been developed. The encoded encapsulin monomers, fused to metallothionein-3, assemble into a series of different sizes and layers with contrasting patterns. The size and shape of these particles are editable, and importantly, different from endogenous intracellular substructures which is convenient for automatic detection and segmentation of tag-expressing cells. These particles are stable under a wide range of fixation conditions. This labeling strategy has been used in multiple types of volume EM methods, making it highly suitable for automated volume-EM analysis. However, the label is not visible at low magnification, meaning that a fluorescent guidance signal is necessary for trimming sparsely labeled specimens after fixation. Moreover, the ability of these particles

to diffuse into very fine structures, especially the synaptic head and axonal bouton (my main interest) has not been tested.

1.5.3.3 Correlative light and electron microscopy (CLEM) method

CLEM is an imaging technique for correlating LM and EM images. One can use the LM signal, typically fluorescence images, as a reference to find the object of interest under EM. Importantly, CLEM is the distinct strategy to correlate functional 2PLSM imaging and EM imaging. After LM imaging, the sample is subjected to EM sample processing, which quenches fluorescence and enhances electron density contrast. The embedded sample is transferred to EM and the object of interest must be repositioned. Because using the LM image itself as reference is still tedious, additional fiducial markers are essentially required for more efficient relocation (e.g. electron-dense antibody labels or near-infrared markers) (Bishop et al., 2011). Alternatively, the specimen can be first embedded and LM imaging can be performed directly on this resin-embedded specimen, so-called post-embedding CLEM. In this case, relocation under EM is less difficult. However, this strategy requires a very high signal-to-noise ratio, ultra-stable fluorescent labels and very gentle fixation methods.

1.5.3.4 Volume electron microscopy

Volume electron microscopy (vEM) refers to an electron microscopy technique with which nanoscale structural details are revealed in 3D space (Fig. 15). The vEM technique enable the study of detailed geometry of synaptic connections at the nanoscale level ("connectomics"). In recent years, vEM and connectomics have progressed in parallel. The overall goal of vEM is to collect stacks of 2D EM images and reconstruct them in 3D. There are two classes of vEM techniques: scanning EM-based vEM (S-vEM) and transmission EM-based vEM (T-vEM). S-vEM combines the SEM with an *in-situ* specimen cutting technique (‘*in-situ* microtome’). Typically, the surface of the thick specimen is scanned by the electron beam, and after the collection of secondary electron beams for the surface layer, the surface of the specimen is removed (sliced) either by a diamond blade (serial block face SEM, SBF SEM) or an ion beam (FIB SEM). Another 3D SEM strategy is array tomography. By collecting serial sections on an appropriate substrate, such as a silicon wafer, the SEM can be performed on this array and a large XY field of view as well as Z-stacks can be achieved.

T-vEM techniques achieve a better resolution compared to S-vEM. However, collection of serial sections is essential for reliable 3D structure reconstruction. Due to the requirement of ultra-thin specimens (typically 30 nm), about 100 serially sectioned slices are needed for a complete reconstruction of a spines of interest (serial sectioning TEM, ssTEM).

In order to reduce the intensive workload of serial sectioning, thicker sections (up to 400 nm) can be cut and investigated by electron tomography: By serially tilting the sample inside the microscope and collecting transmitted electrons for each angle, the internal 3D structure can be computationally reconstructed. To generate a complete reconstruction of a synapse using tomography, only 4-10 serial sections are needed. However, compared to S-vEM and T-vEM of ultrathin sections, 3D reconstruction by tomography works only for a relatively small region - the synapse of interest has to be close to the tilt axis.

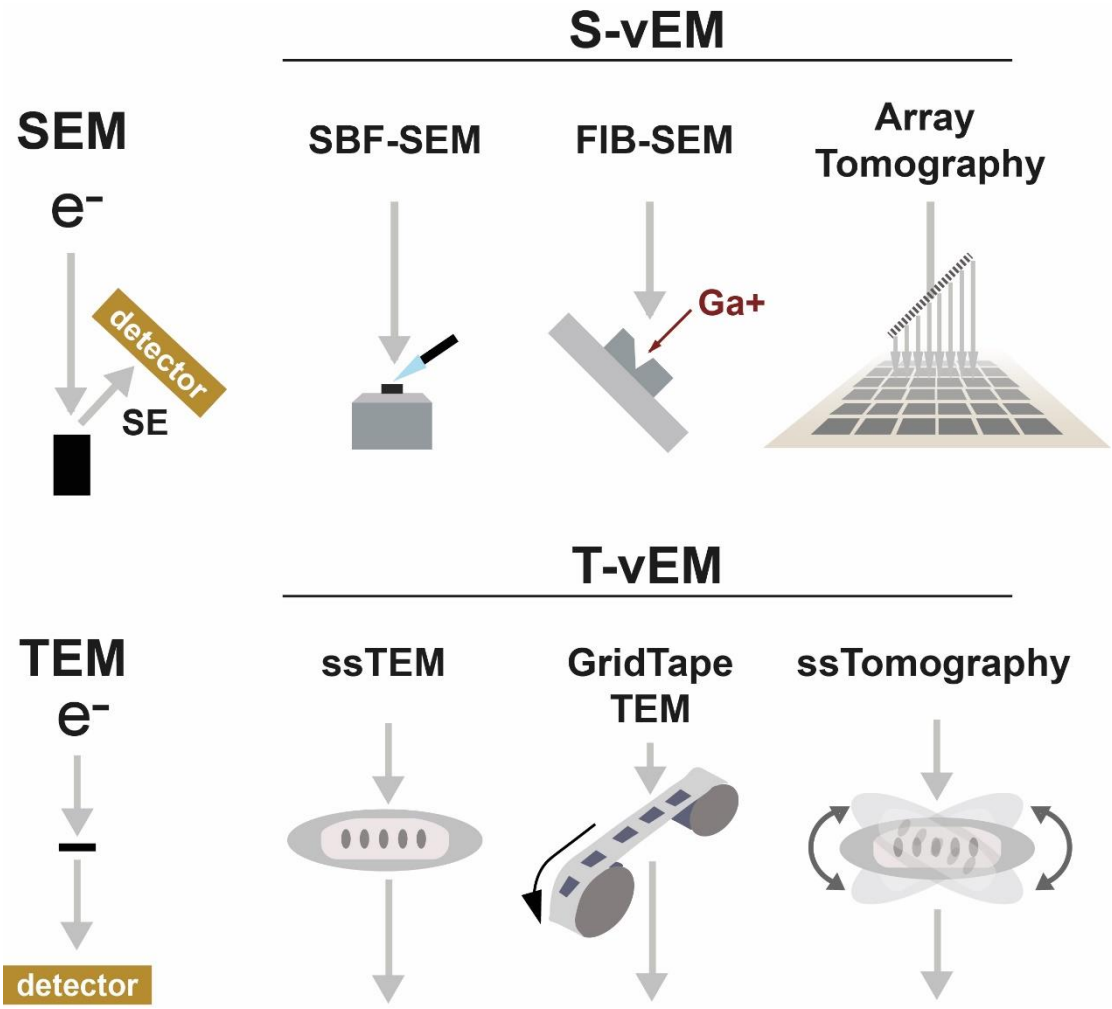

Figure 15: Volume electron microscopy.

Left: Illustrations of SEM vs. TEM. For SEM, the specimen is mounted on a stage and the electron beams of scanned over the surface of it. Secondary electrons (as well as backscattering electrons and

X-rays) were collected by the detectors. For TEM, the electrons pass through the specimen and the detector collects signals underneath. Upper right: SBF-SEM and FIB-SEM are SEM techniques that involve repeatedly removing the surface thin layers of the specimen, followed by the scanning of exposed surface. A diamond knife microtome is used in SBF-SEM and a focused gallium ion beam is used in FIB-SEM to mill the sample. Alternatively, by shooting either a single electron beam or multiple parallel electron beamlets to the serial ultra-thin sections collected on a silicon wafer, the array tomography techniques can also be used to generate 3D EM images. Lower right: by sequentially imaging serial-sectioned ultrathin sections using TEM, 3D reconstruction can be generated. Automated sectioning methods, such as the GridTap technique facilitate this serial sectioning process. The TEM tomogram module can process much thicker sections by specimen tilting and back projection analysis. For 3D reconstruction, fewer slices are needed for ssTomography compared to ssTEM.

1.5.3.5 Other methods

In addition to vEM, super-resolution optical imaging techniques have been developed in recent years to study the ultrastructure of biological samples. There are two ways to overcome the diffraction limit: optimize the sample itself or reduce the excitation volume of optical imaging, for example with pan-expansion microscopy (Damstra et al., 2022) and multi-label *in vivo* stimulated emission depletion microscopy (Willig et al., 2021). However, these alternative techniques cannot visualize unlabeled structures and are not discussed in this dissertation.

1.5.4 Ultrastructural alterations upon plasticity

Ultrastructural alteration of synapses during plasticity was initially proposed in 1973 by Bliss and Lomo, who suggested that the changes of the spine neck could theoretically alter the resistance to synaptic input, thus affecting synaptic strength (Bliss & Lømo, 1973). Experimental evidences for morphological changes in synapses during LTP generation were found shortly after this initial hypothesis (Fifková & Van Harreveld, 1977; Van Harreveld & Fifkova, 1975). Later, by performing more specific LTP stimulation experiments as well as EM imaging of stimulated synapses, researchers found that several morphological alterations at the level of individual synapses occur after *ex vivo* plasticity induction, including: increased spine volume and PSD size and complexity (Toni et al., 1999, 2001), increased post-synaptic polyribosome concentration (Ostroff et al., 2002), increased formation of multi-synaptic boutons (Toni et al., 1999) and multi-innervated spines (Nikonenko et al., 2003), increased probability of containing SER (Borczyk et al., 2019), remodeling of the synaptic vesicle pool (Rey et al., 2020). These changes could alter the information storage capacity of synapses (Bromer et al., 2018; Samavat et al., 2022).

Similar ultrastructural changes have been found to correlate with memory formation *in vivo* (Geinisman et al., 2001; Aziz et al., 2019). At the network and synapse connectome level, large-scale FIB-SEM investigation of the somatosensory cortex of naive animals showed the convergence of synapse size (measured by axon-spine interface) between synapse pairs that experienced LTP and LTD, respectively, supporting the Hebbian plasticity theory (Motta et al., 2019). These findings provide us with the most precise measurement of morphological changes and the most detailed observations of synapses after plasticity induction. Importantly, as illustrated in Fig. 14, the EM methods are unbiased. LM methods rely on the fluorescent labelling of specific structures, while the rest of the unlabeled neuronal structural information is not visible. EM analysis, on the other hand, is not restricted to labeled structures and thus enable the discovery of unexpected changes. However, to this day, a pipeline to study plasticity-induced synaptic changes is lacking. This is due to the challenging aspects of inducing plasticity in a physiological context, as well as locating the synapses of interest in EM data.

1.6 Aims of the dissertation

My overarching aim is to answer this question: whether and how are early and late LTP are different from each other? To achieve this goal, I focused on studying the timing-dependent plasticity induced all-optically, using a method previously established in the lab. The spiking of the pre- and postsynaptic neurons was precisely controlled by light illuminations non-invasively. This allows me to study the late effects of optically-induced STDP (oSTDP) at least 3 days after induction. An ultimate goal was to study the ultrastructure of exactly the synapses which had undergone oSTDP: whether the persistent changes in the relative synaptic inputs after late timing-dependent long-term potentiation (tLTP) were due to changes in the number or size of synaptic connections? The other main aim I had was to investigate the role of CaMKII in early versus late tLTP. My expectation was that CaMKII had an important role in whether early tLTP persisted and became late tLTP. Surprisingly my results showed that early and late tLTP have very different requirements.

The results and discussion of my work are presented here in three parts.

Part 1. Characterization of optogenetic STDP (section 3.1)

The aim of section 3.1 is to further characterize the oSTDP protocol. In this section, I present and discuss the results I obtained mainly testing which parameters are crucial for the

successful induction of spike timing-dependent plasticity. Several different protocols were tested and my recordings contributed to the publication:

Anisimova M, van Bommel B, **Wang R**, Mikhaylova M, Wiegert JS, Oertner TG, Gee CE. Spike-timing-dependent plasticity rewards synchrony rather than causality. Cereb Cortex. 2022 Dec 15;33(1):23-34. doi: 10.1093/cercor/bhac050. PMID: 35203089; PMCID: PMC9758582.

Part 2. Investigating the role of CaMKII in timing-dependent LTP (section 3.2)

The aim of section 3.2 is to answer the question: how does CaMKII activity contribute to early and late tLTP. For achieving this goal, I used an all-optical approach where I combined paAIP2, a photoactivatable CaMKII inhibitor, to specifically inhibit CaMKII activation in the postsynaptic neurons during the induction of oSTDP. The results show that CaMKII is critical for early, but not for late tLTP. To investigate if CaMKII activity is sufficient for the induction of early and late LTP, I used photoactivatable CaMKII (paCaMKII). I found that paCaMKII activation induced strong input strengthening as well as spine head and PSD enlargement. However, these effects were not long lasting.

A manuscript based on my results from part 2 is in preparation, I will be the first author.

Part 3. EM labelling method for the ultrastructural analysis of identified synapses (section 3.3)

The aim of section 3.1 is to develop a pipeline for analyzing the difference of early and late tLTP, induced by oSTDP protocol, on ultrastructure level using EM. This is an extremely ambitious goal as it required establishing a method to label the STDP'd synapses pre- versus post-synaptic side structures differently under EM (Fig. 14). For this purpose, I tested several peroxidase-based labels and found suitable ones. Importantly, this method provides sufficiently strong labeling without obscuring the subcellular structures of interest, in particular the postsynaptic density and the presynaptic active zone and vesicles.

I then achieved reliable co-expression of the tags with optogenetic tools using the Cre-loxP system or the single-cell electroporation.

A manuscript based on my results from part 3 is under review:

Wang R, Schweizer M, Anisimova M, Gee CE, Oertner TG: Ultrastructural analysis of synapses after induction of spike-timing-dependent plasticity.

2. Materials and methods

2.1 Animals

Wild-type Wistar (HsdCpb:Wu, Envigo) or Sprague-Dawley (Hsd:Sprague Dawley®SD® Inotiv) rats were housed and bred at the University Medical Center Hamburg-Eppendorf (UKE) animal facility and sacrificed according to German Law (Tierschutzgesetz der Bundesrepublik Deutschland, TierSchG) with approval from the Behörde für Justiz und Verbraucherschutz (BJV)-Lebensmittelsicherheit und Veterinärwesen Hamburg, and the animal care committee of the UKE.

2.2 Solutions and buffers

Unless specified individually, solutions were stored at 4°C.

2.2.1 Slice preparation and culture solutions

Dissection medium (mM): 248 sucrose, 26 $NaHCO_3$, 10 glucose, 4 KCl, 5 $MgCl_2$, 2 kynurenic acid, and 0.001% phenol red. pH~7.4, osmolality 310 to 320 mOsm/kg (sterile filtered).

Culture medium: for 500 mL: 394 mL Minimal Essential Medium (MEM, Sigma M7278), 100 mL heat-inactivated donor horse serum (Sigma H1138), 1 mM L-glutamine (Gibco 25030-024), 0.01 mg/mL insulin (Sigma I6634), 1.45 mL, 109 mM NaCl (Sigma S5150), 2 mM $MgSO_4$ (Fluka 63126), 1.44 mM $CaCl_2$ (Fluka 21114), 6 µM ascorbic acid (Fluka 11140), and 13 mM D-glucose (Fluka 49152), sterile filtered.

2.2.2 Transfection solutions

Intracellular solution (mM): 135 K-gluconate, 4 $MgCl_2$, 4 Na2-ATP, 0.4 Na-GTP, 10 Na2-phosphocreatine, 3 ascorbate, and 10 HEPES, pH~7. 2 (solution was sterile filtered, aliquoted and stored at -20°C).

HEPES buffer (mM): 145 NaCl, 10 HEPES, 25 D-glucose, 2.5 KCl, 1 NaH_2PO_4, 1 $MgCl_2$, 2 $CaCl_2$. pH~7.4, osmolality 314-318 mOsm/kg

2.2.3 Electrophysiology solutions

Artificial cerebrospinal fluid (ACSF) (mM): 119 NaCl, 11 D-glucose, 2.5 KCl, 1 NaH_2PO_4, 4 $MgCl_2$, 4 $CaCl_2$, pH~7.4, osmolarity 305-315 mOsm/kg

Serum-free recording medium (mM): 99% MEM (Sigma; M7278), 13 D-glucose, 109 NaCl, 2 $MgSO_4$, 1.44 $CaCl_2$, 1 L-glutamine (Gibco 25030), 0.006 ascorbic acid (Fluka 11140), 0.01 mg/mL insulin (Sigma I6634). pH~7.28, osmolarity 310-318 mOsm/kg

2.2.3 Immunohistochemistry solutions

Phosphate buffered solution (PBS): dilute 10x PBS in type I water for 10 times (stored at room temperature).

Carrier buffer: 1% (vol/vol) goat serum, 0.2% bovine serum albumin, 0.3% Triton X-100, diluted in 1x PBS

Blocking buffer: 10% (vol/vol) goat serum, 0.2% bovine serum albumin, 0.3% Triton X-100, diluted in 1x PBS

2.2.4 Electron microscopy solutions

Fixation buffer with 2.5% (vol/vol) glutaraldehyde (GA), 2% PFA: dilute 50% GA and/or 4% PFA in cacodylate buffer to the desired concentration.

Cacodylate buffer (mM): 100 sodium cacodylate,2 $CaCl_2$. pH~7.4

Glycine solution (mM): 20 Glycine,100 sodium cacodylate,2 $CaCl_2$.

Metal-enhanced 3,3'-Diaminobenzidine (DAB): dilute 10x Metal Reinforced DAB Substrate (Thermo 34065) 1:9 in cacodylate buffer (DAB reagent should be freshly prepared before staining).

0.3% H_2O_2 (vol/vol): dilute 30% H_2O_2 in cacodylate buffer to the desired concentration (0.3% H_2O_2 should be freshly prepared immediately prior to staining).

1 % Osmium tetroxide (vol/vol): dilute Osmium tetroxide (molecular weight: 254.23 g/mol) in cacodylate buffer to the desired concentration.

EPON resin (for 50 mL): Glycidyl ether hardener MNA 16.1 g, Glycidyl ether hardener DBA 8.025 g, Glycidyl ether accelerator DMP-30 0.5 g and Glycidyl ether 100 25.85 g. Mix these reagents carefully at room temperature for at least 1 hour, until the color of this mixture turns from light red to gold yellow (EPON resin should be freshly prepared the day of use).

Contrast solutions: (1) 2% Uranyl acetate in 50% methanol; and (2) 0.04 g lead citrate trihydrate, 10 mL water, 5 mL of 1N NaOH (solutions were prepared, and stored at 4 °C in 1.5 mL aliquots. Before use one aliquot was spun down in a centrifuge at 13000 RPM for 10 min).

2.3. Hippocampal slice culture

Rat pups at age P4 to P6 were used for slice preparation as previously described (Gee et al., 2017). Briefly, pups under 80 % CO_2/20 % O_2 anesthesia were decapitated, and hippocampi were dissected in ice-cold slice culture dissection medium (bubbled with 95% O_2/5% CO_2). 400 µm thick slices, cut from the dissected tissue with a tissue chopper, were cultured on 30 mm diameter porous membranes (Millipore PICMORG50), supplied with 1 mL of culture medium underneath, at 37 °C in 5% CO_2. Slices were fed every three to five days by partial (70 %) change of culture medium.

2.4 Transfection

All transfections were performed between 10-14 days in vitro (DIV). Expression time (3 to 10 days) was determined based on calibration pre-experiments.

2.4.1 Plasmids and Viral Vectors

DNA plasmids (Table 1) were mixed and diluted to the desired concentration in ice-cold intracellular solution. Viral vectors (Table 2) were prepared at the Vector Core Facility, UKE. Immediately before the experiment, viral vectors were diluted to the desired titer in ice-cold HEPES buffer.

Table 1: List of Plasmid mixtures for single-cell electroporation

Experiment	Plasmid	Concentration	Producer	Expression Time
oSTDP electro-physiology	pAAV-hSyn-CheRiff-eGFP	0.5 ng/µL	Addgene #51697	7-10 days (CA1)
	pCl-Syn-mKate2-N	10 ng/µL	In the lab: I. Ohmert*	
	pAAV-CaMKIIP-mEGFP-P2A-paAIP2	20 ng/µL	Addgene #91718	
paCaMKII electro-physiology	pAAV-CaMP0.4-FHS-paCaMKII-WPRE3 or …-paCaMKII(SD)-…	50 ng/µL	A gift from Professor Hideji Murakoshi, National Institute for Physiological Sciences, Japan	3-6 days (CA1)
	pCl-Syn-mKate2-N	10 ng/µL	In the lab: I. Ohmert*	
paCaMKII 2p-imaging	pAAV-CaMP0.4-FHS-paCaMKII-WPRE3	50 ng/µL	A gift from Professor Hideji Murakosh…	3-6 days (CA1)
	pCl-Syn-mKate2-N	10 ng/µL	In the lab: I. Ohmert*	
	pCl-Syn-Xph20-eGFP-CCR5TC	20 ng/µL	In the lab: I. Ohmert*	
	pCl-Syn-LSSmOrange	2 ng/µL	In the lab: I. Ohmert*	
paCaMKII EM	pAAV-CaMP0.4-FHS-paCaMKII-WPRE3	50 ng/µL	A gift from Professor Hideji Murakoshi…	3-7 days (CA1)
	pAAV-EF1α-dAPEX2	10 ng/µL	Addgene #117173	
oSTDP EM-CA1	pAAV-hSyn-CheRiff-eGFP	0.5 ng/µL	Addgene #51697	7-9 days (CA1)
	pAAV- EF1α-dAPEX2	10 ng/µL	Addgene #117173	
oSTDP EM-CA3	pCl-Syn-ChrimsonR-TdT	10 ng/µL	In the lab: I. Ohmert*	7-9 days (CA3)
	pAAV- EF1α-SYP-HRP	10 ng/µL	Addgene #117185	

*Here means that the plasmid was modified by I. Ohmert according to our requirements. The sources of these plasmids are listed in appendix: 'Plasmids in this PhD project'.

Table 2: List of virus vectors for virus transducing

Experiment	Virus	Titer (WPRE)	Producer	Expression time
oSTDP and paCaMKII electro-physiology	AAVrh10 Syn-ChrimsonR-tdT	4.38E+13 vg/mL	UKE HEXT	6-10 days (CA3)
oSTDP EM-CA3	AAV9 Syn-SYP-HRP IRES Cre	6E+13 vg/mL	UKE HEXT	7-9 days (CA3)
	AAV9 hSyn-DIO-ChrimsonR-mRuby2-ST	1.05E+14 vg/mL	UKE HEXT	
oSTDP EM-CA1	AAVrh10 CamKIIP-dAPEX2-IRES-CRE	3E+13 vg/mL	UKE HEXT	7-9 days (CA3)
	AAVrh10 CAG-DIO-CheRiff	2.3E+13 vg/mL	UKE HEXT	
paCaMKII-virus c-Fos investigation	AAVrh10 hSyn-DIO-FHS-paCAMKII	5E+13 vg/mL	UKE HEXT	7-9 days (CA1)
	AAVrh10 CamKIIP-dAPEX2-IRES-CRE	3.3E+13 vg/mL	UKE HEXT	
	AAVrh10 CMV-GFP	9.14E+11 vg/mL	UKE HEXT	
PaAIP2-virus c-Fos investigation	AAV9 CaMKIIP-mEGFP-P2A-paAIP2	1.54E+13 vg/mL	UKE HEXT	7-9 days (whole hippocampus)
	AAVrh10 Syn-ChrimsonR-tdT	4.38E+13 vg/mL	UKE HEXT	

2.4.2 single cell electroporation

Thin-wall glass pipettes had a resistance of 10-14 MΩ when loaded with 1.3 µL of plasmid mixture. Slice cultures were kept in a sterile, prewarmed HEPES solution and transferred to a microscope under HEPA-filtered air. Single cell electroporation was performed as previously described (Wiegert et al., 2017). Briefly, a positive pressure was kept in the pipette while approaching the target cell, and when the pipette touched a CA1 pyramidal neuron, the pressure was released. I then waited for the resistance to increase to about 20 to 50 MΩ. After the desired seal was generated, the DNA was ejected by a train of negative voltage steps (50x, -12 V, 50 Hz, 0.5 ms), delivered using an Axoporator 800A (Molecular Devices). Depending on the experimental requirements, either 5-15 adjacent cells or 2-5 non-adjacent cells were transfected.

2.4.3 Adeno-associated virus (AAV) injection

Depending on the experimental requirements, either region-specific virus injection or whole-slice virus drop was applied. Briefly, for virus injection, 1 µL of viral vector solution at the desired titer was loaded into a thin-wall glass pipette pulled and broken to a tip diameter of approximately 10 µm. The pipette was injected locally into the region of interest and pressure pulses were applied to deliver the virus. For whole slice virus transduction, 3 µL of viral vector solution was loaded into the thin-wall glass pipette pulled and broken to a tip diameter of approximately 30 µm. The pipette was placed on top of the slice, pressure pulses were applied to push the virus drop on to the tip of the pipette. The pipette was moved down to gently touch the slice and therefore the virus drop with a volume of approximately 125 nL was delivered to the whole slice evenly.

2.5 electrophysiology

The electrophysiology setup (Fig. 16) was based on an Olympus BX61W1 epifluorescence microscope. Typically, both LED fibers and the laser were used for multi-targeted, region-specific optical stimulation. The cell of interest was recorded in the whole-cell patch clamp configuration. Patch electrodes were freshly pulled and filled with 1.2 µl of intracellular solution before the experiment, with a resistance of 3 MΩ to 4 MΩ. The slice culture, with the membrane attached, was placed in the recording chamber under the objective, and the curved gold wire was placed on the membrane to fix the position of the slice during the experiment. The temperature was maintained at 31-33℃ by heating the perfusion solution and the condenser. The solution was recycled through the perfusion, and supplied with pre-humidified carbogen (95 % O2/5 % CO2). pH and osmolality were maintained by changing 80% of the solution every 2 hours.

All experiments were performed using the Axopatch 200B amplifier (Axon Instruments, Inc.), National Instruments boards, and Ephus software (in Matlab R2016B) (Suter et al., 2010). Recordings with series resistance (Rs) greater than 15 mΩ were excluded.

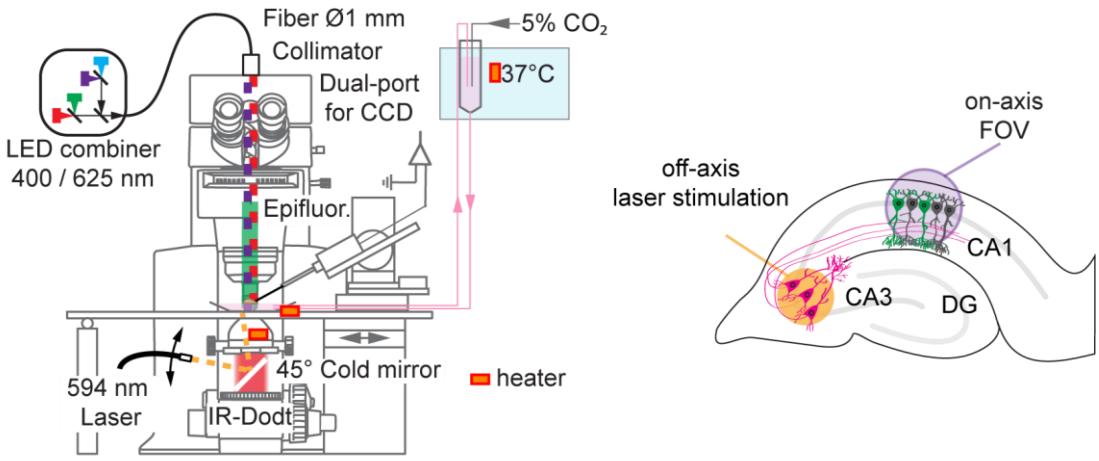

Figure 16 :Electrophysiology experiment setup.

Left: The electrophysiology experiment setup contains four major compartments: the microscope, optical stimulation system, perfusion and heating system, and whole-cell patch clamp system. The microscope is based on an Olympus BX61W1 microscope, a 40x objective is used for patching. The condenser is constantly heated to 40 degrees. The optical stimulation combines the fixed on-axis LEDs through the objective, and the moveable off-axis laser through the condenser, placed by a swinging arm. The experimental solution is gravity perfused (bubbled with 95% O_2/5% CO_2), pre-warmed in the water bath and at the patching chamber, to about 31°C. Right: While patching, CA1 region was moved to the center of the field of view (FOV) and illuminated by the LEDs, and CA3 was illuminated by the off-axis laser. Figure adapted from Anisimova et al., 2022

2.5.1 Acute-plasticity-inducing experiment

Experiments were performed between DIV 18-24. The serum-free medium for recording was supplemented with D-serine (30 µM, Tocris Bioscience; 0226), freshly added before the experiment. The electroporated CA1 region was placed at the center of the field of view, using a 40x water immersion objective (Fig. 16). The off-axis laser spot through the condenser was placed at the ChrimsonR virus-expressing CA3 region. Regions of interest were confirmed by checking the expression of mKate2 (electroporation) or tdTomato (AAV) (using an mCherry filter set to avoid unwanted activation of constructs).

Recordings were performed in voltage-clamp mode (holding voltage -70 mV, liquid junction potential corrected), the slope of the excitatory postsynaptic potential (EPSC) was used as a measure of excitatory input strength. In each slice culture, one CA1 cell, CheRiff-expressing or non-transfected (NT), was recorded. CA3 ChrimsonR-expressing cells were illuminated at a fixed position with 1 ms laser 594 nm pulses (at 0.05 Hz, repeated 10 times), while CA1 cells were patched to record the EPSC. Next, the membrane voltage clamp was released by switching to current clamp mode, and plasticity-inducing stimuli, either causal/anti-causal pairing or paCaMKII activation, were delivered. For causal/anti-causal

paired cells, the spike patterns were monitored, and cells showing unwanted spiking patterns (details discussed in 3.1.1.1) were excluded. The recording was then switched back to voltage-clamp mode and the post-stimulation effect was recorded. The strength of the synaptic connection was determined by the average of the initial EPSC slope (Fig. 17).

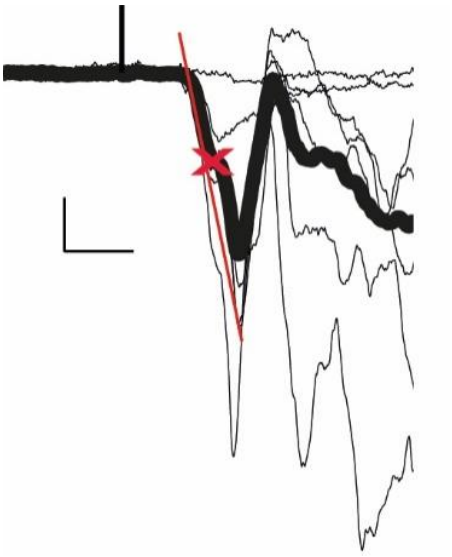

Figure 17: EPSC slope calculation

An example of EPSC slope calculation. The horizontal line indicates the presynaptic optical stimulation. The thin lines indicate the EPSC recordings from one cell and the thick line indicates the average of the recordings. The first peak (red cross) was detected automatically, and a linear function (red line) was fitted to the 20%-60% of the curve from the start of the EPSC to this peak, and the slope was calculated from this linear function. Scale bar: 10 ms, 100 pA.

2.5.2 Incubator stimulation

For investigating the long-term synaptic strength alteration and the expression of immediate early genes, slices were optically stimulated noninvasively in the incubator as previously described (Anisimova et al., 2022). Briefly, 1-2 days before stimulation, the last medium changed was performed and the slice was centered in the 35mm culture dish, to avoid potential interference to the cell. A stimulation tower, mounted with two LEDs (Fig. 18) was placed in the incubator. Optical stimulations, programmed by a Master-8 stimulator (AMPI), were applied to the slice.

For immediate early gene immunohistochemistry experiments, slices were fixed 1 hour after stimulation. For synaptic strength measurement experiments, the slices were kept in the incubator for another 1-3 days.

For pharmacological manipulation, drugs were applied to the slice in different ways as listed below (Table 3). For batch quality control and data normalization, a positive and a negative control condition, listed below, were also included in the experiments.

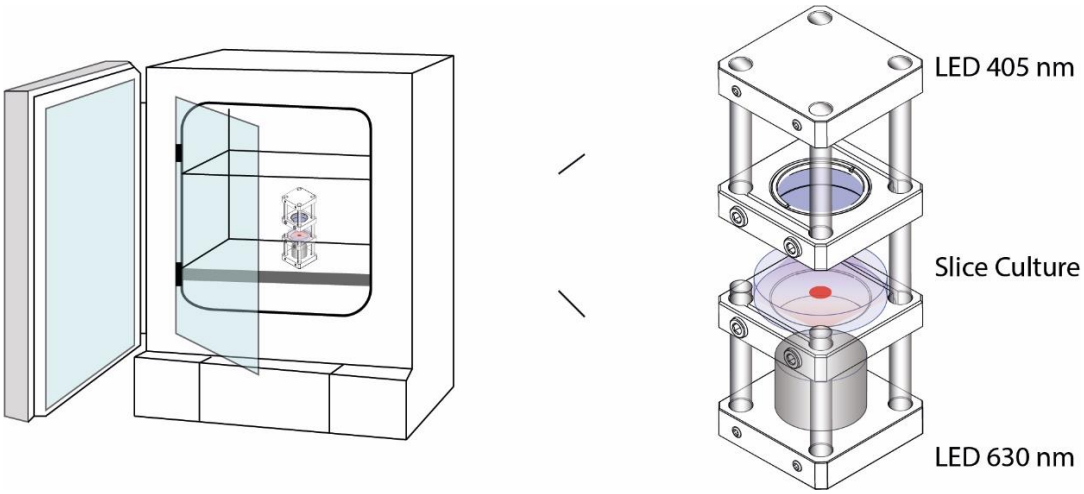

Figure 18: Incubator stimulation setup.

The setup of the incubator stimulation. Left: A stimulation tower was placed in the culture incubator. Right: Optical stimulation was delivered by collimated LED light sources, controlled outside the incubator. Figures adapted from Anisimova et al., 2022

Table 3: Pharmacological manipulations

Treatment	Procedures
zeta-inhibitor-pipette (ZIP)	ZIP and scrambled ZIP (scr-ZIP) was applied three hours after incubator stimulation. Specifically, ZIP was diluted to 1 µM by pre-warmed, old culture medium (to avoid the unwanted effect from fresh medium stimulation, (Anisimova et al., 2022). 50 µl of 1µM ZIP was added directly onto the slice, followed by moving the slice to 800 µl of 1 µM ZIP. The slices were then moved back to the incubator and kept for another two days, then one day before the patch-clamp experiment, the slices were moved back to normal medium (old, pre-warmed).
Positive control	KCl was diluted to 50 mM by HEPES buffer. Slices were treated for two minutes x two times using warm 50 mM KCl/HEPES. This stimulation is able to elevate c-Fos expression reliably in neurons across different hippocampus regions (Schoenenberger et al., 2009), termed 'High K^+'.
Negative control	Slices were handled as stimulated conditions, but no optical stimulations were applied. Then slices were fixed directly.
TTX application	1 µM TTX was applied in the same way as ZIP.

2.5.3 Stimulated slices synaptic strength measurement

Measurements were performed between DIV 21-27 (9 to 13 days after transfection) as previously described (Anisimova et al., 2022). The illumination strategy is the same as in 2.5.1. Briefly, for each cell, CA3 ChrimsonR-expressing cells were illuminated at a fixed position with a 1 ms laser pulse of 594 nm (at 0.05 Hz, repeated 10 times), while CA1 cells

were patched to record the EPSC (the average of 10 sweeps was used to fit the EPSC slope). Transfected (TF) and non-transfected (NT) cells were patched sequentially.

For each slice, 1-5 TF cells and at least 3 NT cells were recorded. The relative input strength was calculated as shown below:

$$Relative\ Input\ Strength = \frac{TFslope\ -\ Average\ NT\ Slope}{\frac{1}{2}(TFslope\ +\ Average\ NT\ Slope)}$$

For each TF cell, the optical spike threshold was measured as the first step of each recording. The cells that were not able to spike properly were discarded.

2.5.4 Measurement of cell parameters

Measurements were performed between DIV 18-27. To measure the optical threshold of the spike, the optical stimulation pulse was delivered from an on-axis LED fiber through a 40x water immersion objective and the membrane potential was measured in cell-attached mode. The minimum light intensity that elicited a spike was recorded as the optical threshold.

In whole-cell voltage clamp mode, a 5 mV test pulse was applied to measure membrane resistance and capacitance. In the whole-cell current clamp mode, the resting membrane potential was recorded and current steps (-800 pA to 400 pA) were injected to measure the action potential threshold voltage, and number of spikes at 400 p.

2.6 Chronic two-photon imaging

In order to follow the morphological changes of the spine over time, I used a customized two-photon imaging (2P imaging) setup (Fig. 19), optimized for long-term 2P imaging of organotypic slice cultures. The overall goal is to mimic the slice culture incubator environment as closely as possible while performing 2P imaging. Briefly, a temperature-controlled recording chamber (titanium) with a glass bottom and a transparent side wall (polycarbonate) was connected to the imaging objective by an elastic latex membrane to form an airtight compartment. To reduce condensation, a second cylinder (Perspex) with lid was closed around the inner chamber. The temperature was kept stable over days of

imaging by three external heating systems: (1) A closed-loop heating plate under the chamber. A temperature sensor was placed inside the recording medium to send the sample temperature to the heating plates. The target temperature was set at 36 ℃ to avoid overheating. (2) A constant-current heater connected to the condenser. (3) A constant-current heater connected to the objective. The osmolarity and pH of the imaging solution were kept stable by a constant flow of humidified pressurized air with 5% CO_2 to the inner chamber. The slice culture insert was placed in the imaging chamber, weighted down by a gold ring placed on the rim of the tissue insert. 5 mL (1 mL underneath and 4 mL on top) of culture medium was used for each imaging session. All equipment in contact with the slice culture was sterilized. The two-photon microscope (Rapid3D, Rapp Optoelectronics) was equipped with a 25x, NA 1.05 objective (Olympus XLPLN25XWMP2), a Ti:Sapphire laser (Chameleon Ultra II, Coherent) tuned to 950 nm was used to excite GFP and LSSmOrange fluorescence. Imaging was controlled by ScanImage under MATLAB R2023a (Pologruto et al., 2003). Laser power was adjusted using the 'P/Z Adjust' function, 'Exponential' mode, with Lz set to 350 ~ 1100 to compensate for the depth attenuation of the laser power. Emission photons were collected by two sets of photomultiplier tubes (PMTs H7422P-40, Hamamatsu), red and green photons separated by 525/50 and 607/70 emission filters (Chroma), with the upper PMTs collecting photons through the objective and the lower PMTs collecting photons through the condenser (oil immersion, Olympus, 1.4 NA). Tissues were scanned bidirectionally at a frame rate of 0.57 Hz. Stacks of images were acquired with a step size of 0.75 µm, 6x digital zoom, 1024x1024 pixels, 80 to 150 images per stack.

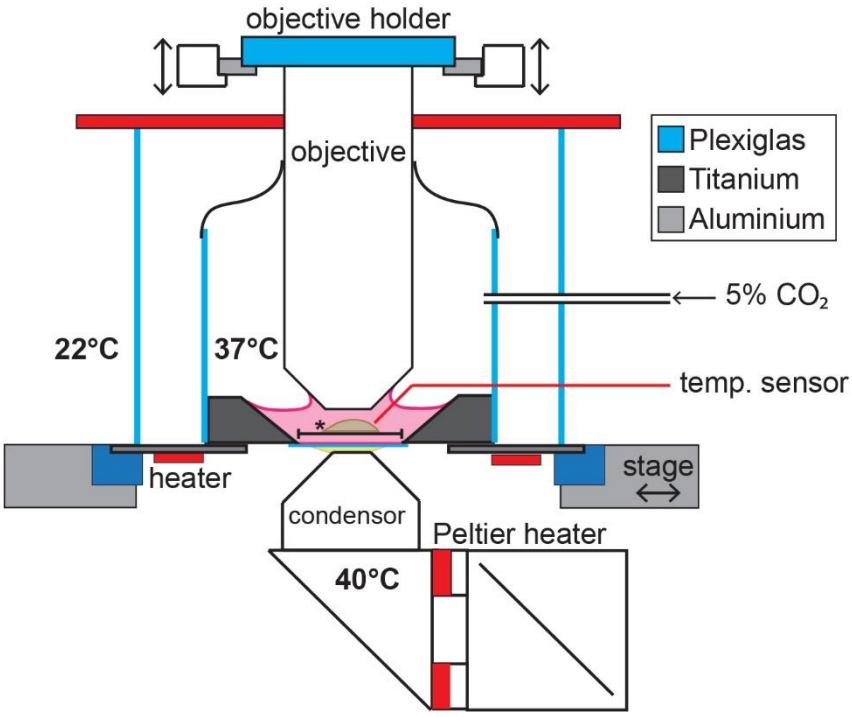

Figure 19: Chronic two-photon imaging setup.

A heated titanium base plate with glass bottom holds the slice culture insert. An elastic membrane was used to connect the objective with the chamber, to create a nearly air-tight, sterile imaging environment. The chamber is constantly supplied with pre-humified 5% CO_2 + 95% synthetic air. Photons are collected through the objective and the condenser.

2.7 Immunohistochemistry and confocal imaging

Slices were fixed in 4% PFA for 30 minutes at room temperature and then washed three times in 1x PBS for 10 minutes each time. To avoid unspecific primary antibody binding, slices were incubated in blocking buffer for two hours, followed by primary antibody incubation in carrier solution at 4℃ overnight. The next day, the slices were washed three times and incubated in secondary antibodies for another two hours at room temperature. Before mounting, the slices were washed once more with either PBS or PBS containing DAPI (1:10,000). Antibody details are listed in Table 4. Imaging was usually performed on the same day or the first day after staining. For long-term storage, the edge of the coverslip on the mounted sections was covered with nail polish and stored in a -20 ℃ freezer. Images for the c-Fos expression level analysis experiments were acquired using a Zeiss laser scanning confocal microscope (LSM900, Axio imager M2, with a 20x, 0.8 NA air objective). For image acquisition, a z-stack, with 3 µm steps with a resolution of 1024x1024 pixels, was acquired for each region of interest. Lasers and filters were set using the dye selection program,

Zen3.5 including: DAPI, Alexa 488, Alexa 568, Alexa 647, 'best signal' function. All acquisitions were performed sequentially to avoid spectral cross talk.

To validate virus transduction and to assess c-Fos expression in some virus/plasmid initial characterization experiments, a Zeiss Apotome (with a 10x air objective) was used for image acquisition and stitching.

Table 4: Antibodies

Immunogen	Host	Label	Producer and Catalog. #	Dilution
tRFP	rabbit	none	Evrogen #AB233-EV	1:1000
GFP	chicken	none	Invitrogen #A10262	1:1000
c-Fos	rat	none	Synaptic Systems #226017	1:1000
Cre 2D8	mouse	none	Merck Millipore #MAB3120	1:500
dsRED	rabbit	none	Clontech #632496	1:500
chicken	goat	Alexa Fluor 488	Invitrogen #2566343	1:1000
Rabbit	goat	Alexa Fluor 568	Thermofisher #A11011	1:1000
Mouse	goat	Alexa Fluor 647	Invitrogen #A21236	1:1000
Rat	goat	Alexa Fluor 647	Invitrogen #A21247	1:1000

2.8 Image analysis

2.8.1 Two-photon dataset analysis

The 2P live imaged synaptic spines were first detected and tracked, raw data was extracted during this process. Next, these raw data were further analyzed and visualized.

Synapse detection

The field of view (176 µm (x) x 176 µm (y) x 50 to 120 µm (z)) contains up to a thousand spines. In order to analyze thousands of objects, including not only detection for each time point but also tracking of objects over time, we developed a pipeline for automatic spine detection and tracking. This pipeline was written in Python 3.9 environment and includes four main steps: (1) denoising, (2) time-lapse rigid registration, (3) deep-learning based model generation and object detection, (4) time-lapse tracking.

Step 1: denoising

For denoising, a median filter with a radius of 1 pixel was applied to the image in 3D, and then the bidirectional scan artifact was corrected.

Step 2: time-lapse rigid registration

I used the large-stokes-shift fluorophore LSSmOrange (Shcherbakova et al., 2012), to fill the cells and use a single laser wavelength to image both the fluorescence coming from

the PSD and to determine spine volume. This avoids spectral aberrations arising from the use of different excitation wavelengths or any offset due to misalignment of the lasers (see Fig. 39). As a result, only the time axis registration is needed. To maximumly avoid the effect of background noise, which usually exists in the blue wavelengths range, the LSSmOrange dendrite skeleton signal was used for registration. The rigid method was used for registration.

Step 3: deep-learning-based model generation and object detection

The GFP channel (GFP intrabody targeting PSD-95, Xph20-eGFP-CCR5TC) was used for the object (spot) detection. A deep learning based 3D polygon (star-convex) detection method, StarDist algorithm (Weigert et al., 2020) was implanted for our spot detection. Three main steps were performed for spot detection: (1) ground truth annotation, (2) model training, and (3) spot detection and output generation.

Step 3.1 ground-truth annotation

In order to annotate our 3D dataset in order to generate the ground truth, an annotation plugin in the Napari viewer called 'SpotFi' was written. Briefly, the 3D dataset was divided into 64x64x64 pixel tiles, and the manual annotation can be done on each tile separately. Ideally, 5-10 tiles, distributed on both the main and small dendritic branches, from each time point should be annotated.

Step 3.2 model training

The annotation files are fed into the StarDist network training. Briefly, 80% of the ground-truth annotated data set was used for training and the remaining 20% was used for validation. 32 rays were used for distance map prediction, the probability threshold was set to 0.1-0.5, depending on the specific model, and the optimized non-maximum suppression (NMS) threshold was set to 0.01. Approximately 100 epochs of training are applied until the loss function output is less than 0.1. The model is further validated online in Napari-SpotFi and retrained if necessary. The validated model was used for the next steps.

Step 3.3 Spot detection and output generation

Only after successful training and validation was a given model used for spot detection. The detected spots were saved as three separate channels: (1) spot 'dummy' channel containing uniform intensity, same size 'dummy' spots for the next step: object tracking; (2) detected spots segmented GFP channel; (3) detected spots segmented LssmOrange channel.

Finally, the output files were generated, including: (1) A HDF5 file containing: z stacks, 4 channels (registered GFP, registered LSSmOrange, spot-dummy, segmented GFP-detected PSD, segmented LSSmOrange-detected spine head), and time-lapse. (2) an XML file in BigDataViewer format, as input for the next tracking step.

Step 4: time-lapse tracking

Time axis tracking was performed using the Fiji-Mastodon (beta-26) plugin (Wolff et al., 2018) (https://github.com/mastodon-sc/mastodon). A maximum of 2 gaps between time points are accepted for tracking. After the tracking is finished, only the spines that were successfully tracked in 80% of the time points were kept from further analysis (will be discussed in 3.2.4.3).

Data plotting

Based on the raw data, the intensity change of each spine was plotted over time. Fluorescence bleaching was then corrected: 2 to 4 regions were selected on the main branch of the dendrite, and the average bleaching on these dendritic regions was used as the standard for the bleaching correction of the spine. The bleach-corrected data were used for further calculations (except for the calculation of spine entropy, which is not affected by bleaching). The growth was calculated as:

$$Growth = \Delta intensity / average\ baseline\ intensity$$

$$Early\ Growth = \frac{average\ intensity\ of\ 0\ to\ 2\ hours\ after\ stimulation\ -\ average\ baseline\ intensity}{average\ baseline\ intensity}$$

$$Late\ Growth = \frac{average\ intensity\ of\ 2\ to\ 5\ hours\ after\ stimulation\ -\ average\ baseline\ intensity}{average\ baseline\ intensity}$$

The average intensity and standard deviation (SD) of the whole track was used to calculate the coefficient of variation (CV). For the probability intensity distribution plot in Fig. 40 b and d, for each slice, the average baseline intensity was calculated, then each slice data was normalised to this value. After normalisation was performed for each slice, all the spots were pooled together to calculate distribution. The number of bins utilized in the entropy calculation was determined based on the number of detected spines in each slice, as presented by Hacine-Gharbi and colleagues, to avoid bias (Hacine-Gharbi et al., 2012). To compute the cluster features (Fig. 47, 48, 49), Fiji, SNT plugin (Arshadi et al., 2021) was used to create the dendritic tree object for each slice, and only the spines sitting on the same branch are considered as neighbors for further computations.

2.8.2 Immunohistochemistry Dataset Analysis

For the single cell electroporated dataset c-Fos expression analysis, the image stacks were loaded in Fiji (ImageJ). A maximum intensity projection (MIP) was made, and the sections for MIP were determined based on the cell-filler channel. The outline of the nuclei was drawn based on the DAPI channel and the cell-filler channel. Next, the average intensity was recorded for each region of interest (ROI) in the c-Fos channel. For the paAIP2 and ChrimsonR AAV transfection dataset c-Fos expression level analysis, image stacks were loaded into Imaris 10.1.0 software and analysis was performed using the Imaris 'spot' object, and the 'spot' object was placed manually. Specifically, the Z position was moved to the pyramidal cell layer. Then, only the paAIP2-GFP channel was kept visible and spots were randomly placed on GFP-positive neurons, then the c-Fos-Alexa 647 channel was turned on and the position of the spots was carefully adjusted by reference to the c-Fos spots, and the paAIP2-positive c-Fos expression level was recorded based on the average intensity of the c-Fos channel spots. Next, a second round of random spot positioning was performed, but by turning on both the paAIP2-GFP and ChrimsonR-TdTomato channels and randomly placing spots on GFP-negative and TdTomato-positive neurons. The data were then recorded as paAIP2-negative c-Fos expression levels.

Imaris 10.1.0 was also used to analyze the co-expression rate of Cre-HRP and Flex-ChrimsonR. For the false positive group, the Cre and DAPI channels were turned on and about 25 nuclei with both cre and DAPI staining were randomly selected from each image. Then the mRuby channel was turned on and the percentage of Cre+ mRuby- spots was determined. Then selection was started from mRuby and DAPI channels, and the percentage of mRuby+ Cre- spots was calculated. Finally, the data sets were polled to calculated the co-expression rate.

2.9 Transmission Electron Microscopy and Electron Tomography

2.9.1 DAB staining

Each slice culture was fixed with 2.5% GA + 2% PFA for 1 min at 37°C, transferred to ice-cold 2.5% GA + 2% PFA for 1 h, followed by 3 x 10 min washing in cacodylate buffer (all washing steps below were performed with cacodylate buffer on ice. Slices can be stored in

cacodylate buffer at 4°C for up to 3 weeks prior to DAB staining). The section was then incubated with 20 mM glycine for 15 min, followed by 3 x 10 min washes. Endogenous peroxidase was blocked by 0.3% H_2O_2 incubation for 15 min, followed by 3 x 10 min washing. To detect weak signals, a metal enhanced DAB kit was used for DAB staining. To allow DAB to penetrate throughout the tissue, the section was incubated with 1 x DAB reagent for 1 h. After this pre-penetration step, stabilized hydrogen peroxide solution (diluted 1:100) was added to initialize DAB staining. After 30 min to 2 h of staining (depending on the expression level), the section was washed three times and incubated overnight with 3% GA. The next day, the sections were washed 3 times. The stained sections were then microdissected to the CA1 or CA3 stained region and stored in cacodylate buffer at 4°C for up to 3 weeks before Osmium tetroxide (OsO_4) staining.

2.9.2 Osmium tetroxide staining and resin embedding

OsO_4 staining was performed after DAB staining. The sections were washed in cacodylate buffer 2 x 5 min, followed by 20 minutes of 1% OsO_4 incubation on ice. Then, the sections were transferred to cacodylate buffer for washing for about an hour, with buffer replacement every 5 minutes before resin embedding.

EPON 812 was prepared in advance. Dissected specimens were washed in an ethanol series for dehydration (30%, 50%, 70%, 80%, 90%, 100% x 2, 15 min each), then transferred to 100% propylene oxide (2 times, 10 min each). Next, specimens were pre-embedded in a 1:1 mixture of EPON resin and propylene oxide for 90 min, then transferred to a 2:1 mixture of EPON resin and propylene oxide for 2 h, then transferred to pure EPON resin and incubated overnight. The next day, the embedded specimens were placed on a resin block and baked in an oven at 58°C for a minimum of 48 hours.

2.9.3 Grid coating, slicing and serial section collection

Prior to coating, the grids were cleaned in acetone, rinsed in distilled water and air dried. A Formvar coating unit (cylindrical separator funnel) was filled with chloroform and a clean microscope slide was placed underneath. The valve was opened to allow the solution to drain slowly over the slide, forming a thin film. The film was then transferred to the

surface of a cuvette filled with distilled water. Clean grids were placed on the floating film (shiny side up). To lift the coated grids out of the water, a piece of parafilm was placed on top and transferred to a Petri dish for storage. Coffer slot grids (0.4 x 2 mm) were used for electron tomography and 100 mesh grids (3.05 mm O.D.) for regular TEM. A diamond knife was used for serial sectioning. Series of semi-thin sections (300 nm) were collected for electron tomography and ultrathin sections (30 to 50 nm) for TEM.

2.9.4 Contrasting

For acquiring clearer images, post-staining contrast was used. Each grid was placed on a drop of 100 µl uranyl acetate solution for 15 minutes then washed in water, air dried in a grid box, and placed on a drop of lead citrate for 1 minute. After another round of washing and drying the samples were ready for imaging. All contrasting steps were performed in a closed Petri dish.

2.9.5 Imaging

A JEOL JEM-2100 Plus electron microscope, at 200 kV acceleration voltage, with a JEOL recorder and CCD camera system (EMSIS) was used for image acquisition. Single-tilt transmission electron tomography was performed. 1:20 diluted 15 nm gold particles were applied to both sides of the copper grid as fiducials. Regions of interest were defined based on dendritic staining. Serial tomography was performed on each ROI, magnification was verified in different specimens, from x6000 to x10000, tilt angle started at approximately -60°, ended at approximately +60°, with 1° increment for each view. Tomograms were saved in mrc format.

2.9.6 Registration

There are two registration steps (Fig. 20). Step 1: to align the views for tomogram generation; Step 2: to align the tomogram series for volume reconstruction.

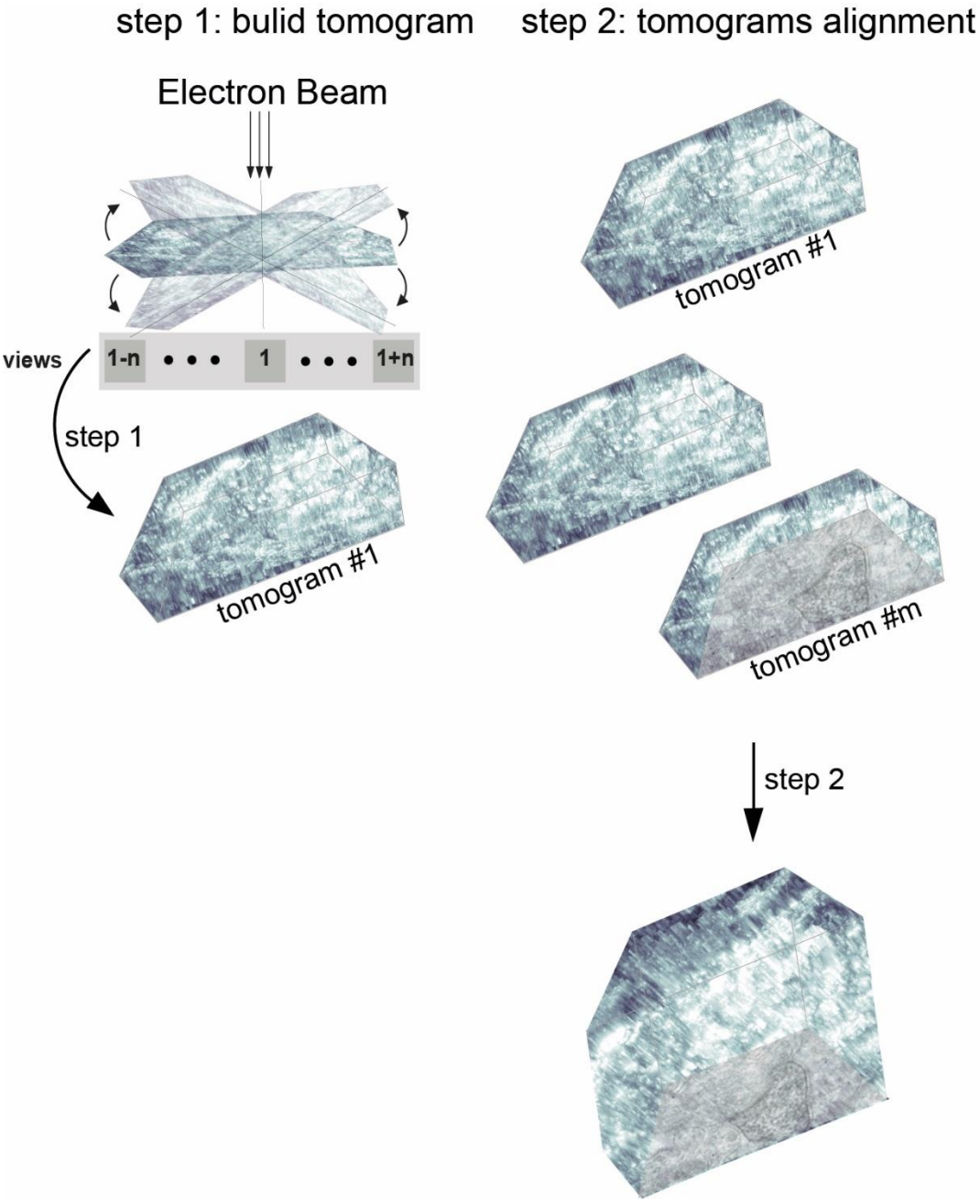

Figure 20: Serial tomogram generation.

Two steps are needed for serial tomograms generation. Step 1 is to build a tomogram from one section, using the tilted angle ('views') and fiducial model as references; step 2 is to align multiple tomograms from serial sectioned samples, to generate a bigger volume of the dataset.

2.9.6.1 Step 1

IMOD 4.11, Etomo module (https://bio3d.colorado.edu/imod/doc/tomoguide.html), single axis mode was used for tomogram generation. Briefly, mrc data was loaded and pixel size was extracted from the header. All the standard steps (including: denoising, cross-correlation-based coarse alignment, fiducial model generation, fine alignment, tomogram

positioning, filtering, creating aligned stack, and building tomogram) were performed. For the fiducial model generation, the seed model was generated using the automatic mode, 21-31 seed points were distributed on two surfaces, and the 'Fix Fiducial Model' function was used to make sure that a sufficiently low amount of points were missed while tracking. For the tomogram positioning, a 600 nm sample tomogram was created for boundary model generation. For the tomogram generation, the SIRT-like filter at 4 iterations was used. The rec tomogram was saved as output. Tomogram series, created from the serial sections, were stored for the next step of volume reconstruction.

2.9.6.2 Step 2

Series of tomograms, the .rec datasets were loaded in Fiji using the 'Import Bio-Formats' function. Tomograms were checked and unwanted blurry views were removed from each tomogram. Then the multiple tomograms were combined as one image series using the stacks tools-Concatenate function. The concatenated file was saved as TIFF file. Next, the trak-EM2 plugin (Cardona et al., 2012) (https://github.com/trakem2/TrakEM2) was used for serial tomograms alignment. The TIFF file was loaded to trak-EM2 as image series. Tomograms were aligned using the 'align layers manually using landmarks' function, elastic method. Landmarks were placed at the last view of tomogram #n-1 and the first view of tomogram #n. Alignment was applied by propagating the alignment to the first section. A series of alignments were performed until the whole volume was aligned. If there were m tomograms to be aligned, m-1 steps of alignment were needed to be done. Finally, the aligned volume was saved as a TIFF file using the 'export-make flat image' function.

2.9.7 Segmentation, reconstruction, and visualization

Segmentation, reconstruction, and visualization was performed using Imaris 10.1.0. The aligned electron tomograms were loaded to Imaris, and the 3D surface object was used for the segmentation of spine head, axon-spine interface (ASI), and PSD. Structures were manually segmented by drawing outlines to cover the objects. ASI and PSD was generated by projecting the ASI and PSD 3D surface objects to spine head (in this process, PSD thickness was not considered for analysis due to resolution limitation and interference of dAPEX2 labeling). These 2D objects was created using an Imaris-Xtension (under python 3.7): surface-surface contact area (https://github.com/Ironhorse1618/Python3.7-Imaris

XTensions/blob/master/XT_MJG_Surface_Surface_ContactArea2.py). The spine head complexity index and PSD complexity index were calculated (details will be discussed in 3.2.2.3). Segmentation and proofreading were performed by two experimenters both blind to the experimental conditions. Unblinding occurred only after the data analysis was complete.

2.10 Statistics

Sample sizes are listed by 'N' and 'n', 'N' represents the number of slice cultures (experimental repetitions) and 'n' represents the number of cells or spines, depending on the experiment. For the median ± IQR error bars, 25% to 75% interquartile range was plotted. GraphPad Prism 10 and MATLAB R2022b was used for statistical tests. Statistical details are listed in the figure legends and Table 7.

3. Results and Discussion

3.1 Optogenetic induction of spike-timing-dependent plasticity (oSTDP)

Previously, it was shown in the lab that by using two channelrhodopsins (CheRiff and ChrimsonR, which have spectrally distinct activation wavelengths, Fig. 21a), early (20 min) tLTP or tLTD can be induced by pairing presynaptic action potentials with a burst of postsynaptic action potentials (± 10 ms) and when induced in the incubator, late tLTP is the outcome of the same stimulation (Fig. 6, Anisimova et al., 2022). Based on the functional characterization of CheRiff and ChrimsonR (Fig. 21a), the stimulation parameters for plasticity experiments were set previously in the lab as follows: (1) 1.2 mW/mm^2 of violet light and 8 mW/mm^2 of red-light flashes were used for all inductions. (2) Around 30 to 50 CA3 neurons should be transduced, based on the characterization of c-Fos expression patterns after causal pairing vs. number of ChrimsonR-CA3 neurons (Fig. 21b): too few ChrimsonR-CA3 neurons are not able to drive sufficient synaptic input to postsynaptic CA1 neurons, while too many would generate sufficient depolarization to spike every postsynaptic neuron (both CheRiff-expressing and non-transfected).

As I wished to investigate the role of CaMKII in STDP, I further characterized the oSTDP protocol while recording the membrane potential of the postsynaptic neuron ("in bath" optical pairing), and also 3 days after oSTDP induction.

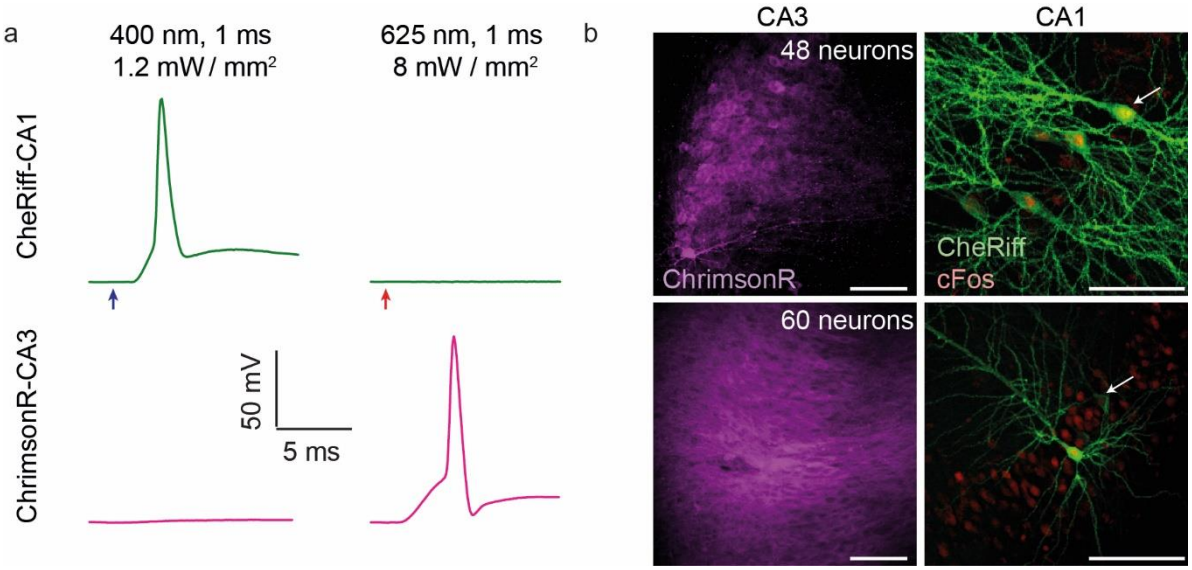

Figure 21: criteria of the oSTDP experiments.

(a) Example recordings of a CA1 neuron expressing CheRiff and a CA3 neuron expressing ChrimsonR. Violet and red light flashes were applied at the time indicated by the arrows. Only the CheRiff

expressing neuron fired an action potential after the violet light flash and the ChrimsonR expressing neuron only after the red light. (b) Slices fixed and stained against c-Fos one hour after causal pairing stimulation (see methods and Fig. 22). The number of ChrimsonR expressing neurons were counted. In the CA1 region c-Fos expression was seen only in the CheRiff expressing neurons when there were 48 ChrimsonR AAV transduced CA3 neurons. When 60 CA3 neurons were transduced c-Fos was detected throughout the CA1. Scale bar: 100 µm. Image adapted from Anisimova et al., 2022.

3.1.1 Characterization of presynaptic and postsynaptic neuron firing during optical pairing

I first further characterized the pre- and postsynaptic neuron activities during optical stimulations. In particular, I performed experiments to determine how reliably CA1 and CA3 neurons followed the light stimulation applied during oSTDP induction. Briefly, 2 to 5 CA1 pyramidal neurons were electroporated with DNA encoding CheRiff-eGFP and soluble mKate2 (Fig. 22a). CheRiff is completely insensitive to wavelengths above about 540 nm and ChrimsonR has a red-shifted activation spectrum and is generally not very light sensitive, therefore violet light can be used to spike CheRiff expressing neurons without activating ChrimsonR neurons and yellow/red light will spike ChrimsonR neurons and have no effect on CheRiff. Therefore, exciting mKate2 fluorescence, which was used to localize transfected CA1 neurons, does not activate CheRiff. In CA3, about 40 PNs were AAV-transduced with ChrimsonR-tdTomato. In the recording chamber, a CA1 CheRiff-expressing cell was patched, and light pulses were delivered to induce action potentials in CA3 ChrimsonR-expressing cells and EPSCs in the postsynaptic CheRiff-expressing cells. During pairing, violet light was used to spike CA1 CheRiff-expressing cells with precise timing control (Fig. 22b). In an oSTDP experiments, after recording baseline EPSCs for about 5 minutes, one EPSC is paired with three postsynaptic action potentials (3 APs at 50 Hz), either causally or anti-causally (Fig. 22b). The pairing was repeated 300 times at 5 Hz and to assess whether synaptic plasticity was induced, EPSCs are recorded for another 25 minutes (Nevian & Sakmann, 2006). Causal pairing (when the presynaptic neuron fires and the EPSC occurs before the CA1 neuron spikes) induces early timing-dependent long-term potentiation (early tLTP), whereas anti-causal-pairing induces early timing-dependent long-term depression (early tLTD) (Fig. 6, Anisimova et al., 2022).

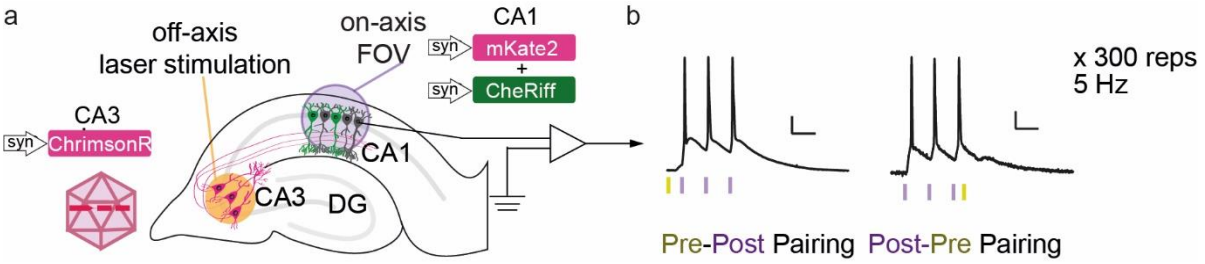

Figure 22: Acute oSTDP pairing paradigm.

(a) The transfection and optical stimulation strategy. Hippocampus slice culture CA3 PNs were transduced by AAV injecting carrying ChrimsonR-tdTomato, CA1 PNs were transfected by single-cell electroporation carrying CheRiff-eGFP. A CA1 CheRiff cell was recorded by whole-cell patch clamp, and the pre-synaptic side activity was triggered by off-axis yellow light stimulation; whereas in-axis violet-light pulses triggered the postsynaptic side activity. (b) Current clamp recordings from CA1 CheRiff cells during optical pairing. One yellow pulse (594 nm) was coupled with 3 violet (405 nm) flashes (20 ms intervals), causally (+12 ms) or anti-causally (-8 ms), repeated at 5 Hz. The yellow light-induced EPSP, violet light-induced action potentials. Scale bars: 20 mV, 100 ms.

3.1.1.1 Fidelity of CA1 (postsynaptic) neuron firing during oSTDP

As mentioned above, optogenetic spike thresholds of CA3 and CA1 neurons were carefully measured (Fig. 21). However, the fidelity of optogenetic spike induction during pairing was not determined. To do so, I analyzed in detail the spiking pattern of CA1 neurons during pairing in 24 experiments (Fig. 23, 24). In general, the spiking pattern of 67% of the analyzed in-bath experiments were considered successful (Fig. 23), producing the desired pattern of EPSCs and spiking and meeting the following criteria: (1) In more than 90% of the 300 pairings there were 2 or 3 postsynaptic spikes. (2) In less than 3% of the 300 pairings there were more spikes than expected. In 16.7 % of the experiments, CA1 neurons fired exactly one spike after every single violet light pulse (i.e. exactly 900 action potentials). 50 % had either a few pairings with extra spikes or a few with fewer spikes than expected. Fig. 24

illustrates examples of unsuccessful in-bath pairing with complex spike bursts appearing in 16.7 % of pairings (a, b) or a failure of the CA1 neuron to fire spikes (16.7%, c).

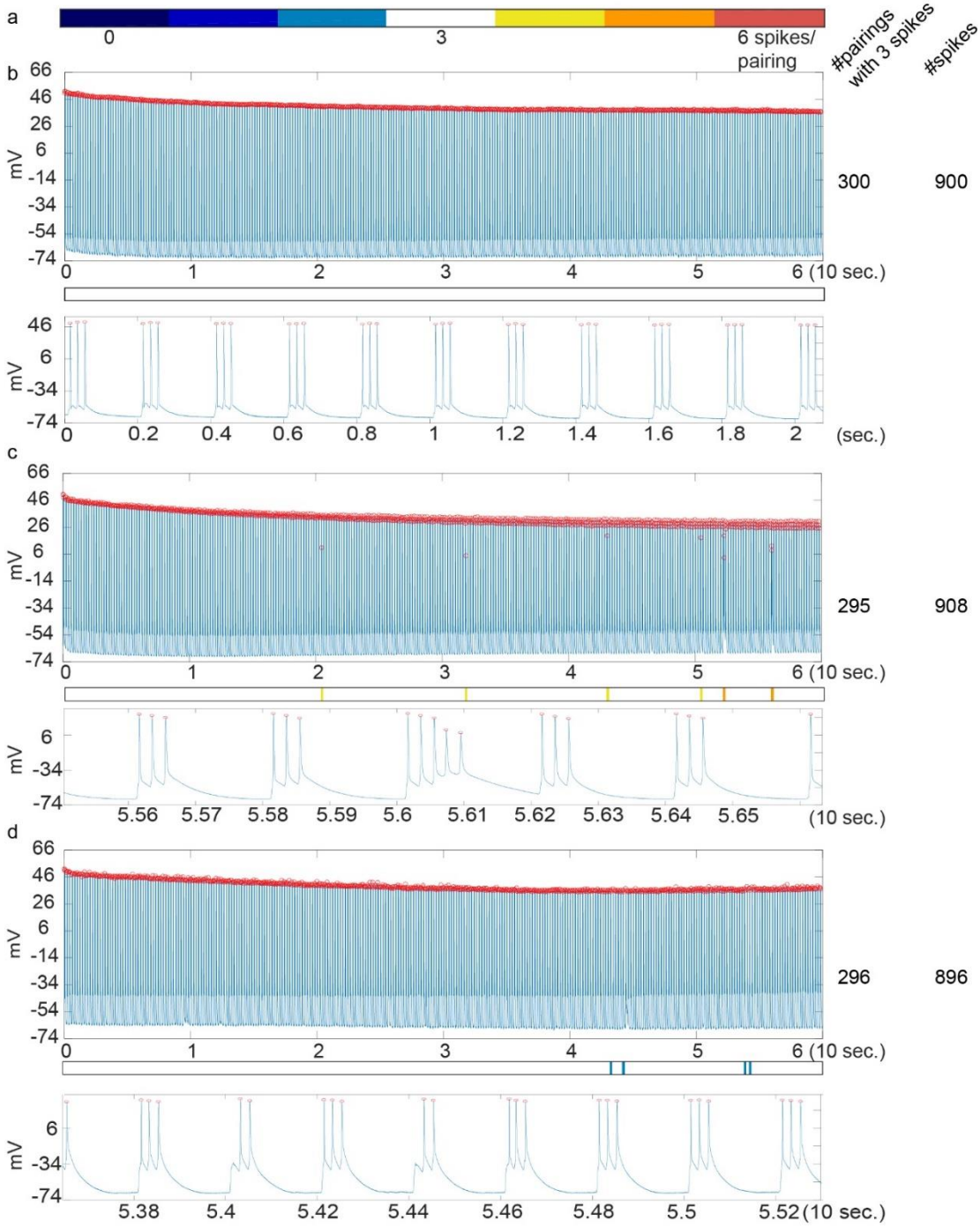

Figure 23: Examples of successful pairings during oSTDP induction

Current-clamp traces from postsynaptic CA1 neurons during paired light stimulation. (a) The scale bar of spiking patterns. (b) An example of a perfect pairing trace. Ideally, the CA1 cells spike 900 times (in 300 pairs, spikes are labelled by the red circles) during the optical pairing period. The lower trace shows the zoom-in detailed recordings. 4/24 recordings had a perfect spiking pattern. (c) An example of a slightly over-firing CheRiff neuron. 6/24 recordings showed such a spiking pattern. (d) An example of a slightly under-firing CheRiff neuron. 6/24 recordings showed such a spiking pattern.

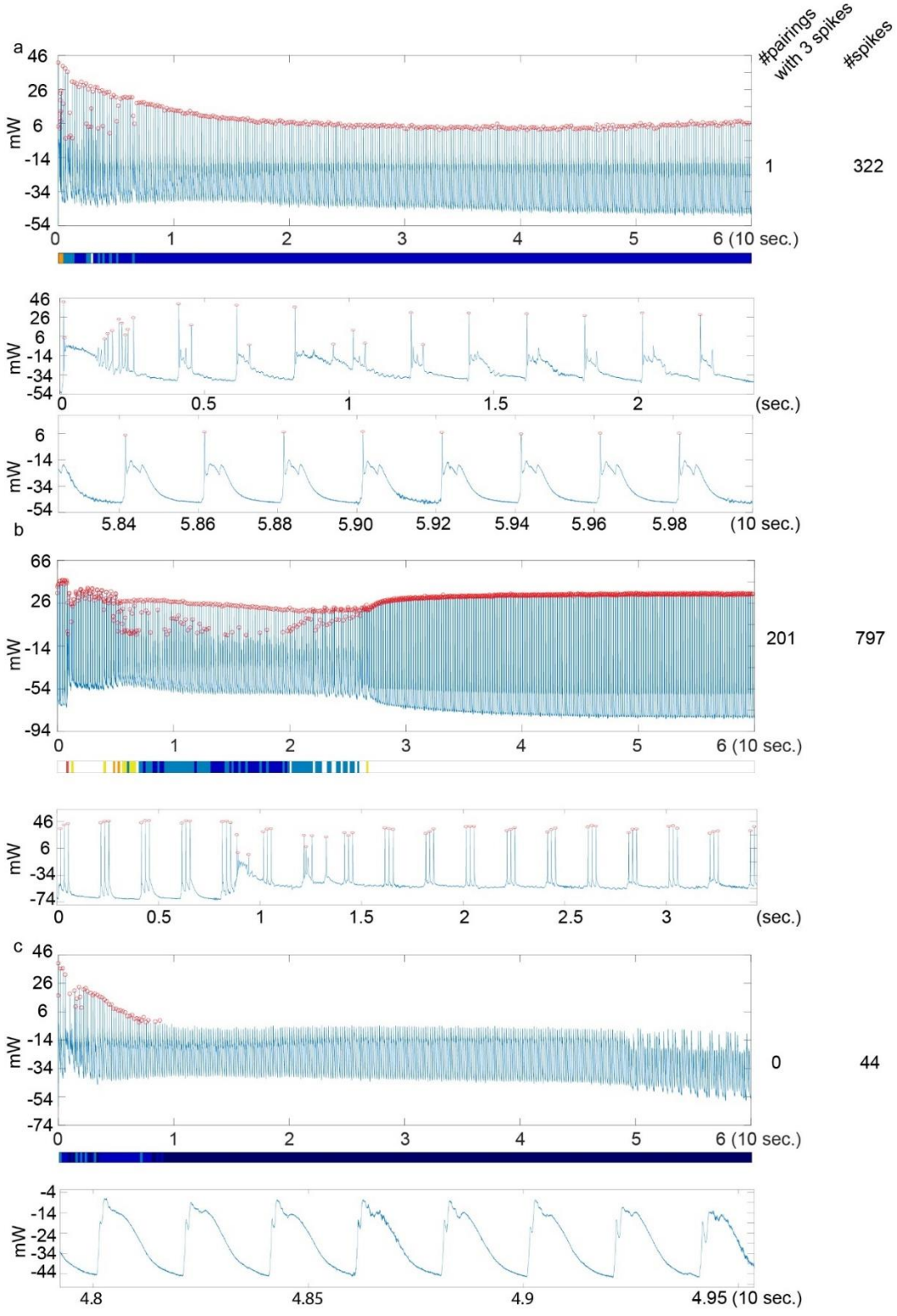

Figure 24: Failure modes of light stimulation.

Current-clamp traces from postsynaptic CA1 neurons during paired light stimulation. The spiking pattern color bar is the same as in Fig. 23a. (a) Initially, the postsynaptic neuron fires complex spike bursts, followed by single-spike responses to only the first of three violet light pulses (3/24 experiments). (b) One experiment showed long-lasting complex burst spikes, corresponding to Vm ramping. After recovery of Vm, the cell returns to the expected 3-spike pattern (1/24 experiments). (c) This CA1 neuron failed to fire action potentials for most of the pairing period (4/24 experiments).

3.1.1.2 Fidelity of CA3 neuron spiking during optical stimulation

The result presented in 3.1.1.2 is in the publication: Anisimova M, van Bommel B, **Wang R**, Mikhaylova M, Wiegert JS, Oertner TG, Gee CE. Spike-timing-dependent plasticity rewards synchrony rather than causality. Cereb Cortex. 2022 Dec 15;33(1):23-34. doi: 10.1093/cercor/bhac050. PMID: 35203089; PMCID: PMC9758582.

While applying in-bath causal/anti-causal pairing stimulation, the activity of CA3 ChrimsonR-expressing cells is not directly monitored. I wanted to ensure that the ChrimsonR CA3 neurons were not bursting during the pairing and verify that they reliably fired single action potentials after the red-light flashes. In Fig. 25 (Supplementary Fig. 1 from Anisimova et al., 2022) panels A to C illustrate why using the synapsin promoter to drive ChrimsonR expression in CA3 is important to prevent bursting. As local inhibitory interneurons are also expressing ChrimsonR and are simultaneously activated by the red light, a large inhibitory input is triggered a few ms after the light induced direct depolarization of the CA3 pyramidal neuron. This together with using short light pulses ensures the CA3 neurons fire single action potentials. To confirm the ability of CA3 neurons to follow the optical stimulation, I recorded their activity in cell-attached mode while applying 5 Hz, 635 nm optical stimulation. 78% of the recorded neurons were able to follow the 5 Hz optical stimulations perfectly (Fig. 25), suggesting that our optical stimulation method and CA3 channelrhodopsin expression strategy was compatible with induction of oSTDP. In the last trace of Fig.25D there are small amplitude spikes also seen. As I was unsure of their origin, I concluded that in this recording the CA3 cell might have been spiking but a second possibility is that these are ephaptic spikelets originating from neighboring neurons (Michalikova et al., 2019).

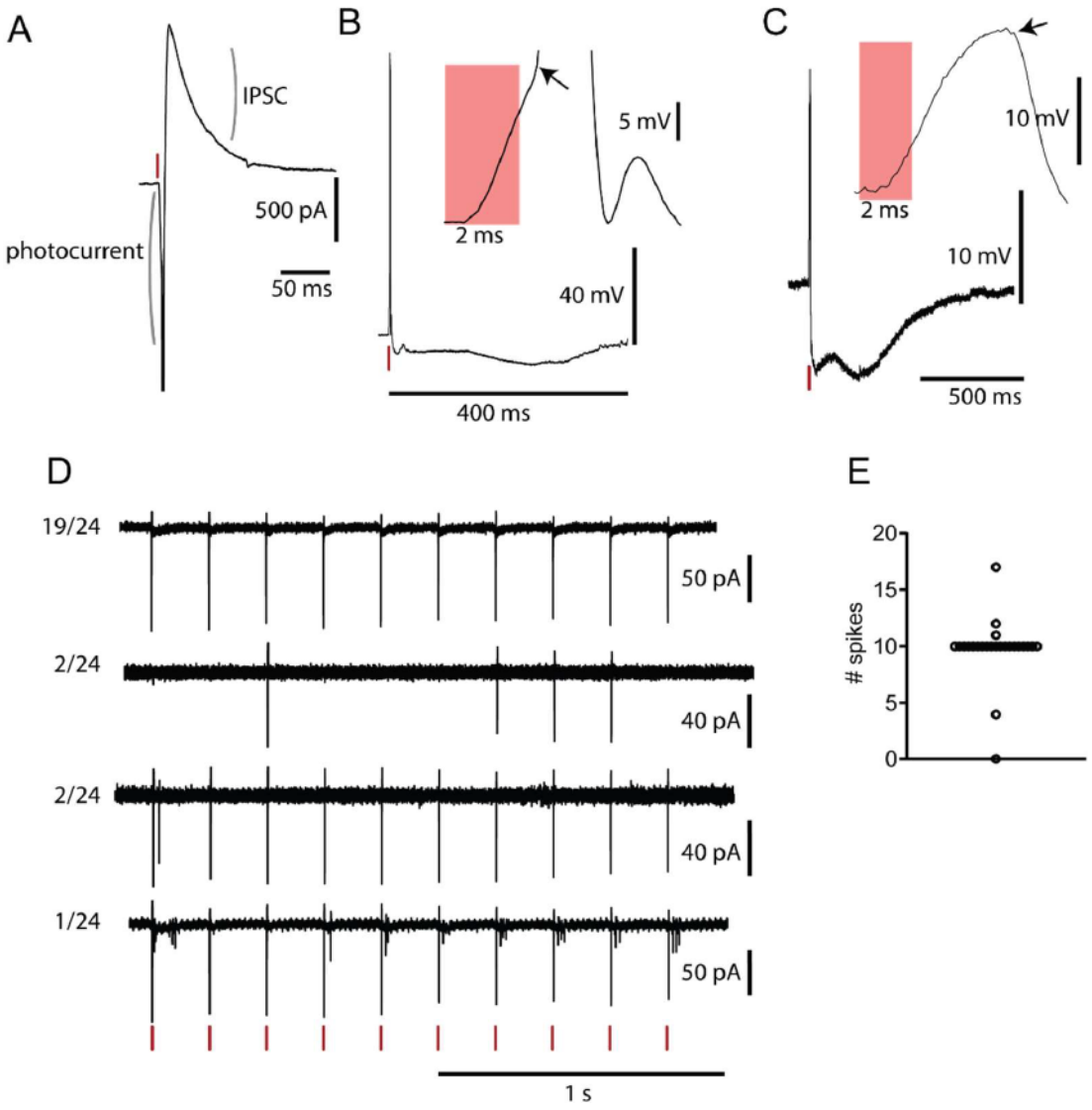

Figure 25: CA3 ChrimsonR neurons reliably follow optical stimulation.

rAAV2/10 synapsin-ChrimsonR-tdTomato was locally injected into CA3. A, A ChrimsonR-CA3 cell voltage-clamped at -54.4 mV. The light intensity was at spike threshold for this neuron (determined in cell-attached mode, 2.8 mW /mm^2). Note the outward inhibitory postsynaptic current immediately following the truncated inward photo- and action current. B, Same neuron stimulated with light supra-threshold for this neuron in current clamp (10 mW /mm^2). A single action potential is elicited followed by a pronounced hyperpolarization. Note, the light (red shading) is off before the action potential is initiated (arrow in inset, time 2.5 ms after start of light flash). C, Response of same neuron to light stimulation sub-threshold for this neuron (2.5 mW /mm^2). Note the photoresponse is truncated by an inhibitory postsynaptic potential 5 ms after start of the light flash (arrow in inset). D, Example cell-attached recordings of ChrimsonR-CA3 neurons in medium in response to 10 x 2 ms 8 mW /mm^2 625 nm at 5 Hz. 19 of 24 neurons fired exactly 10 spikes, 2 of 24 less than 10, 2 of 24 1-2 extra spikes and 1 of 24 may have fired small bursts of spikes. E, quantification of number of spikes fired from 24 cell-attached recordings as in D. (Supplementary Figure 1, Anisimova et al., 2022).

3.1.2 Characterization of input strength 3 days after oSTDP: EPSC amplitude of non-transfected neurons predicts outcome

When we applied the optical causal pairing protocol in the incubator (Fig. 18) and measured the input strength of the paired cells 3 days later, relative to the neighboring non-transfected cells (Fig. 26), we observed that tLTP persists for at least 3 days, which we called late tLTP (Anisimova et al., 2022). Late tLTP after oSTDP did not correlate with passive cellular parameters (e.g. membrane capacitance, input resistance, etc.), suggesting that tLTP is not maintained by a change in postsynaptic neuron excitability. In the earlier experiments several intensities of yellow light were used and the lowest intensity of light, which induced EPSCs in both the NT and CheRiff-expressing CA1 neurons was used for analysis. This was done primarily to avoid activating NT CA3 neurons due to recurrent excitation in CA3. It was assumed that if NT CA3 neurons were driven to spike during the readout, the contribution of these non-paired synaptic inputs to the CA1 neurons would obscure plasticity-induced potentiation. Also, it is known that when many CA3 neurons are stimulated at 5 Hz this directly causes NT CA1 neurons to begin firing complex spike bursts and induces theta LTP (Thomas et al., 1996). This was an additional reason to ensure that the number of CA3 neurons transduced and expressing ChrimsonR was kept low (Anisimova et al., 2022).

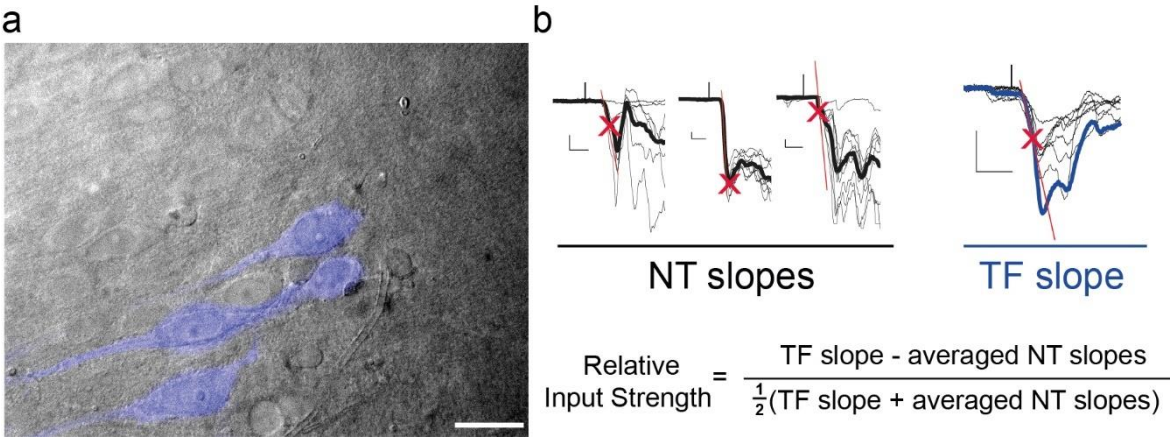

Figure 26: Relative input strength calculation 3 days after incubator pairing.

(a) Representative Dodt-contrast image of the CA1 region with overlaid epifluorescence image of CheRiff and mKate2 transfected (TF, blue) pyramidal neurons (PNs). Neighboring unlabeled grey cells are non-transfected (NT) cells. Scale bar: 36 µm. (b) The calculation of relative input strength onto TF PNs. Individual excitatory postsynaptic currents (EPSCs) were recorded from at least 3 NT and 1 TF CA1 pyramidal neurons (thin grey lines) and averaged (thick black/blue lines, average of 10 sweeps). The first peak of the average EPSC was detected (red cross) and the initial slope measured (indicated by thin red line). Vertical black lines indicate the time of optical stimulation of the presynaptic CA3 neurons (594 nm, 2 ms). The intensity of laser was set to evoke an EPSC of 100-200 pA in the first neuron and kept constant for all recordings from the same slice. The example sweeps are the voltage

clamp recordings from one slice. PNs were sequentially recorded from a single field of view per slice without moving. Relative input strength was calculated using the equation shown. Scale bar:10 ms, 100 pA.

When I began to perform in-incubator causal pairing and measured the input strength 3 days later, I initially failed to reproduce the expected causal pairing-induced late tLTP: no difference in input strength was observed between the paired and unpaired groups (Fig. 27a, Fig. 6). I hypothesized that too many CA3 neurons were transduced and spiking during the oSTDP induction (see Fig. 21b, the lower images). Since the amplitude of the EPSC in the non-transfected (NT) CA1 neurons is a good proxy for the number of light-activated presynaptic CA3 neurons, I plotted EPSC amplitude vs the relative input strength onto the transfected CheRiff expressing CA1 neurons 3 days after the in-incubator oSTDP pairing. In the large majority (6 out of 7) of experiments where the average NT EPSC amplitude was below -200 pA, the causally paired CheRiff expressing neuron showed late tLTP (Fig. 27b). Importantly, this inverse correlation between the NT EPSC amplitude and CheRiff neuron relative input strength was not observed in slices without oSTDP (unpaired). When slices in which the EPSC amplitude in the NT neurons was larger than 200 pA (-) were excluded from the dataset, the relative input strength onto paired and unpaired CheRiff-expressing neurons was highly significant (Fig. 27c). This analysis confirms that oSTDP is no longer synapse specific when too many CA3 neurons are stimulated during induction. As using the EPSC amplitude in the NT neurons is much easier than attempting to count the number of virus-expressing CA3 neurons, I applied the criterion that NT EPSC amplitude must be < 200 pA (-) threshold to the rest of my experiments.

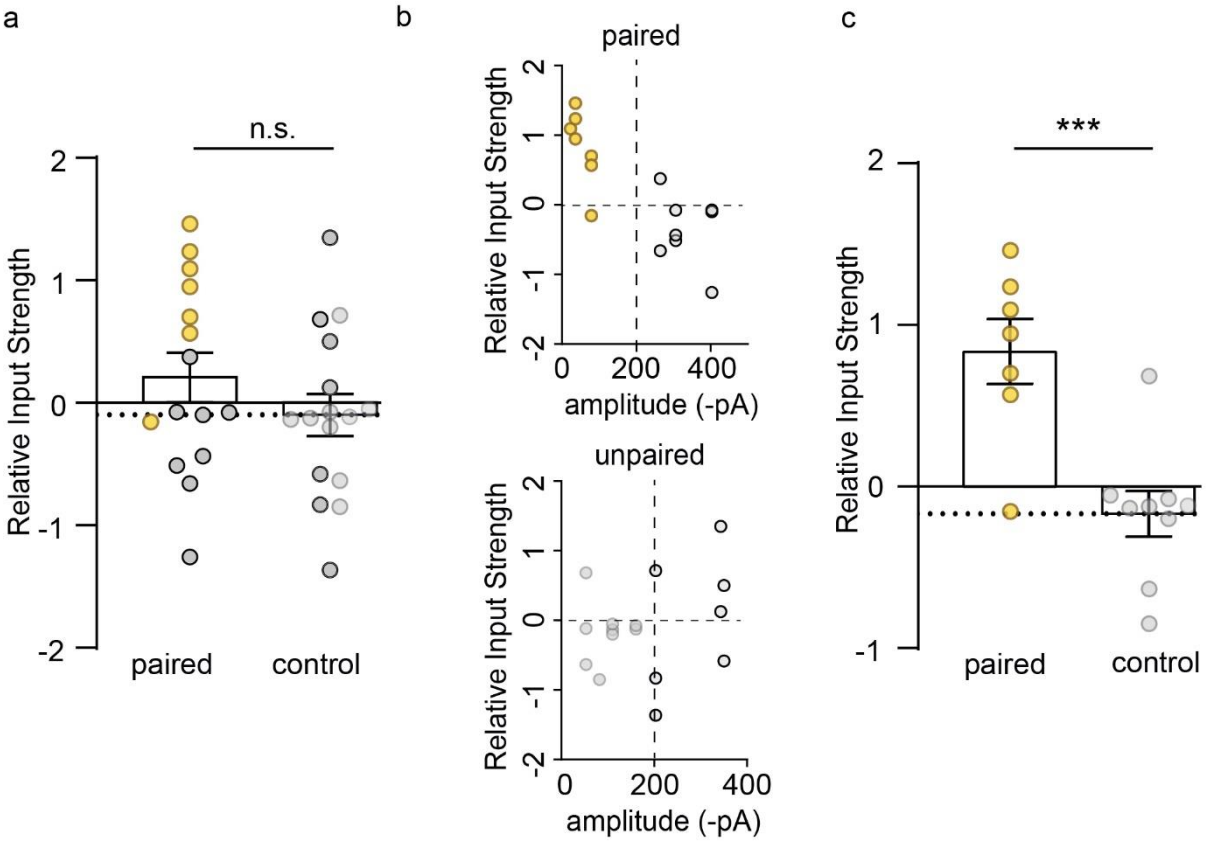

Figure 27: The effect of EPSC amplitude on the relative input strength 3 days after oSTDP.

(a) Without considering the EPSC amplitude, there was no difference in input strength between the paired and the unpaired group. Orange and grey dots represent experiments with EPSC amplitude < 200 pA; black dots represent experiments with EPSC amplitude > 200 pA. Unpaired t-test, ns: not significant. (b) Replot of data in (a) to show the relationship of input strength versus the average NT amplitude in paired (upper) and unpaired (lower) groups. Color-coded as shown in (a). (c) LTP was observed in the paired group with < 200 pA amplitude. In (a) n = 15, 16, in (c) n = 7, 9. Unpaired t-test, ***P < 0.001; ns: not significant. Data plotted as mean ± SEM.

3.1.3 Discussion and perspectives

The specificity of long-term plasticity induction by oSTDP

About 67% of the in-bath pairing experiments were considered successfully stimulated. Regarding the unsuccessful pairings, there are typically two types of failures; those with or those without complex bursts. When complex bursts occur, there is a corresponding ramping of membrane voltage (Fig. 24b) and a slow recovery. During the recovery phase, the cell failed to spike 3 times/pair, which means that the complex burst activities caused inhibition of simple spiking, the so-called "post-complex burst pause" originally reported in Purkinje cells (Latham & Paul, 1970), and later in hippocampus (Ranck, 1973). It is possible that this pause results in the failure of oSTDP spike pattern generation.

More rarely, the patched neurons were silent throughout the induction period, most likely because CheRiff electroporation did not work well in these cases. When I observed failure of the pairing I usually stopped the recording so it is possible that tLTP was still induced.

In addition, I found a strong inverse correlation between the EPSC amplitude in non-transfected neurons and the input strength difference between paired and non-transfected neurons 3 days after pairing. Selective input strengthening was only detected in experiments where the average EPSC of non-transfected neurons was smaller than -200pA. I suspect that in the experiments with large EPSCs, spiking or even complex spike bursts are driven in both the CheRiff and the non-transfected postsynaptic neurons. When many CA3 neurons are driven to spike at 5 Hz, this theta stimulation induces LTP at Schaffer collateral synapses (Thomas et al., 1996) and cFos expression in the CA1 neurons (Fig. 21). Thus, I hypothesize that the synapse specificity of the pairing is lost and the spiking non-transfected CA1 neurons will also undergo Hebbian-like LTP. There will therefore be little or no difference in input strength between paired and non-transfected CA1 neurons. Indeed, after excluding all experiments with too large EPSCs, 6 out of 7 experiments showed strong enhancement of the relative input strength (Fig. 27). Thus, the number of transfected CA3 neurons is a critical parameter for oSTDP, and using the EPSP amplitude in NT cells as a selection criterion greatly improves the reliability of the oSTDP protocol. These insights were crucial for the next part of my PhD project.

3.2 The role of CaMKII in STDP

3.2.1 Inhibiting CaMKII activity during the induction of oSTDP

CaMKII is thought to be one of the most important memory molecules that transform transient synaptic activity events into long-lasting synaptic plasticity, possibly through its autophosphorylation feature (J. Lisman et al., 2012). Whether CaMKII is essential to induce and/or to maintain synaptic plasticity is still controversial. In recent years, a photon-activatable CaMKII activity inhibitor, paAIP2 (Murakoshi et al., 2017) was developed by fusing AIP2 (a peptide inhibitor of CaMKII activity) with the LOV2 domain (a reversible photochromic switch). CaMKII activity can be manipulated with a high temporal and spatial accuracy using light to activate paAIP2 (Fig. 28a).

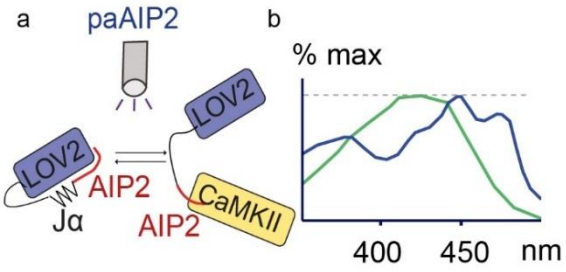

Figure 28: paAIP2 and CheRiff.

(a) Construction of paAIP2. AIP2 is a peptide inhibitor of CaMKII. Photon-activatable AIP2, paAIP2 is to fuse AIP2 to the reversible photochromic switcher, LOV2 domain. paAIP2 can be activated by optical illumination and deactivated when the light is off. (b) The blue line indicates the absorbing spectrum of paAIP2, and the green line indicates the activation spectrum of CheRiff. The CheRiff activation can be coupled with paAIP2 activation by UV-blue light illumination. (Y: maximum absorption/activation percentage, X: wavelength.) Adapted from Murakoshi et al., 2017 & Nagasawa et al., 2023.

3.2.1.1 paAIP2 activation blocks oSTDP induction

CaMKII activity during the induction of LTP, but not before, nor after, is critical for strengthening of synaptic input (Murakoshi et al., 2017). To investigate whether CaMKII activity also plays a critical role in timing-dependent plasticity in the hippocampus, I combined paAIP2 with our oSTDP protocol. paAIP2 and CheRiff have similar activation spectra (Fig. 28b), therefore CaMKII will be inhibited during optical pairing stimulation of CheRiff + paAIP2 expressing cells (Fig. 29, Fig. 30a).

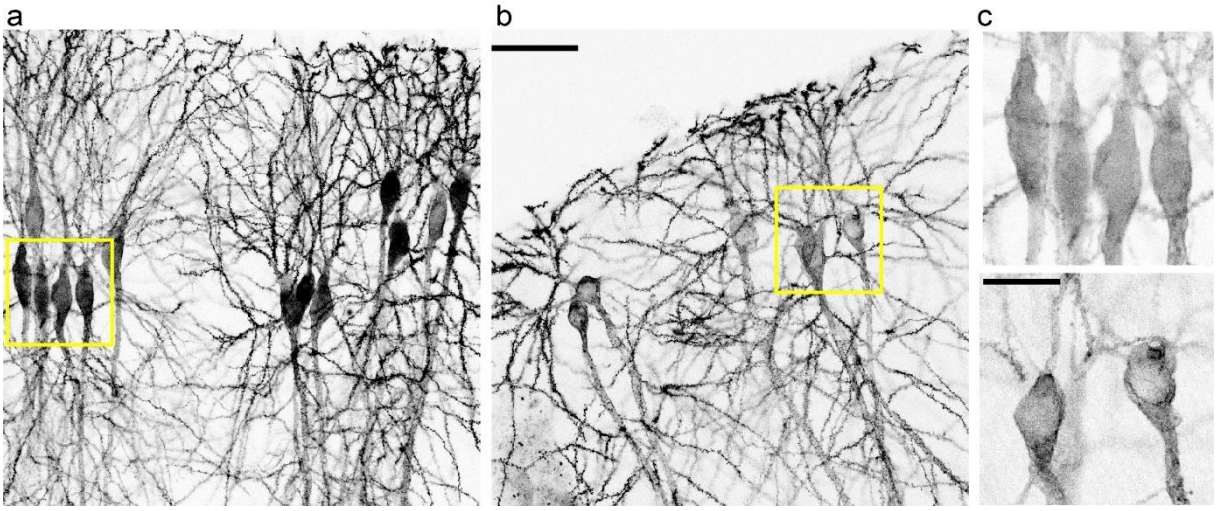

Figure 29: GFP staining of CheRiff-eGFP + eGFP-2A-paAIP2 or CheRiff-eGFP only CA1 neurons.

(a) The contrast-inverted maximum intensity projection of confocal Z-stack images of eGFP in pyramidal neurons expressing paAIP2 + CheRiff expression. The eGFP expressed from the same plasmid as paAIP2 is soluble and fills the cytosol including the nucleus whereas CheRiff is fused to eGFP and appears at the membrane. (b) Neurons expressing only CheRiff-eGFP have fluorescence more concentrated at the membrane and excluded from the nucleus. (c) top: zoom in, single optical section from region indicated with the yellow square in (a); bottom: zoom in, single optical section from the region indicated with the yellow square in (b) Scale bar: 50 µm (a, b), 20 µm (c).

After recording a baseline of light-induced EPSCs in CA1 neurons, the slice culture was illuminated by 405 nm light for 1 second (20 Hz x 3 pulses, repeated at 5 Hz, 1.2 mW/mm^2) to pre-activate paAIP2 and inhibit CaMKII 10 s before the start of optical pairing. Optical pairing stimulation was applied as described above (Fig. 21). As typically the initial EPSC is rapidly followed by strong inhibition, I analyzed the initial slope as a measure of excitatory input strength. Only experiments that were successfully paired were accepted, using the criteria in 3.1.1. In the CheRiff-only group (Fig.30b, c, d), pre-post (causal) pairing induced early tLTP while post-pre (anti-casual) pairing induced early tLTD. When CaMKII activity was acutely inhibited during the induction period of oSTDP (paAIP2+CheRiff co-expression group), early tLTP and early tLTD were completely blocked. In non-transfected control neurons, no change in input strength was observed. Therefore, CaMKII activity during plasticity induction is indeed critical for the early phase (~25 minutes) of timing-dependent plasticity in the hippocampus.

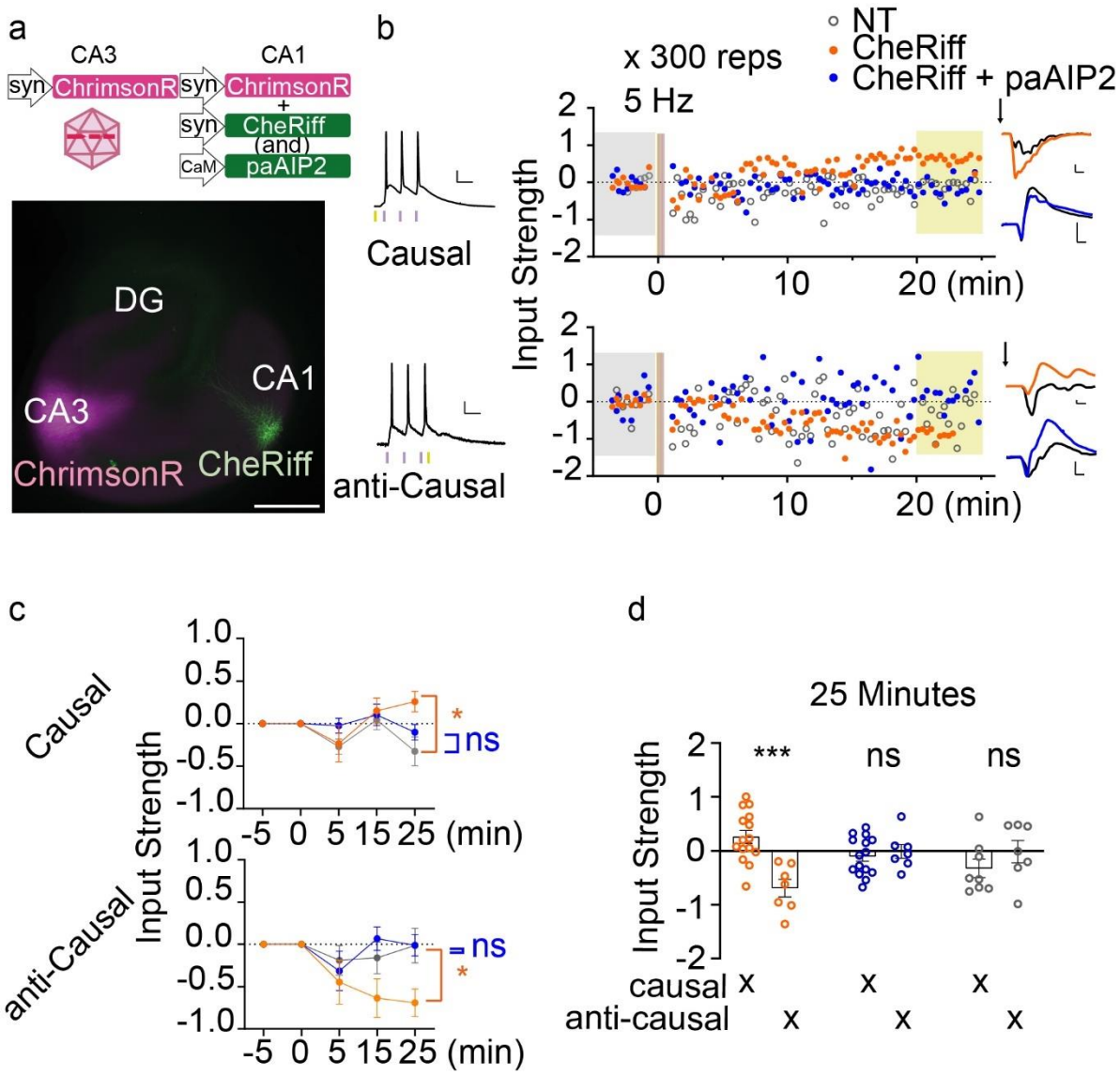

Figure 30: Inhibition of CaMKII activity blocks the induction of early tLTP and early tLTD.

(a) CA3 neurons were transduced to express ChrimsonR by AAV injection. CheRiff (with or without paAIP2) and mKate2 were expressed by CA1 PNs after single-cell electroporation. Scale bar: 500 µm (b) Left: pairing flashes as described in Fig. 22b. 10 seconds before the application of pairing pulses, 1 second of 405nm pulses were applied to inhibit CaMKII activity, followed by 9 seconds of waiting. Scale bars 20 mV, 100 ms. Middle: example experiments of causal (top) and anti-causal (bottom) pairing with or without CaMKII activation, time 0 indicates the start of the pairing protocol. Right: average trace of baseline EPSCs (as grey boxes area in the middle, black lines) and 20-25 minutes EPSCs (as yellow boxes area in the middle, orange or blue lines). Arrows indicate the timepoint of presynaptic optical stimulation. Scale bars: 100 pA, 5 ms. (c) Average input strength alterations over time. Upper: causal pairing results, paAIP2 activation blocked tLTP 25 minutes after inducing. Lower: anti-causal pairing results, paAIP2 activation blocked tLTD 25 minutes after induction. Causal: NT, CheRiff, CheRiff +paAIP2: n =8, 15, 15; anti-causal: n =7, 7, 7. Data plotted as mean ± SEM. Two-way ANOVA followed by Dunnett's multiple comparisons, compared to NT group. *P < 0.05; ns: not significant. (d) The input strength at 25 minutes after pairing. Left to right: n = 15, 7, 15, 7, 8, 7. Data plotted as mean ± SEM. Unpaired t-test, ***P < 0.001, ns: not significant.

3.2.1.2 CaMKII inhibition does not affect basal transmission

Recent studies suggest that CaMKII silencing can depress basal synaptic transmission (Barcomb et al., 2016; Tao et al., 2021b). To test this possibility, I applied the same pre-post pairing protocol to CA1 neurons expressing only paAIP2, but not CheRiff (Fig. 31a). In each slice culture, a pair of paAIP2-only and NT cells was patched sequentially and the same presynaptic optical stimulation was applied to record the baseline. After recording each baseline, a pairing protocol was performed (in the absence of postsynaptic CheRiff). The baseline slope of each pair of paAIP2 and NT cells was identical (Fig. 31b), suggesting that expression of paAIP2 did not reduce the input strength. More importantly, after optical inhibition of CaMKII, no reduction in input strength was observed in the paAIP2 group compared to baseline (Fig. 31c, d), which was also identical to the NT group. These results show that the acute optogenetic inhibition of CaMKII used in our experiments did not affect synaptic transmission, but blocked the induction of synaptic plasticity (Fig. 30).

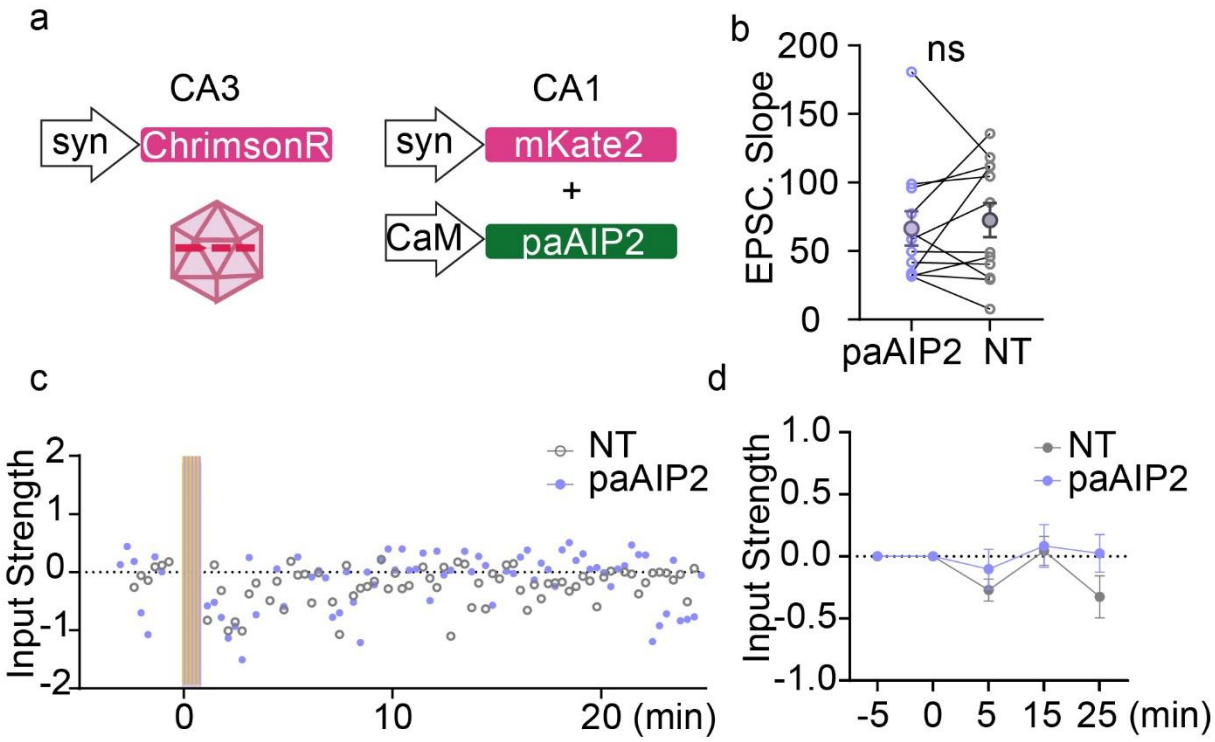

Figure 31: Expression and activation of paAIP2 does not affect basal transmission

(a) Constructs expression strategy. CA3 AAV transducing and CA1 single-cell electroporation was performed. (b) Average baseline slopes for 5 minutes of sequentially recorded paAIP2 and NT neurons. Paired comparisons were performed between the two cells recorded from the same slice, same dose of optical stimulation was applied to each slice. Individual recordings illustrated by the open circles, and mean± SEM shown by the close dots. Paired t-test. NT, paAIP2: n = 12, 12. ns: not significant, $p > 0.05$. (c) Example recordings before and after optical pairing stimulations, from NT

and paAIP2 cells. (d) Average, normalized input strength alteration measurements over 30 minutes. NT, paAIP2: n = 7, 10. Data shown as mean ± SEM, two-way ANOVA. ns: not significant (genotype).

3.2.1.3 The late phase of long-term potentiation does not require CaMKII activity

As briefly discussed in 3.1.2, by using the incubator illumination tower (Fig. 18) and the patch-clamp experimental strategy (Fig. 24), it was previously found in the lab that causal pairing induces tLTP that lasts for at least 3 days. Surprisingly, anti-causal pairing also induced tLTP after 3 days (Anisimova et al., 2022). Thus, although the timing window of early oSTDP is very similar to "classical" STDP (Bi & Poo, 2001), the timing window of late oSTDP is different: only potentiation is observed 3 days after optical pairing (Fig. 6 and Fig. 32).

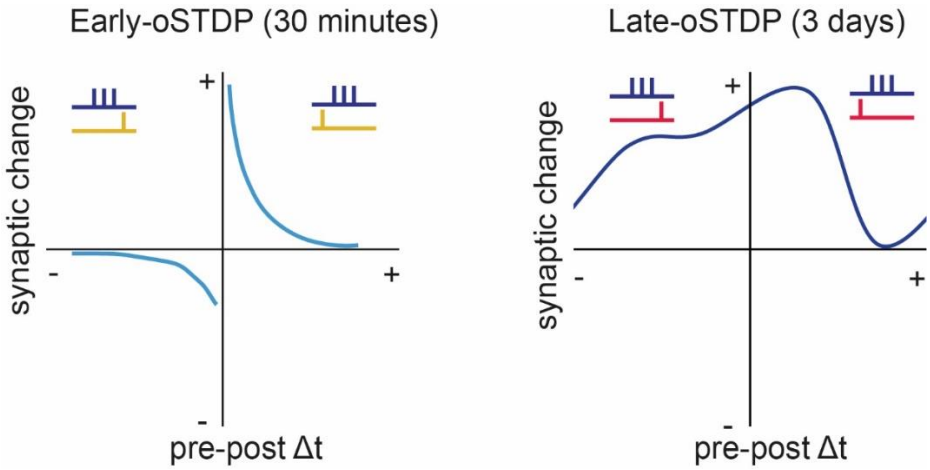

Figure 32: Early *versus* late hippocampal oSTDP timing window.

Left: The timing window of early oSTDP is similar to the classic asymmetric STDP timing window: pre-post causal pairing induces LTP, and post-pre, anti-causal pairing induces LTD. Right: The timing window of late oSTDP is axially symmetric, both causal and anti-causal pairing induced potentiation at the late phase (right figure, adapted from Anisimova et al., 2022).

To investigate the function of CaMKII in late tLTP, I performed oSTDP experiments in the incubator with postsynaptic expression of paAIP2. Only recordings that passed the criteria discussed in 3.1.2 were kept. In CheRiff-only expressing cells (Fig. 33, orange circles), both causal and anti-causal pairing resulted in the potentiation of input strength after 3 days, confirming our published results (Anisimova et al., 2022). When CaMKII activity was blocked in the postsynaptic neuron during the pairing protocol (Fig. 33, blue circles), late tLTP remained intact. On the other hand, when anti-causal pairing was applied to paAIP2+CheRiff cells, the outcome was identical to "no pairing" controls, indicating complete

block of late tLTP. Note that the means of both control columns are negative. This reduction of synaptic input compared to neighboring non-transfected neurons has been observed previously (Anisimova et al., 2022) and appears to be a side effect of channelrhodopsin expression or electroporation.

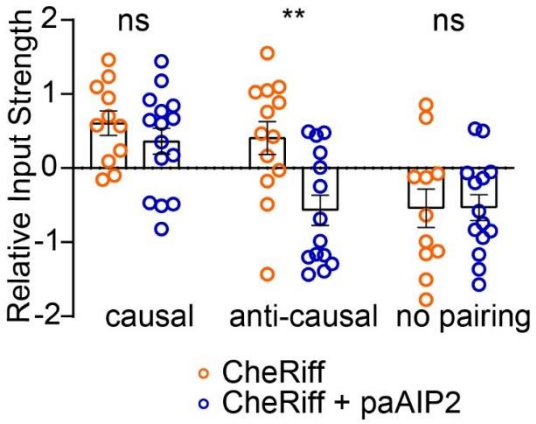

Figure 33: Optogenetic inhibition of CaMKII activity does not block late tLTP.

Optogenetic inhibition of CaMKII does not block the development of causal pairing induced late tLTP, and it blocked the anti-causal pairing induced late tLTP. From left to right: n = 11, 15, 13, 14, 11, 14. Data plotted as mean ± SEM. Unpaired t-test, **P < 0.01; ns: not significant.

Taken together, these results suggest that: (1) in contrast to the CaMKII-dependent early tLTP, a parallel CaMKII-independent pathway is responsible for the development of late tLTP. In other words, late tLTP is not simply a continuation or stabilization of early tLTP, but relies on a completely different induction pathway that does not require CaMKII activity and takes considerable time to fully express. (2) Anti-causal pairing induces early depression, but late potentiation. (3) Both the early depression and late potentiation caused by anti-causal pairing are abolished by paAIP2 activation, suggesting that CaMKII might serve as the synaptic tag for early LTD. It has been shown that LTD induced CaMKII activation phosphorylates GluA1 at a different site (S567) compared to LTP (S831), promoting synaptic depression (Coultrap et al., 2014). It is interesting to investigate the role of CaMKII at different stages of tLTD, the mechanism of which is largely unknown.

3.2.1.4 PKMζ activation is required for late tLTP

My data demonstrate that the molecular mechanisms of early and late long-term plasticity are distinct. It is possible that synapses are “tagged” by causal pairing independent of CaMKII activity. These tagged synapses seem to be able to slowly develop late tLTP which is maintained for at least 3 days. An atypical isoform of PKC, termed PKMζ, is critical for the maintenance of late synaptic plasticity and long-term memory: PKMζ synthesis is activated by many LTP-relevant signaling molecules, including CaMKII (Patel & Zamani, 2021). To

investigate the mechanism of causal pairing-induced tLTP, I blocked the activity of PKMζ for the two days immediately after induction of tLTP by causal pairing. Application of the PKMζ peptide inhibitor ZIP (ζ-inhibitor peptide) blocked L-tLTP in both groups (with or without CaMKII optical inhibition during the tLTP induction phase, Fig. 34). Thus, late tLTP requires activation of PKMζ. A scrambled protein (scr-ZIP) was added in the control experiments.

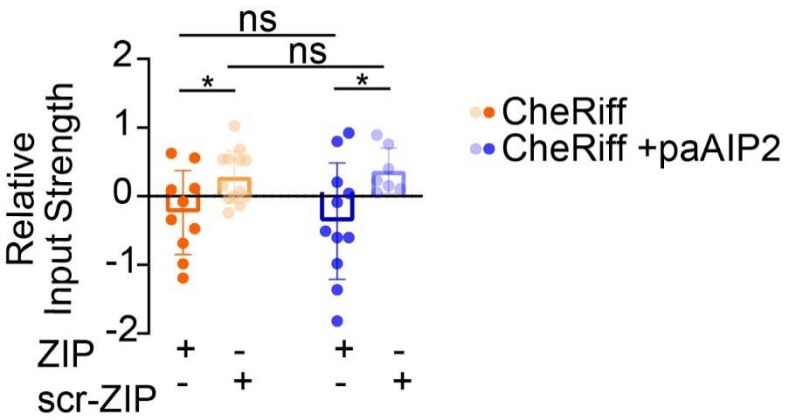

Figure 34: PKMζ is required for timing-dependent late long-term potentiation.

ZIP blocks both CaMKII-dependent and independent late tLTP. Left to right, n = 10, 13, 11, 7. Data plotted as mean ± SEM. Two-way ANOVA, **P < 0.01; ns: not significant.

ZIP has been shown to be associated with neurotoxicity (LeBlancq et al., 2016; Sadeh et al., 2015). In my experiments, 2 days of ZIP incubation did not induce any obvious changes in neuronal viability (which would have prevented successful patch-clamp recordings). To further assess potential toxic side effects, I examined the effect of ZIP on resting membrane voltage, spiking threshold, number of spikes induced by 200 pA current injections (excitability), and membrane capacitance. I observed no significant differences compared to neurons in slice cultures treated with scrambled ZIP protein (Fig. 35).

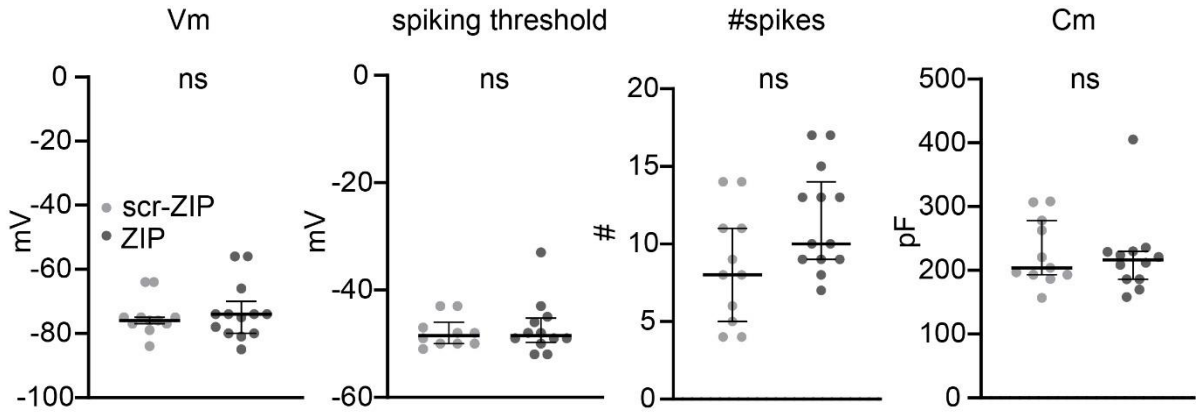

Figure 35: ZIP does not have effects on cell parameters.

Bath application of ZIP does not have significant effects on PN resting membrane voltage (Vm), spiking threshold, number of spikes evoked by 400 pA current and membrane capacitance (Cm). Data plotted as median ± IQR. From left to right, n = 11, 13; 10, 12; 11, 13; 11, 12. Mann-Whitney test, ns; not significant.

3.2.1.5 Timing-dependent plasticity induction-induced c-Fos expression

The c-Fos protein, encoded by one of the most studied immediate early genes (IEG), *FOS*, functions as a transcription factor in neurons. In 1987, an increase in c-Fos expression was reported in brain regions that had experienced seizures (Morgan et al., 1987). Since then, many studies have reported that c-Fos is rapidly and transiently expressed in response to external stimuli, and its expression in turn elevates the expression of synaptic plasticity relative proteins (Alberini, 2009). It is widely accepted that protein synthesis is not only essential for the induction of STDP in the hippocampus (Tanaka et al., 2008), but for long-lasting synaptic plasticity in general (Santini et al., 2014). Therefore, c-Fos expression is an appropriate marker to follow the fate of neurons that have undergone STDP induction. Based on this logic, I used c-Fos expression as a readout to evaluate whether CaMKII is critical for the generation of late, long-lasting synaptic plasticity. On the other hand, by examining the patterns and levels of c-Fos expression, focusing on the role of CaMKII in this process, I aim to better understand the molecular underpinnings of c-Fos expression and synaptic plasticity.

CaMKII activity is not required for oSTDP-induced c-Fos expression

To investigate whether CaMKII activity is required for c-Fos expression, I first confirmed that the neurons that developed tLTP induced by the oSTDP protocol indeed express c-Fos. As shown in Fig. 36, CheRiff-only cells express more c-Fos than the negative control (non-transfected neurons). No significant difference was observed compared to the positive control (high K^+). In paAIP2+CheRiff cells, CaMKII activity was blocked during the optical tLTP induction, but c-Fos expression was not reduced. These results suggest that c-Fos expression after oSTDP does not require CaMKII activation.

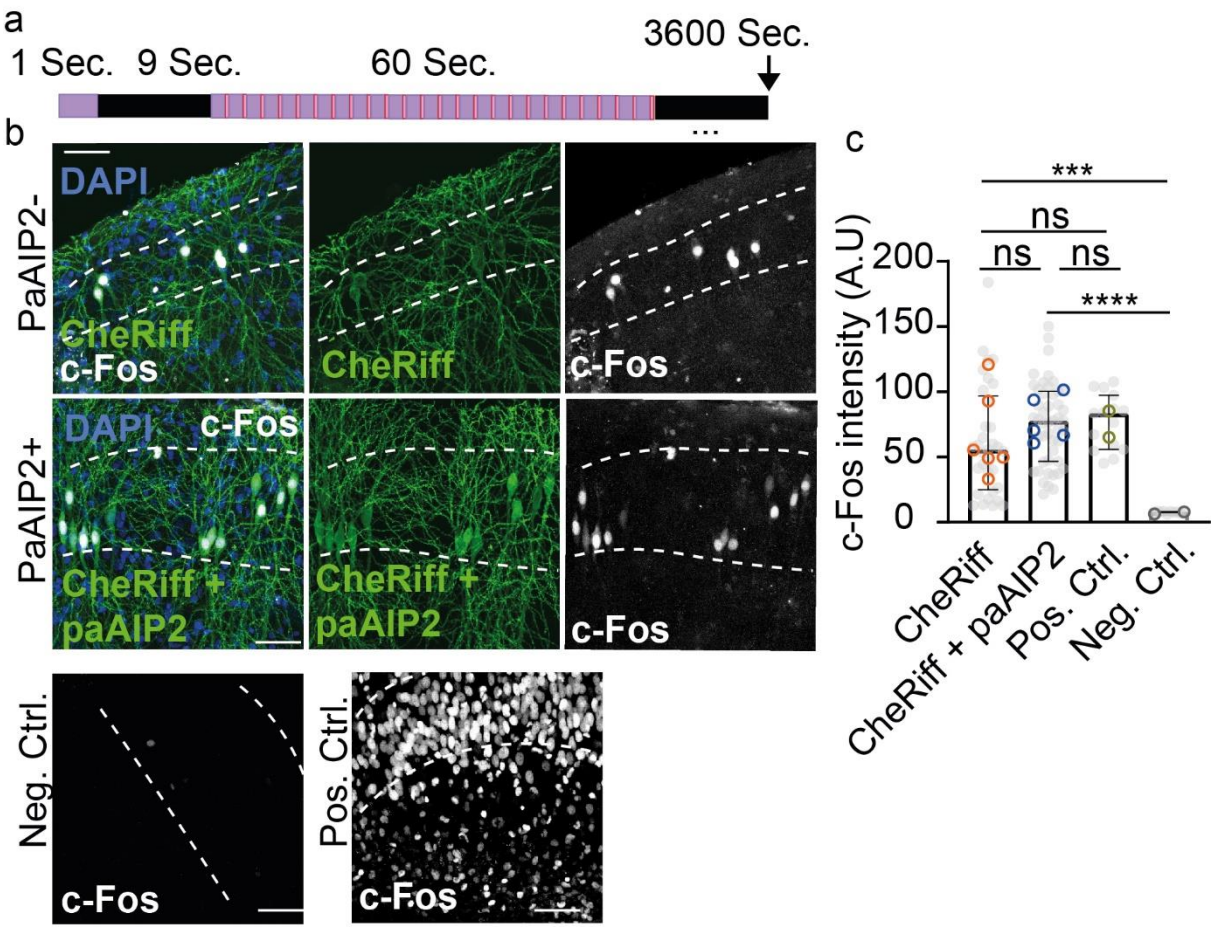

Figure 36: oSTDP-induced c-Fos expression is independent of CaMKII activity.

(a) Experimental protocol. Causal pairing stimulation (violet-red light flashes for 60 seconds) was applied in the incubator, with CaMKII activity blocked 9 seconds ahead of time, by 405 nm light. After the stimulation the slice culture was kept in the incubator for one hour, then fixed (indicated by the arrow) for immunohistochemistry staining. (b) Representative images. Top row: causal pairing induced c-Fos expression in CheRiff only neurons. Middle: The lack of CaMKII activation does not block causal pairing induced c- c-Fos expression in CheRiff+PaAIP2 neurons. For top and middle row, from left to right images are shown as: overlap of all channels, CheRiff (+CheRiff), and c-Fos only. Bottom: no light control (Neg. Ctrl.) and High K^+ positive control (Pos. Ctrl.), c-Fos channel only. Cell body layer is indicated by the dash lines. Maximum intensity projection was made including all the slices containing soma signals. Scale bar:50 µm. Brightness was enhanced with the same LUT across different conditions. (c) The quantification of c-Fos expression. Optical inhibition of CaMKII activity during the induction of tLTP did not block c-Fos expression. From left to right: n = 33, 47, 15, 10 (grey dots); N = 6, 5, 2, 2 (coloured circles). Data plotted as median ± IQR (by n). Kruskal-Wallis test followed by Dunn's multiple comparisons. ****P < 0.0001, ***P < 0.0005, ns: not significant (CheRiff vs. paAIP, p = 0.4751; CheRiff vs. positive control, p = 0.7217, CheRiff+paAIP2 vs. positive control, p > 0.9999). A.U. arbitrary units.

CaMKII activity is not required for spiking-induced c-Fos expression

As I show in 3.2.1.3, CaMKII activity is not required during plasticity induction for late tLTP. Apparently, a late onset pathway requiring PKMζ is responsible for the formation of late plasticity, and is independent of CaMKII activity during induction. Similar to c-Fos, PKMζ

expression is under control of phosphorylated CREB (cyclic AMP responsive element binding protein, Pramio et al., 2023) I wanted to know whether increased gene expression, normally associated with late forms of LTP, is completely independent of CaMKII; or whether CaMKII activity during the first hour after stimulating neurons is required for the increase in gene expression. To address this question, I wanted to optically inhibit CaMKII activity for the entire time between stimulating the neurons and fixing to stain for c-Fos expression. However, CheRiff-expressing neurons is also sensitive to prolonged 405nm light illumination, which is required for paAIP2 activation. I therefore switched to a c-Fos expression induction protocol that only uses ChrimsonR.

The c-Fos expression induction protocol using ChrimsonR was previously characterized in the lab (Anisimova et al., 2023). Specifically, it was shown that spiking neurons at very high (50 Hz) or very low (0.1 Hz) frequency using ChrimsonR induces c-Fos expression in the absence of fast synaptic transmission. This process is not cell autonomous, but requires glutamate release and mGluR activation. Since the activation spectrum of ChrimsonR is largely separated from paAIP2, it is possible to continuously inhibit CaMKII by photostimulation of paAIP2 without causing ChrimsonR neurons to fire action potentials. As shown in Fig. 37 and Suppl. Fig. 1, persistent inhibition of CaMKII during and after stimulation at 0.1 Hz or 50 Hz did not reduce c-Fos expression. Thus, CaMKII activity is not required for activity-dependent expression of c-Fos. It will be interesting in the future to test directly if oSTDP-induced PKMζ expression and late tLTP are also completely independent of CaMKII.

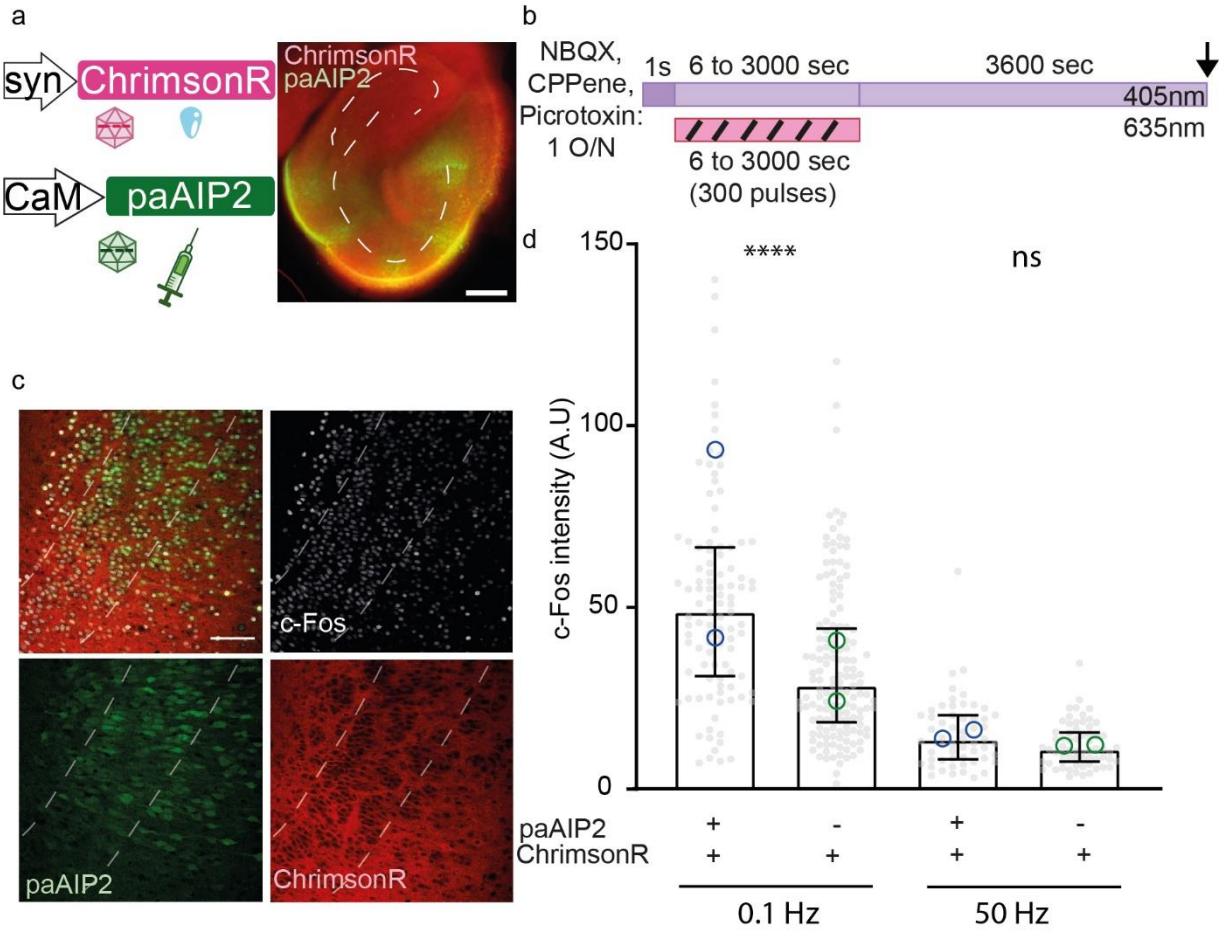

Figure 37: CaMKII activity is not essential for spike-induced c-Fos expression.

(a) Transduction strategy. A drop of ChrimsonR-AAV suspension was applied to the slice culture to generate distributed expression. paAIP2-AAV was locally injected to different areas including CA3 and CA1. In these areas, neurons expressed both paAIP2 and ChrimsonR or only ChrimsonR. Scale bar: 400 µm (b) Experimental protocol. AMPA, NMDA and GABA channels were blocked pharmacologically one night ahead of optical stimulation. 635 nm LED pulses were given at either 0.1 Hz or 50 Hz, and at the same time, 405 nm illumination was applied to block CaMKII activation. During the following hour, violet illumination was kept on to continuously deactivate CaMKII. (c) Representative images of virus transduction and c-Fos expression in CA1. Merged images were contrast-enhanced for visualization, raw grayscale images are shown for separate channels. Scale bar: 100 µm (d) Blocking CaMKII activity did reduce c-Fos expression triggered 0.1 Hz, but not by 50 Hz spike trains. From left to right: n = 103, 149, 56, 64 (grey dots); N = 2, 2 (colored circles). Data plotted as median ± IQR (by n). Mann-Whitney test, ****P < 0.0001, ns: not significant. A.U. arbitrary units.

3.2.2 Plasticity induction by optogenetic CaMKII activation

As shown by inhibition, CaMKII activity is required for early tLTP but is not necessary for late tLTP and c-Fos expression. However, CaMKII activation may still be sufficient for LTP induction. Early studies using biochemical methods and introducing purified active CaMKII

into the target cell have suggested that CaMKII is sufficient for LTP (Shirke & Malinow, 1997). In 2017, Murakoshi and co-authors developed a photoactivatable CaMKII, paCaMKII (Shibata et al., 2021). They fused the CaMKIIα kinase domain with a LOV2 domain (Fig. 38a). These subunits integrate into the CaMKII enzyme complexes and enable optical manipulation of the CaMKII holoenzyme activity. Both functional and structural LTP at the level of individual spines was induced by 2P activation of paCaMKII. However, whether functional plasticity induced by paCaMKII persists for days is unknown.

3.2.2.1 paCaMKII activation in CA1 pyramidal cells induces LTP

To investigate whether acute CaMKII activation is sufficient to induce synaptic strengthening, paCaMKII was expressed in CA1 PNs (Fig. 38a, b). To stimulate a set of input synapses and assess their strength, I transfected CA3 neurons with ChrimsonR and performed whole-cell recordings in CA1 to measure red light-evoked EPSCs. A violet light pulse (405 nm, 0.1 mW/mm^2, 100 seconds) activated paCaMKII and rapidly induced LTP that lasted for at least 25 min (Fig. 38 c, d). As normally CaMKII is activated by calcium entering through NMDA receptors, blocking NMDA receptors by CPPene did not impair paCaMKII-induced LTP (Fig. 38 d). Control CA1 neurons expressing paCaMKII-SD (super dark, light-insensitive) subjected to the same optical stimulation did not show LTP.

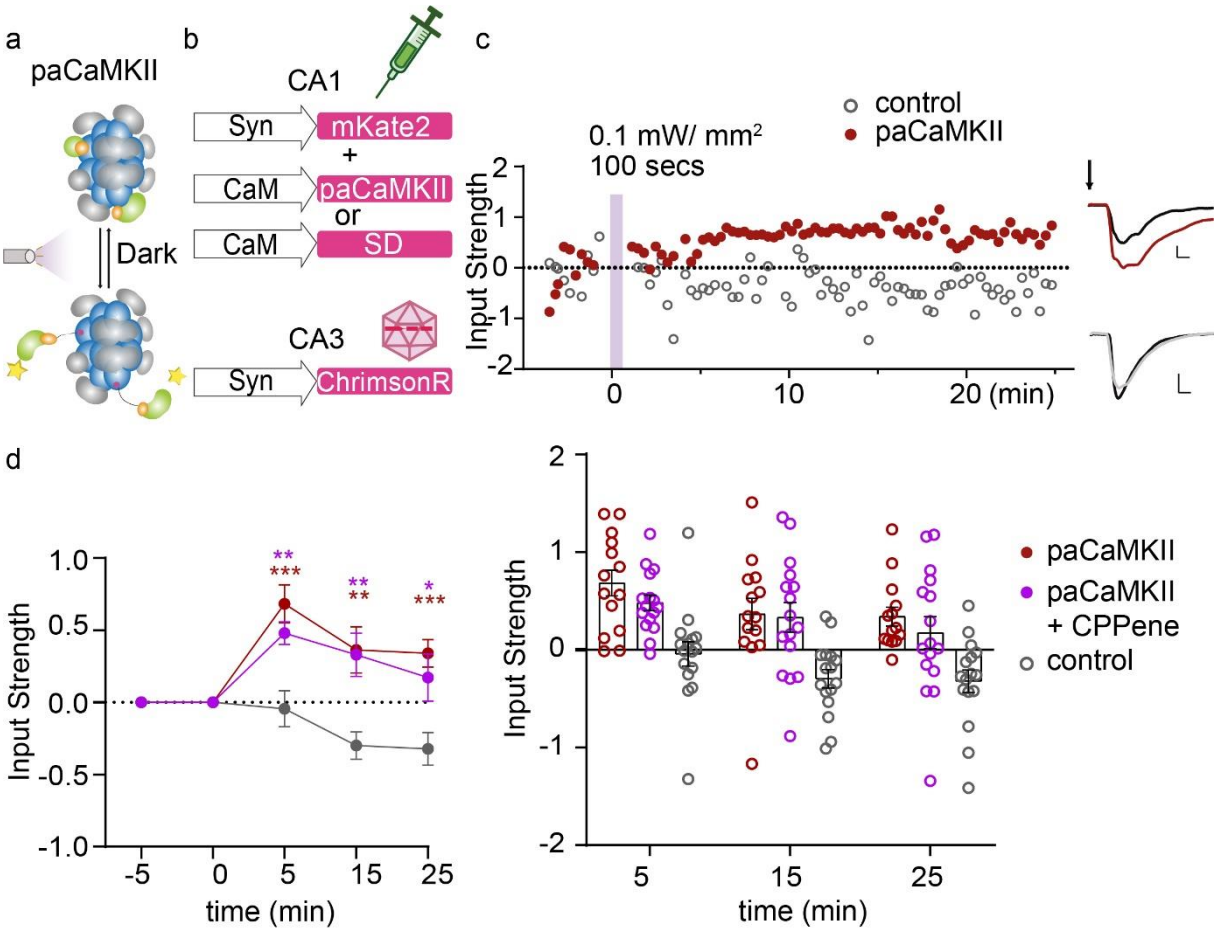

Figure 38: paCaMKII activation induces early LTP.

(a) paCaMKII activation by UV-blue light. Image adapted from Murakoshi et al., 2017. (b) CA3 neurons expressed ChrimsonR and CA1 neurons were electroporated with paCaMKII or paCaMKII-SD (control) together with mKate2. (c) Example time-course of EPSC strength with (red) and without (grey) activation of paCaMKII (violet bar at t = 0). At right are average EPSCs from the baseline (t < 0, black) and 20-25 minutes after stimulation of paCaMKII. The arrow indicates the time of red-light flashes used to spike the CA3 neurons. Scale bars: 100 pA, 5 ms. (d) Left: average input strength comparisons, paCaMKII activation induces a rapid and long-lasting early input strengthening. Control, paCaMKII, paCaMKII + CPPene, n = 16, 14, 16. Two-way ANOVA followed by Dunnett's multiple comparisons (compared to control), ***P < 0.001, **P < 0.01, *P < 0.05. Right: experimental results as shown in left. From left to right, n = 14, 16, 16 for all the three time points. Data plotted as mean ± SEM.

3.2.2.2 Changes in spine volume and PSD size associated with paCaMKII-induced LTP

Biochemical activation of CaMKII induces spine volume enlargement, filopidia growth and formation of new spines (Jourdain et al., 2003; Pi et al., 2010). Similar results have been reported after paCaMKII activation (Shibata et al., 2021; Tullis et al., 2023). Murakoshi and colleagues suggested that the paCaMKII-induced spine volume enlargement lasts for at least 240 min. I wished to extend this timescale and monitor both the spine volumes and the size

of the PSDs, which are a better proxy for synaptic strength. I used a two-photon microscope, combined with a sterile CO_2 supply and a closed-loop heating system that mimics the incubator environment under the microscope objective (Fig. 19). Under optimal conditions, i.e. stable osmolarity, pH and temperature, thousands of spines could be imaged for over 50 hours. This large dataset allowed me to study both the spatial and temporal characteristics of individual spines and their PSDs.

Tracking the dynamics of synapses upon paCaMKII activation

To image PSD and spine volume simultaneously, an eGFP-labeled intrabody against PSD95 and a soluble fluorophore (LSSmOrange) were co-transfected into CA1 PNs together with paCaMKII (Fig. 39a). Previously by introducing GFP-tagged PSD95 into the cells, researchers have imaged PSD and spine volume simultaneously. However, overexpression of PSD-95 itself has been found to potentiate AMPAR EPSCs and disrupt LTP (Ehrlich & Malinow, 2004; Stein et al., 2003). Xph20 fused to eGFP binds specifically to PSD95 and does not appear to affect synaptic transmission or synaptic plasticity (Rimbault et al., 2024). To ensure that unbound protein does not accumulate in the cytosol the zinc finger sequence from CCR5TC linked with the $KRAB_A$ transcriptional repressor domain is included in the protein and the zinc finger binding domain was added upstream of the promoter. By using the large Stokes shift fluorescent protein LSSmOrange, spine volume and the eGFP-labeled PSDs were imaged simultaneously using the same 2P excitation wavelength and detected in separate channels (Fig. 39b). Using a single 2P laser wavelength avoids image offsets produced by chromatic aberration or misalignment of two lasers. For chronic spine tracking, the apical dendrite region in stratum radiatum was imaged every 30 minutes (Fig. 39d). After 2 h of baseline recording, paCaMKII was activated and post-stimulation effects were tracked over many hours (Fig. 39c, every 30 minutes for the first 3 stacks, then every hour to minimize bleaching). Green fluorescent PSDs were automatically detected in every image stack (Fig. 39e) based on a 3D convex polygon detection algorithm (Weigert et al., 2020) and tracked over time (Wolff et al., 2018). The volume of the spine head was estimated from the red fluorescence intensity inside the PSD volume (convolved with the PSF). Changes in PSD size and spine volume were analyzed and plotted according to their position on the dendritic tree (Fig. 39f).

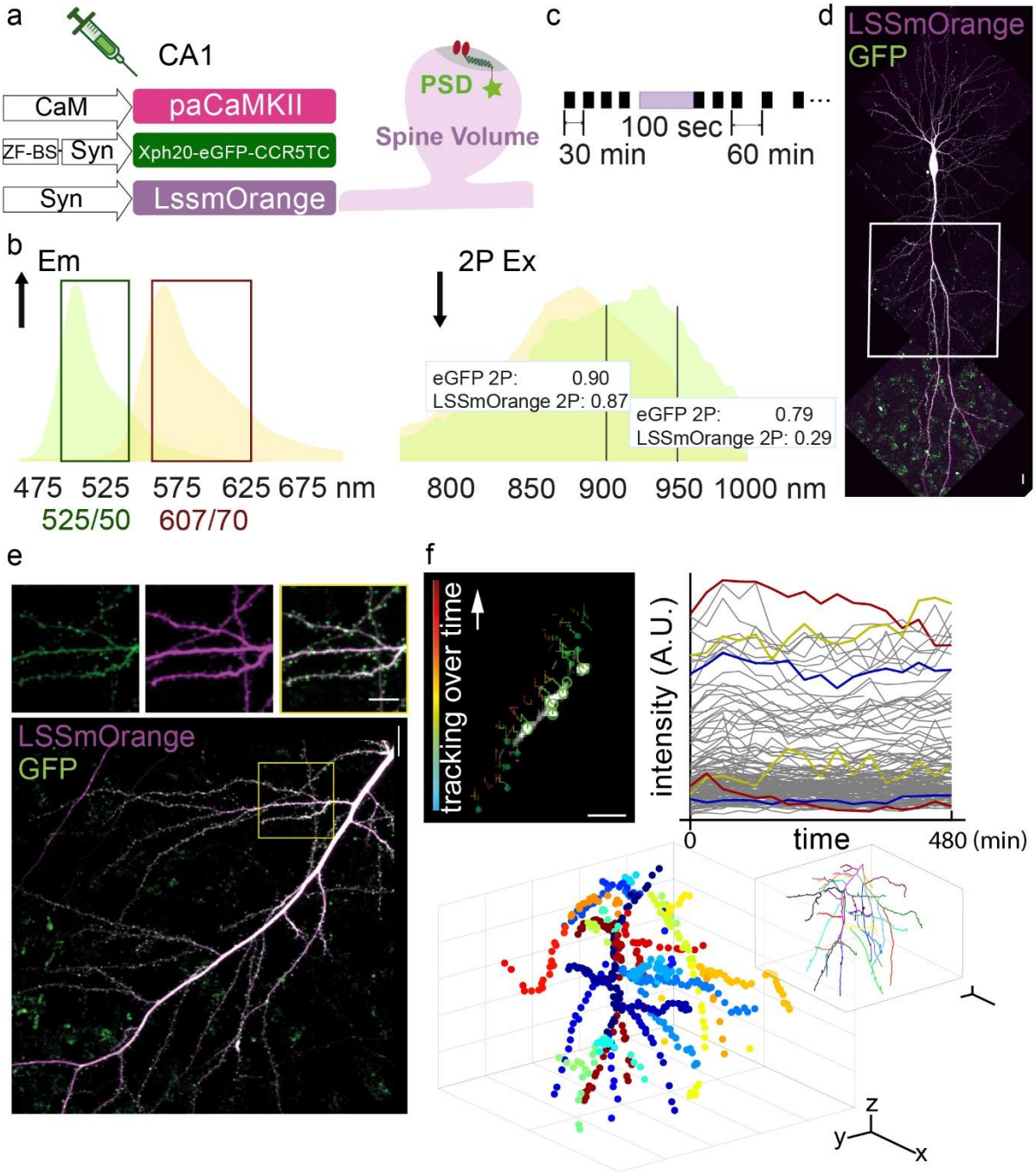

Figure 39: large-scale chronic imaging of paCaMKII activated neurons.

(a) CA1 pyramidal neurons expressed paCaMKII, Xph20-eGFP and LSSmOrange to activate CaMKII with light, label the PSDs and measure spine volume, respectively. (b) Emission (Em) and excitation (Ex) spectra of LSSmOrange (orange shading) and eGFP (green shading). Boxes on the emission spectra indicate the detected wavelengths, bandpass filters are given below. Vertical lines on the excitation spectra indicate example wavelengths for which the fractions of peak excitation for the two fluorophores are given. (c) Illustration of experiments. A baseline was recorded consisting of 4 image stacks (black bars) taken every 30 minutes. Violet bar indicates optical stimulation of paCaMKII. Immediately after the next image stack was taken then every 30 min for three stacks, then every hour. (d) The proximal apical dendrite (white square) was imaged. Scale bar: 10 µm. (e) Z-projection showing labeled PSDs (green) and filled dendrites and spines (magenta), areas of overlap

in the merged image appear white. Scale bars: 13 µm (upper), 8 µm (lower). (f) Upper left: Example eGFP-PSD puncta detected and tracked automatically over time. Scale bar: 40 µm. Upper right: Plot of intensities over time of 131 detected spines from one experiment. Example enlarging (yellow), shrinking (red) and stable (blue) spines are highlighted. Lower, dendritic tree was tracked (upper insert) and detected spines were grouped by their locations on the dendrite (color coded spots). Scale bars: x: 42.5 µm, y: 17 µm, z: 5 µm. A.U. arbitrary units.

paCaMKII activation induces structural LTP lasting for hours

Following LTP induction, actin polymerizes and reorganizes. Enlargement of spine head and PSD means that the synapse can accommodate more transmitter receptors. I observed that global optical activation of paCaMKII induces rapid enlargement of spine heads and PSDs (Fig. 40a, e), a finding in line with previous single-spine paCaMKII activation experiments (Shibata et al., 2021). Interestingly, the PSD enlargement is very long-lasting. At least 14 h after a brief paCaMKII activation, PSDs are still significantly larger compared to control experiments whereas spine head enlargement is only significant in the first 5 h. Considering previous results suggesting that CaMKII is more critical for protein synthesis-independent LTP (Sacktor & Fenton, 2018), these data implied that PSD-relevant proteins are possibly transported from unpotentiated synapses. In addition, the PSD and spine volume intensity distributions appeared to be right-skewed (Fig. 40b, c, f, g and Fig.43), which has been reported across many previous studies and such right-skewed size distributions have been suggested to facilitate the operation of efficient information encoding capacity (Arellano et al., 2007; Eggl et al., 2023; Hazan & Ziv, 2020; Karbowski & Urban, 2023; Loewenstein et al., 2011). I also statistically analyzed which type of distribution my data have. As expected the intensities were not normally distributed, they were also not strictly gamma, exponentially, nor lognormally distributed ($P < 0.05$, Table. 5). The best fits were however, with the lognormal distribution. Another consideration of the results is that in the 'no light, PSD' group, an unexpected significant difference was observed between the baseline and 180 to 840 min intensity distributions (Fig. 40c, d). This may be due to the fluctuation in intensity of relatively small PSDs and the high sensitivity of the Kolmogorov-Smirnov test, as no significant increase in the proportion of large PSDs or increase in the average PSD value was observed compared to baseline.

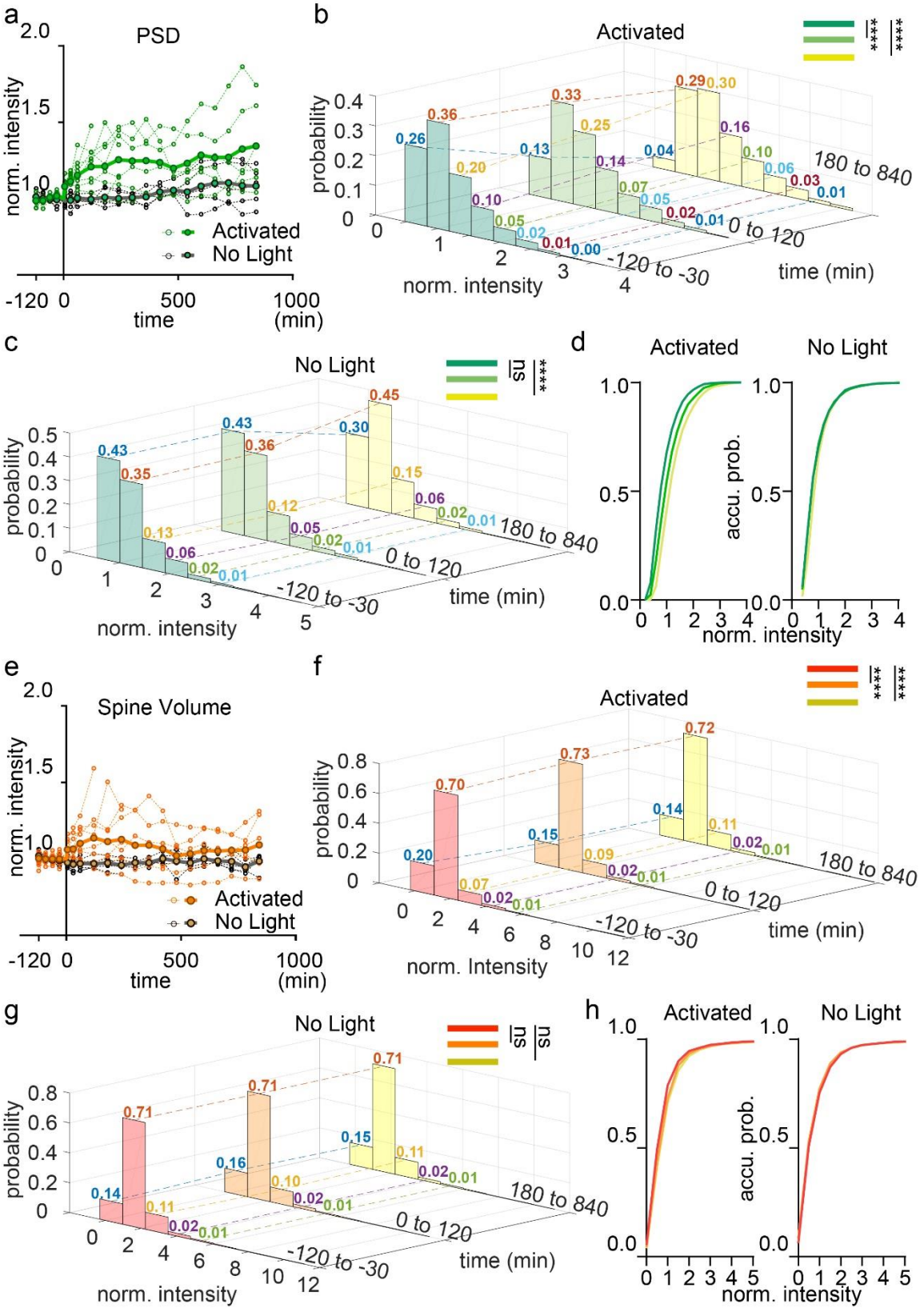

Figure 40: paCaMKII activation induces structural plasticity.

(a-d) PSD alteration after paCaMKII activation. (a) Average (solid lines) PSD-eGFP intensity vs time of CA1 neurons. Light was applied to stimulate paCaMKII at t = 0. Points joined by dashed lines are averages from individual cultures. N = 9, 7 (cultures); n = 3947, 5799 (spines). There was a significant difference between the activated and no light groups from 1-14 hours after paCaMKII activation (P <

0.05, mixed-effects model (REML) followed by Šídák's multiple comparisons, details in Table 7). (b) individual PSD-eGFP intensity histograms at baseline (-120 to -30 min), 0 to 120 minutes after and 180 to 840 minutes after activation of paCaMKII. The probability of each bin is written on the bar. (c) As in(b) but with no light applied at t = 0. (d) Cumulative probability distribution of data shown in b and c. N = 6, 5; n = 2948, 2953 (only experiments longer than 840 minutes were considered). ****P < 0.0001, ns, not significant (Kolmogorov-Smirnov test). In b-d, dark green represents baseline (-120 to -30 min), light green represents early effect (0 to 120 min) and yellow represents late effects (180 to 840 min). (e-h) As in (a-d) but for spine head volume (LSSmOrange intensity). (e) Spine volume was significantly different between the activated and no light groups from 1-5 hours (P < 0.05). (h) There was no difference in the cumulative distributions of spine volume. In f-h, dark red represents baseline (-120 to -30 min), orange represents early effect (0 to 120 min) and yellow represents late effects (180 to 840 min).

Table 5: Kolmogorov-Smirnov test P-values of spine intensity compared to typical distributions

Typical distribution	PSD						Spine head volume					
	activated			control			activated			Control		
	baseline	0 -120	180-840	baseline	0 -120	180-840	baseline	0 -120	180-840	baseline	0 -120	180-840
Normal	4.35E-30	1.22E-28	1.21E-30	2.86E-104	4.18E-95	1.61E-75	6.14E-52	5.42E-54	2.47E-47	9.58E-92	2.91E-94	1.94E-85
Gamma	4.37E-10	1.04E-06	1.34E-09	8.69E-14	8.92E-12	3.53E-10	5.23E-22	5.20E-22	1.51E-18	5.47E-11	3.13E-11	1.46E-10
Exponential	3.51E-288	2.94E-277	3.21E-312	2.88E-76	2.15E-75	5.24E-78	5.32E-308	6.69E-321	n.a.*	4.58E-65	6.90E-60	4.89E-56
Lognormal	6.83E-05	0.013	0.0027	0.018	0.0086	0.26	3.39E-10	6.05E-11	6.14E-08	0.085	0.45	0.75

*the n.a. means that the probability value is too small to be represented in 64 bits.

Since the spine volume and PSD changed with different time courses after paCaMKII activation, I next analyzed the PSD/spine head volume ratio. Immediately after paCaMKII activation, the increase in eGFP and LSSmOrange intensity were closely correlated remaining near 1 (Fig. 41). Over time the ratio increased, reflecting that PSD enlargement persists while spine volume slowly returns to baseline.

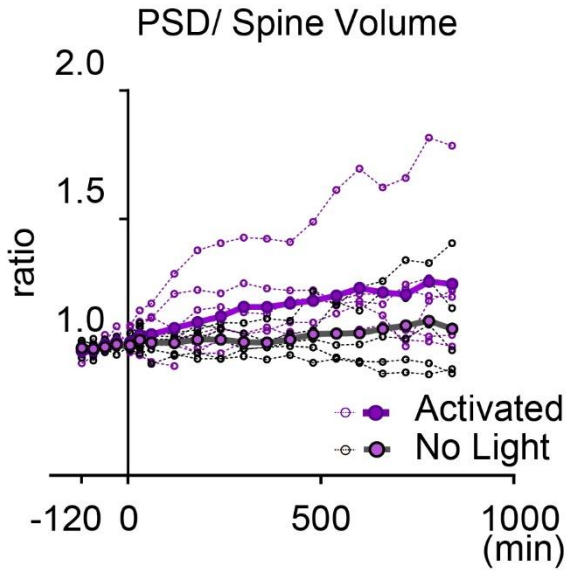

Figure 41: Brief paCaMKII activation triggers slow increase in PSD concentration in spines.

Time course of PSD/spine volume ratio in paCaMKII activated (violet) and control group (black).

Individual experiments are illustrated by dashed lines, grand averages as solid lines.

N = 9, 7 cultures; 3947, 5799 spines.

Dynamics of individual synapses

Next, I analyzed the dynamics of individual spines and PSDs. I extracted the following parameters (Fig. 42):

I_0	average baseline intensity
I	intensity after stimulation (mean intensity in 0-2 h window)
$\Delta I = I - I_0$	change in intensity
$\Delta I/I_0$	relative change in intensity (growth)
CV	coefficient of variation of intensity over time (entire track)

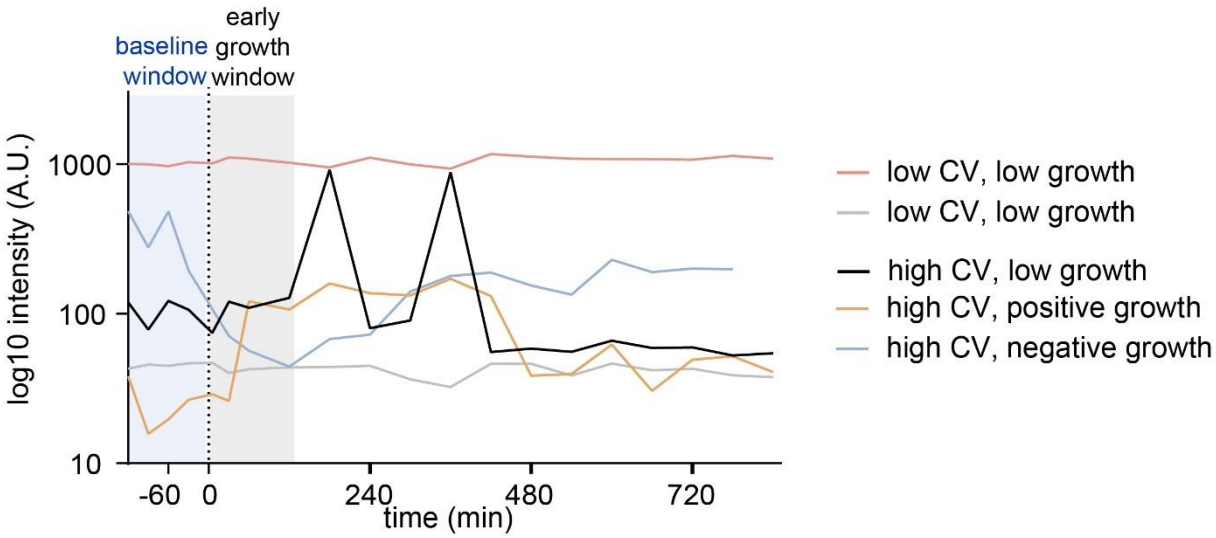

Figure 42: PSD intensity tracks, 5 examples

Examples of PSD dynamics. The whole tracking period was used to calculate CV, and the baseline (blue window) and 2 hours after time 0 (gray window) was used to calculate early growth. The synapses that are highly stable over time have low CV and growth (red and gray lines). The synapses that are highly dynamic, but did not grow/shrink have high CV and low growth (black line). The synapses that are highly stable and enlarge or shrink over time have high CV and positive/ negative growth (orange and blue lines).

By analyzing tracked PSDs and the associated spine volume information, I investigated the distribution of the extracted parameters over the entire population. To combine data from different experiments with different expression levels and laser intensities, I normalized the distributions of baseline intensities to their mean value before combining the data. The resulting histograms (probability density functions) show that optical activation did not affect the distribution of baseline intensities (Fig.43, left).

Activation of paCaMKII shifted the early growth to the positive side for both PSD and spine head volume distributions (Fig.43, middle). The CV of PSD intensities was also increased, but the CV of spine volume was not affected (Fig. 43, right).

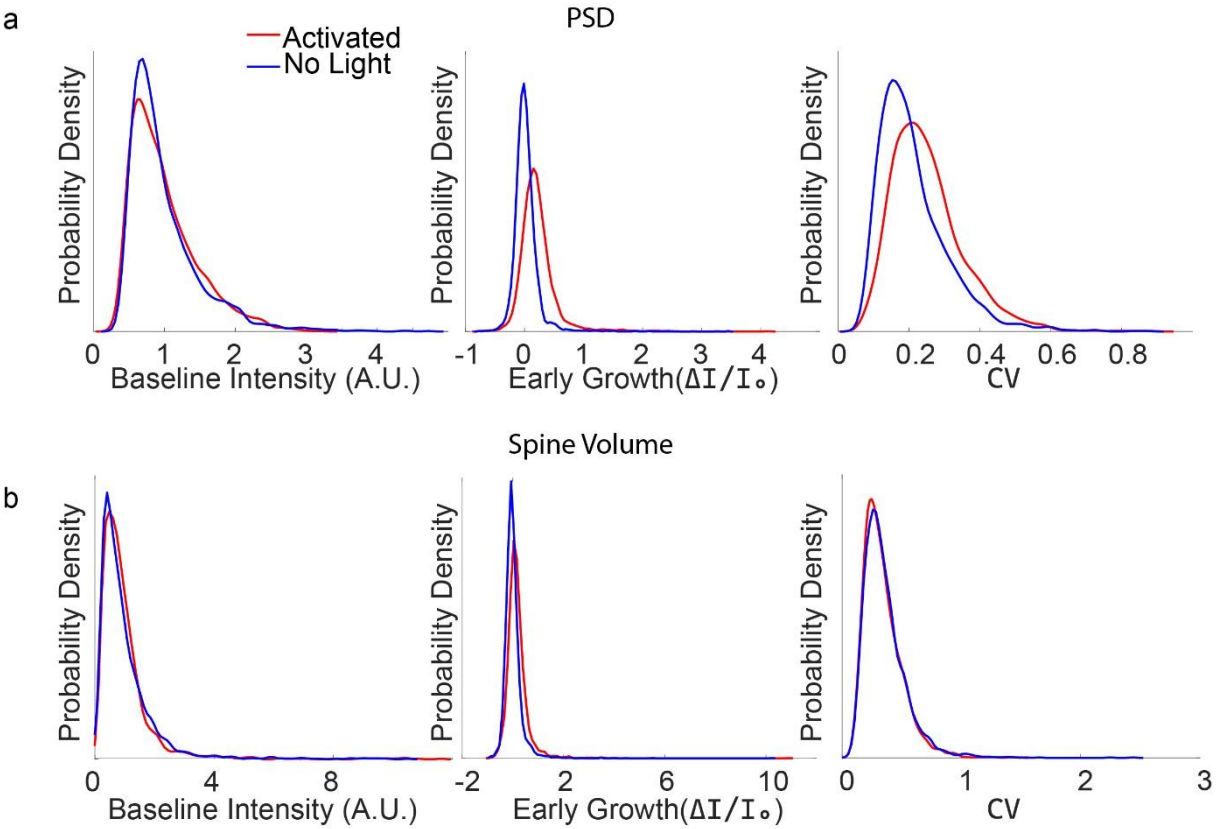

Figure 43: Probability distribution of baseline signal intensity, growth and CV.

The baseline intensity, growth factor and coefficient of variation (CV) probability distributions of PSD (a) and spine volume (b) signals. In general, with or without paCaMKII activation (red or blue), there are no difference of baseline intensities. paCaMKII activation induced increasing growth of synapses and spine volumes and increasing CV of synapses, but not spine volumes. N = 6 (activated), 5 (no light); n = 2948, 2953. A. U. = arbitrary units.

As there was a large overlap between the parameters extracted from CaMKII activated and non-stimulated ("no light") synapses, I next tested if the combination of parameters would better separate the populations (Fig. 44, Suppl. Fig. 3). Plotting baseline intensity vs CV showed that larger spines were generally more stable in both groups (Fig. 44, left). CaMKII activation induced growth and increased CV of PSDs, shifting the median of the population to the upper right (Fig. 44, right).

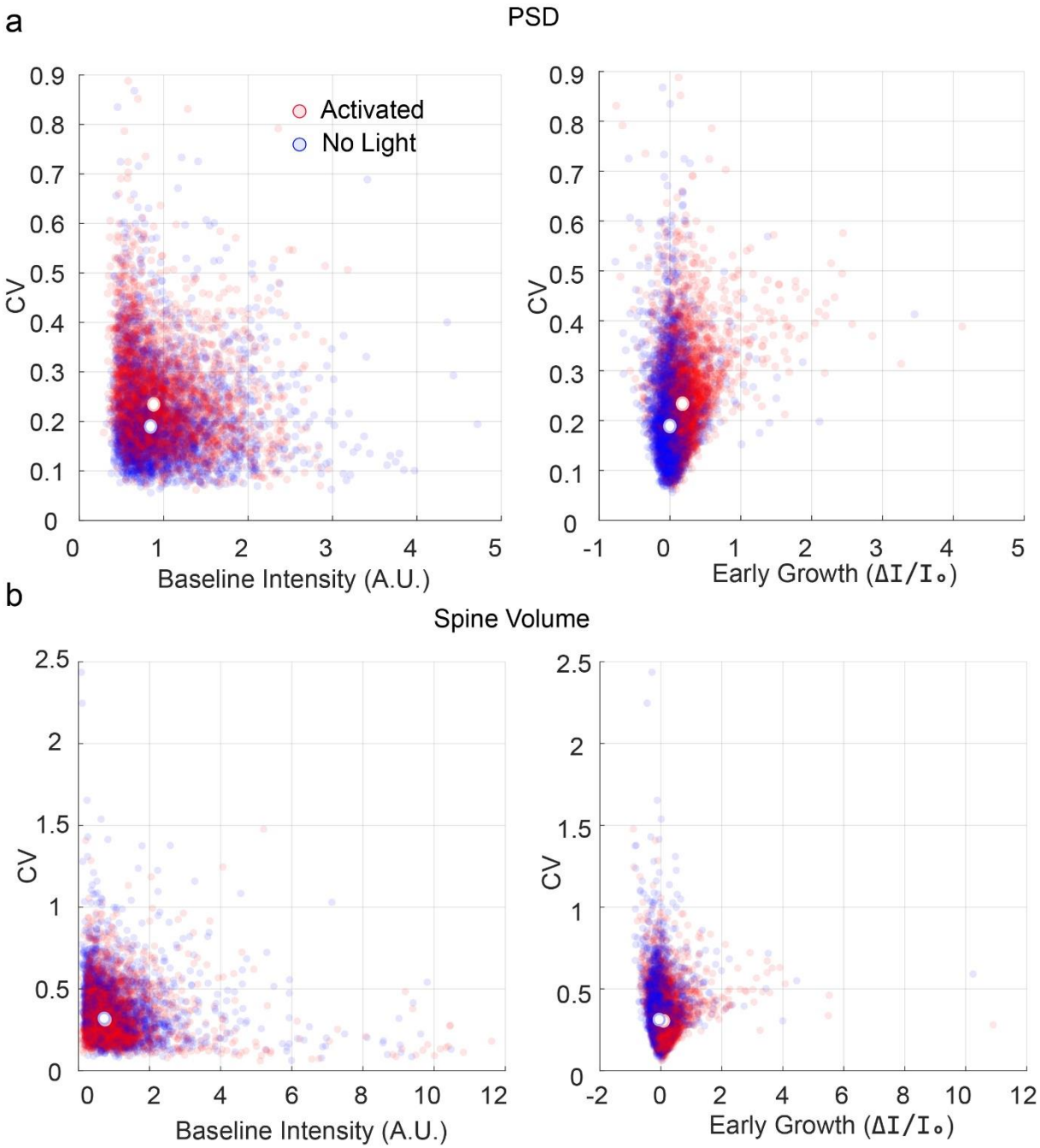

Figure 44: Baseline intensity, growth and CV of individual synapses

The baseline intensity, CV and growth calculated for individual PSDs (a) and spine volumes (b). The white dots represent the medians. N = 6 activated neurons (2948 synapses), 5 control neurons (2953 synapses).

To find out whether large and small synapses grow equally after CaMKII activation, I analyzed a time window 2-5 h after paCaMKII activation (Suppl. Fig. 4, Fig. 45a, d) vs non-activated controls (Fig. 45b, e). Two to five hours after stimulation, paCaMKII activation induced PSD and spine volume growth were sustained and correlated (Fig. 45, Suppl. Fig. 5).

For statistical analysis, I binned synapses according to the initial size of their PSD or spine volume in quartiles (Fig. 45c, f). All four size groups showed highly significant PSD growth and spine head volume increases compared to controls. The effect size was largest for the group of small synapses: PSDs increased by 50% and head volume by 30%. The group of large synapses reacted by only 22% PSD growth and 11% volume increase. In the non-stimulated controls, there is a tendency for initially small synapses to get bigger and big synapses to get smaller, which I interpret as regression to the mean. I also binned synapses according to growth factor (Fig. 45 b-e, right) and the regression appears to be clearer: the shrinking synapses have bigger baseline intensity. Importantly, this regression effect is much smaller than the CaMKII-induced growth (Fig. 45c, f).

I conclude that a one-time paCaMKII activation sets into motion a slow growth process of PSDs that is most pronounced in initially small synapses, but affects synapses of all sizes. Likewise, spine head volume increases in spines of all sizes, with the largest relative changes in small spines.

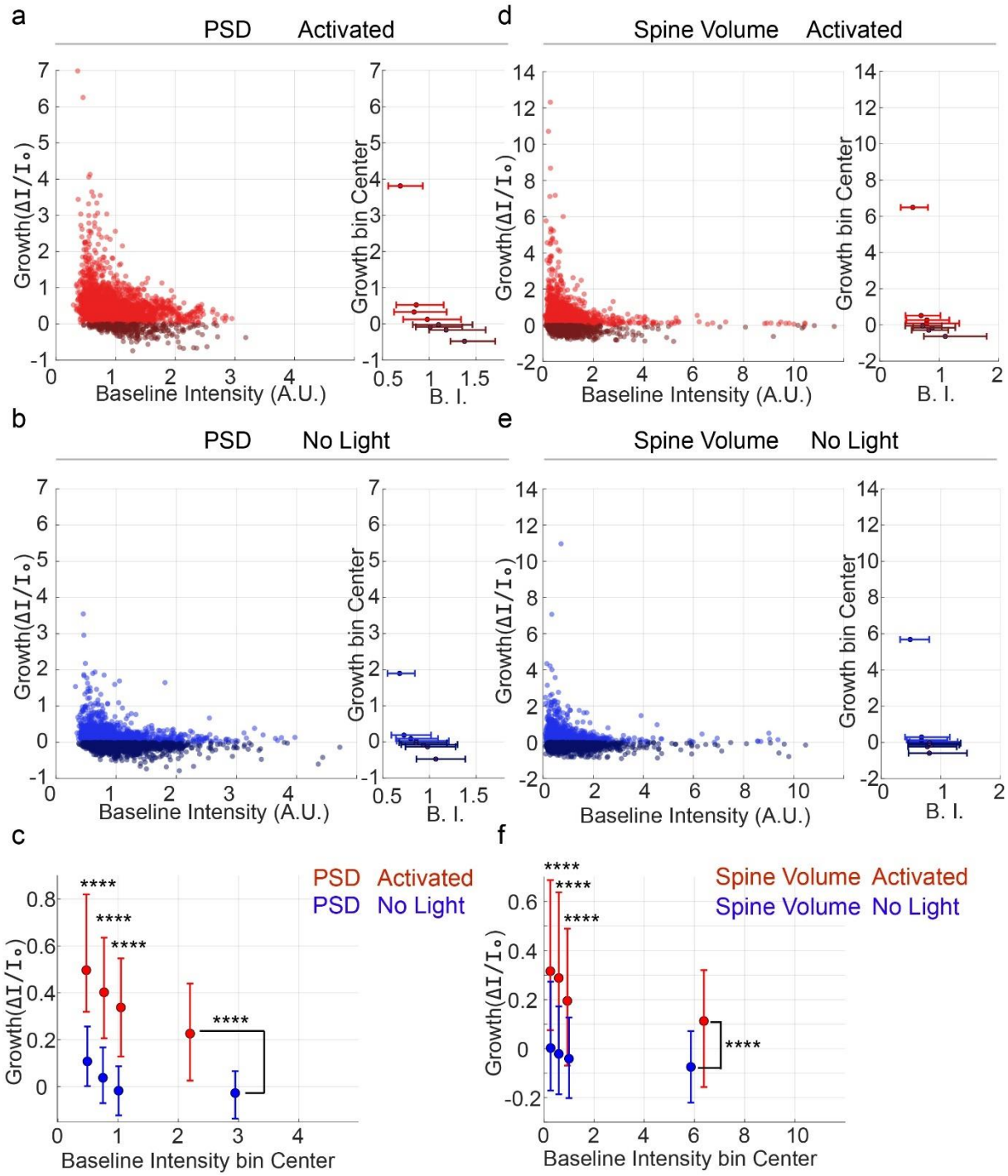

Figure 45: Baseline intensity and late growth of individual synapses

The relationship of baseline intensity (B. I.) vs late growth calculated for individual PSDs (a-c) and spine volumes (d-f), with or without paCaMKII activation. ***Lefts of a, b, d, e***: scatter plots of individual synapses parameters. Light red and blue dots: enlarging PSDs (spine volumes). Dark red and blue dots: shrinking PSDs (spine volumes). ***Rights of a, b, d, e***: late growth factors are binned in quartiles separately for grow and shrink synapses. (c) and (f): baseline intensities are binned in quartiles. Mann-Whitney test, ****P < 0.0001. Data plotted as median ± IQR. N = 4 activated neurons (2433 synapses), 5 control neurons (2953 synapses). A.U. arbitrary units.

Global paCaMKII activation does not increase the information capacity of PSDs

As mentioned above, the right-skewed distribution profile of PSD and spine head volume facilitates the organization of optimal information storage in neural networks, as revealed by computational analysis (Buzsáki & Mizuseki, 2014; Humble et al., 2019). Indeed, a recent comparative study showed that the information encoded in the geometry and structure of dendritic spines in the mammalian brain approaches the theoretical maximum (Karbowski & Urban, 2023). Since the distribution profile of PSD and spine head intensity was strongly affected by paCaMKII activation (Fig. 40, 43), I was curious whether the information capacity is altered upon paCaMKII activation. For this purpose, I calculated the Shannon entropy (Shannon, 1948) of the intensity distribution profile:

$$H(X) = -\sum p(x) log^2 p(x) = E[-log^2 p(X)]$$

X is the full population of intensities at each time point of interest and p(x) is the probability of each outcome X calculated for each *bin* (i.e., possible synaptic strength of the system). The greater the variability in PSD or spine head volume, the broader the distribution of synaptic strengths, resulting in higher entropy. However, upon optical activation of CaMKII, no significant change in entropy was observed in the PSD or spine head volume distribution (Fig. 46). There are previous evidences that LTP induction at a subset of synapses causes an increase in population entropy (Eggl et al., 2023; Samavat et al., 2024). In my experiments, simultaneous CaMKII activation in every synapse causes a shift towards larger synapses, but not really a broadening of the distribution. Also, the light stimulus was not spatially structured, but was homogenous. It would be interesting to use this measure after restricted CaMKII activation in a subset of synapses, e.g. by patterned illumination.

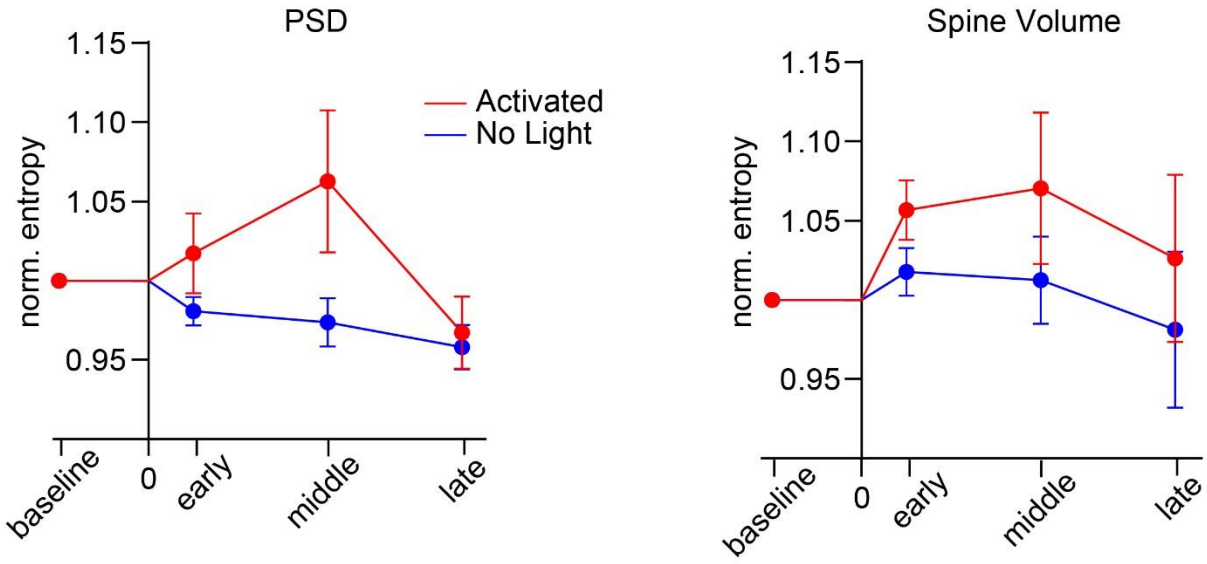

Figure 46: neither PSD nor spine volume carries more information after paCaMKII activation.
No difference of average entropy calculated by PSD nor spine volume intensities was observed after paCaMKII activation compared to the control: early: 0-60 minutes after stimulation; middle: 120-300 minutes after stimulation, 360-840 minutes after stimulation. N = 9, 7 (slices); n = 3947, 5799 (spines). Data plotted as mean ± SEM.

Spatially clustered plasticity

After performing time-lapse analysis and investigating the relationship of different dynamic features across the whole population of spines, I next analyzed the spatial properties of structural plasticity: Do neighboring spines show similar changes? Or do they engage in competitive interactions for shared synaptic resources, resulting in opposite size changes? I decided to consider two factors: CV and early growth. I selected in each slice culture the spines with the most extreme values for CV (20 most dynamic and 20 most stable) and for growth (20 largest growth and 20 most shrunken) (Fig.47, yellow center spines). I calculated the average CV and growth of the neighbors of these selected "center spines" (Fig. 47, white asterisks) to see if these features were spatially clustered (4 neighbors per central spine, selected by comparing Euclidean distances of the spines on the same dendrite.

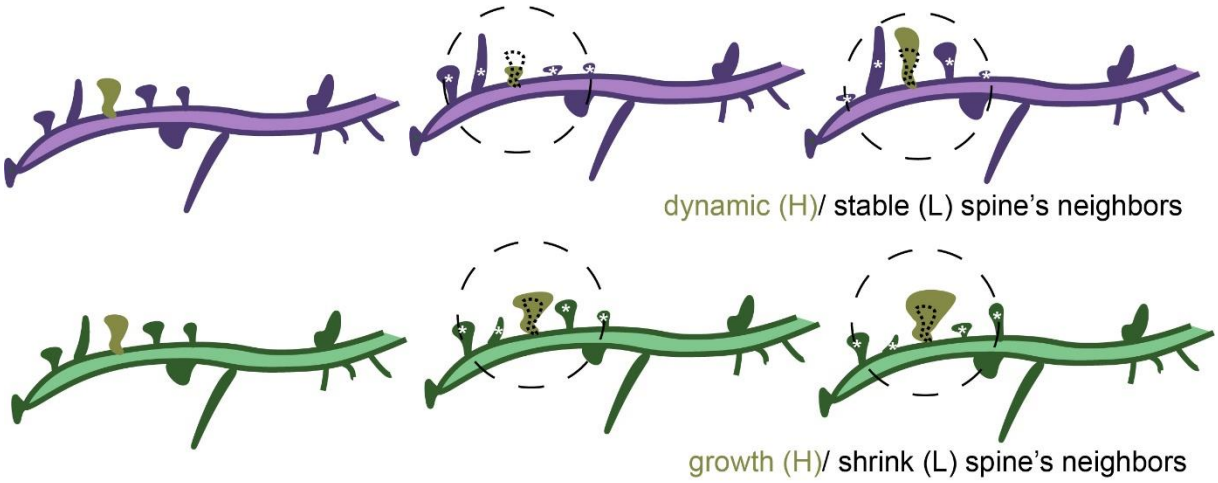

Figure 47: Analysis of spatial correlations.

Analysis of clustered plasticity. Top: spines that are highly dynamic (high CV, 'H') or stable (low CV, 'L') were selected. The closest 4 neighbors (white asterisks) of the selected spines (yellow) were used to calculate neighboring spines CV. Bottom: the same analysis was applied to neighbors of spines that are strongly growing (positive growth, 'H') or shrinking (negative growth, 'L').

Clustering of CV values of PSD and volume changes was evident in both no light and in neurons with CaMKII activation (Fig. 48a), meaning that spines (PSDs) that are highly dynamic (Fig. 48b, 'centers') are surrounded by dynamic spines (PSDs) and vice versa (Fig.48c, 'neighbors'). Next, I wanted to find out if the groups of dynamic spines changed in similar or opposite directions. Without stimulation, neighbors of growing PSDs/spines were indistinguishable from neighbors of shrinking PSDs/spines (Fig. 49). paCaMKII activation induced strong PSD growth and spine head volume enlargement in a weakly clustered fashion: In the optically activated groups, 'high growth' neighbors had slightly higher growth values compared to the 'low growth' neighbors. This rules out the possibility that PSDs and spine heads grow at the cost of their closest neighbors, which would generate inverse correlations, and argues for weak collaboration between neighboring synapses during the CaMKII-induced growth process.

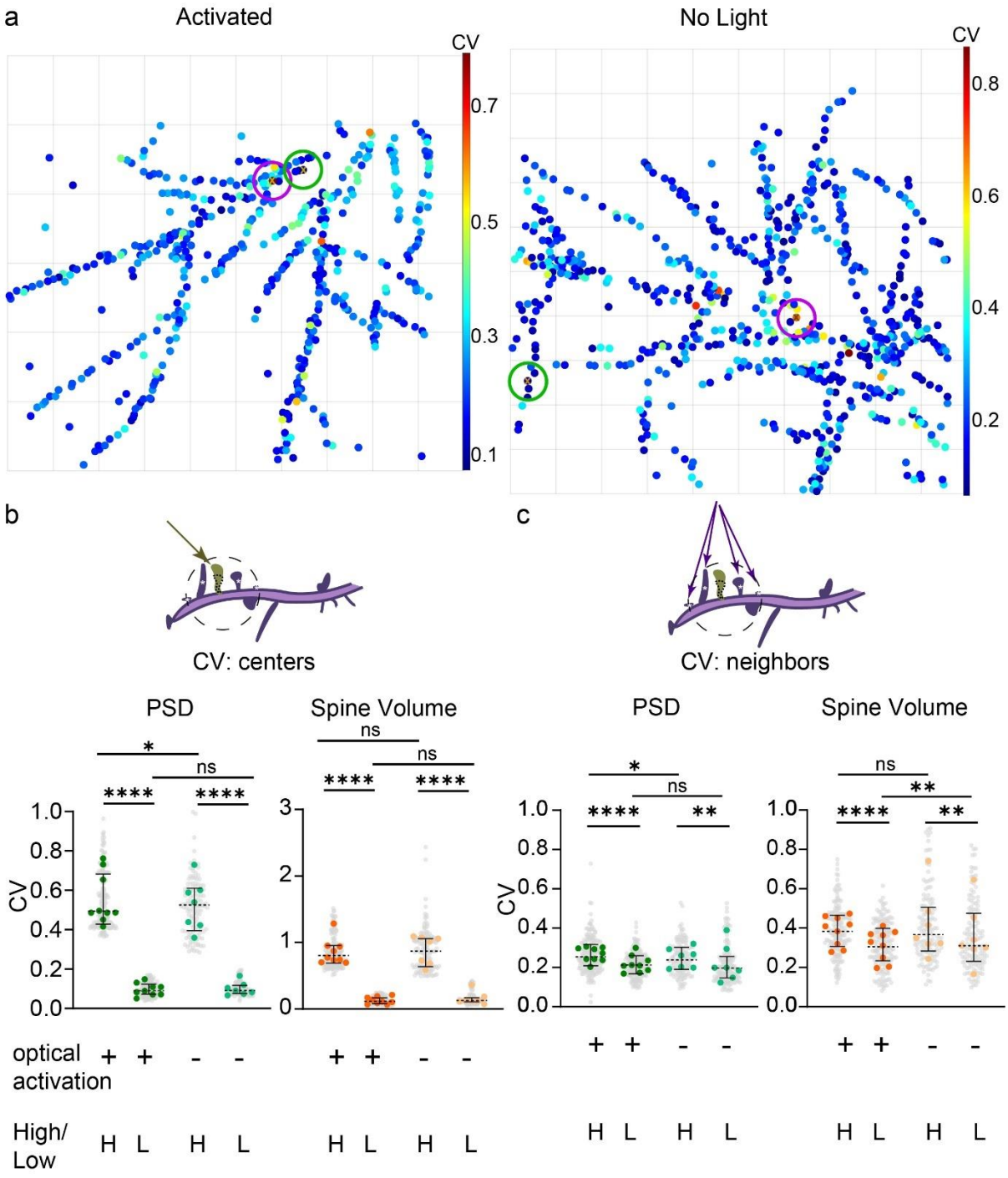

Figure 48: Neighboring synapses have similar dynamics

(a) Example CV spatial plots. The detected spines are shown as colored dots, with color representing the CV. The purple and green circles show hot spots with clusters of dynamic and stable spines, respectively. (b) 'Centers' are the detected spines with highest and lowest CV for PSD size and spine volume. Green points are the average CV of the PSDs from the selected 'high' and 'low' CV spines per slice, grey points the individual centers. Orange points are the average CV of the spine volume of the selected 'high' and 'low' CV of volume per slice, grey points are the individual centers. (c) 'Neighbors' are the four closest spines to each center. Green and orange points are the averages per culture, grey points are the average of the 4 neighbors. N = 9, 9, 7, 7, 9, 9, 7, 7; n = 180, 180, 140, 140, 180, 180, 140, 140. Data plotted as median ± IQR. Two-way ANOVA followed by Fisher's multiple comparisons, ****P < 0.0001, **P < 0.01, *P < 0.05, ns, not significant.

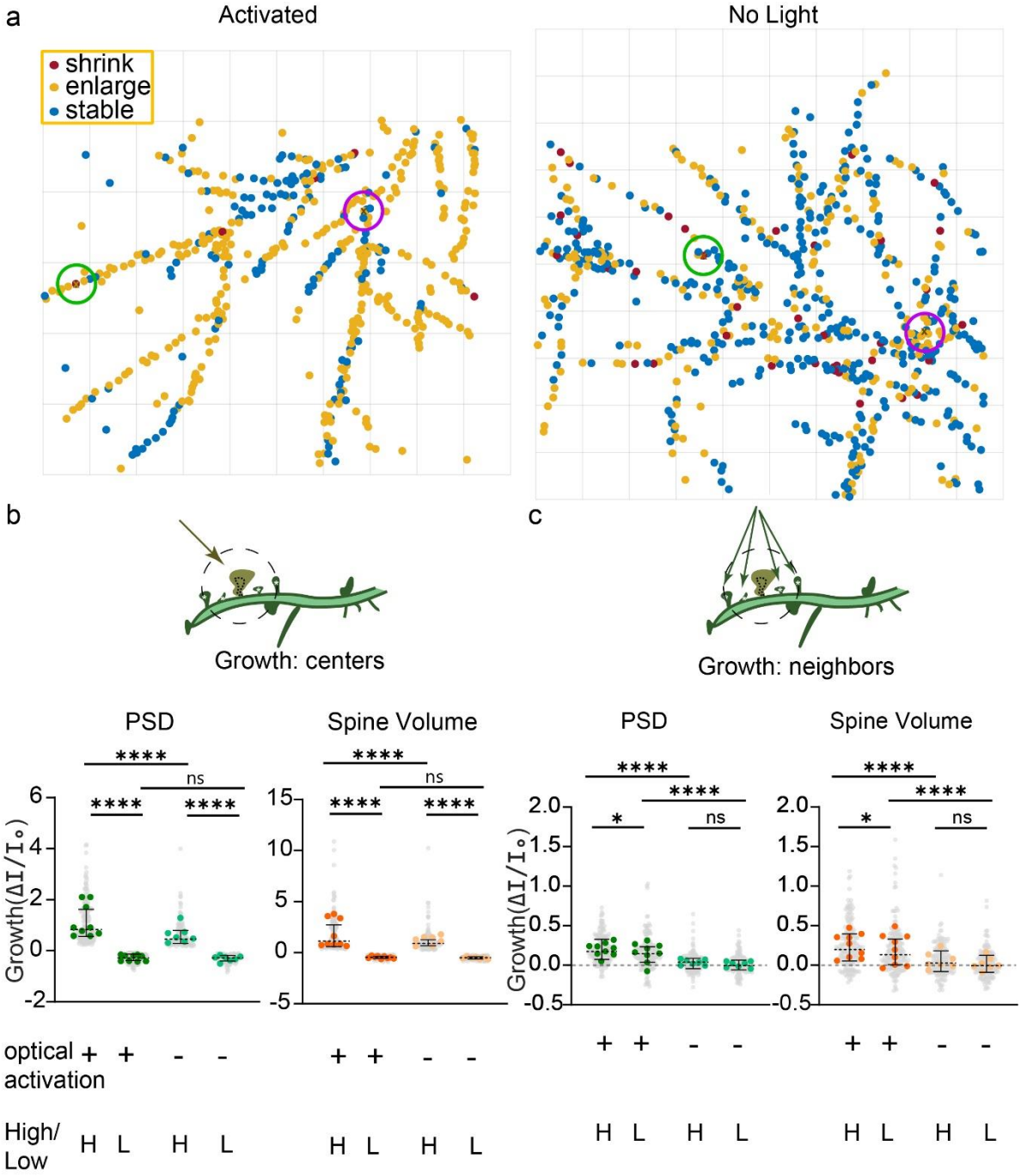

Figure 49: Spine growth is weakly clustered after CaMKII activation

(a-c) As in Figure 48 except the most enlarged (H) and least growing (L, shrinking) spines were selected. N = 9, 9, 7, 7, 9, 9, 7, 7; n = 180, 180, 140, 140, 180, 180, 140, 140. Data plotted as median ± IQR (by n). Two-way ANOVA followed by Fisher's multiple comparisons, ****P < 0.0001, *P < 0.05, ns, not significant.

3.2.2.3 Ultrastructural plasticity after paCaMKII activation

In order to examine the details of the structural changes induced by CaMKII activation, I set out to study synaptic ultrastructure with electron microscopy. To identify the paCaMKII-expressing neuron, expression of an electron-dense label was required. dAPEX2, a peroxidase-based genetic tag was electroporated into CA1 PNs together with paCaMKII (Fig. 50a, further details about the development of peroxidase tags to label optogenetically manipulated PNs in 3.3). In a first attempt, the slice culture was fixed 10 min after optical activation of paCaMKII. Next, after osmium staining of micro-dissected sample (Fig. 50b, c), the sample was serially sectioned and then imaged by electron tomography, focusing on the labeled dendritic structures (Fig. 50c). The image stacks were aligned (Fig. 20), the PSDs, spine heads, and axon-spine interfaces (ASI) were manually annotated and reconstructed (Fig. 50c). In addition to the size, I calculated the PSD complexity index (CI), a critical indicator of LTP (Toni et al., 2001):

$$\mathrm{CI} = \frac{(\text{PSD perimeter})^2}{4\pi(\text{PSD area})}$$

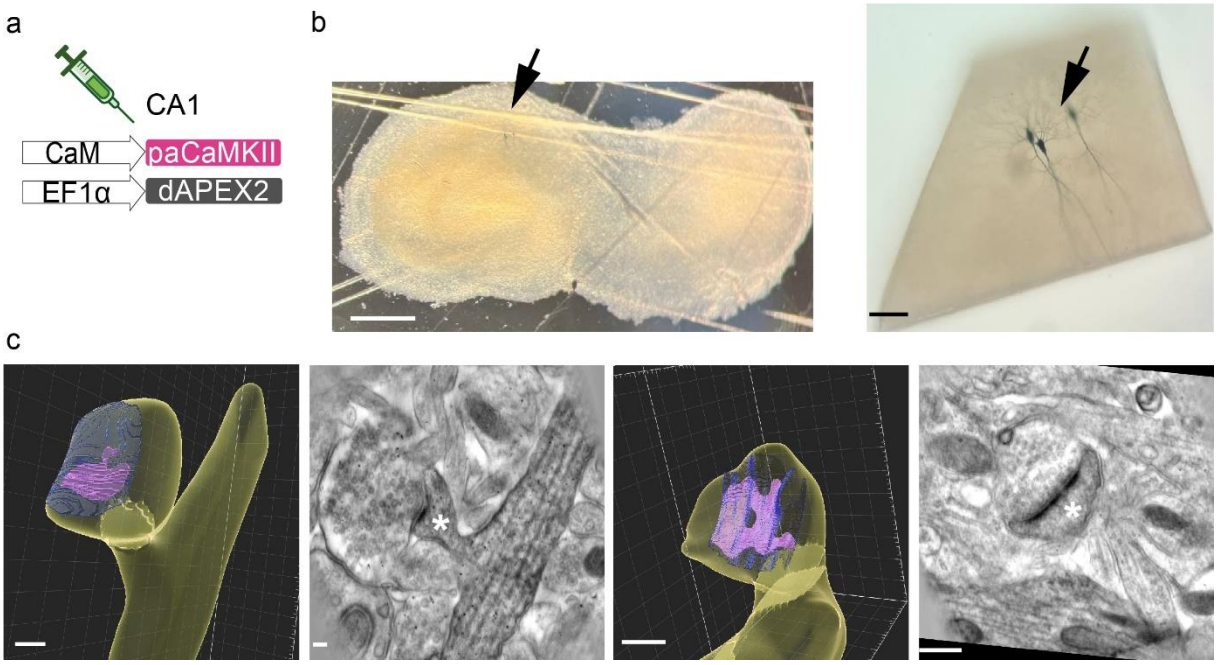

Figure 50: Synaptic ultrastructure after paCaMKII activation.

(a) transfection: paCaMKII and dAPEX2 was co-transfected to CA1 PNs by single-cell electroporation. (b) After DAB staining, transfected PNs appeared to be dark-brown, indicated by the arrows, and the stained cells were dissected for further experiments (right). Scale bar: 700 µm, 60 µm. (c) example reconstructions. The left 3D rendering structures are reconstructed from the labeled spines (white asterisks) in the right EM images. Yellow: spine head and connected dendrites; magenta: PSDs; semi-transparent blue: ASIs. Scale bars, from left to right: 100 nm, 100 nm, 300 nm, 300 nm.

Spines on branches of the apical dendrite in stratum radiatum receive inputs from CA3 (and entorhinal cortex). At these synapses, paCaMKII activation induced a trend to ASI, PSD and spine volume enlargement (Fig. 51). The PSD/ASI ratio was not affected. The complexity of the PSD also trended to be increased by CaMKII activity. However, due to the limited sample size, none of these differences were significant. In addition, I analyzed synapses on basal dendrites, mainly because it was relatively easy to find these synapses in EM. Unexpectedly, basal synapses reacted to CaMKII activity with a significant *decrease* in PSD area. Spine volume and ASI were not affected, resulting in a significant decrease in PSD/ASI ratio. The complexity of PSDs was unchanged. These paCaMKII-induced structural changes are so rapid (10 min) that they are most likely independent of protein synthesis. Global paCaMKII activation seems to shift the balance of excitatory input from the basal to the apical dendrites.

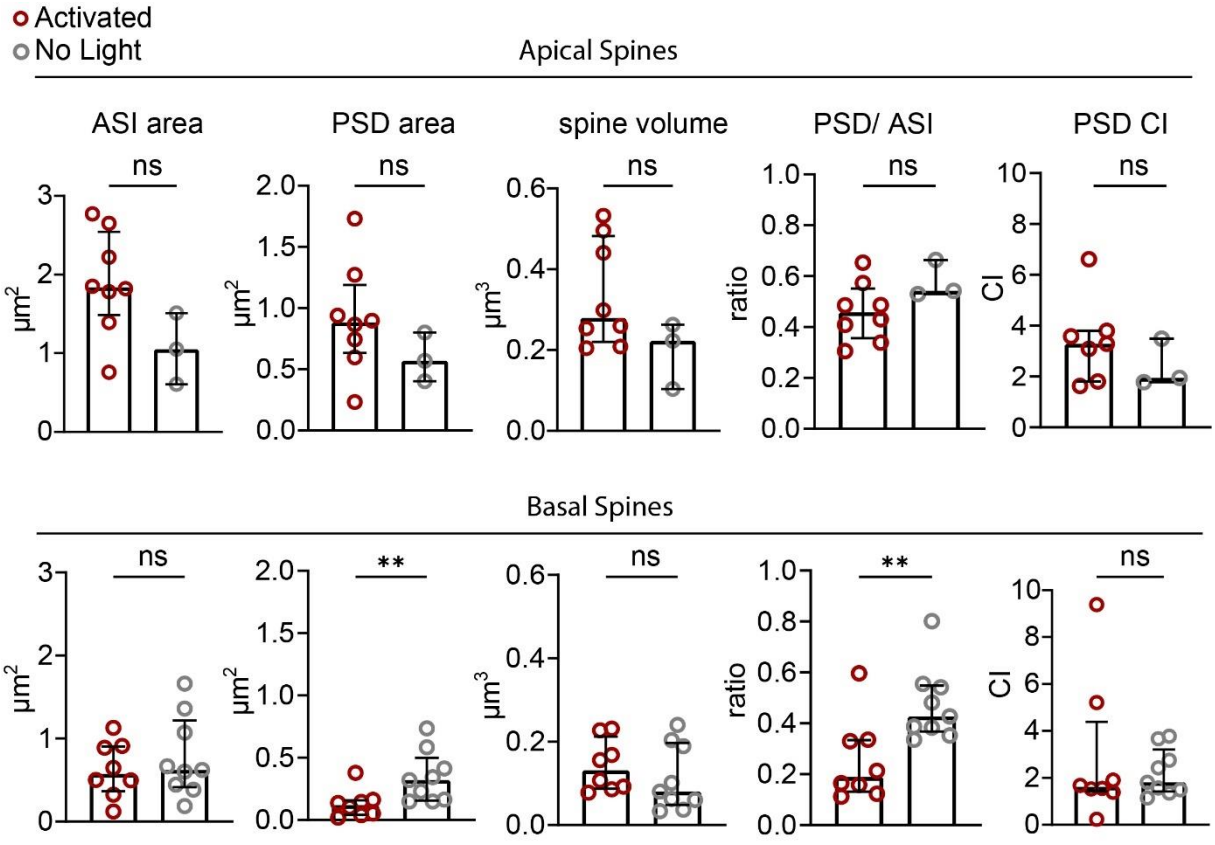

Figure 51: Effects of paCaMKII activation on synaptic ultrastructure

paCaMKII activation (red markers) induced opposite changes in PSD area in apical (upper row) vs basal synapses (lower row). N = 1 for all groups; n = 8, 3, 8, 3, 8,3, 8, 3, 7, 3; 8, 9, 8, 9, 8, 9, 8, 9. Data plotted as median ± IQR (by n). Mann-Whitney test, **P < 0.01, ns, not significant.

The geometry of the spine neck is regulated by neuronal activity, and spines with wide necks are generally more strongly coupled to the dendrite, allowing for more efficient synaptic transmission (Bloodgood & Sabatini, 2005). I noticed that most paCaMKII-activated spines have extremely wide and short necks (Fig. 52). The difference to non-stimulated spines was highly significant in the sample of basal spines; the sample of apical spines was too small for meaningful statistics. The widening and shortening of spine necks reduces the electrical resistance, improves signal transmission while maintaining biochemical compartmentalization, and thus supports synaptic potentiation (Araya et al., 2014; Tønnesen et al., 2014). My data show that these morphological adaptations happen within 10 min of CaMKII activation.

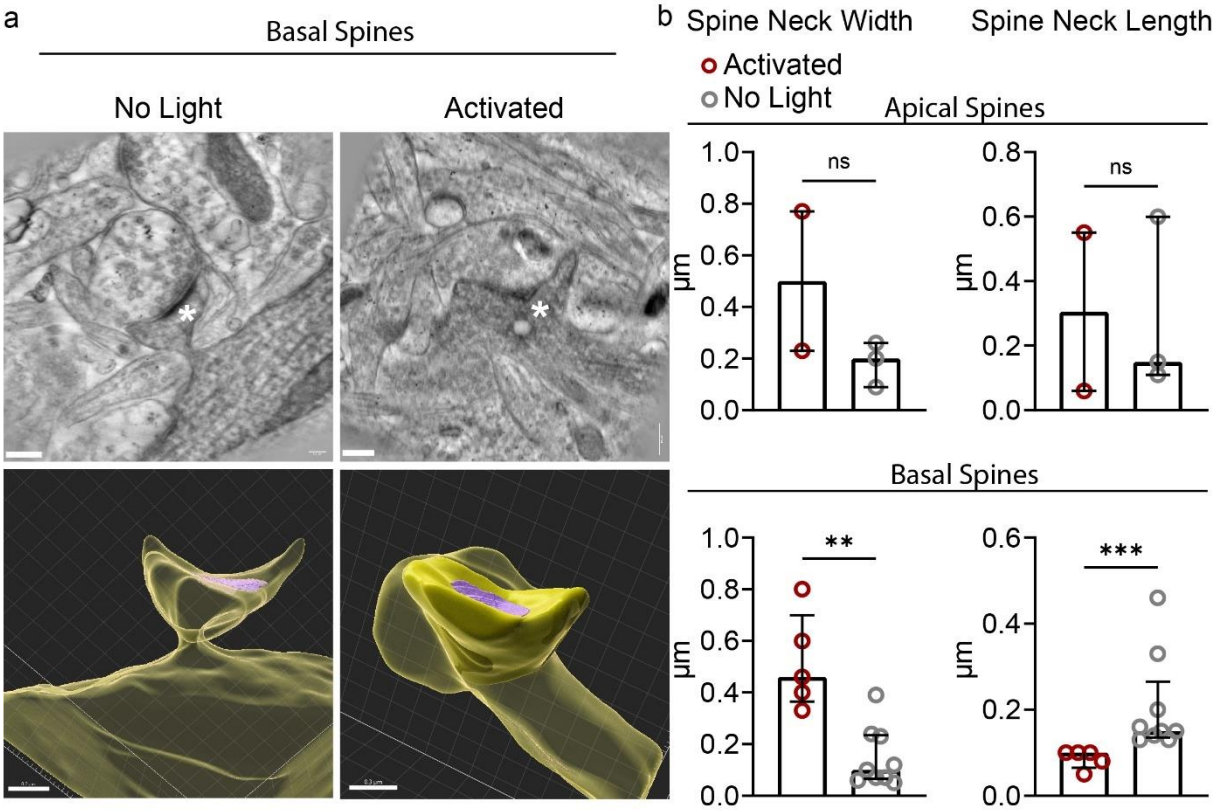

Figure 52: widen of spine neck was induced by paCaMKII activation.

(a) representative control vs paCaMKII activated spine neck from basal spines. The scale bars: no light: 200 nm; activated: 300 nm. (b) paCaMKII activation induced the widen and shorten of spine neck in basal spines. A similar trend was observed in apical spines. N = 1 for all groups, n = 2, 3, 2, 3, 5, 9, 5, 9. Data plotted as median ± IQR (by n). Mann-Whitney test, ***P < 0.001, **P < 0.01, ns, not significant.

Considering the absolute size of the ASI area and PSD area in the control group, my measurements are larger (on average) than published EM measurements. There are two possible reasons: First, in my dataset, all the labeled spines were manually selected and

imaged, albeit blind to the condition (activated/ no light). Selected spines are biased towards larger sizes because large spines are easier to find. This could be solved in the future by using an automatic localization strategy (will be discussed in 3.3.5). Second, overexpression of paCaMKII may result in some enlargement of spine heads and PSDs (Shibata et al., 2021). Although these two technical limitations can't be ignored, they should influence the paCaMKII-activated and the no-light control group in a similar fashion. This is why we used paCaMKII-expressing neurons (without activation light) as controls.

3.2.2.4 Global LTP induced by cell-wide paCaMKII activation is not long-term stable

Whole cell patch-clamp recordings during paCaMKII activation showed early LTP of CA3 inputs (Fig. 38). To test for late LTP, I activated paCaMKII inside the incubator (see 3.1.2, Fig. 25) and assessed the strength of CA3 inputs to paCaMKII-activated CA1 neurons and neighboring non-transfected neurons 1 or 2 days later by whole-cell patch-clamp recording. No input strengthening was observed 1 or 2 days after paCaMKII activation (Fig. 53). Thus, a one-time paCaMKII activation did produce early, but not long-lasting LTP. Homeostatic mechanisms may prevent permanent potentiation of all synapses on a neuron ("downscaling").

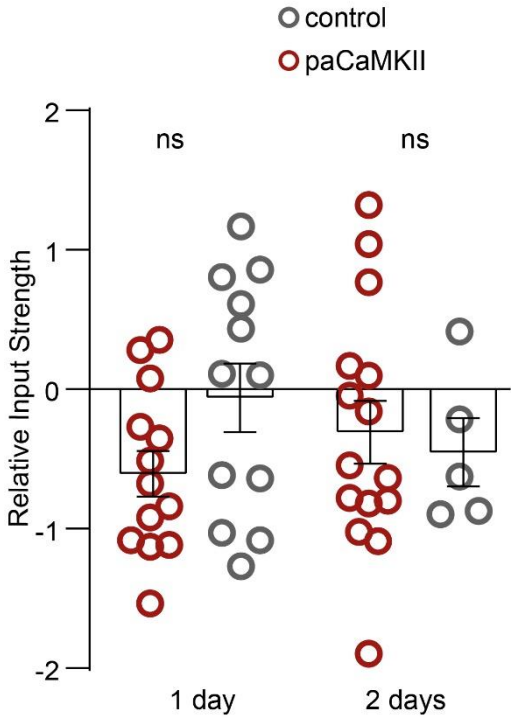

Figure 53: LTP induced by paCaMKII is not stable

After one and two days of paCaMKII activation, no input strengthening was observed. Each data point represents the difference of input strength to a paCaMKII neuron and to its neighbors. In control experiments, paCaMKII was not activated. n = 13, 12, 15, 5. Data plotted as mean ± SEM. Unpaired t-test, ns, not significant.

3.2.2.5 paCaMKII activation does not induce significant elevation of c-Fos expression

In 3.2.1.5, I showed that inhibition of CaMKII activity during LTP induction is not necessary for the LTP induction induced c-Fos expression. Here I tested whether CaMKII activation itself, without Ca^{2+} influx, is able to induce c-Fos expression. I fixed slice cultures 1 h after paCaMKII activation and performed c-Fos staining (Fig. 54). The statistical analysis of paCaMKII-activated cells did not show a significant increase in c-Fos expression compared to the negative control. However, some paCaMKII-activated cells generated strong c-Fos expression (Fig. 54a, Suppl. Fig.2). Taken together, paCaMKII activation induced c-Fos expression very mildly and sparsely, but not statistically significantly.

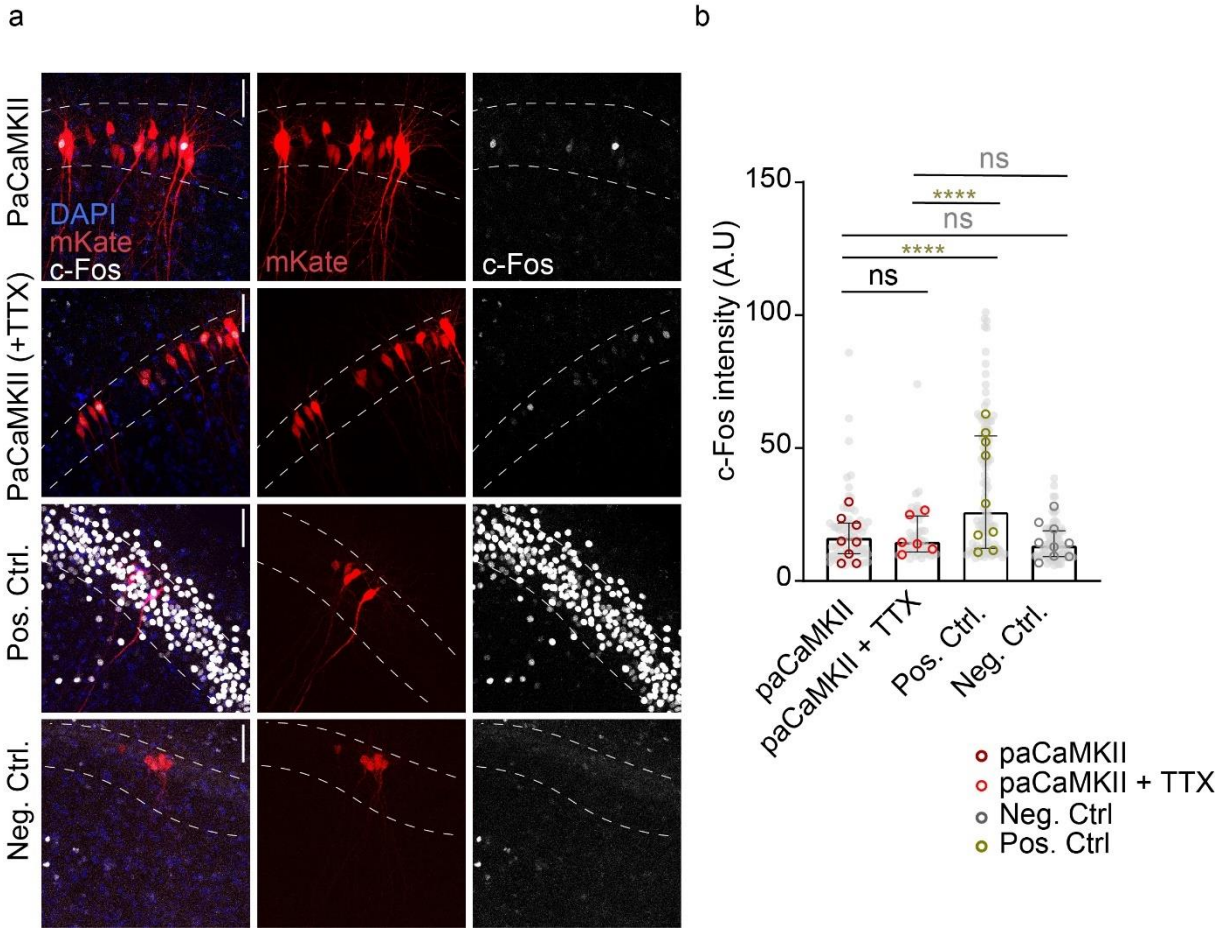

Figure 54: paCAMKII activation does not induce significant increase of c-Fos expression.

(a) Representative images. Maximum intensity projection was made, and all the slices containing soma signals were included. Dash lines indicate the cell body layers. Scale bars: 50 µm. (b) paCaMKII activation does not induce significant increase of c-Fos expression compared to negative control. N = 8, 6, 8, 9; n = 76, 71, 104, 52. Data plotted as median ± IQR (by n). Kruskal-Wallis test followed by Dunn's multiple comparisons, ****P < 0.0001, ns, not significant. A.U. arbitrary units.

3.2.3 Summary

I combined optogenetic induction of spike-timing-dependent plasticity (oSTDP) with the photoactivatable CaMKII inhibitor paAIP2 to study the role of CaMKII in synaptic plasticity. Whole-cell patch clamp experiments demonstrated that CaMKII activity during plasticity induction is essential for early tLTP. Late tLTP, however, was not affected by CaMKII inhibition, suggesting that there is a CaMKII-independent pathway that is responsible for the development of late tLTP. Blocking CaMKII activity during oSTDP did not block c-Fos expression, again pointing to the activation of multiple signaling pathways activated by oSTDP.

To investigate whether CaMKII activity is sufficient for input strengthening, I used photoactivatable CaMKII (paCaMKII). Acutely, a rapid and strong input strengthening was observed (early LTP), but no late LTP (1 or 2 days after induction) could be detected. Together, these data suggest that CaMKII activation induces early LTP, but other signaling pathways are responsible for late LTP.

In the second part of this subchapter, I investigated the structural changes induced by paCaMKII activation using two different methods: (1) chronic 2P imaging: tracking the changes in spine head and PSD size over 16 hours with a large field of view; (2) electron tomography: quantitative measurement of ultrastructural changes 10 min after paCaMKII activation. I observed rapid enlargement of PSD and spine head, increase of PSD complexity and spine neck widening. These morphological changes are the substrate of the functional synaptic potentiation triggered by paCaMKII activation. The spine head enlargement lasted for about 5 hours on apical dendrites, PSD enlargement lasted even longer. Unexpectedly, spines and PSDs on basal dendrites changed in the opposite direction, suggesting that synaptic plasticity rules are determined locally by mechanisms downstream of CaMKII.

3.2.4 Discussion and perspectives

3.2.4.1 What does paAIP2, paCaMKII and PKMζ experiment tell us about the maintenance of LTP?

CaMKII is not the synaptic tag for late LTP

The idea that CaMKII activity is essential for LTP induction is well accepted (Incontro et al., 2018; Malinow et al., 1989; Murakoshi et al., 2017). However, these studies used induction protocols that lead to extremely strong calcium influx: Pairing of synaptic activity with a step depolarization of the postsynaptic neuron to 0 mV, glutamate uncaging in zero Mg^{2+}, or high-frequency (200 Hz) presynaptic stimulation. In contrast, I used optogenetic tools to induce STDP, which is arguably more physiological. I could show that STDP, like other induction protocols, absolutely requires CaMKII activity in the early phases. Interestingly, late tLTP was not affected by paAIP2 activation. This means that the development of late tLTP relies on a CaMKII-independent pathway, different from the mechanism of early LTP. Does this mean there could be late memory without early memory? A very recent paper reports that CaMKII inactivation in the amygdala indeed blocks short-term (1 hour) but not long-term (1 to 4 days) fear memory (Shin et al., 2024). According to the synaptic tagging hypothesis (Frey & Morris, 1997), synapses are molecularly tagged during LTP induction. This tag serves as a transient marker that indicates which synapses are candidates for late, long-term changes through delayed uptake of plasticity-related proteins. CaMKII has been discussed as a synaptic tag, but my findings suggest that other proteins must be serving the role of tags. Possibly, a much longer inhibition of CaMKII in the period after the oSTDP induction would affect late tLTP but the reappearance of memory reported by Shin et al., also speaks against this. PKMζ is one of the most important plasticity-related proteins. The inhibition of PKMζ only impacts the maintenance, but not the induction of LTP (Sacktor & Fenton, 2018). I found that delayed PKMζ blockade after causal pairing indeed abolished late tLTP both with and without inhibition of CaMKII. Taken together, CaMKII is necessary for the induction of early LTP. In contrast, the late tLTP, which manifests as selective input strengthening days later, is independent of CaMKII and requires the sustained activity of PKMζ.

Late LTP is thought to require protein synthesis and thus the activation of transcription factors (Kelleher et al., 2004). I found no correlation between CaMKII activation

and c-Fos expression. Activation of paCaMKII (without Ca^{2+} influx) did not induce c-Fos expression. Inhibition of CaMKII did not block cFos expression induced by 50 or 0.1 Hz stimulation or by the oSTDP protocol. Many literatures report that CaMKII and/or CaMKIV regulate the phosphorylation of IEGs transcription factors such as CREB, which then initiates *FOS* transcription and c-Fos expression. According to my results, this pathway does not fully explain the mechanism of c-Fos expression, emphasizing the complex nature of intracellular signaling networks involved in synaptic plasticity.

Open questions about CaMKII downstream signaling

CaMKII activation has three classes of downstream effects that are thought to be the mechanism of LTP maintenance: the autophosphorylation of CaMKII itself ('autophosphorylation'), the phosphorylation of downstream targets ('enzymatic') and the formation of CaMKII/NMDA receptor complex ('structural'). The relative importance of these mechanisms remains highly controversial. While the CaMKII/NMDA receptor complex has been considered as one of the very promising models to explain the mechanisms underlying LTP since 20 years ago (J. E. Lisman & Zhabotinsky, 2001). Tools have been developed to dissect the enzymatic and structural effect of CaMKII. The CaMKII I205K mutation is thought to disable CaMKII/NMDA receptor complex formation only, however there is also evidence that the I205K mutation impacts the affinity of CaMKII for CaM (Chao et al., 2011). More recently, ATP-competitive inhibitors, for example AS105, AS283, AS397 and ruxolitinib, have been made which are believed to block only the CaMKII kinase activity without effects on CaMKII/NMDA receptor complex formation. Application of some of these inhibitors did not block LTP induction and maintenance, suggesting that the enzymatic activity of CaMKII is not required (Barcomb et al., 2013; Tullis et al., 2023). Tullis and co-authors even found that the blockade of CaMKII enzymatic function enhanced the LTP in T286 mutated tissue, implying that LTP is also developed independently of CaMKII autophosphorylation. The main concern is that the evidence supporting the efficacy and specificity of ATP-competitive inhibitors is primarily derived from *in vitro* biochemical assays, while their specificity *in vivo* remains unproven. Another very recent study also supports the importance of a CaMKII/NMDA receptor complex, however, they claimed that it is the CaMKII autophosphorylation that maintains LTP by initiating and stabilizing the CaMKII/NMDA receptor complex, independent of phosphorylation of downstream targets (Chen et al., 2024). For solving these debates, a comprehensive characterization of these enzymatic/structural dissection tools is needed to

be performed in a more physiological condition. Dual imaging of CaMKII and NMDA receptor could also improve our understanding of this topic, for example by using CaMKII intrabody (Cook et al., 2021) and GluN2B probes (Marchand et al., 2012). An even better strategy would be to create a FRET/FLIM tool that detects CaMKII/NMDAR binding, which is however challenging.

3.2.4.2 Tracking synapses chronically

The spine volume and PSD enlargement

The result presented in 3.2.2.2 (Fig. 40) shows that upon CaMKII activation, both spine head and PSD enlarged rapidly. If we focus on the first few minutes after stimulation, there was no difference of PSD concentration (PSD/spine volume) compared to the control, which means that they enlarged synchronously. Chronically, hours after CaMKII activation, PSD enlargement persisted while spine volume returned to baseline levels, resulting in increased PSD concentration (Fig. 41).

The structural basis of spines is the cytoskeleton, formed mainly by F-actin. A larger spine typically accommodates more receptors, primarily AMPA receptors, which enhances synaptic transmission. The PSD, visualized here by intrabody targeting to the PSD scaffolding protein PSD-95, is the protein-dense area in which the receptors and synaptic signaling molecules are mainly located. I show that CaMKII activation is sufficient for initiating these processes. The activity-induced expansion of spine volume and PSD are highly correlated, but not always synchronous. In the 10 min after glutamate uncaging, spine volume expansion is more transient than PSD (Steiner et al., 2008). I managed to follow both spine volumes and PSDs for up to 16 hours, visualizing the slow growth process that is triggered by one-time activation of CaMKII. In summary, these data suggest that while spine volume enlargement is essential for the rapid and initial changes in synaptic plasticity, the PSD is likely more important for the long-term stability of synaptic strength. The persistent structural changes in the PSD help anchor receptors and signaling complexes, ensuring that potentiated synapses remain stronger over time.

CaMKII activation primarily promotes growth in initially small synapses.

By plotting the baseline intensity vs late growth of each individual synapses (Fig.45), I observed a tendency for initially small synapses to get bigger and big synapses to get

smaller, in the absence of paCaMKII activation. That can be explained by the regression toward the mean: in a population of biological data, extreme values often return to more typical values over time. The paCaMKII activation, on the other hand, induced significant PSD and spine volume enlargements in all four baseline size groups compared to the control, and the impact level was largest for the synapses that have smaller initial sizes. Smaller spines have been considered as the preferential sites for LTP induction, whereas larger spines are more likely to remain stable (Matsuzaki et al., 2004). Such preferential formation of LTP on small spines has been reported, upon repetitive single-spine glutamate uncaging (Eggl et al., 2023; Matsuzaki et al., 2004) or global chemical LTP induction (Hosokawa et al., 1995; Paulin et al., 2016). This enhanced likelihood of enlargement in small spines helps balance the stability across synaptic connections. There are studies suggested that such observations are likely due to the fact that smaller spines experience stronger Ca^{2+} influx during synaptic activation (Nimchinsky et al., 2004; Noguchi et al., 2005; Sobczyk et al., 2005), however my results show that the CaMKII activation itself, independent of Ca^{2+} influx, results in a similar effect. At the population level of synapses, the initial spine PSD or head volume somewhat predicts its future direction of change.

Interestingly, in this time-frame of 2-5 hours after paCaMKII activation, the PSD and spine volume enlargement remains strong. Considering my results that paCaMKII activation induced rapid synapses enlargement in PN apical regions but did not induce the elevation of c-Fos expression, it is very possible that such enlargement is nucleus protein-synthesis independent. Candidate sources of PSD proteins could be local trafficking from un-potentiated synapses(Noguchi et al., 2016), long-range transportation from other regions (will be discussed in 3.2.4.3), and local RNA translation (Perez et al., 2021). It would be interesting to perform this chronic imaging with the protein-synthesis blocker in the future.

Dynamic synapses form clusters on the dendrite

Spatial analysis of neighboring spines shows that: first, highly dynamic “hot spots” spontaneously formed on CA1 dendrites: high CV spines have high CV neighbors. Second, the activation of paCaMKII induced weakly clustered spine enlargement: compared to shrinking spines, enlarging spines are more likely to have enlarging neighbors.

Spatial clustering is thought to be critical for enhancing synaptic efficacy and coordinating local synaptic inputs during plasticity. The generation of spikes relies on the

nonlinear summation of dendritic activities induced by spatially colocalized and temporally synchronized synaptic activities. Such integration allows the neuron to amplify and process these spatially and temporally correlated signals more effectively (Losonczy & Magee, 2006). Reflecting this principle, spine imaging experiments show that neighboring synapses are spontaneously co-activated more frequently than distant ones (Kerlin et al., 2019; Takahashi et al., 2012; Wilson et al., 2016; Winnubst et al., 2015), possibly driven by synchronized presynaptic activities (Bloss et al., 2018). Such spatial co-activation pattern impacts the threshold of timing-dependent synaptic plasticity induction through spatial integration of Ca^{2+} (Tazerart et al., 2020). In addition, as mentioned above, neighboring spines are very likely to effectively share plasticity-related proteins and other resources through local transport, leading to cooperative plasticity within the cluster (Kastellakis & Poirazi, 2019). My observations demonstrate that structurally dynamic synapses are not randomly distributed on CA1 dendrites in organotypic slice culture. This is remarkable, since these cultures never received any structured input from sensory organs or in the form of artificial stimulation. Ongoing spontaneous activity in the cultures seems to be sufficient to sort synapses on dendrites into “hot spots”, indicating that this is a fundamental property of neuronal network self-organization. Previous studies have found that the clustered increase in synaptic strength is mediated by NMDA receptor-dependent local Ca^{2+} elevation (Takahashi et al., 2012). My result shows that without Ca^{2+} influx, the intracellular CaMKII activation is sufficient to induce clustered synapse enlargement. Shibata and co-authors’ single spine paCaMKII activation experiments showed that the clustered activation (multiple nearby spines) of paCaMKII induces a longer-lasting spine volume increase compared to single spines paCaMKII activation (Shibata et al., 2021). How would CaMKII activation be involved in the clustered synaptic structure alteration? It is either (or both) CaMKII activation induces local transportation or synthesis of plasticity-relevant signaling molecules, or the neighboring spines’ share common physiological features, for example receiving clustered axonal input, sharing the same store of Ca^{2+} from dendritic shaft ER, or sharing a similar synapse memory developed from prior synchronized activities, etc. Taking previous evidence into account, the activated CaMKII itself has little chance to be transported to adjacent spines (Khan et al., 2012; Lee et al., 2009; Zhang et al., 2008). The molecules involved in local diffusion-driven plasticity clustering are more likely to be downstream factors of CaMKII activation, with slower decay kinetics in their activation. Looking back to the spatial-

temporal activation of synaptic plasticity molecules (Fig. 7), candidates include for example Rho GTPase family and H-Ras. A recent experiment confirmed that single spine activation of paCaMKII did increase the activation of neighboring spines' Cdc42 activity, although not strongly (Shibata et al., 2021).

It is rather clear that the CaMKII downstream factors are involved in clustering. The question is whether the spatially clustered trend of alteration (enlarging hot spots) I observed is purely due to paCaMKII activation, or if the local architecture (e.g. clustered inputs) is also critical? In the current dataset, I used the time window of 0-2 hours after stimulation to calculate the growth. In this time frame, there is a possibility that spontaneous presynaptic activity could be involved in the formation of the cluster after the optical activation. One of the next steps would be to use the time immediately after stimulation timepoint to calculate the growth and to see if the 'enlargement hotspot' is still observed. It is also important to analyze the spatial correlation of the high CV hotspots and the high growth clusters, to see if the two tend to overlap. Such information can tell us whether the formation of the high growth area upon paCaMKII activation is driven by prior synaptic memory.

Limitations and perspectives of current 2P imaging work

The data presented in 3.2.2.2 reveals important findings, however more biological information is yet to be extracted from my experiments. For example, my cluster analysis shows that the most dramatically enlarged spines are surrounded by spines with similar characteristics. Considering that the PSD enlarges so rapidly, the proteins are most likely being trafficked from local regions, at least for the first few minutes. Therefore, it is possible that the "enlarging hot area" is surrounded by something like "shrinking hot areas" whose proteins are transported to the most enlarging spines. To figure this out, I will need to set a distance threshold, say 5 µm, to search for dramatically enlarged spines' neighbors. I will then set this 5 µm radius region as the centroid and calculate the average growth of the regions located at different distances from the centroid. Alternatively, rather than shrinking to support the potentiated spines, non-potentiated spines may directly disappear. Consistent with these ideas, it has been shown that the single spine LTP induction induces both of the patterns mentioned above: (1) Between 10 to 40 µm surrounding enlarging spines, it is more likely to find shrinking spines (El-Boustani et al., 2018); (2) sLTP induction of

single spines increased the lifetime of their neighboring spines (< 5 µm), while for the spines located between 5 µm to 10 µm to the activated spine, their lifetime was shorter than the distal ones (Wiegert et al., 2018). It would be interesting to see whether the global activation of CaMKII, but not single spine LTP induction, also have a similar effect. However, it is difficult to extract spine lifetime (turnover) information from my current dataset due to the limited accuracy of automatic spot detection, which is the major technical limitation of the current work.

The current analysis pipeline is not capable of analyzing newly formed and disappearing spines (spine turnover). The reason is that PSDs are detected separately for each time point and then tracked over all time points. Short tracks, i.e. objects that are detected in <80% of time points, are discarded (Fig.55a). To solve this problem, a manual post-hoc correction is needed after the automatic detection. To do this, we need to create a dataset for this task that contains the critical tracking information and the aligned image series (Fig. 55b). This dataset should be prepared in a format that can be easily visualized in 3D, e.g. a tiff file opened in Imaris. More efforts on spine detection for analyzing the spine dynamics, especially turnover, is needed in the future.

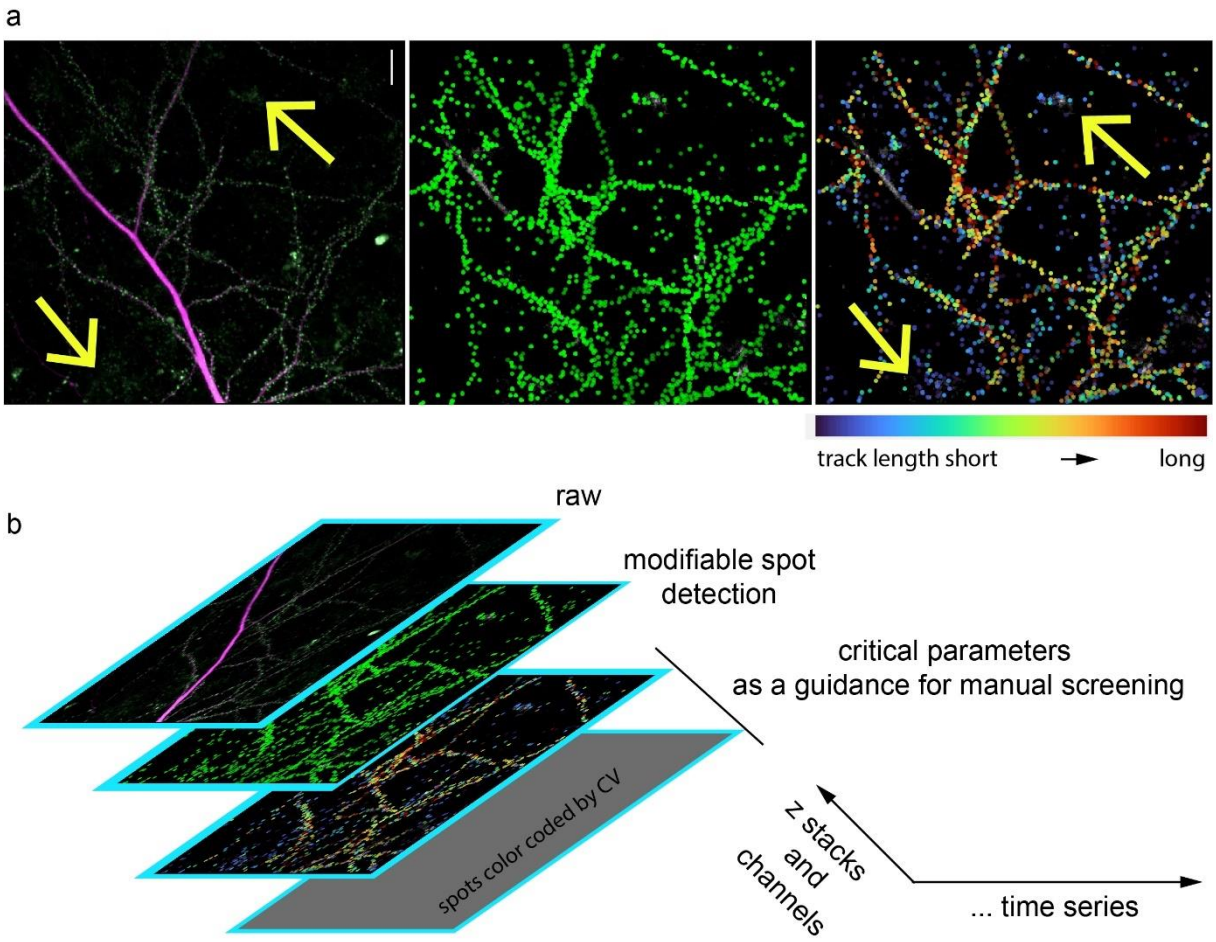

Figure 55: Dealing with the detection errors.

a. Filtering out false-positive detections by excluding short tracks. Left: after image denoising, unspecific signals still exist (yellow arrows). Middle: False-positive detections. Left: due to the fact that the unspecific signals are always highly dynamic or completely randomly distributed, the time-lapse tracking length of these false-positive detections are usually very short, while the long tracks (warmer spots) are highly likely to be real signals. b. multiple-channel image stack series for manual screening. The ideal dataset should contain (1) raw (registered) image stacks. (2) the raw spot detection result, this channel should be editable. (3) and (4) detected spots color coded by critical spine dynamic feature information. These two channels can be used as a guidance for manual screening.

3.2.4.3 apical and basal spines ultrastructure plasticity

Using dAPEX2 labeling and electron tomography, I analyzed spine head and PSD ultrastructural changes upon paCaMKII activation. For spines on the apical dendritic tree, I found a trend of increasing spine volume and PSD area in CaMKII-activated spines. Surprisingly, basal spines show a different change: PSD area was decreased, whereas spine volume was not affected. These data suggest that apical and basal spines respond differently to CaMKII activation. Indeed CA1 PNs basal and apical spines have different physiological

features, including size, presynaptic connection, presence of Ca^{2+} permeable AMPA receptors and electrical conduction (Häusser et al., 2000; Mattison et al., 2014; Spruston, 2008; Tada & Sheng, 2006). Importantly, basal spines are generally more stable than apical ones, and plasticity is more difficult to be induced there (Jain et al., 2024; Knafo et al., 2004; Murakami et al., 2006; Ramachandran et al., 2015). Compared to the apical CA1 spines that form the majority of SC connections, basal spines have been less studied, and how they respond to CaMKII activation remains largely unknown.

One possible explanation for the decrease in PSD in basal spines is that PSD-95 is transported from basal to apical dendrites. As discussed in 3.2.4.2, PSD proteins can be trafficked across different spines. In these experiments, neighboring spines were monitored, in a range of about 5 µm. Long-range trafficking of PSD proteins is more dependent on microtubule-based pathways, mainly kinesin and dynein mediated cargo transport. The typical distance between CA1 proximal apical spines and basal spines in our culture is 50 to 150 µm, and considering that the typical speed of microtubule-based transport is about 0.5 to 2 µm/sec (Hirokawa et al., 2009), protein transport from basal to apical spines will take 25 seconds to 5 minutes. Therefore, it would be interesting to fix the illuminated culture within 25 seconds, and to analyze whether a similar pattern of structural changes is observed. However, our current electron tomography imaging method is too time-consuming. An improvement of volume EM imaging efficiency is needed. While a lower resolution, but much simpler and higher throughput experiment is the 2P chronic imaging upon paCaMKII activation, by taking a larger ROI covering both apical and basal areas.

Furthermore, these results demonstrate that dAPEX2 labeling is suitable for analyzing ultrastructural properties of optogenetically manipulated spines. In the next subchapter (3.3), I will describe the development of a workflow to study the ultrastructural alteration of the spines that its pre- and post-synaptic sides were paired with a positive or negative timing. This workflow combines peroxidase-based genetic tags including dAPEX2 and oSTDP protocol.

3.3 A dual labelling method for ultrastructural analysis of synapses after optogenetic stimulation

As shown in 3.1, by using spectrally separated channelrhodopsins, ChrimsonR and CheRiff, at the pre- or postsynaptic side of CA1 SC synapses, we can control the spike timing all-optically to induce tLTP and tLTD that last for days. By co-expressing CheRiff with paAIP2, we can manipulate CaMKII activities in parallel with tLTP and tLTD induction. Using STED microscopy, putative connecting synapses can be identified, based on the fluorescent proteins tagged to the channelrhodopsins (Fig. 56).

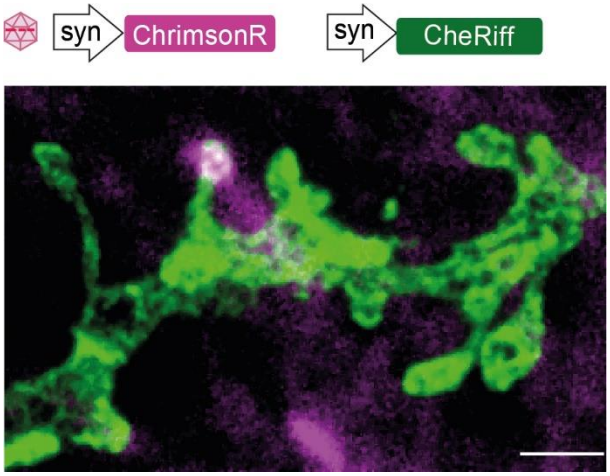

Figure 56 :STED image of putative synapse between ChrimsonR and CheRiff neuron.

Spiny dendrite of a CheRiff-expressing CA1 neuron (with eGFP cell filler). A putative connection (white) is made by a ChrimsonR-expressing axon (magenta) from CA3.
Scale bar: 1 µm. Image from Anisimova, 2020.

Can we find out more about the structural alterations that are responsible for synaptic potentiation? There are two main possibilities: (1) the PSD size of the LTP-induced synapse permanently increases, facilitating the formation of additional active zones and a higher density of receptors (Nusser et al., 1998). (2) New connections between synchronized neurons are formed (Medvedev et al., 2014). Studying the structural features of the ChrimsonR-CheRiff connections provides us with an opportunity to explore this topic. To accomplish this goal, I developed an EM labeling method for achieving the ultrastructural analysis of all-optically manipulated synapses. EM imaging has two major advantages for studying the structural features of the ChrimsonR-CheRiff connections: (1) High spatial resolution: The typical hippocampus synapse size approaches the diffraction limit of conventional LM, preventing direct visualization of subcellular synaptic structure. (2) Non-biased sampling: Fluorescence-based methods generally allow visualization of labeled

synapses, but provide no information about the surrounding unlabeled structures and cells. In contrast, EM provides an unbiased technique for detailed examination of the ultrastructure of specific synaptic connections and the surrounding synapses. This advantage is important, because surrounding synapses are perfect internal controls for analyzing the difference between manipulated synapses (Fig. 57, labeled) and their neighbors (Fig. 57, unlabeled).

To visualize the ChrimsonR-CheRiff synapse under EM, stable co-expression of optogenetic tools and peroxidase-based tags (HRP and APEX) is required. In this section, I will describe my efforts in developing the co-expression system and establishing a correlative optogenetic-electrophysiology-EM workflow.

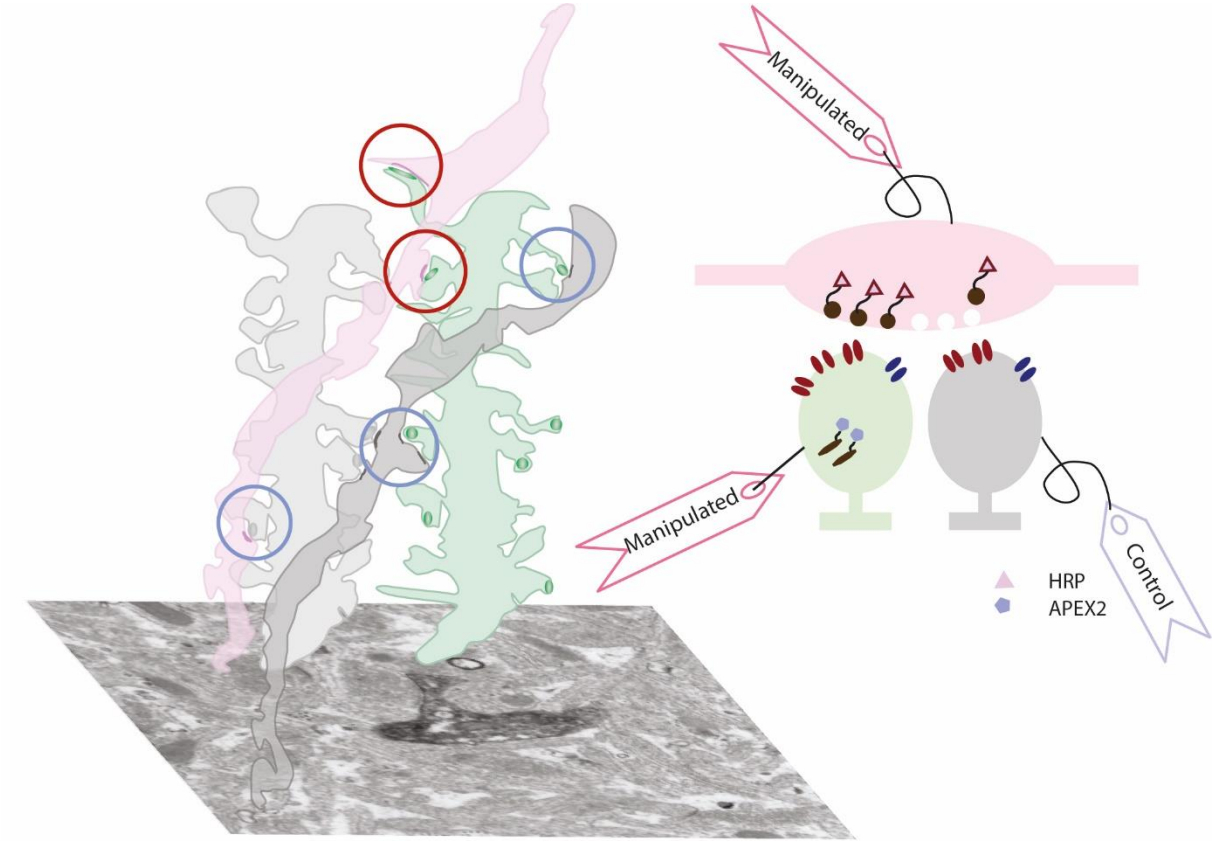

Figure 57: Locating oSTDP-tLTP synapses in electron microscopy.

Taking advantage of un-biased imaging of EM, in the same FOV both paired synapses (pre- and post-synaptic side labeled) and controls (pre-, post-only, and unlabeled synapses) can be analyzed.

3.3.1 Characterization of tags and optimization of staining procedures

My strategy was to label organelles or subcellular structures that are present in each synapse, rather than filling the entire cell with black precipitate, which would obscure the ultrastructure. I systematically tested and evaluated several tags (Table 6). Ultimately, I selected the plasmid pAAV-SYP-HRP to label synaptic vesicles on the presynaptic side and the plasmid pAAV-dAPEX2 to label the cytoplasm on the postsynaptic side (gifts from David Ginty, Zhang et al., 2019).

Table 6: List of tested tags.

plasmid	Target peptide and subcellular structure	Whether tested	Reason for not choosing	Source
APEX2-NES	* Nuclear export signal, NES. * Cytoplasm.	Tested. Healthy cells. Cytosolic and nuclear staining.	The labelling is not reliably work. Signals are weak.	Alice Ting Lab, Addgene #39486 (Lam et al., 2015)
APEX2-Actin	* Nomenclature Committee abbreviation, NCTB. * Cytoskeleton beta-actin	Tested. Strong labelling. Healthy cells. Cytosolic, nuclear, dendrite and spine labelling.	The distribution pattern of the staining makes it hard to see PSD in spine head.	Alice Ting Lab Addgene #66172 (Lam et al., 2015)
APEX2-tubulin	* tubulin alpha 1b (TUBA1B) * Cytoskeleton microtubule	Tested. Strong labelling. Cell looks damaged. Dendrite and spine labelling.	Only broadly expressed in dendrite, rarely in spine head.	Alice Ting Lab, Addgene #66171 (Lam et al., 2015)
ER-dAPEX2	* Igκ leader sequence and ER retention sequence KDEL * ER lumen	Not tested.	ER only exist in large spine heads.	David Ginty lab, Addgene #39486 (Q. Zhang et al., 2019)
ChR2-mAPEX2	* Growth-associated protein 43, GAP43. * Axonal membrane.	Not tested.	The distribution pattern of the staining makes it hard to see subcellular structures. (Kuwajima et al., 2020)	Kristen M. Harris lab, (Kuwajima et al., 2020)
Mito-V5-APEX2	* Matrix localization sequence from COX4. * Mitochondria matrix.	Tested. Strong labelling. Healthy cells. Boutons labelling.	Only exist in a small proportion of boutons.	Alice Ting Lab, Addgene #72480 (Lam et al., 2015)

To investigate the functional co-expression of these tags and channelrhodopsins, I prepared two plasmid mixtures: (1) SYP-HRP with ChrimsonR and (2) dAPEX2 with CheRiff, and electroporated these mixtures into CA3 and CA1 pyramidal neurons, respectively. After 7 to 10 days of expression, I performed DAB staining to assess tag functionality and whole-cell patch-clamp recordings to assess channelrhodopsins functionality. The expressing cells

showed the expected ability to generate optical currents. However, after one to three hours of DAB staining, the response was notably weak (Fig. 58, top panel). A paper suggesting that it's still possible to find the label under EM after heavy metal staining, even though the DAB signal is weak under LM. Because the LM DAB signal is generated by the photon absorption of the DAB polymer, which is caused by its polycyclic structure. While under EM, the electron density is from osmium redox reactions (Joesch et al., 2016). However, I was not able to find any signal under EM when the DAB reaction is weak, and the NaHS reduction after DAB staining suggested by Joesch and co-authors was not helpful. Extending the reaction time is not an option because too long staining time can damage the subcellular structure and abolish the electron density under EM (Joesch et al., 2016; Lam et al., 2015; Q. Zhang et al., 2019). I then tried metal-enhanced DAB staining, which can theoretically enhance the DAB signal more than 40-fold, and it did indeed significantly enhance the DAB signal under both LM and EM (Fig. 58).

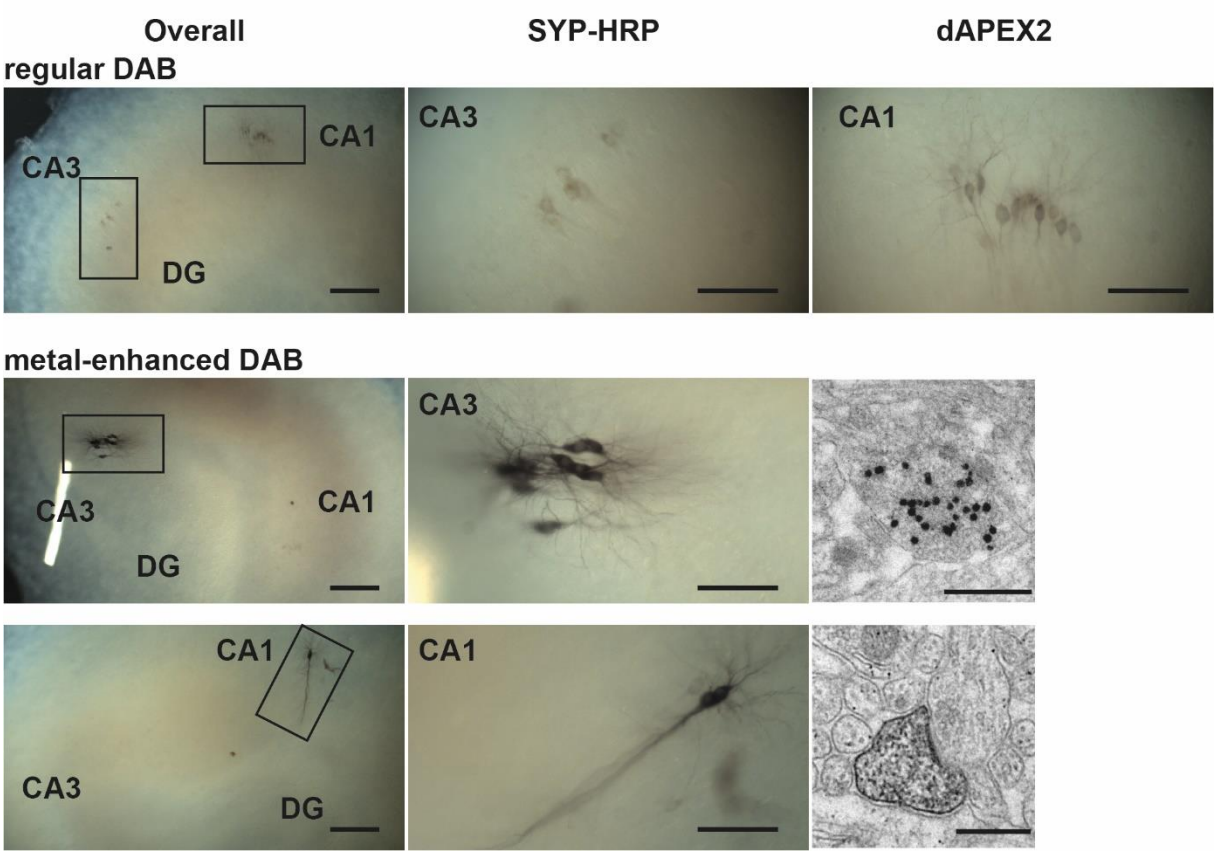

Figure 58: Metal-enhanced DAB substrate significantly improved DAB staining.

Top: DAB reaction generates weak staining signals for both SYP-HRP and dAPEX2 electroporated cells. Middle and bottom: By using metal-enhanced DAB substrate, the DAB staining was significantly

improved. Scale bars: 0.25 mm (left 3 LM images), 0.1 mm (right 4 LM images) and 500 nm (2 EM images).

Taken together, SYP-HRP and dAPEX2 are suitable for labeling synapses on the presynaptic and postsynaptic sides, respectively. The metal-enhanced DAB substrate is important for signal enhancement, which is critical for sample trimming and EM imaging.

3.3.2 Development of co-expression system

To induce oSTDP, a cluster of CA3 PNs are needed to be densely transduced with ChrimsonR via CA3 AAV injection (Anisimova et al., 2022). To generate AAV-conducted co-expression of ChrimsonR and SYP-HRP, I initially attempted to build one plasmid containing SYP-HRP, ChrimsonR and fluorescent protein and pack it into a single AAV. However, it failed to express because the total size of this plasmid (SYP-HRP-P2A-ChrimsonR-mCerulean, 8320 bp) exceeds the AAV packaging capacity (about 4500 bp). Then I packaged the plasmid into a lentivirus, which has a larger packaging capacity (about 8000 bp) compared to AAV, which again did not work. Next, I tried to prepare two AAVs, one containing ChrimsonR and fluorescent protein, the other containing SYP-HRP, and inject the mixture of them. This was also not satisfactory, because the co-expression rate of two independent viruses is low. Electroporating a number of CA3 cells is not an option due to the inherently low throughput.

3.3.2.1 SYP-HRP-dependent expression of ChrimsonR

To solve this problem, I developed a method using two AAVs, one containing a Cre-dependent ChrimsonR, the other encoding Cre recombinase together with SYP-HRP. Local injection of this mixture resulted in good co-expression of the EM tag and channelrhodopsin (96% of ChrimsonR cells, Fig. 59a-c). Regarding the CA1 PNs, no further optimization was needed. The single-cell electroporation of a mixture of dAPEX2 and CheRiff satisfies the experimental requirement of combing optogenetic electrophysiology and EM (Fig. 59d).

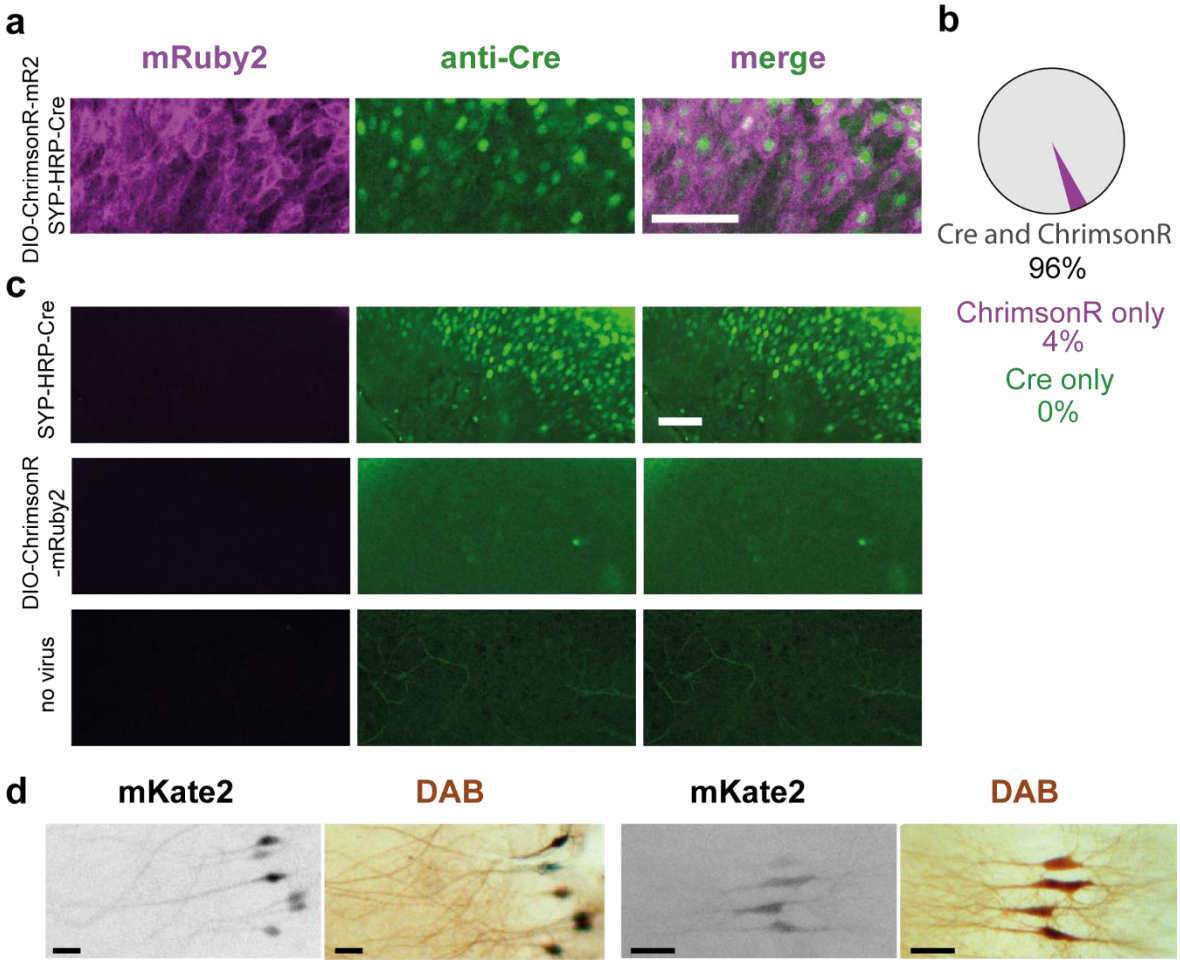

Figure 59: SYP-HRP-Cre + Flex-ChrimsonR and CheRiff + dAPEX2 co-expression.

(a) CA3: A mixture of rAAV9-syn-DIO-ChrimsonR-mRuby2-ST and rAAV9-syn-SYP-HRP-IRES-Cre was co-injected into CA3. Slices were fixed and immunostained against mRuby2 (magenta) and cre (green). (b) Quantification of co-expression rate of ChrimsonR-mRuby2 and syp-HRP-IRES-Cre. n = 202 cells. (c) Application of the individual viruses or no virus. (d) Two examples of co-expression in CA1 pyramidal neurons electroporated with plasmids encoding dAPEX2, mKate2 and CheRiff-eGFP. On the left mKate2 fluorescence several days before fixation. On the right corresponding brown DAB staining. Scale bars: a and c: 100 µm; d: 40 µm (left two); 70 µm (right two)

3.3.2.2 Validation of the tools expressing neurons functions

Next, I checked whether optical STDP could be induced in slice cultures expressing tags and channelrhodopsin (Fig. 60a). Indeed, the CA3 ChrimsonR + SYP-HRP expressing PNs were able to follow 5 Hz optical stimulation (8mW/mm^2, Fig. 60b) and the pre-post pairing activity pattern can be achieved in the CA1 CheRiff + dAPEX2 PN (Fig. 60c). Importantly, all-optical tLTP induction could be generated (Fig. 60d). Taken together, the expression of EM tags did not prevent oSTDP.

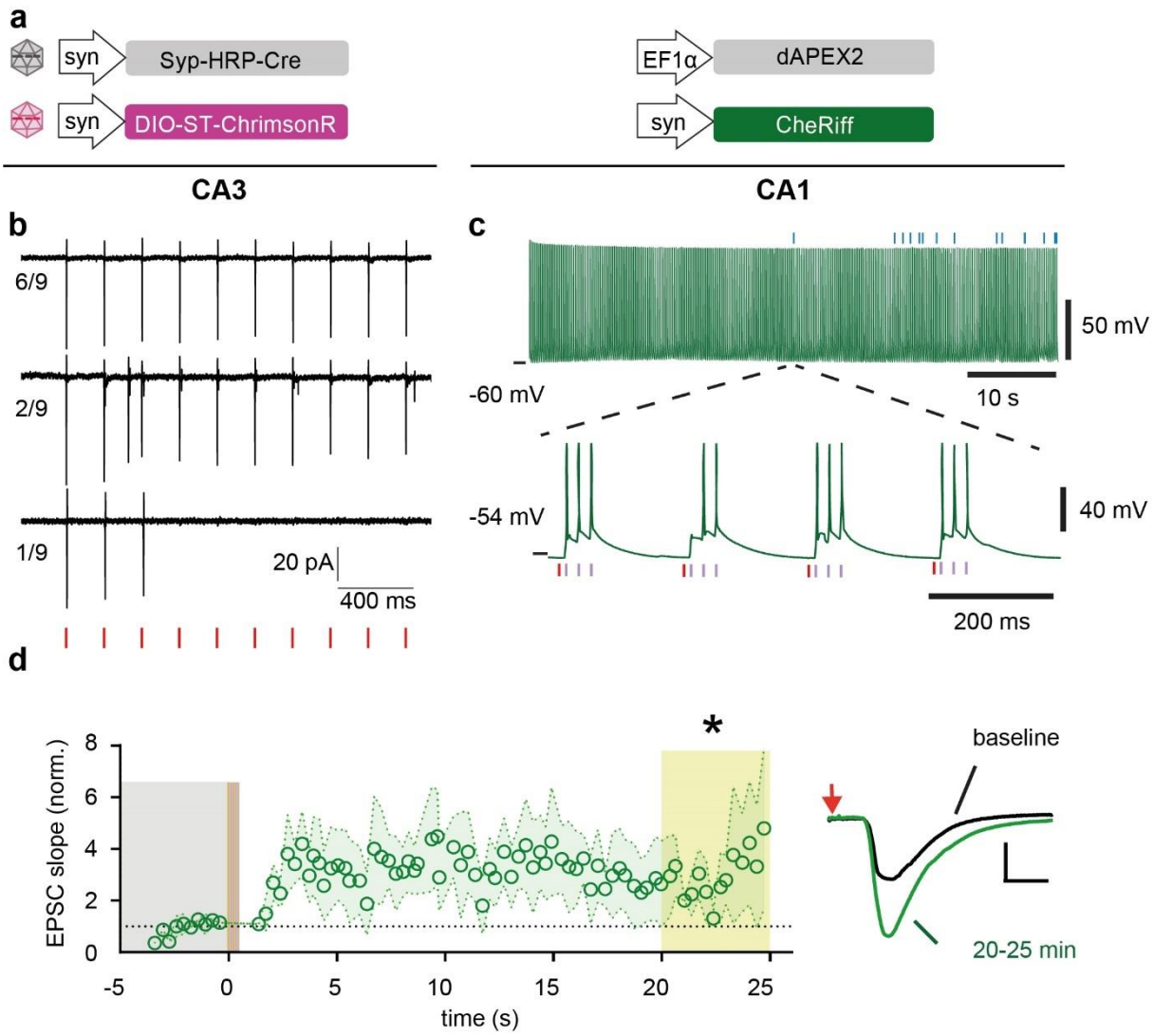

Figure 60: The expressing of tools does not interfer all-optical tLTP induction.

(a) expression of tools in CA3 and CA1, by AAV injection and single-cell electroporation, respectively. (b) Representative cell-attached recordings of CA3 expressing PNs, subjected to 635 nm, 8 mW/mm^2, 1me optical pulsed delivered at 5Hz. In 9 recorded neurons, 6 of them perfectly followed the 5Hz light pulses, 2 slightly burst and 1 missed the majority of the spikes. (c) Representative current-clamp recordings of a CA1 expressing PN (bottom: zoom-in view), subjected to the optical pairing stimulations. Blue ticks indicate the pairs that contain only 2 spines, instead of 3. In this example, 286 out of 300 pairs spike 3 times per pair (886 spikes in total, out of 900 spikes). (d) The effect of optical pairing on EPSC slopes, calculated from voltage-clamp recordings. tLTP was induced as expected after the optical pairing (indicated by the bar stared from time 0). n = N = 4, Normalized to baseline, data plotted as mean ± SEM. Paired t-test, *P < 0.05. Scale bars: 200 pA, 10 ms. The red arrow indicates the EPSC induction pulse.

3.3.2.3 Validation of the normal structure

Transfected/transduced PNs had normal electrophysiological properties. The next step was to validate whether these PNs have normal ultrastructure. Expressing cells could be easily identified by electron-dense DAB staining of the soma (Fig. 61). At low magnification under TEM, the cell morphology looked typical.

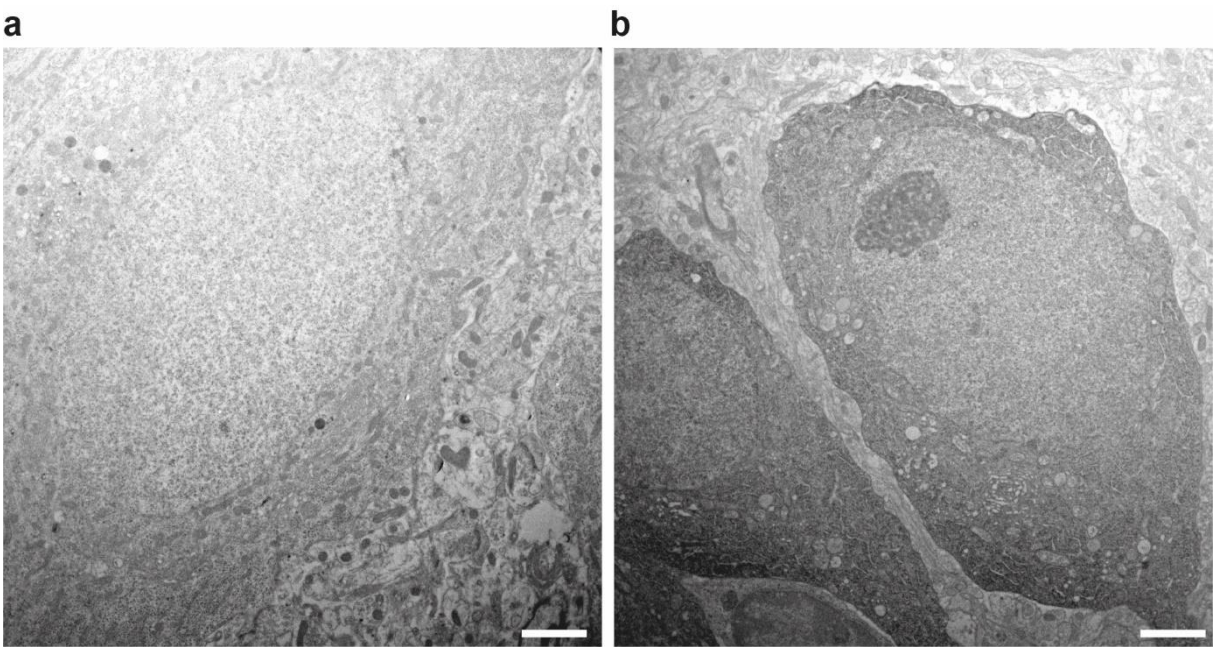

Figure 61: DAB deposition at somata area.

Low magnification TEM of Syp-HRP-Cre /Flex-ST-ChrimsonR cell body in CA3 (left) and dAPEX2 /CheRiff cell bodies in CA1 (right). Scale bar: 2 μm.

Moreover, at higher magnifications, normal morphology of organelles (e.g. N: nucleus envelop, ER, Golgi body, mitochondria and lysosomes) were observed for both CA3 (Fig. 62) and CA1 (Fig. 63) expressing cells. Taken together, transfected/transduced PNs have normal morphology under EM.

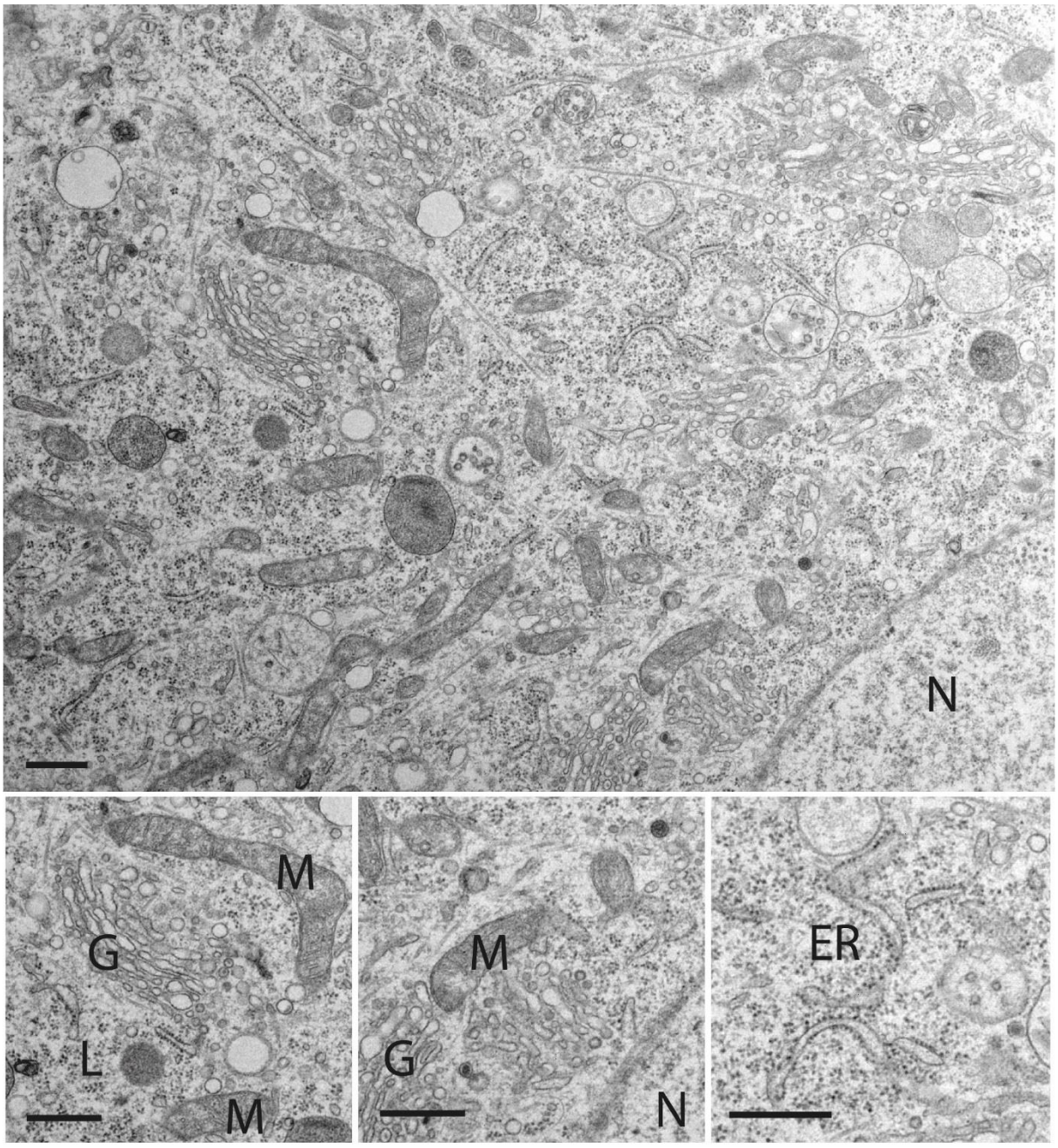

Figure 62: SYP-HRP and ChrimsonR co-expressing cells have normal morphology.

(a) zoom-out view shows the somata area of SYP-HRP labeled cell. (b) In zoom-in views, Normal morphology of organelles including N: nucleus, ER: endoplasmic reticulum, G: Golgi body, M: mitochondria and L: lysosomes are visible. Scale bars: 500 nm.

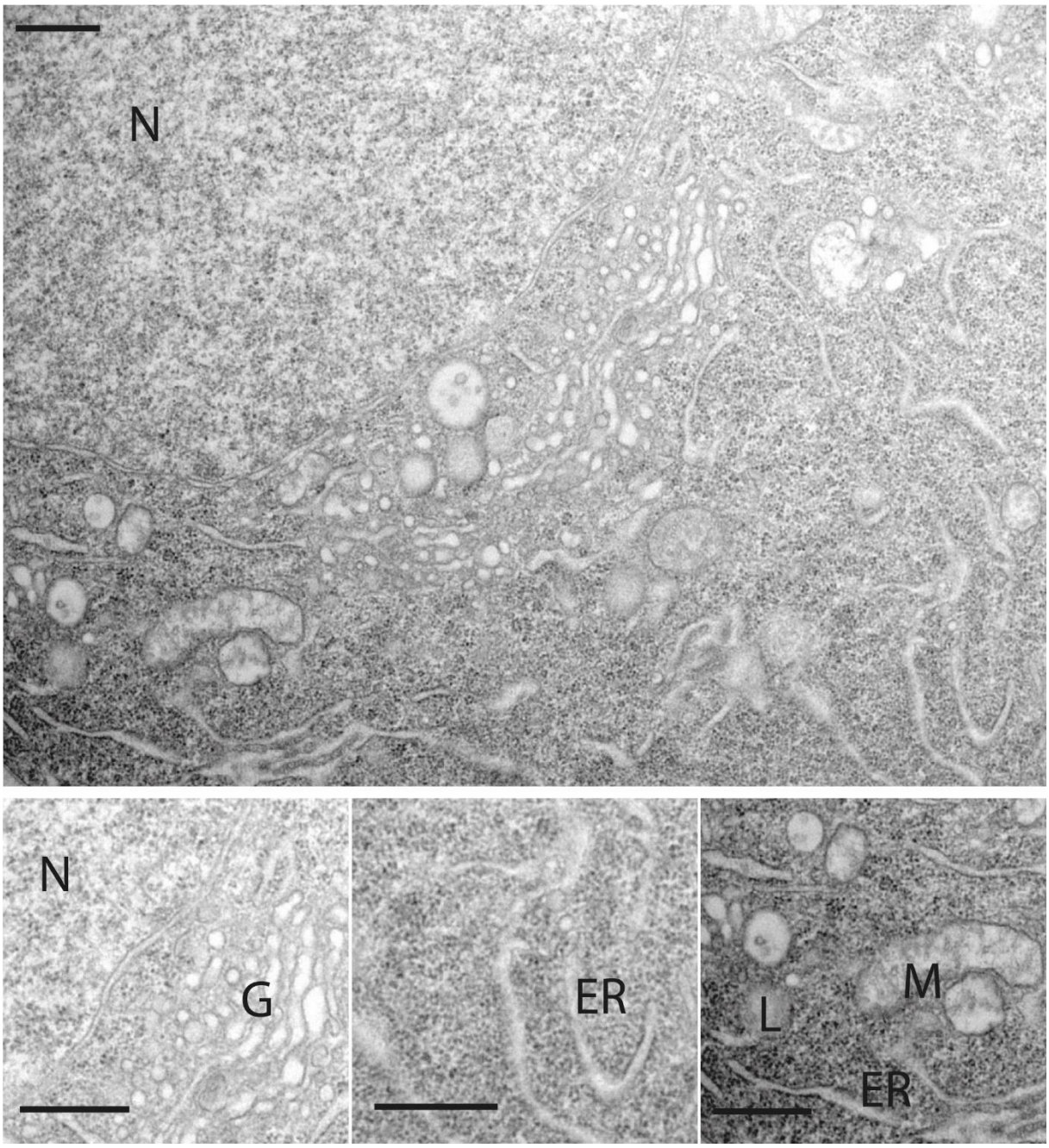

Figure 63: dAPEX2 and CheRiff co-expressing cells develop normal morphology.

(a) zoom-out view shows the somata area of dAPEX2 labeled cell. (b) In zoom-in views, Normal morphology of organelles including N: nucleus, ER: endoplasmic reticulum, G: Golgi body, M: mitochondria and L: lysosomes are visible. The brightness and contrast are different due to the cytoplasm dAPEX2 condensation, which does not have effects on morphology itself. Scale bars: 2 µm top; 500 nm bottoms.

3.3.3 Locating labeled synapses in EM

Specimens were trimmed under visual control using the stained CA1 neurons as a guide prior to osmium tetroxide fixation, and then trimmed again after semithin sectioning. Serial ultrathin sections were collected for EM examination. As shown in Fig. 64, causally paired, potentiated synapses could be found, characterized by electron dense labeling: boutons of transduced CA3 axons were identified by labeled synaptic vesicles, and spines of transfected CA1 dendrites could be identified by a granular black precipitate in the cytoplasm (Fig. 64a). In the same FOV, I could find not only the pre- and post-synaptic double-labeled synapse, but also different control synapses (Fig.57, Fig.64b). I calculated the percentage of labeled synapses out of the total amount of synapses (estimated from the size of the search area for finding the double-labeled synapse and the synapse intensity on my sample), and the percentage of double-labeled synapses is about 0.03%.

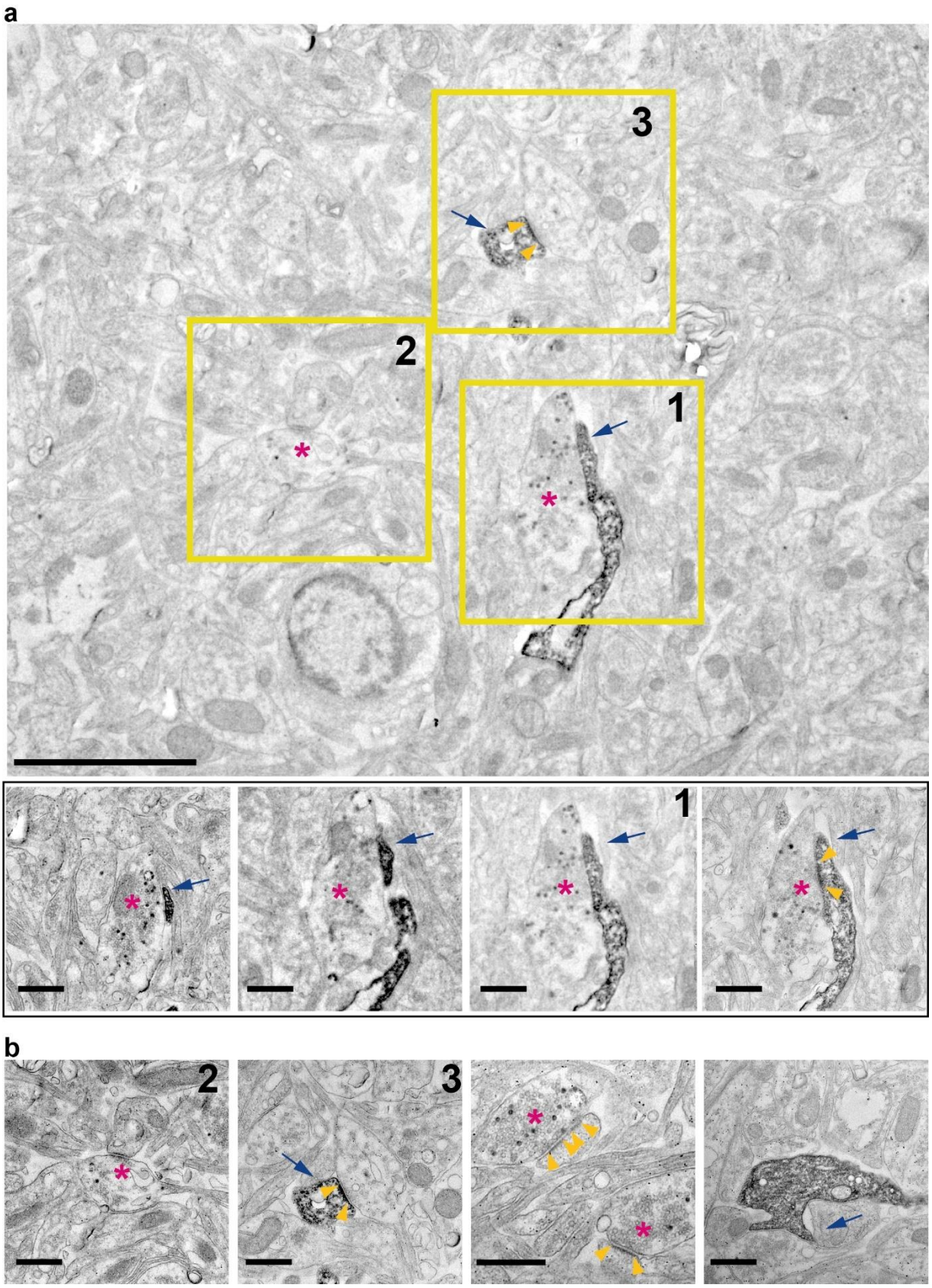

Figure 64: Orthogonal pre- and post-synapse specific labeling.

(a) Top: In the same FOV, both the pre- (asterisk) and postsynaptic (arrow) double-labelled synapse (**1**) and single labelled synapses (**2**, pre- only and **3**, postsynaptic only) can be found. Bottom: Serial sections through a dually pre- (red asterisk) and postsynaptic (black arrow) labeled synapse. A

postsynaptic density becomes visible in only the last image (arrow heads). (b) Higher magnification examples of pre-and postsynaptic-only labeling (**2** and **3** correspond to a). Scale bars: 2 µm (a, top), 500 nm (a, bottoms and b).

3.3.4 Summary

By correlating optogenetic techniques and peroxidase-based genetic tags, I developed a method to study the ultrastructural changes of tLTP from minutes to days after plasticity induction. Taking advantage of the Cre/LoxP system, I achieved stable and dense co-expression of the two critical tools, generating dark synaptic vesicles in optogenetically activated presynaptic terminals.

SYP-HRP-Cre provides labeling of presynaptic vesicles and NES-dAPEX2 labels the postsynaptic cytoplasm. This strong labeling allows the combination of these tools with volume electron microscopy methods which are ideal for connectome studies of neuronal systems. In addition, I have also constructed a NES-dAPEX2-Cre plasmid, together with SYP-HRP-Cre, these tools can be combined with any Cre-dependent optogenetic tools to study the ultrastructural alternation after optogenetic manipulation, suitable for both in vitro and in vivo work. Importantly the workflow (Fig. 65) can be combined with any common EM protocol, particularly suitable for research on ultrastructural changes after optogenetic manipulation of neuronal activities.

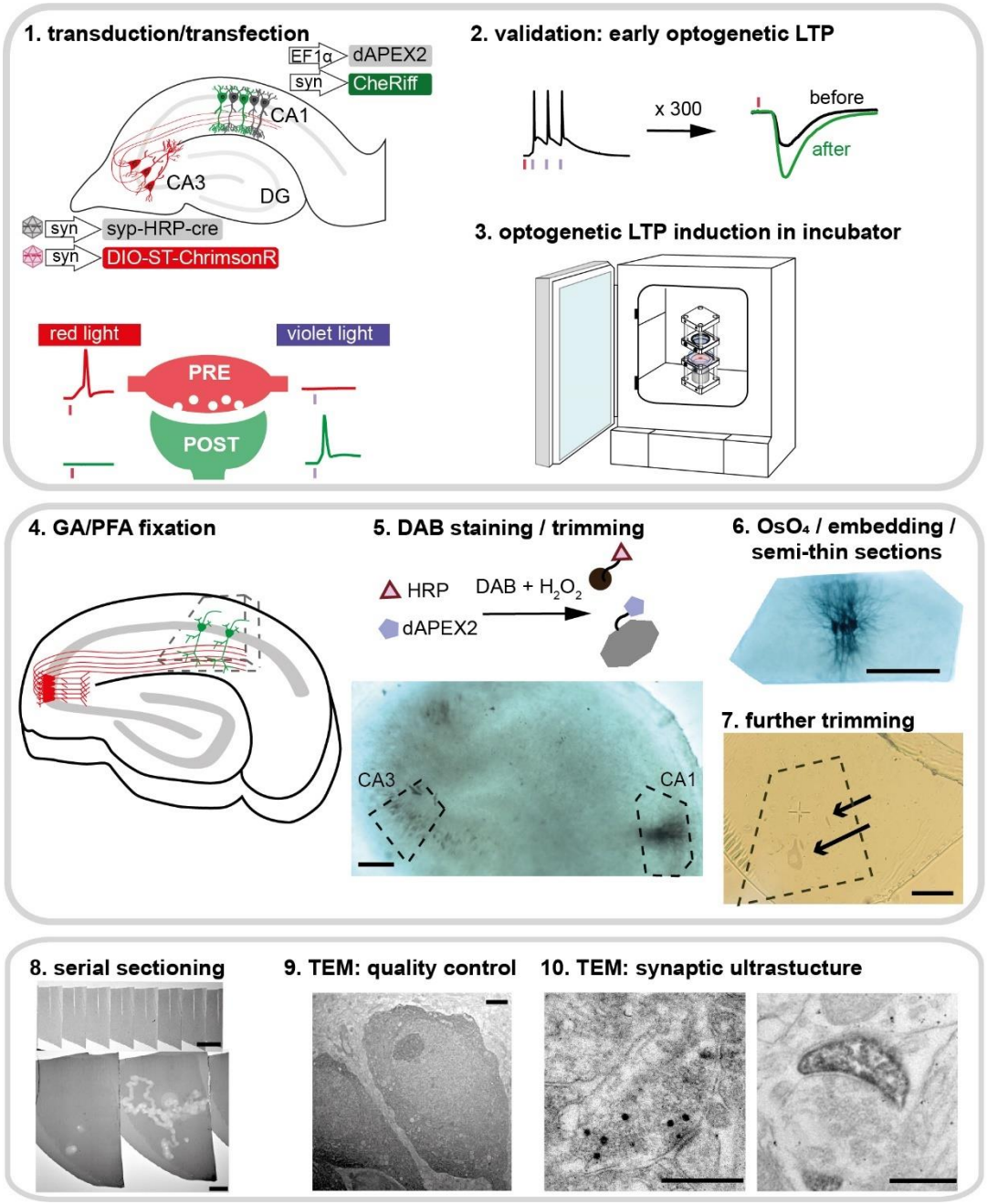

Figure 65: Work-flow of correlative functional and structural method to study the mechanism of STDP.

Steps listed in the workflow. Arrows in Step 7 are pointing to labeled soma and dendrites, found in semi-thin slice, which can be used as the visual guidance for further trimming. Scale bars: 5 and 6: 200 µm; 7: 20 µm; 8: 60 µm, 20 µm; 9 and 10: 500 nm.

3.3.5 Discussion and perspectives

3.3.5.1 Why using different tags for pre- and postsynaptic compartment?

Heme peroxidases are popular electron microscopy labels. When the expressing cells are fixed and incubated with H_2O_2 and DAB, peroxidases catalyze the polymerization. This reaction further leads to the deposition of DAB, and after OsO_4 staining, this DAB deposition subsequently triggers the osmium redox reaction, generating electron density. The most commonly used peroxidase-based EM tags are HRP and APEX. HRP produces strong contrast in EM (Porstmann et al., 1985). Its conformation is stabilized by disulfide bonds and both domains of HRP contain a calcium binding site (Zakharova et al., 2011). Therefore, HRP loses its enzymatic activity when expressed in the reducing and Ca^{2+} deficient cytosolic environment of cells (Hopkins et al., 2000; Martell et al., 2012), but works fine inside acidic presynaptic vesicles. APEX, an engineered monomeric ascorbate peroxidase (Lam et al., 2015; Martell et al., 2012), was engineered to overcome the limitations of HRP, as it lacks disulfide bonds and calcium binding sites. dAPEX2 is the dimeric, mutated version of APEX with significantly improved enzymatic activity. However, in some cases, the dimerization induced mis-localization of tags (Zhang et al., 2019), making it difficult to label organelles. Therefore, I used HRP to tag presynaptic vesicles and dAPEX2 to label the cytoplasm of the post-synaptic neuron, taking advantage of both types of tags.

3.3.5.2 Localization of double-labeled synapses

The LM DAB signal helps to trim the sample as precisely as possible (Fig.65, step 7), however to manually find double-labeled synaptic connections proved to be very challenging. Considering an average release probability of 0.5, and the amplitude of optogenetic-stimulation-triggered EPSPs, about 0.1% spines are connected to activated boutons (Megías et al., 2001), which means that in the optimal case I have to search ~1000 boutons to find one example. In practice, the percentage of double-labeled synapses was even lower (about 0.03%, estimated from the search area). To increase the throughput, volume EM methods and automated detection would be highly desirable, for example array tomography or GridTapeTEM, combined with machine-learning-aided detection.

3.3.5.3 Earlier approaches to investigate synaptic ultrastructure after optogenetic stimulation

Research on ultrastructural alterations associated with synaptic plasticity utilizing channelrhodopsins and optogenetic techniques has been published before (Kuwajima et al., 2020). The authors attempted to investigate ultrastructural mechanism of HFS-induced long-lasting LTP (3 h) using optogenetic stimulation, which is a significant technical improvement over the electrical stimulation-induced 'TBS-LTP circuit' vs 'control stimulation-control circuit' method (Cao & Harris, 2012), as discussed in 1.5.3. Instead of assuming that all the spines in the 'LTP circuit' are potentiated, by co-expressing the channelrhodpsin with a membrane-targeted APEX2 (mAPEX2), Kuwajima and co-authors identified the potentiated spines which are connected to the labeled boutons. However, they had to conduct nanogold labelling that was conjugated to mAPEX2, because the expression of mAPEX2 obscures the structure of the PSD (personal communication). Compared to this study, the method I present in this chapter has several advantages: (1) STDP-induced tLTP lasts for days; (2) tLTP was induced in culture medium which is a very natural environment; (3) STDP highlights the critical role of causality in the modulation of synaptic strength, aligning with Hebb's original postulate (Caporale & Dan, 2008); (4) Using the two tags presented here, no additional procedures (nanogold staining) are needed.

3.3.5.4 Limitations and perspectives

In this proof-of-concept work, manually collected serial ultrathin sections were imaged using TEM, and double-labeled synapses were manually identified. While it is possible to identify double-labeled synapses in a single section, it would be desirable to reconstruct the entire 3D morphology for quantitative analysis. The next step would be to optimize the procedures for array tomography, FIB-SEM or GridTape TEM. According to studies combining DAB staining and automatic vEM methods (Ayuso-Jimeno et al., 2022; Horstmann et al., 2013; Sonomura et al., 2013; Zhang et al., 2019), this labeling method appears to be well-suited for automated sectioning or block-face imaging techniques, which significantly improves the efficiency of 3D reconstruction of specific synapses. As discussed in 3.2.2.3, I attempted to use the serial sectioning electron tomography method to analyze the structure of dAPEX2-labeled spines, which provides excellent 3D information of synaptic

ultrastructure, but only close to the tilt axis. The small field of view means that neighboring synapses cannot be used as controls, and localization of double-labeled synapses remains difficult. In the future, a full-3D approach seems to be more promising.

Once a higher throughput of data collection is established and co-expression is further optimized in the future, a long-standing question can be answered: How does plasticity induction affect the concentration of PSD in the spine head at different stages of plasticity? In other words, which grows faster, spine volume or PSD? Results from the Harris lab using ssTEM that in the hippocampus, LTP induction does not change the overall PSD/spine volume ratio after 2 hours, while an increased ratio was observed in spines containing polyribosomes and a decreased ratio in spines containing SER spine apparatus (Chirillo et al., 2019). However, results from the Radwanska lab, using SBF-SEM, rather show the opposite: LTP induction and memory formation increases the overall PSD/spine volume ratio, while it does not change the ratio in the spine-containing SER spine apparatus (Borczyk et al., 2019; Śliwińska et al., 2020). Even more contradictory, other EM results from different groups show that overall, at least within 2 hours after stimulation, LTP induction induces a decreased PSD/spine volume ratio (Bosch et al., 2014; D. Meyer et al., 2014; Sun et al., 2021; Toni et al., 2001) and such a decrease is consistent with live 2P imaging results (Bosch et al., 2014; Kopec et al., 2006; D. Meyer et al., 2014). If we only consider the results of EM experiments, in which the artifacts of PSD protein overexpression do not occur, then such inconsistencies could be due to: (1) the artifact of the LTP induction protocol using the high-frequency glutamate uncaging method or chemical LTP. The glutamate uncaging LTP protocol can possibly induce extra-synaptic receptor activations (Franks et al., 2003), and the uncaging laser irradiation itself affects spine volume (Sun et al., 2021); and chemical LTP stimulations are likely to result in homeostatic plasticity (Turrigiano, 2012). (2) The intrinsic heterogeneity of the spines. For example, the presence of SER and polyribosomes could potentially determine the changes in PSD/spine head volume ratio after LTP. The method presented in this chapter is able to solve these problems and helps us to understand the mechanism of synaptic plasticity.

With the method presented in this part, I wish to solve these puzzles in the future.

4. Appendix

4.1 Supplemental figures

4.1.1 No correlation between CaMKII activation and c-Fos expression

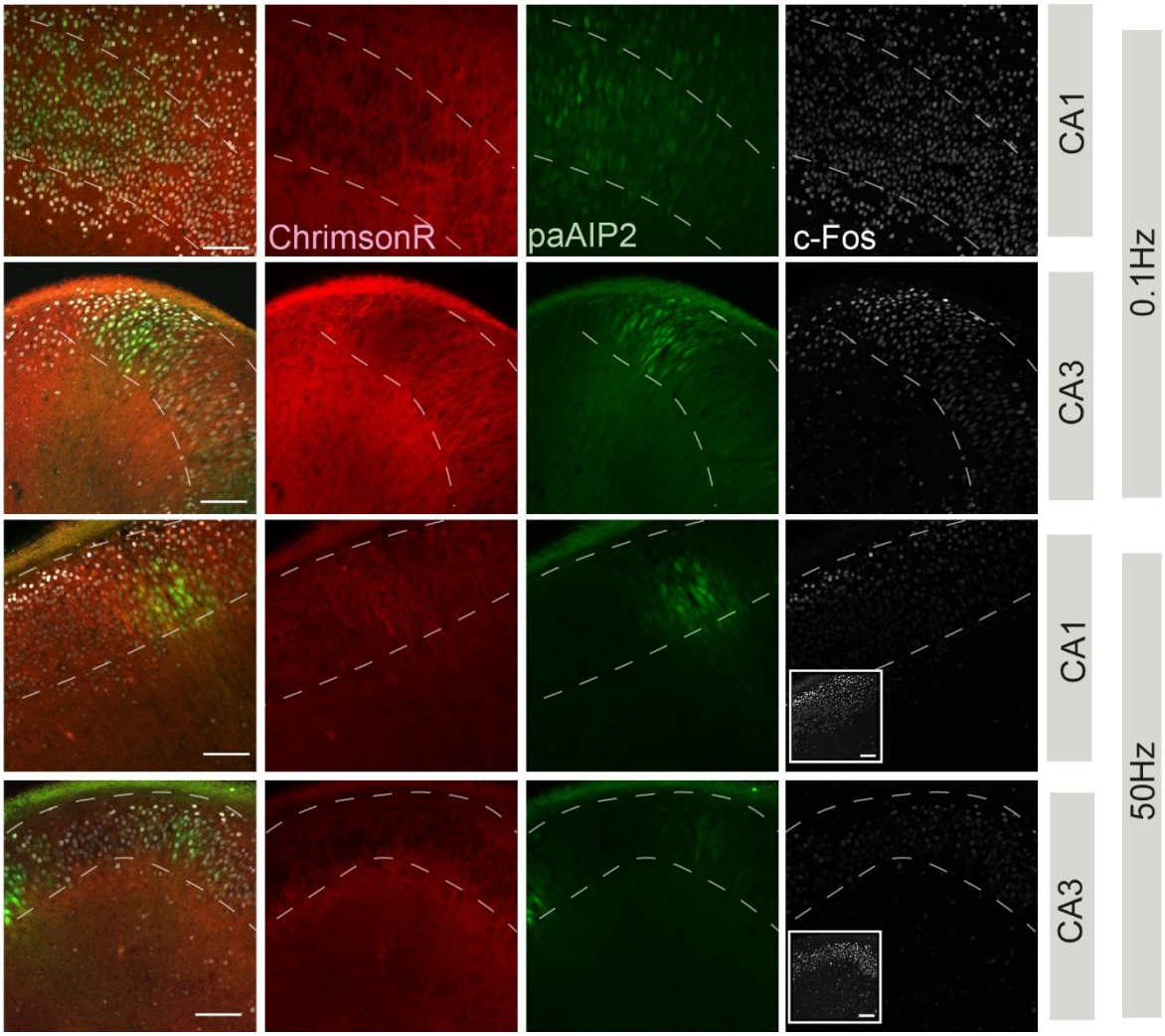

Supplement figure 1: paAIP2 activation does not block spike-induced c-Fos expression: examples from different regions.
representative images as in Fig. 37c, different regions. Brain regions and the frequency of stimulations are listed in the figure. Merged images were contrast-enhanced for visualization, and raw images were shown for separate channels. The maximum intensity projection including 5 slices at the middle of PN soma layer were used to create example images. The merged image's contrast was adjusted for clearer visualization, and the raw images were presented for the separate channels. The inserts are contrast-enhanced images. Scale bars: 100 µm.

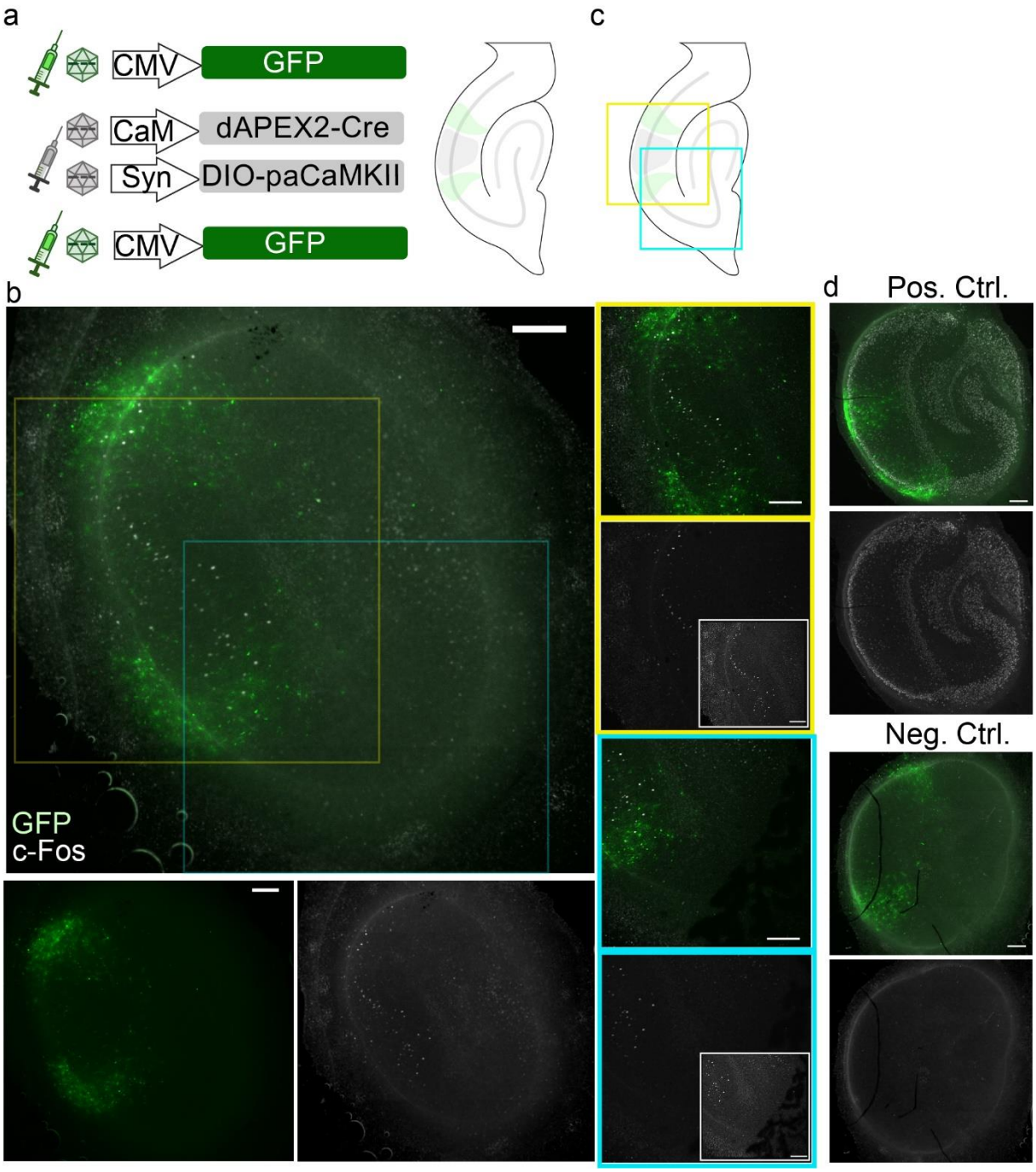

Supplement figure 2: paCAMKII activation mildly increased c-Fos expression.
A larger number of CA1 PNs expressed paCaMKII and the paCaMKII activation induced c-Fos expression very mildly and sparsely, but not statistically significantly. (a) AAV transduction strategy, our available paCaMKII AAV is Cre dependent and do not have a fluorescent tag. Therefore, In CA1, the dark DIO-paCaMKII AAV expression was driven by a Cre virus, and the expression region of paCaMKII was marked by two sites of GFP AAV injections. (b) Representative widefield fluorescence images of c-Fos expression upon paCaMKII activation. Only at the AAV injection site, c-Fos was expressing mildly. (c) The middle and edge of injection areas were marked by yellow and cyan squares, and zoom-in confocal images are shown below. (d) Positive (virus injection plus high K^+ stimulation) and negative control (no Cre virus, but only Cre-on paCaMKII, plus optical stimulation) images. The merged image's contrast was adjusted for clearer visualization, and the raw images were presented for the separate channels. The inserts showed a contrast-enhanced version. Scale bars: 200 μm.

4.1.2 Dynamic of individual synapses: chronic 2p imaging of paCaMKII activated neurons

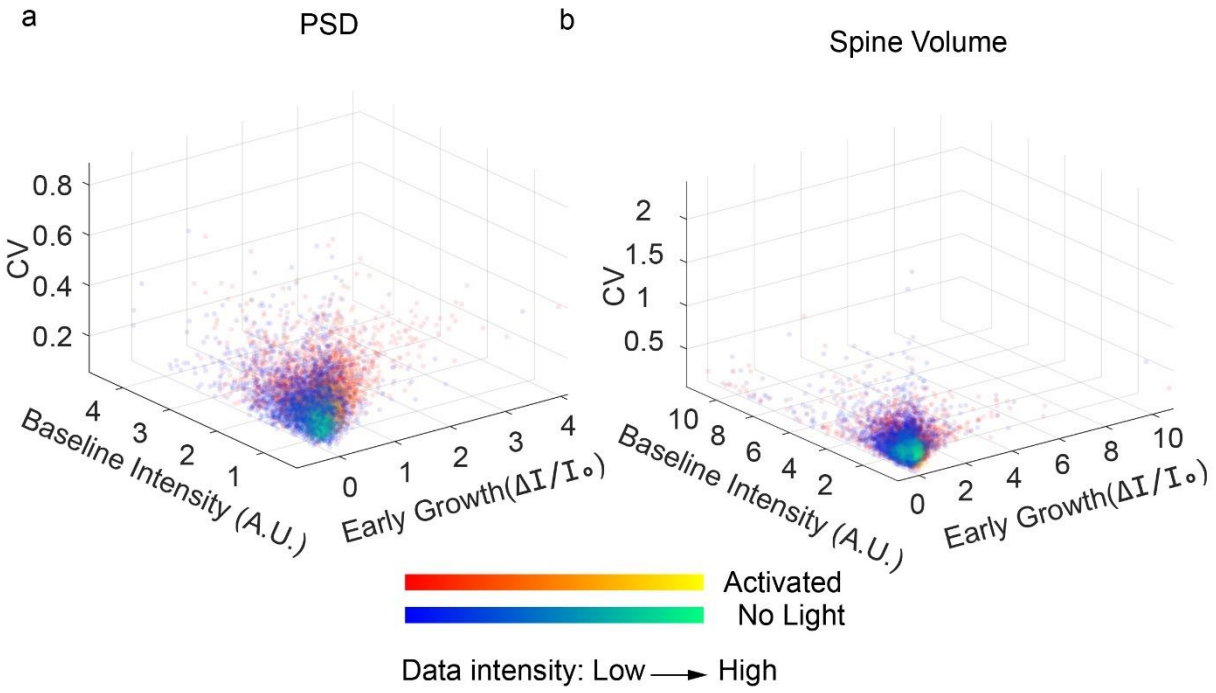

Supplement figure 3: overall relationship of baseline signal intensity, growth factor and CV.

The overall relationship of baseline intensity, CV and early growth, as shown in Fig. 43, 44. Data points are color coded by the intensity of data, the majority of spines are located at the bottom, meaning that most of the spines are highly stable. N = 6 (activated), 5 (no light); n = 2948, 2953. A.U. arbitrary units.

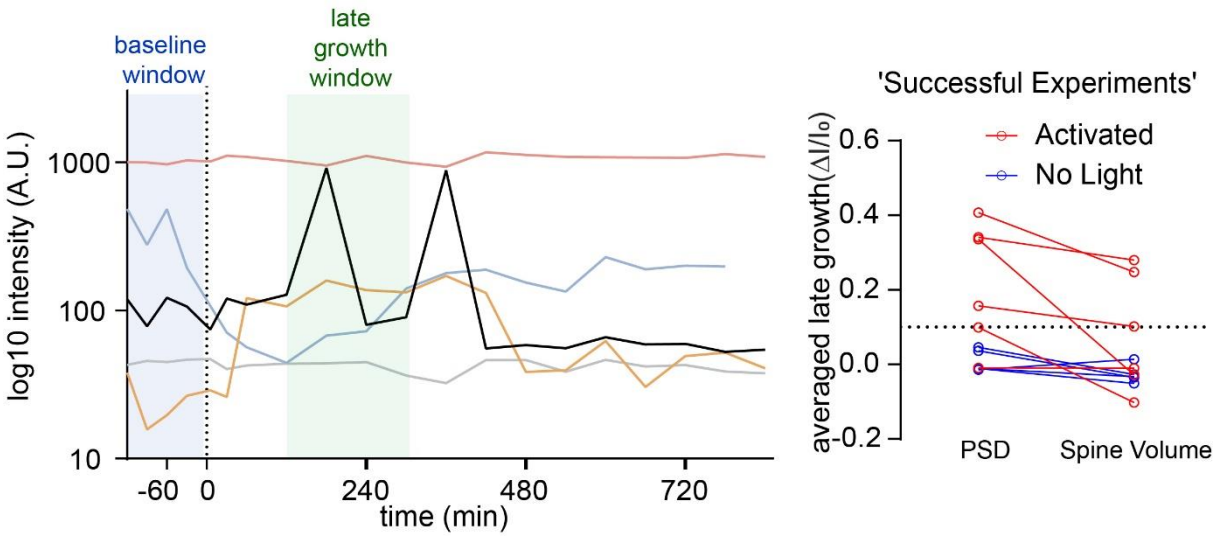

Supplement figure 4: Late growth calculation
Left: The baseline (blue window) and 2 to 5 hours after stimulation (green window) was used to calculate late growth. Right:In 4 out of 6 paCaMKII activated experiments (red), their average PSDs developed over 110% of late growth (late growth > 0.1) and considered as successful, although the spine volume alterations are more variable . These 4 experiments were kept for the analysis in Fig.45.

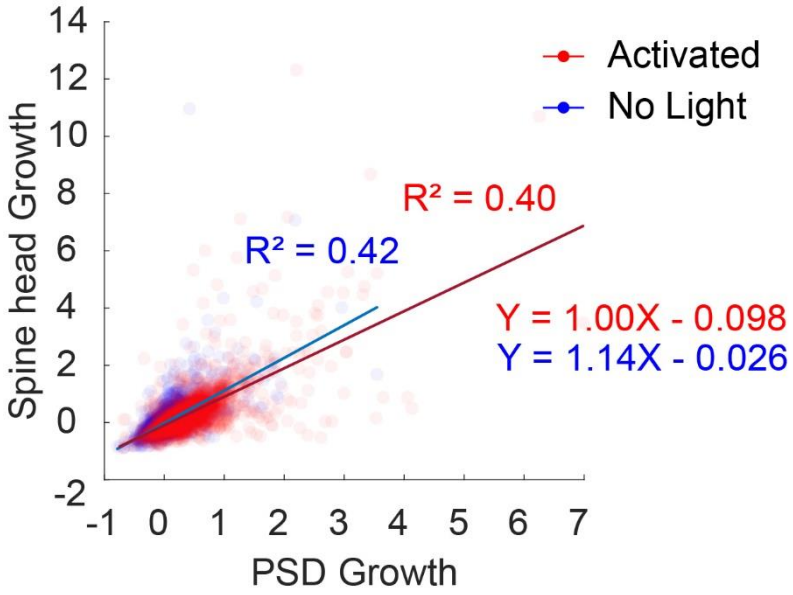

Supplement figure 5: The correlation of PSD vs spine head growth.
N = 4 activated neurons (2433 synapses), 5 control neurons (2953 synapses).

4.2 Statistics Table

Table 7: Statistics.

Figure	Group	n	test	Post-hoc multiple comparisons
Fig. 27a	paired vs upaired	15, 16.	Unpaired t-test, P = 0.2532.	na
Fig. 27c	paired vs upaired	7, 9.	Unpaired t-test, P = 0.0009.	na
Fig. 30c (1)	causal: NT, CheRiff, CheRiff + paAIP2, across time	8, 15, 15.	Two-way ANOVA. Time, F (2.378, 83.23) = 2.946, P = 0.0491; genotype, F (2, 35) = 0.9579, P = 0.3935; Interaction, F (8, 140) = 2.046, P = 0.0453.	Dunnett's, compared to NT as control. 5 min, 15 min, 25 min: NT vs. CheRiff, P = 0.9818, 0.7825, 0.0246. NT vs. PaAIP2, P = 0.1052, 0.9084, 0.4045.
Fig. 30c (2)	anti-causal: NT, CheRiff, CheRiff + paAIP2, across time	7, 7, 7.	Two-way ANOVA. Time, F (2.246, 40.43) = 3.383, P = 0.0388; genotype, F (2, 18) = 3.986, P = 0.0369; Interaction, F (8, 72) = 1.976, P = 0.0617.	Dunnett's, compared to NT as control. 5 min, 15 min, 25 min: NT vs. CheRiff, P = 0.6350, 0.2265, 0.0449. NT vs. PaAIP2, P = 0.8764, 0.5428, 0.9998.
Fig. 30d	Causal vs anti-causal at 25minutes: CheRiff, CheRiff + paAIP2, NT.	15, 7, 15, 7, 8, 7.	Unpaired t-test, CheRiff, P = 0.0002; CheRiff + paAIP2, P = 0.5805; NT, P = 0.2610.	na
Fig. 31b	paAIP2 vs NT	12, 12.	Paired t-test, P = 0.5857.	na

Fig. 31d	paAIP2 vs NT at across time.	10, 7.	Two-way ANOVA. Time, F (2.332, 37.31) = 2.172, P = 0.1209; genotype, F (1, 16) = 1.156, P = 0.2983; Interaction, F (4, 64) = 1.053, P = 0.3870.	Šídák's multiple comparisons at 5 min, 15 min, 25 min: P = 0.9051, > 0.9999, 0.5460.
Fig. 33	CheRiff vs CheRiff + paAIP2 in causal, anti-causal paired and unpaired.	11, 15, 13, 14, 11, 14.	Unpaired t-test, causal, P = 0.3382; anti-causal, P = 0.0034; unpaired, P = 0.9764.	na
Fig. 34	CheRiff vs CheRiff + paAIP2, with ZIP or scr-ZIP.	10, 13, 11, 7.	Two-way ANOVA, ZIP: F (1, 37) = 10.86, P = 0.0022; genotype: F (1, 37) = 0.01063, P = 0.9184; interaction: F (1, 37) = 0.3234, P = 0.5730.	ZIP, CheRiff vs CheRiff + paAIP2, P = 0.6251; scr-ZIP, CheRiff vs CheRiff + paAIP2: P = 0.7521; CheRiff, ZIP vs scr-ZIP, P = 0.0447; CheRiff vs CheRiff + paAIP2, P = 0.0146.
Fig. 35	ZIP vs scr-ZIP.	11,13; 10,12; 11,13; 11,12.	Mann-Whitney test, Vm: P = 0.6576; Vthreshold: P = 0.8587; #spikes: P = 0.0732; Cm: P = 0.8212.	na
Fig. 36c	CheRiff, CheRiff + paAIP2, positive control, negative control.	33, 47, 15, 17.	Kruskal-Wallis test, P < 0.0001.	Dunn's, CheRiff vs. paAIP, P = 0.4751; CheRiff vs. Pos Ctrl, P = 0.7217; CheRiff vs. Neg Ctrl, P = 0.0004; PaAIP vs. Pos Ctrl, P > 0.9999; PaAIP vs. Neg Ctrl, P < 0.0001; Pos Ctrl vs. Neg Ctrl P < 0.0001.
Fig. 37d	paAIP2 vs paAIP2+ ChrimsonR, at 0.1 Hz or 50 Hz, respectively.	103, 149, 56, 64.	Mann-Whitney test, 0.1 Hz, P < 0.0001; 50 Hz, P = 0.0651	na
Fig. 38d (left)	paCaMKII vs control and paCaMKII + CPPene vs control, across time.	16, 16, 14.	Two-way ANOVA. Time, F (2.401, 103.2) = 10.51, P < 0.0001; genotype, F (2, 43) = 11.19, P = 0.0001; Interaction, F (8, 172) = 5.982, P < 0.0001.	Dunnett's, paCaMKII vs control at: 5min, P = 0.0009, 15 min, P = 0.0035. 25min, P = 0.0003; paCaMKII + CPPene vs control at 5 min, P = 0.0030, 15 min, P = 0.0031, 25 min, P = 0.0362.
Fig. 40a	paCaMKII vs control over time.	9, 7	Mixed-effects model (REML). Time, F (20, 219) = 6.484, P < 0.0001; optical stimulation, F (1, 14) = 12.09, P = 0.0037; Interaction, F (20, 219) = 3.281, P < 0.0001.	Šídák's, multiple comparisons P values from baseline (x4) to post stimulation effects (x16): 0.701, 0.8283, 0.829, 0.7003, 0.1278, 0.0551, 0.0195, 0.0018, 0.0016, 0.0002, 0.0011, 0.0031, 0.0198, 0.0704, 0.0098, 0.003, 0.0115, 0.0104, 0.0004, 0.0001
Fig.40b (as Fig. 40d, left),1	paCaMKII activated, baseline vs 0 to 120 minutes after stimulation	2948	Kolmogorov-Smirnov test, P < 0.0001, D = 0.1629.	na
Fig.40b (as Fig. 40d, left), 2	paCaMKII activated, baseline vs 180 to 840 minutes after stimulation	2948	Kolmogorov-Smirnov test, P < 0.0001, D = 0.2956.	na
Fig.40c (as Fig. 40d, right), 1	No stimulation, baseline vs 0 to 120 minutes after time 0.	2953	Kolmogorov-Smirnov test, P = 0.8838, D = 0.01524.	na
Fig.40c (as Fig. 40d, right), 2	No stimulation, baseline vs 180 to 840 minutes after time 0.	2953	Kolmogorov-Smirnov test, P < 0.0001, D = 0.1351.	na
Fig. 40e	paCaMKII vs control over time.	9,7	Mixed-effects model (REML). Time, F (3.304, 37.17) = 0.9636, P = 0.4266; optical stimulation, F (1, 14) = 5.928, P = 0.0289; Interaction, F (20, 225) = 2.266, P = 0.0021.	Šídák's, multiple comparisons P values from baseline (x4) to post stimulation effects (x16): 0.3865, 0.985, 0.5586, 0.5802, 0.0051, 0.0088, 0.0074, 0.0403, 0.0757, 0.0251, 0.2271, 0.2277, 0.4504, 0.5876, 0.3401, 0.4132, 0.2809, 0.1753, 0.0812, 0.2269
Fig.40f (as Fig. 40h, left), 1	paCaMKII activated, baseline vs 0 to 120 minutes after	2948	Kolmogorov-Smirnov test, P < 0.0001, D = 0.06874.	na

	stimulation			
Fig.40f (as Fig. 40h, left), 2	paCaMKII activated, baseline vs 180 to 840 minutes after stimulation	2948	Kolmogorov-Smirnov test, P < 0.0001, D = 0.08940.	na
Fig.40g (as Fig. 40h, right), 1	No stimulation, baseline vs 0 to 120 minutes after time 0.	2953	Kolmogorov-Smirnov test, P = 0.2208, D = 0.02719.	na
Fig.40g (as Fig. 40h, right), 2	No stimulation, baseline vs 180 to 840 minutes after time 0.	2953	Kolmogorov-Smirnov test, P = 0.4975, D = 0.02148.	na
Fig.41	paCaMKII activated vs control over time.	9, 7	Mixed-effects model (REML). Time, F (20, 225) = 5.428, P < 0.0001; optical stimulation, F (1, 14) = 3.063, P = 0.1020; Interaction, F (20, 225) = 1.490, P = 0.0861.	Šídák's, multiple comparisons P values from baseline (x4) to post stimulation effects (x16): 0.8389, 0.9229, 0.8848, 0.8767, 0.8377, 0.7565, 0.5832, 0.3419, 0.3094, 0.1662, 0.0655, 0.0617, 0.0586, 0.0823, 0.0454, 0.0156, 0.0544, 0.1106, 0.037, 0.0162.
Fig.45c and f	PSD or spine volume, paCaMKII activated vs control in different bins	Small to big, activated: 608, 608, 609, 608; control:738, 738, 739, 738.	Mann-Whitney test, for all the bin centers: P < 0.0001	
Fig.46 (left)	paCaMKII vs control over time.	9, 7	Mixed-effects model (REML), time, F (1.541, 20.80) = 1.862, P = 0.1854; optical stimulation, F (1, 14) = 2.186, P = 0.1614; Interaction, F (4, 54) = 2.106, P= 0.0926.	60 min, 240 min, 420 min: P = 0.2028, 0.0908, 0.7425.
Fig.46 (right)	paCaMKII vs control over time.	9,7	Mixed-effects model (REML), time, F (1.889, 25.51) = 1.310, P = 0.2862; optical stimulation, F (1, 14) = 1.303, P = 0.2727; Interaction, F (4, 54) = 0.6269, P = 0.6454.	60 min, 240 min, 420 min: P = 0.1289, 0.3153, 0.5444.
Fig. 48b (left)	PSD: paCaMKII vs control, high or low CV spines	180, 180, 140, 140	Two-way ANOVA, optical stimulation, F (1, 636) = 3.226, P = 0.2031; H/L, F (1, 636) = 2588, P < 0.0001; Interaction F (1, 636) = 1.623, P = 0.0729.	Fig. 45 f (left)
Fig. 48b (right)	Spine volume: paCaMKII vs control, high or low CV spines	180, 180, 140, 140	Two-way ANOVA, optical stimulation, F (1, 636) = 4.556, P = 0.0332; H/L, F (1, 636) = 2248, P < 0.0001; Interaction F (1, 636) = 0.02965, P = 0.8634.	Fig. 45 f (right)
Fig. 48c (left)	PSD: paCaMKII vs control, high or low CV cluster	180, 180, 140, 140	Two-way ANOVA, optical stimulation, F (1, 636) = 1.514, P = 0.2190; H/L, F (1, 636) = 33.81, P < 0.0001; Interaction F (1, 636) = 2.456, P = 0.1176.	Fisher's multiple comparisions, High CV cluster: paCaMKII vs control, P = 0.0483; Low CV cluster: paCaMKII vs control, P = 0.8118; paCaMKII activated: H vs L, P< 0.0001; control: H vs L: P = 0.0048.
Fig. 48c (right)	Spine volume: paCaMKII vs control, high or low CV cluster	180, 180, 140, 140	Two-way ANOVA, optical stimulation, F (1, 636) = 9.104, P = 0.0027; H/L, F (1, 636) = 28.99, P < 0.0001; Interaction F (1, 636) = 0.8931, P = 0.3450.	Fisher's multiple comparisions, High CV cluster: paCaMKII vs control, P = 0.2433; Low CV cluster: paCaMKII vs control, P = 0.0052; paCaMKII activated: H vs L, P < 0.0001; control: H vs L: P= 0.0032.
Fig. 49b (left)	PSD: paCaMKII vs control, high or low slope spines	180, 180, 140, 140	Two-way ANOVA, optical stimulation, F (1, 636) = 47.85, P < 0.0001; H/L, F (1, 636) = 888.7, P < 0.0001; Interaction F (1, 636) = 47.65, P < 0.0001.	Fisher's multiple comparisions, High slope spines: paCaMKII vs control, P < 0.0001; Low slope spines: paCaMKII vs control, P < 0.7175; paCaMKII activated: H vs L, P < 0.0001; control: H vs L: P < 0.0001.
Fig. 49b (right)	Spine volume: paCaMKII vs control, high or low slope spines	180, 180, 140, 140	Two-way ANOVA, optical stimulation, F (1, 636) = 15.23, P= 0.0001; H/L, F (1, 636) = 561.6, P< 0.0001; Interaction F (1, 636) =15,23, P= 0.0010.	Fisher's multiple comparisions, High slope spines: paCaMKII vs control, P < 0.0001; Low slope spines: paCaMKII vs control, P < 0.6731; paCaMKII activated: H vs L, P < 0.0001; control: H vs L: P < 0.0001.

Fig. 49c (left)	PSD: paCaMKII vs control, high or low slope cluster	180, 180, 140, 140	Two-way ANOVA, optical stimulation, F (1, 636) = 151.3, P < 0.0001; H/L, F (1, 636) = 7.443, P = 0.0065; Interaction F (1, 636) = 0.2190, P = 0.6399.	Fisher's multiple comparisions, High slope cluster: paCaMKII vs control, P < 0.0001; Low slope cluster: paCaMKII vs control, P< 0.0001; paCaMKII activated: H vs L, P= 0.0160; control: H vs L: P= 0.1324.
Fig. 49c (right)	Spine volume: paCaMKII vs control, high or low slope cluster	180, 180, 140, 140	Two-way ANOVA, optical stimulation, F (1, 636) = 84.23, P< 0.0001; H/L, F (1, 636) = 4.990, P= 0.0258; Interaction F (1, 636) = 0.1427, P = 0.7057.	Fisher's multiple comparisions, High slope cluster: paCaMKII vs control, P < 0.0001; Low slope cluster: paCaMKII vs control, P < 0.0001; paCaMKII activated: H vs L, P = 0.0488; control: H vs L: P = 0.2164.
Fig. 51: apical spines	paCaMKII vs control	8, 3, 8, 3, 8,3, 8, 3, 7, 3	Mann-Whitney test, from left to right: P = 0.0848, 0.1939, 0.2788, 0.01333, 0.5167.	na
Fig. 51: basal spines	paCaMKII vs control	8, 9, 8, 9, 8, 9, 8, 9	Mann-Whitney test, from left to right: P = 0.6730, 0.0050, 0.2766, 0.0055, 0.9626.	na
Fig.52 (b): apical spines	paCaMKII vs control	2, 3, 2, 3	Mann-Whitney test, from left to right: P = 0.4000, 0.8000.	na
Fig. 52 (b): basal spines	paCaMKII vs control	5, 9, 5, 9	Mann-Whitney test, from left to right: P = 0.0020, 0.0005.	na
Fig. 53	paCaMKII vs control, in day 1 or day 2 (independently)	13, 12; 15, 5	Unpaired t-test. Day 1: P = 0.0718. Day 2: P = 0.7337	na
Fig.54 (b)	paCaMKII vs paCaMKII (TTX) vs positive control vs negative control	76, 71, 104, 52	Kruskal-Wallis test, P < 0.0001.	Dunn's multiple comparisions: paCaMKII vs negative control: P = 0.3533; paCaMKII (TTX) vs negative control: P = 0.4104; paCaMKII vs positive control: P < 0.0001; paCaMKII (TTX) vs positive control: P= 0.0006; paCaMKII vs paCaMKII (TTX), P > 0.9999; positive control vs negative control, P < 0.0001.
Fig. 60 (d)	20-25 minutes post-stimulation vs baseline	4, 4	Paired t-test, P = 0.0444	na

References

Alberini, C. M. (2009). Transcription Factors in Long-Term Memory and Synaptic Plasticity. *Physiological Reviews*, *89*(1), 10.1152/physrev.00017.2008. https://doi.org/10.1152/physrev.00017.2008

Andrade-Talavera, Y., Fisahn, A., & Rodríguez-Moreno, A. (2023). Timing to be precise? An overview of spike timing-dependent plasticity, brain rhythmicity, and glial cells interplay within neuronal circuits. *Molecular Psychiatry*, *28*(6), 2177–2188. https://doi.org/10.1038/s41380-023-02027-w

Anisimova, M. (2020). *Investigating the long-term effects of spike-timing-dependent plasticity and the activity-dependence of cFos expression in hippocampal pyramidal neurons using optogenetics* [doctoralThesis, Staats- und Universitätsbibliothek Hamburg Carl von Ossietzky]. https://ediss.sub.uni-hamburg.de/handle/ediss/8763

Anisimova, M., Lamothe-Molina, P. J., Franzelin, A., Aberra, A. S., Hoppa, M. B., Gee, C. E., & Oertner, T. G. (2023). *Neuronal FOS reports synchronized activity of presynaptic neurons* (p. 2023.09.04.556168). bioRxiv. https://doi.org/10.1101/2023.09.04.556168

Anisimova, M., Van Bommel, B., Wang, R., Mikhaylova, M., Wiegert, J. S., Oertner, T. G., & Gee, C. E. (2022). Spike-timing-dependent plasticity rewards synchrony rather than causality. *Cerebral Cortex*, *33*(1), 23–34. https://doi.org/10.1093/cercor/bhac050

Araya, R., Vogels, T. P., & Yuste, R. (2014). Activity-dependent dendritic spine neck changes are correlated with synaptic strength. *Proceedings of the National Academy of Sciences*, *111*(28), E2895–E2904. https://doi.org/10.1073/pnas.1321869111

Ardestani, G., West, M. C., Maresca, T. J., Fissore, R. A., & Stratton, M. M. (2019). FRET-based sensor for CaMKII activity (FRESCA): A useful tool for assessing CaMKII activity in response to Ca2+ oscillations in live cells. *Journal of Biological Chemistry*, *294*(31), 11876–11891. https://doi.org/10.1074/jbc.RA119.009235

Arellano, J. I., Benavides-Piccione, R., Defelipe, J., & Yuste, R. (2007). Ultrastructure of dendritic spines: Correlation between synaptic and spine morphologies. *Frontiers in Neuroscience*, *1*(1), 131–143. https://doi.org/10.3389/neuro.01.1.1.010.2007

Arshadi, C., Günther, U., Eddison, M., Harrington, K. I. S., & Ferreira, T. A. (2021). SNT: A unifying toolbox for quantification of neuronal anatomy. *Nature Methods*, *18*(4), Article 4. https://doi.org/10.1038/s41592-021-01105-7

Artola, A., Bröcher, S., & Singer, W. (1990). Different voltage-dependent thresholds for inducing long-term depression and long-term potentiation in slices of rat visual cortex. *Nature*, *347*(6288), 69–72. https://doi.org/10.1038/347069a0

Ayuso-Jimeno, I. P., Ronchi, P., Wang, T., Gallori, C. E., & Gross, C. T. (2022). Identifying long-range synaptic inputs using genetically encoded labels and volume electron microscopy. *Scientific Reports*, *12*(1), Article 1. https://doi.org/10.1038/s41598-022-14309-4

Aziz, W., Kraev, I., Mizuno, K., Kirby, A., Fang, T., Rupawala, H., Kasbi, K., Rothe, S., Jozsa, F., Rosenblum, K., Stewart, M. G., & Giese, K. P. (2019). Multi-input Synapses, but Not LTP-Strengthened Synapses, Correlate with Hippocampal Memory Storage in Aged Mice. *Current Biology*, *29*(21), 3600-3610.e4. https://doi.org/10.1016/j.cub.2019.08.064

Barcomb, K., Coultrap, S. J., & Bayer, K. U. (2013). Enzymatic Activity of CaMKII Is Not Required for Its Interaction with the Glutamate Receptor Subunit GluN2B. *Molecular Pharmacology*, *84*(6), 834–843. https://doi.org/10.1124/mol.113.089045

Barcomb, K., Hell, J. W., Benke, T. A., & Bayer, K. U. (2016). The CaMKII/GluN2B Protein Interaction Maintains Synaptic Strength*. *Journal of Biological Chemistry*, *291*(31), 16082–16089. https://doi.org/10.1074/jbc.M116.734822

Barria, A., & Malinow, R. (2005). NMDA receptor subunit composition controls synaptic plasticity by regulating binding to CaMKII. *Neuron*, *48*(2), 289–301. https://doi.org/10.1016/j.neuron.2005.08.034

Bats, C., Groc, L., & Choquet, D. (2007). The Interaction between Stargazin and PSD-95 Regulates AMPA Receptor Surface Trafficking. *Neuron*, *53*(5), 719–734. https://doi.org/10.1016/j.neuron.2007.01.030

Bayer, K. U., LeBel, E., McDonald, G. L., O'Leary, H., Schulman, H., & De Koninck, P. (2006). Transition from reversible to persistent binding of CaMKII to postsynaptic sites and NR2B. *The Journal of Neuroscience: The Official Journal of the Society for Neuroscience*, *26*(4), 1164–1174. https://doi.org/10.1523/JNEUROSCI.3116-05.2006

Bayer, K.-U., De Koninck, P., Leonard, A. S., Hell, J. W., & Schulman, H. (2001). Interaction with the NMDA receptor locks CaMKII in an active conformation. *Nature*, *411*(6839), 801–805. https://doi.org/10.1038/35081080

Bear, M. F. (1999). Homosynaptic long-term depression: A mechanism for memory? *Proceedings of the National Academy of Sciences of the United States of America*, *96*(17), 9457–9458.

Bennett, M. K., Erondu, N. E., & Kennedy, M. B. (1983). Purification and characterization of a calmodulin-dependent protein kinase that is highly concentrated in brain. *The Journal of Biological Chemistry*, *258*(20), 12735–12744.

Berretta, N., Berton, F., Bianchi, R., Brunelli, M., Capogna, M., & Francesconi, W. (1991). Long-term Potentiation of NMDA Receptor-mediated EPSP in Guinea-pig Hippocampal Slices. *The European Journal of Neuroscience*, *3*(9), 850–854. https://doi.org/10.1111/j.1460-9568.1991.tb00096.x

Bi, G., & Poo, M. (1998). Synaptic Modifications in Cultured Hippocampal Neurons: Dependence on Spike Timing, Synaptic Strength, and Postsynaptic Cell Type. *The Journal of Neuroscience*, *18*(24), 10464–10472. https://doi.org/10.1523/JNEUROSCI.18-24-10464.1998

Bi, G., & Poo, M. (2001). Synaptic Modification by Correlated Activity: Hebb's Postulate Revisited. *Annual Review of Neuroscience*, *24*(1), 139–166. https://doi.org/10.1146/annurev.neuro.24.1.139

Bishop, D., Nikić, I., Brinkoetter, M., Knecht, S., Potz, S., Kerschensteiner, M., & Misgeld, T. (2011). Near-infrared branding efficiently correlates light and electron microscopy. *Nature Methods*, *8*(7), Article 7. https://doi.org/10.1038/nmeth.1622

Blankenship, A. G., & Feller, M. B. (2010). Mechanisms underlying spontaneous patterned activity in developing neural circuits. *Nature Reviews Neuroscience*, *11*(1), 18–29. https://doi.org/10.1038/nrn2759

Bliss, T. V. P., & Collingridge, G. L. (1993). A synaptic model of memory: Long-term potentiation in the hippocampus. *Nature*, *361*(6407), 31–39. https://doi.org/10.1038/361031a0

Bliss, T. V. P., & Lømo, T. (1973). Long-lasting potentiation of synaptic transmission in the dentate area of the anaesthetized rabbit following stimulation of the perforant path. *The Journal of Physiology*, *232*(2), 331–356. https://doi.org/10.1113/jphysiol.1973.sp010273

Bloodgood, B. L., & Sabatini, B. L. (2005). Neuronal Activity Regulates Diffusion Across the Neck of Dendritic Spines. *Science*, *310*(5749), 866–869. https://doi.org/10.1126/science.1114816

Bloss, E. B., Cembrowski, M. S., Karsh, B., Colonell, J., Fetter, R. D., & Spruston, N. (2018). Single excitatory axons form clustered synapses onto CA1 pyramidal cell dendrites. *Nature Neuroscience*, *21*(3), 353–363. https://doi.org/10.1038/s41593-018-0084-6

Borczyk, M., Śliwińska, M. A., Caly, A., Bernas, T., & Radwanska, K. (2019). Neuronal plasticity affects correlation between the size of dendritic spine and its postsynaptic density. *Scientific Reports*, *9*(1), 1693. https://doi.org/10.1038/s41598-018-38412-7

Bortolotto, Z. A., & Collingridge, G. L. (1998). Involvement of calcium/calmodulin-dependent protein kinases in the setting of a molecular switch involved in hippocampal LTP. *Neuropharmacology*, *37*(4–5), 535–544. https://doi.org/10.1016/s0028-3908(98)00058-6

Bosch, M., Castro, J., Saneyoshi, T., Matsuno, H., Sur, M., & Hayashi, Y. (2014). Structural and Molecular Remodeling of Dendritic Spine Substructures during Long-Term Potentiation. *Neuron*, *82*(2), 444–459. https://doi.org/10.1016/j.neuron.2014.03.021

Bromer, C., Bartol, T. M., Bowden, J. B., Hubbard, D. D., Hanka, D. C., Gonzalez, P. V., Kuwajima, M., Mendenhall, J. M., Parker, P. H., Abraham, W. C., Sejnowski, T. J., & Harris, K. M. (2018). Long-term potentiation expands information content of hippocampal dentate gyrus synapses. *Proceedings of the National Academy of Sciences*, *115*(10), E2410–E2418. https://doi.org/10.1073/pnas.1716189115

Brown, C. N., & Bayer, K. U. (2024). Studying CaMKII: Tools and standards. *Cell Reports*, *43*(4). https://doi.org/10.1016/j.celrep.2024.113982

Buard, I., Coultrap, S. J., Freund, R. K., Lee, Y.-S., Dell'Acqua, M. L., Silva, A. J., & Bayer, K. U. (2010). CaMKII 'autonomy' is required for initiating but not for maintaining neuronal long-term information storage. *The Journal of Neuroscience: The Official Journal of the Society for Neuroscience*, *30*(24), 8214–8220. https://doi.org/10.1523/JNEUROSCI.1469-10.2010

Burgin, K. E., Waxham, M. N., Rickling, S., Westgate, S. A., Mobley, W. C., & Kelly, P. T. (1990). In situ hybridization histochemistry of Ca2+/calmodulin-dependent protein kinase in developing rat brain. *Journal of Neuroscience*, *10*(6), 1788–1798. https://doi.org/10.1523/JNEUROSCI.10-06-01788.1990

Buzsáki, G., & Mizuseki, K. (2014). The log-dynamic brain: How skewed distributions affect network operations. *Nature Reviews Neuroscience*, *15*(4), 264–278. https://doi.org/10.1038/nrn3687

Cao, G., & Harris, K. M. (2012). Developmental regulation of the late phase of long-term potentiation (L-LTP) and metaplasticity in hippocampal area CA1 of the rat. *Journal of Neurophysiology*, *107*(3), 902–912. https://doi.org/10.1152/jn.00780.2011

Caporale, N., & Dan, Y. (2008). Spike Timing–Dependent Plasticity: A Hebbian Learning Rule. *Annual Review of Neuroscience*, *31*(1), 25–46. https://doi.org/10.1146/annurev.neuro.31.060407.125639

Cardona, A., Saalfeld, S., Schindelin, J., Arganda-Carreras, I., Preibisch, S., Longair, M., Tomancak, P., Hartenstein, V., & Douglas, R. J. (2012). TrakEM2 Software for Neural Circuit Reconstruction. *PLOS ONE*, *7*(6), e38011. https://doi.org/10.1371/journal.pone.0038011

Carroll, R. C., Beattie, E. C., von Zastrow, M., & Malenka, R. C. (2001). Role of AMPA receptor endocytosis in synaptic plasticity. *Nature Reviews. Neuroscience*, *2*(5), 315–324. https://doi.org/10.1038/35072500

Castillo, P. E. (2012). Presynaptic LTP and LTD of excitatory and inhibitory synapses. *Cold Spring Harbor Perspectives in Biology*, *4*(2), a005728. https://doi.org/10.1101/cshperspect.a005728

Chang, J.-Y., Nakahata, Y., Hayano, Y., & Yasuda, R. (2019). Mechanisms of Ca2+/calmodulin-dependent kinase II activation in single dendritic spines. *Nature Communications*, *10*(1), 2784. https://doi.org/10.1038/s41467-019-10694-z

Chang, J.-Y., Parra-Bueno, P., Laviv, T., Szatmari, E. M., Lee, S.-J. R., & Yasuda, R. (2017). CaMKII Autophosphorylation Is Necessary for Optimal Integration of Ca 2+ Signals during LTP Induction, but Not Maintenance. *Neuron*, *94*(4), 800-808.e4. https://doi.org/10.1016/j.neuron.2017.04.041

Chao, L. H., Stratton, M. M., Lee, I.-H., Rosenberg, O. S., Levitz, J., Mandell, D. J., Kortemme, T., Groves, J. T., Schulman, H., & Kuriyan, J. (2011). A mechanism for tunable autoinhibition in the structure of a human Ca2+/calmodulin-dependent kinase II holoenzyme. *Cell*, *146*(5), 732–745. https://doi.org/10.1016/j.cell.2011.07.038

Chen, X., Cai, Q., Zhou, J., Pleasure, S. J., Schulman, H., Zhang, M., & Nicoll, R. A. (2024). CaMKII autophosphorylation is the only enzymatic event required for synaptic memory. *Proceedings of the National Academy of Sciences*, *121*(26), e2402783121. https://doi.org/10.1073/pnas.2402783121

Chirillo, M. A., Waters, M. S., Lindsey, L. F., Bourne, J. N., & Harris, K. M. (2019). Local resources of polyribosomes and SER promote synapse enlargement and spine clustering after long-term potentiation in adult rat hippocampus. *Scientific Reports*, *9*(1), 3861. https://doi.org/10.1038/s41598-019-40520-x

Citri, A., & Malenka, R. C. (2008). Synaptic Plasticity: Multiple Forms, Functions, and Mechanisms. *Neuropsychopharmacology*, *33*(1), 18–41. https://doi.org/10.1038/sj.npp.1301559

Cook, S. G., Buonarati, O. R., Coultrap, S. J., & Bayer, K. U. (2021). CaMKII holoenzyme mechanisms that govern the LTP versus LTD decision. *Science Advances*, *7*(16), eabe2300. https://doi.org/10.1126/sciadv.abe2300

Coultrap, S. J., Freund, R. K., O'Leary, H., Sanderson, J. L., Roche, K. W., Dell'Acqua, M. L., & Bayer, K. U. (2014). Autonomous CaMKII Mediates Both LTP and LTD Using a Mechanism for Differential Substrate Site Selection. *Cell Reports*, *6*(3), 431–437. https://doi.org/10.1016/j.celrep.2014.01.005

Damstra, H. G., Mohar, B., Eddison, M., Akhmanova, A., Kapitein, L. C., & Tillberg, P. W. (2022). Visualizing cellular and tissue ultrastructure using Ten-fold Robust Expansion Microscopy (TREx). *eLife*, *11*, e73775. https://doi.org/10.7554/eLife.73775

Dan, Y., & Poo, M.-M. (2006). Spike timing-dependent plasticity: From synapse to perception. *Physiological Reviews*, *86*(3), 1033–1048. https://doi.org/10.1152/physrev.00030.2005

De Koninck, P., & Schulman, H. (1998). Sensitivity of CaM kinase II to the frequency of Ca2+ oscillations. *Science (New York, N.Y.)*, *279*(5348), 227–230. https://doi.org/10.1126/science.279.5348.227

De Simoni, A., Griesinger, C. B., & Edwards, F. A. (2003). Development of rat CA1 neurones in acute versus organotypic slices: Role of experience in synaptic morphology and activity. *The Journal of Physiology*, *550*(Pt 1), 135–147. https://doi.org/10.1113/jphysiol.2003.039099

Debanne, D., Gähwiler, B. H., & Thompson, S. M. (1998). Long-term synaptic plasticity between pairs of individual CA3 pyramidal cells in rat hippocampal slice cultures. *The Journal of Physiology*, *507*(1), 237–247. https://doi.org/10.1111/j.1469-7793.1998.237bu.x

Denk, W., Strickler, J. H., & Webb, W. W. (1990). Two-Photon Laser Scanning Fluorescence Microscopy. *Science*, *248*(4951), 73–76. https://doi.org/10.1126/science.2321027

Derkach, V., Barria, A., & Soderling, T. R. (1999). Ca2+/calmodulin-kinase II enhances channel conductance of alpha-amino-3-hydroxy-5-methyl-4-isoxazolepropionate type glutamate receptors. *Proceedings of the National Academy of Sciences of the United States of America*, *96*(6), 3269–3274. https://doi.org/10.1073/pnas.96.6.3269

Dingledine, R., Borges, K., Bowie, D., & Traynelis, S. F. (1999). The glutamate receptor ion channels. *Pharmacological Reviews*, *51*(1), 7–61.

D.o Hebb. (1949). *The Organization Of Behavior*. http://archive.org/details/in.ernet.dli.2015.226341

Dudek, S. M., & Bear, M. F. (1992). Homosynaptic long-term depression in area CA1 of hippocampus and effects of N-methyl-D-aspartate receptor blockade. *Proceedings of the National Academy of Sciences*, *89*(10), 4363–4367. https://doi.org/10.1073/pnas.89.10.4363

Eggl, M. F., Chater, T. E., Petkovic, J., Goda, Y., & Tchumatchenko, T. (2023). Linking spontaneous and stimulated spine dynamics. *Communications Biology*, *6*(1), 1–13. https://doi.org/10.1038/s42003-023-05303-1

Ehrlich, I., & Malinow, R. (2004). Postsynaptic Density 95 controls AMPA Receptor Incorporation during Long-Term Potentiation and Experience-Driven Synaptic Plasticity. *Journal of Neuroscience*, *24*(4), 916–927. https://doi.org/10.1523/JNEUROSCI.4733-03.2004

El-Boustani, S., Ip, J. P. K., Breton-Provencher, V., Knott, G. W., Okuno, H., Bito, H., & Sur, M. (2018). Locally coordinated synaptic plasticity of visual cortex neurons in vivo. *Science*, *360*(6395), 1349–1354. https://doi.org/10.1126/science.aao0862

Fiala, J. C., Kirov, S. A., Feinberg, M. D., Petrak, L. J., George, P., Goddard, C. A., & Harris, K. M. (2003). Timing of neuronal and glial ultrastructure disruption during brain slice preparation and recovery in vitro. *Journal of Comparative Neurology*, *465*(1), 90–103. https://doi.org/10.1002/cne.10825

Fifková, E., & Van Harreveld, A. (1977). Long-lasting morphological changes in dendritic spines of dentate granular cells following stimulation of the entorhinal area. *Journal of Neurocytology*, *6*(2), 211–230. https://doi.org/10.1007/BF01261506

Fonnum, F. (1984). Glutamate: A neurotransmitter in mammalian brain. *Journal of Neurochemistry*, *42*(1), 1–11. https://doi.org/10.1111/j.1471-4159.1984.tb09689.x

Franks, K. M., Stevens, C. F., & Sejnowski, T. J. (2003). Independent sources of quantal variability at single glutamatergic synapses. *The Journal of Neuroscience: The Official Journal of the Society for Neuroscience*, *23*(8), 3186–3195. https://doi.org/10.1523/JNEUROSCI.23-08-03186.2003

Frey, U., & Morris, R. G. M. (1997). Synaptic tagging and long-term potentiation. *Nature*, *385*(6616), 533–536. https://doi.org/10.1038/385533a0

Gähwiler, B. H., Capogna, M., Debanne, D., McKinney, R. A., & Thompson, S. M. (1997). Organotypic slice cultures: A technique has come of age. *Trends in Neurosciences*, *20*(10), 471–477. https://doi.org/10.1016/S0166-2236(97)01122-3

Garaschuk, O., Hanse, E., & Konnerth, A. (1998). Developmental profile and synaptic origin of early network oscillations in the CA1 region of rat neonatal hippocampus. *The Journal of Physiology*, *507*(1), 219–236. https://doi.org/10.1111/j.1469-7793.1998.219bu.x

Gee, C. E., Ohmert, I., Wiegert, J. S., & Oertner, T. G. (2017). Preparation of Slice Cultures from Rodent Hippocampus. *Cold Spring Harbor Protocols*, *2017*(2), pdb.prot094888. https://doi.org/10.1101/pdb.prot094888

Geinisman, Y., Berry, R. W., Disterhoft, J. F., Power, J. M., & Zee, E. A. V. der. (2001). Associative Learning Elicits the Formation of Multiple-Synapse Boutons. *Journal of Neuroscience*, *21*(15), 5568–5573. https://doi.org/10.1523/JNEUROSCI.21-15-05568.2001

Giese, K. P., Fedorov, N. B., Filipkowski, R. K., & Silva, A. J. (1998a). Autophosphorylation at Thr286 of the alpha calcium-calmodulin kinase II in LTP and learning. *Science (New York, N.Y.)*, *279*(5352), 870–873. https://doi.org/10.1126/science.279.5352.870

Giese, K. P., Fedorov, N. B., Filipkowski, R. K., & Silva, A. J. (1998b). Autophosphorylation at Thr286 of the α Calcium-Calmodulin Kinase II in LTP and Learning. *Science*, *279*(5352), 870–873. https://doi.org/10.1126/science.279.5352.870

Göppert-Mayer, M. (1931). Über Elementarakte mit zwei Quantensprüngen. *Annalen Der Physik*, *401*(3), 273–294. https://doi.org/10.1002/andp.19314010303

Hacine-Gharbi, A., Ravier, P., Harba, R., & Mohamadi, T. (2012). Low bias histogram-based estimation of mutual information for feature selection. *Pattern Recognition Letters*, *33*(10), 1302–1308. https://doi.org/10.1016/j.patrec.2012.02.022

Hanson, P. I., Kapiloff, M. S., Lou, L. L., Rosenfeld, M. G., & Schulman, H. (1989). Expression of a multifunctional Ca2+/calmodulin-dependent protein kinase and mutational analysis of its autoregulation. *Neuron*, *3*(1), 59–70. https://doi.org/10.1016/0896-6273(89)90115-3

Hanson, P. I., & Schulman, H. (1992). Inhibitory autophosphorylation of multifunctional Ca2+/calmodulin-dependent protein kinase analyzed by site-directed mutagenesis. *Journal of Biological Chemistry*, *267*(24), 17216–17224. https://doi.org/10.1016/S0021-9258(18)41915-1

Harris, K. M. (2020). Structural LTP: From synaptogenesis to regulated synapse enlargement and clustering. *Current Opinion in Neurobiology*, *63*, 189–197. https://doi.org/10.1016/j.conb.2020.04.009

Harris, K. M., Kuwajima, M., Flores, J. C., & Zito, K. (2024). Synapse-specific structural plasticity that protects and refines local circuits during LTP and LTD. *Philosophical Transactions of the Royal Society B: Biological Sciences*, *379*(1906), 20230224. https://doi.org/10.1098/rstb.2023.0224

Harris, K., & Stevens, J. (1989). Dendritic spines of CA 1 pyramidal cells in the rat hippocampus: Serial electron microscopy with reference to their biophysical characteristics. *The Journal of Neuroscience*, *9*(8), 2982–2997. https://doi.org/10.1523/JNEUROSCI.09-08-02982.1989

Harvey, C. D., & Svoboda, K. (2007). Locally dynamic synaptic learning rules in pyramidal neuron dendrites. *Nature*, *450*(7173), 1195–1200. https://doi.org/10.1038/nature06416

Harvey, C. D., Yasuda, R., Zhong, H., & Svoboda, K. (2008). The Spread of Ras Activity Triggered by Activation of a Single Dendritic Spine. *Science*, *321*(5885), 136–140. https://doi.org/10.1126/science.1159675

Harward, S. C., Hedrick, N. G., Hall, C. E., Parra-Bueno, P., Milner, T. A., Pan, E., Laviv, T., Hempstead, B. L., Yasuda, R., & McNamara, J. O. (2016). Autocrine BDNF–TrkB signalling within a single dendritic spine. *Nature*, *538*(7623), Article 7623. https://doi.org/10.1038/nature19766

Häusser, M., Spruston, N., & Stuart, G. J. (2000). Diversity and dynamics of dendritic signaling. *Science (New York, N.Y.)*, *290*(5492), 739–744. https://doi.org/10.1126/science.290.5492.739

Hazan, L., & Ziv, N. E. (2020). Activity Dependent and Independent Determinants of Synaptic Size Diversity. *The Journal of Neuroscience: The Official Journal of the Society for Neuroscience*, *40*(14), 2828–2848. https://doi.org/10.1523/JNEUROSCI.2181-19.2020

Herring, B. E., & Nicoll, R. A. (2016). Long-Term Potentiation: From CaMKII to AMPA Receptor Trafficking. *Annual Review of Physiology*, *78*(1), 351–365. https://doi.org/10.1146/annurev-physiol-021014-071753

Hirokawa, N., Noda, Y., Tanaka, Y., & Niwa, S. (2009). Kinesin superfamily motor proteins and intracellular transport. *Nature Reviews Molecular Cell Biology*, *10*(10), 682–696. https://doi.org/10.1038/nrm2774

Hofer, S. B., Mrsic-Flogel, T. D., Bonhoeffer, T., & Hübener, M. (2009). Experience leaves a lasting structural trace in cortical circuits. *Nature*, *457*(7227), 313–317. https://doi.org/10.1038/nature07487

Holtmaat, A., Wilbrecht, L., Knott, G. W., Welker, E., & Svoboda, K. (2006). Experience-dependent and cell-type-specific spine growth in the neocortex. *Nature*, *441*(7096), 979–983. https://doi.org/10.1038/nature04783

Hopkins, C., Gibson, A., Stinchcombe, J., & Futter, C. (2000). Chimeric molecules employing horseradish peroxidase as reporter enzyme for protein localization in the electron microscope. *Methods in Enzymology*, *327*, 35–45. https://doi.org/10.1016/s0076-6879(00)27265-0

Horstmann, H., Vasileva, M., & Kuner, T. (2013). Photooxidation-Guided Ultrastructural Identification and Analysis of Cells in Neuronal Tissue Labeled with Green Fluorescent Protein. *PLOS ONE*, *8*(5), e64764. https://doi.org/10.1371/journal.pone.0064764

Hosokawa, T., Rusakov, D. A., Bliss, T. V., & Fine, A. (1995). Repeated confocal imaging of individual dendritic spines in the living hippocampal slice: Evidence for changes in length and orientation associated with chemically induced LTP. *The Journal of Neuroscience: The Official Journal of the Society for Neuroscience*, *15*(8), 5560–5573. https://doi.org/10.1523/JNEUROSCI.15-08-05560.1995

Hudmon, A., & Schulman, H. (2002). Structure-function of the multifunctional Ca2+/calmodulin-dependent protein kinase II. *The Biochemical Journal*, *364*(Pt 3), 593–611. https://doi.org/10.1042/BJ20020228

Humble, J., Hiratsuka, K., Kasai, H., & Toyoizumi, T. (2019). Intrinsic Spine Dynamics Are Critical for Recurrent Network Learning in Models With and Without Autism Spectrum Disorder. *Frontiers in Computational Neuroscience*, *13*, 38. https://doi.org/10.3389/fncom.2019.00038

Incontro, S., Díaz-Alonso, J., Iafrati, J., Vieira, M., Asensio, C. S., Sohal, V. S., Roche, K. W., Bender, K. J., & Nicoll, R. A. (2018). The CaMKII/NMDA receptor complex controls hippocampal synaptic transmission by kinase-dependent and independent mechanisms. *Nature Communications*, *9*(1), 2069. https://doi.org/10.1038/s41467-018-04439-7

Ishida, A., Kameshita, I., & Fujisawa, H. (1998). A novel protein phosphatase that dephosphorylates and regulates Ca2+/calmodulin-dependent protein kinase II. *The Journal of Biological Chemistry*, *273*(4), 1904–1910. https://doi.org/10.1074/jbc.273.4.1904

Jain, A., Nakahata, Y., Pancani, T., Watabe, T., Rusina, P., South, K., Adachi, K., Yan, L., Simorowski, N., Furukawa, H., & Yasuda, R. (2024). Dendritic, delayed, stochastic CaMKII activation in behavioural time scale plasticity. *Nature*, *635*(8037), 151–159. https://doi.org/10.1038/s41586-024-08021-8

Ji, Y., Li, B., Reed, T. D., Lorenz, J. N., Kaetzel, M. A., & Dedman, J. R. (2003). Targeted Inhibition of Ca2+/Calmodulin-dependent Protein Kinase II in Cardiac Longitudinal Sarcoplasmic Reticulum Results in Decreased Phospholamban Phosphorylation at Threonine 17*. *Journal of Biological Chemistry*, *278*(27), 25063–25071. https://doi.org/10.1074/jbc.M302193200

Joesch, M., Mankus, D., Yamagata, M., Shahbazi, A., Schalek, R., Suissa-Peleg, A., Meister, M., Lichtman, J. W., Scheirer, W. J., & Sanes, J. R. (2016). Reconstruction of genetically identified neurons imaged by serial-section electron microscopy. *eLife*, *5*, e15015. https://doi.org/10.7554/eLife.15015

Jourdain, P., Fukunaga, K., & Muller, D. (2003). Calcium/Calmodulin-Dependent Protein Kinase II Contributes to Activity-Dependent Filopodia Growth and Spine Formation. *Journal of Neuroscience*, *23*(33), 10645–10649. https://doi.org/10.1523/JNEUROSCI.23-33-10645.2003

Karbowski, J., & Urban, P. (2023). Information encoded in volumes and areas of dendritic spines is nearly maximal across mammalian brains. *Scientific Reports*, *13*(1), 22207. https://doi.org/10.1038/s41598-023-49321-9

Kasai, H., Fukuda, M., Watanabe, S., Hayashi-Takagi, A., & Noguchi, J. (2010). Structural dynamics of dendritic spines in memory and cognition. *Trends in Neurosciences*, *33*(3), 121–129. https://doi.org/10.1016/j.tins.2010.01.001

Kasai, H., Matsuzaki, M., Noguchi, J., Yasumatsu, N., & Nakahara, H. (2003). Structure–stability–function relationships of dendritic spines. *Trends in Neurosciences*, *26*(7), 360–368. https://doi.org/10.1016/S0166-2236(03)00162-0

Kastellakis, G., & Poirazi, P. (2019). Synaptic Clustering and Memory Formation. *Frontiers in Molecular Neuroscience*, *12*. https://doi.org/10.3389/fnmol.2019.00300

Kelleher, R. J., Govindarajan, A., & Tonegawa, S. (2004). Translational Regulatory Mechanisms in Persistent Forms of Synaptic Plasticity. *Neuron*, *44*(1), 59–73. https://doi.org/10.1016/j.neuron.2004.09.013

Kennedy, M. B., Bennett, M. K., & Erondu, N. E. (1983). Biochemical and immunochemical evidence that the 'major postsynaptic density protein' is a subunit of a calmodulin-dependent protein kinase. *Proceedings of the National Academy of Sciences of the United States of America*, *80*(23), 7357–7361. https://doi.org/10.1073/pnas.80.23.7357

Kerlin, A., Mohar, B., Flickinger, D., MacLennan, B. J., Dean, M. B., Davis, C., Spruston, N., & Svoboda, K. (2019). Functional clustering of dendritic activity during decision-making. *eLife*, *8*, e46966. https://doi.org/10.7554/eLife.46966

Khan, S., Reese, T. S., Rajpoot, N., & Shabbir, A. (2012). Spatiotemporal maps of CaMKII in dendritic spines. *Journal of Computational Neuroscience*, *33*(1), 123–139. https://doi.org/10.1007/s10827-011-0377-1

Knafo, S., Ariav, G., Barkai, E., & Libersat, F. (2004). Olfactory learning-induced increase in spine density along the apical dendrites of CA1 hippocampal neurons. *Hippocampus*, *14*(7), 819–825. https://doi.org/10.1002/hipo.10219

Koester, H. J., & Sakmann, B. (1998). Calcium dynamics in single spines during coincident pre- and postsynaptic activity depend on relative timing of back-propagating action potentials and subthreshold excitatory postsynaptic potentials. *Proceedings of the National Academy of Sciences of the United States of America*, *95*(16), 9596–9601. https://doi.org/10.1073/pnas.95.16.9596

Kopec, C. D., Li, B., Wei, W., Boehm, J., & Malinow, R. (2006). Glutamate Receptor Exocytosis and Spine Enlargement during Chemically Induced Long-Term Potentiation. *The Journal of Neuroscience*, *26*(7), 2000–2009. https://doi.org/10.1523/JNEUROSCI.3918-05.2006

Kristensen, A. S., Jenkins, M. A., Banke, T. G., Schousboe, A., Makino, Y., Johnson, R. C., Huganir, R., & Traynelis, S. F. (2011). Mechanism of Ca2+/calmodulin-dependent kinase II regulation of AMPA receptor gating. *Nature Neuroscience*, *14*(6), 727–735. https://doi.org/10.1038/nn.2804

Kuwajima, M., Ostrovskaya, O. I., Cao, G., Weisberg, S. A., Harris, K. M., & Zemelman, B. V. (2020). Ultrastructure of light-activated axons following optogenetic stimulation to produce late-phase long-term potentiation. *PLOS ONE*, *15*(1), e0226797. https://doi.org/10.1371/journal.pone.0226797

Lam, S. S., Martell, J. D., Kamer, K. J., Deerinck, T. J., Ellisman, M. H., Mootha, V. K., & Ting, A. Y. (2015). Directed evolution of APEX2 for electron microscopy and proteomics. *Nature Methods*, *12*(1), 51–54. https://doi.org/10.1038/nmeth.3179

Latham, A., & Paul, D. H. (1970). Climbing iibre responses of cerebellar Purkinje cells. *The Journal of Physiology*, *207*(2), 56P-57P.

LeBlancq, M. J., McKinney, T. L., & Dickson, C. T. (2016). ZIP It: Neural Silencing Is an Additional Effect of the PKM-Zeta Inhibitor Zeta-Inhibitory Peptide. *The Journal of Neuroscience*, *36*(23), 6193–6198. https://doi.org/10.1523/JNEUROSCI.4563-14.2016

Lee, H.-K., Takamiya, K., Han, J.-S., Man, H., Kim, C.-H., Rumbaugh, G., Yu, S., Ding, L., He, C., Petralia, R. S., Wenthold, R. J., Gallagher, M., & Huganir, R. L. (2003). Phosphorylation of the AMPA Receptor GluR1 Subunit Is Required for Synaptic Plasticity and Retention of Spatial Memory. *Cell*, *112*(5), 631–643. https://doi.org/10.1016/S0092-8674(03)00122-3

Lee, H.-K., Takamiya, K., He, K., Song, L., & Huganir, R. L. (2010). Specific roles of AMPA receptor subunit GluR1 (GluA1) phosphorylation sites in regulating synaptic plasticity in the CA1 region of hippocampus. *Journal of Neurophysiology*, *103*(1), 479–489. https://doi.org/10.1152/jn.00835.2009

Lee, J., Chen, X., & Nicoll, R. A. (2022). Synaptic memory survives molecular turnover. *Proceedings of the National Academy of Sciences*, *119*(42), e2211572119. https://doi.org/10.1073/pnas.2211572119

Lee, S.-J. R., Escobedo-Lozoya, Y., Szatmari, E. M., & Yasuda, R. (2009). Activation of CaMKII in single dendritic spines during long-term potentiation. *Nature*, *458*(7236), 299–304. https://doi.org/10.1038/nature07842

Lee, S.-J. R., & Yasuda, R. (2009). Spatiotemporal Regulation of Signaling in and out of Dendritic Spines: CaMKII and Ras. *The Open Neuroscience Journal*, *3*, 117–127. https://doi.org/10.2174/1874082000903020117

Levy, W. B., & Steward, O. (1983). Temporal contiguity requirements for long-term associative potentiation/depression in the hippocampus. *Neuroscience*, *8*(4), 791–797. https://doi.org/10.1016/0306-4522(83)90010-6

Lisman, J. (1989). A mechanism for the Hebb and the anti-Hebb processes underlying learning and memory. *Proceedings of the National Academy of Sciences of the United States of America*, *86*(23), 9574–9578. https://doi.org/10.1073/pnas.86.23.9574

Lisman, J. E., & Zhabotinsky, A. M. (2001). A model of synaptic memory: A CaMKII/PP1 switch that potentiates transmission by organizing an AMPA receptor anchoring assembly. *Neuron*, *31*(2), 191–201. https://doi.org/10.1016/s0896-6273(01)00364-6

Lisman, J., Schulman, H., & Cline, H. (2002). The molecular basis of CaMKII function in synaptic and behavioural memory. *Nature Reviews Neuroscience*, *3*(3), Article 3. https://doi.org/10.1038/nrn753

Lisman, J., Yasuda, R., & Raghavachari, S. (2012). Mechanisms of CaMKII action in long-term potentiation. *Nature Reviews Neuroscience*, *13*(3), 169–182. https://doi.org/10.1038/nrn3192

Lledo, P. M., Hjelmstad, G. O., Mukherji, S., Soderling, T. R., Malenka, R. C., & Nicoll, R. A. (1995). Calcium/calmodulin-dependent kinase II and long-term potentiation enhance synaptic transmission by the same mechanism. *Proceedings of the National Academy of Sciences of the United States of America*, *92*(24), 11175–11179. https://doi.org/10.1073/pnas.92.24.11175

Loewenstein, Y., Kuras, A., & Rumpel, S. (2011). Multiplicative Dynamics Underlie the Emergence of the Log-Normal Distribution of Spine Sizes in the Neocortex In Vivo. *Journal of Neuroscience*, *31*(26), 9481–9488. https://doi.org/10.1523/JNEUROSCI.6130-10.2011

Losonczy, A., & Magee, J. C. (2006). Integrative Properties of Radial Oblique Dendrites in Hippocampal CA1 Pyramidal Neurons. *Neuron*, *50*(2), 291–307. https://doi.org/10.1016/j.neuron.2006.03.016

Lüscher, C., & Malenka, R. C. (2012). NMDA Receptor-Dependent Long-Term Potentiation and Long-Term Depression (LTP/LTD). *Cold Spring Harbor Perspectives in Biology*, *4*(6), a005710. https://doi.org/10.1101/cshperspect.a005710

Lüscher, C., Nicoll, R. A., Malenka, R. C., & Muller, D. (2000). Synaptic plasticity and dynamic modulation of the postsynaptic membrane. *Nature Neuroscience*, *3*(6), 545–550. https://doi.org/10.1038/75714

Lysova, I., Spiegelhalter, C., Réal, E., Zgheib, S., Anton, H., & Mély, Y. (2018). ReAsH/tetracystein-based correlative light-electron microscopy for HIV-1 imaging during the early stages of infection. *Methods and Applications in Fluorescence*, *6*(4), 045001. https://doi.org/10.1088/2050-6120/aacec1

MacAskill, A. F., & Kittler, J. T. (2010). Control of mitochondrial transport and localization in neurons. *Trends in Cell Biology*, *20*(2), 102–112. https://doi.org/10.1016/j.tcb.2009.11.002

Magee, J. C., & Johnston, D. (1997). A synaptically controlled, associative signal for Hebbian plasticity in hippocampal neurons. *Science (New York, N.Y.)*, *275*(5297), 209–213. https://doi.org/10.1126/science.275.5297.209

Malenka, R. C. (1994). Synaptic plasticity in the hippocampus: LTP and LTD. *Cell*, *78*(4), 535–538. https://doi.org/10.1016/0092-8674(94)90517-7

Malenka, R. C. (2003). The long-term potential of LTP. *Nature Reviews Neuroscience*, *4*(11), 923–926. https://doi.org/10.1038/nrn1258

Malenka, R. C., & Bear, M. F. (2004). LTP and LTD: An embarrassment of riches. *Neuron*, *44*(1), 5–21. https://doi.org/10.1016/j.neuron.2004.09.012

Malenka, R. C., Kauer, J. A., Perkel, D. J., Mauk, M. D., Kelly, P. T., Nicoll, R. A., & Waxham, M. N. (1989). An essential role for postsynaptic calmodulin and protein kinase activity in long-term potentiation. *Nature*, *340*(6234), 554–557. https://doi.org/10.1038/340554a0

Malenka, R. C., & Nicoll, R. A. (1999). Long-term potentiation—A decade of progress? *Science (New York, N.Y.)*, *285*(5435), 1870–1874. https://doi.org/10.1126/science.285.5435.1870

Malinow, R., & Malenka, R. C. (2002). AMPA receptor trafficking and synaptic plasticity. *Annual Review of Neuroscience*, *25*, 103–126. https://doi.org/10.1146/annurev.neuro.25.112701.142758

Malinow, R., Schulman, H., & Tsien, R. W. (1989). Inhibition of postsynaptic PKC or CaMKII blocks induction but not expression of LTP. *Science (New York, N.Y.)*, *245*(4920), 862–866. https://doi.org/10.1126/science.2549638

Marchand, P., Becerril-Ortega, J., Mony, L., Bouteiller, C., Paoletti, P., Nicole, O., Barré, L., Buisson, A., & Perrio, C. (2012). Confocal microscopy imaging of NR2B-containing NMDA receptors based on fluorescent ifenprodil-like conjugates. *Bioconjugate Chemistry*, *23*(1), 21–26. https://doi.org/10.1021/bc100571g

Markram, H., Lübke, J., Frotscher, M., & Sakmann, B. (1997). Regulation of Synaptic Efficacy by Coincidence of Postsynaptic APs and EPSPs. *Science*, *275*(5297), 213–215. https://doi.org/10.1126/science.275.5297.213

Marsden, K. C., Shemesh, A., Bayer, K. U., & Carroll, R. C. (2010). Selective translocation of Ca2+/calmodulin protein kinase IIα (CaMKIIα) to inhibitory synapses. *Proceedings of the National Academy of Sciences*, *107*(47), 20559–20564. https://doi.org/10.1073/pnas.1010346107

Martell, J. D., Deerinck, T. J., Sancak, Y., Poulos, T. L., Mootha, V. K., Sosinsky, G. E., Ellisman, M. H., & Ting, A. Y. (2012). Engineered ascorbate peroxidase as a genetically-encoded reporter for electron microscopy. *Nature Biotechnology*, *30*(11), 1143–1148. https://doi.org/10.1038/nbt.2375

Matsuzaki, M., Ellis-Davies, G. C. R., Nemoto, T., Miyashita, Y., Iino, M., & Kasai, H. (2001). Dendritic spine geometry is critical for AMPA receptor expression in hippocampal CA1 pyramidal neurons. *Nature Neuroscience*, *4*(11), 1086–1092. https://doi.org/10.1038/nn736

Matsuzaki, M., Honkura, N., Ellis-Davies, G. C. R., & Kasai, H. (2004). Structural basis of long-term potentiation in single dendritic spines. *Nature*, *429*(6993), 761–766. https://doi.org/10.1038/nature02617

Mattison, H. A., Bagal, A. A., Mohammadi, M., Pulimood, N. S., Reich, C. G., Alger, B. E., Kao, J. P. Y., & Thompson, S. M. (2014). Evidence of calcium-permeable AMPA receptors in dendritic spines of CA1 pyramidal neurons. *Journal of Neurophysiology*, *112*(2), 263–275. https://doi.org/10.1152/jn.00578.2013

Medvedev, N. I., Dallérac, G., Popov, V. I., Rodriguez Arellano, J. J., Davies, H. A., Kraev, I. V., Doyère, V., & Stewart, M. G. (2014). Multiple spine boutons are formed after long-lasting LTP in the awake rat. *Brain Structure and Function*, *219*(1), 407–414. https://doi.org/10.1007/s00429-012-0488-0

Megías, M., Emri, Z., Freund, T. F., & Gulyás, A. I. (2001). Total number and distribution of inhibitory and excitatory synapses on hippocampal CA1 pyramidal cells. *Neuroscience*, *102*(3), 527–540. https://doi.org/10.1016/s0306-4522(00)00496-6

Meyer, D., Bonhoeffer, T., & Scheuss, V. (2014). Balance and Stability of Synaptic Structures during Synaptic Plasticity. *Neuron*, *82*(2), 430–443. https://doi.org/10.1016/j.neuron.2014.02.031

Meyer, T., Hanson, P. I., Stryer, L., & Schulman, H. (1992). Calmodulin trapping by calcium-calmodulin-dependent protein kinase. *Science (New York, N.Y.)*, *256*(5060), 1199–1202. https://doi.org/10.1126/science.256.5060.1199

Michalikova, M., Remme, M. W. H., Schmitz, D., Schreiber, S., & Kempter, R. (2019). Spikelets in pyramidal neurons: Generating mechanisms, distinguishing properties, and functional implications. *Reviews in the Neurosciences*, *31*(1), 101–119. https://doi.org/10.1515/revneuro-2019-0044

Mohajerani, M. H., & Cherubini, E. (2005). Spontaneous recurrent network activity in organotypic rat hippocampal slices. *European Journal of Neuroscience*, *22*(1), 107–118. https://doi.org/10.1111/j.1460-9568.2005.04198.x

Morgan, J. I., Cohen, D. R., Hempstead, J. L., & Curran, T. (1987). Mapping patterns of c-fos expression in the central nervous system after seizure. *Science (New York, N.Y.)*, *237*(4811), 192–197. https://doi.org/10.1126/science.3037702

Morris, R. G. M., Anderson, E., Lynch, G. S., & Baudry, M. (1986). Selective impairment of learning and blockade of long-term potentiation by an N-methyl-D-aspartate receptor antagonist, AP5. *Nature*, *319*(6056), 774–776. https://doi.org/10.1038/319774a0

Motta, A., Berning, M., Boergens, K. M., Staffler, B., Beining, M., Loomba, S., Hennig, P., Wissler, H., & Helmstaedter, M. (2019). Dense connectomic reconstruction in layer 4 of the somatosensory cortex. *Science*, *366*(6469), eaay3134. https://doi.org/10.1126/science.aay3134

Mulkey, R. M., Endo, S., Shenolikar, S., & Malenka, R. C. (1994). Involvement of a calcineurin/ inhibitor-1 phosphatase cascade in hippocampal long-term depression. *Nature*, *369*(6480), 486–488. https://doi.org/10.1038/369486a0

Mulkey, R. M., Herron, C. E., & Malenka, R. C. (1993). An essential role for protein phosphatases in hippocampal long-term depression. *Science (New York, N.Y.)*, *261*(5124), 1051–1055. https://doi.org/10.1126/science.8394601

Mulkey, R. M., & Malenka, R. C. (1992). Mechanisms underlying induction of homosynaptic long-term depression in area CA1 of the hippocampus. *Neuron*, *9*(5), 967–975. https://doi.org/10.1016/0896-6273(92)90248-C

Mullasseril, P., Dosemeci, A., Lisman, J. E., & Griffith, L. C. (2007). A structural mechanism for maintaining the 'on-state' of the CaMKII memory switch in the post-synaptic density. *Journal of Neurochemistry*, *103*(1), 357–364. https://doi.org/10.1111/j.1471-4159.2007.04744.x

Müller, W., & Connor, J. A. (1991). Dendritic spines as individual neuronal compartments for synaptic Ca2+ responses. *Nature*, *354*(6348), 73–76. https://doi.org/10.1038/354073a0

Murakami, G., Tsurugizawa, T., Hatanaka, Y., Komatsuzaki, Y., Tanabe, N., Mukai, H., Hojo, Y., Kominami, S., Yamazaki, T., Kimoto, T., & Kawato, S. (2006). Comparison between basal and apical dendritic spines in estrogen-induced rapid spinogenesis of CA1 principal neurons in the adult hippocampus. *Biochemical and Biophysical Research Communications*, *351*(2), 553–558. https://doi.org/10.1016/j.bbrc.2006.10.066

Murakoshi, H., Shin, M. E., Parra-Bueno, P., Szatmari, E. M., Shibata, A. C. E., & Yasuda, R. (2017). Kinetics of Endogenous CaMKII Required for Synaptic Plasticity Revealed by Optogenetic Kinase Inhibitor. *Neuron*, *94*(1), 37-47.e5. https://doi.org/10.1016/j.neuron.2017.02.036

Nevian, T., & Sakmann, B. (2006). Spine Ca2+ Signaling in Spike-Timing-Dependent Plasticity. *Journal of Neuroscience*, *26*(43), 11001–11013. https://doi.org/10.1523/JNEUROSCI.1749-06.2006

Nicoll, R. A., & Schulman, H. (2023). Synaptic memory and CaMKII. *Physiological Reviews*, *103*(4), 2877–2925. https://doi.org/10.1152/physrev.00034.2022

Nikonenko, I., Jourdain, P., & Muller, D. (2003). Presynaptic remodeling contributes to activity-dependent synaptogenesis. *The Journal of Neuroscience: The Official Journal of the Society for Neuroscience*, *23*(24), 8498–8505. https://doi.org/10.1523/JNEUROSCI.23-24-08498.2003

Nimchinsky, E. A., Yasuda, R., Oertner, T. G., & Svoboda, K. (2004). The number of glutamate receptors opened by synaptic stimulation in single hippocampal spines. *The Journal of Neuroscience: The Official Journal of the Society for Neuroscience*, *24*(8), 2054–2064. https://doi.org/10.1523/JNEUROSCI.5066-03.2004

Nishiyama, J., & Yasuda, R. (2015). Biochemical Computation for Spine Structural Plasticity. *Neuron*, *87*(1), 63–75. https://doi.org/10.1016/j.neuron.2015.05.043

Nishiyama, M., Hong, K., Mikoshiba, K., Poo, M. M., & Kato, K. (2000). Calcium stores regulate the polarity and input specificity of synaptic modification. *Nature*, *408*(6812), 584–588. https://doi.org/10.1038/35046067

Noguchi, J., Hayama, T., Watanabe, S., Ucar, H., Yagishita, S., Takahashi, N., & Kasai, H. (2016). State-dependent diffusion of actin-depolymerizing factor/cofilin underlies the enlargement and shrinkage of dendritic spines. *Scientific Reports*, *6*(1), 32897. https://doi.org/10.1038/srep32897

Noguchi, J., Matsuzaki, M., Ellis-Davies, G. C. R., & Kasai, H. (2005). Spine-Neck Geometry Determines NMDA Receptor-Dependent Ca2+ Signaling in Dendrites. *Neuron*, *46*(4), 609–622. https://doi.org/10.1016/j.neuron.2005.03.015

Noguchi, J., Nagaoka, A., Hayama, T., Ucar, H., Yagishita, S., Takahashi, N., & Kasai, H. (2019). Bidirectional in vivo structural dendritic spine plasticity revealed by two-photon glutamate uncaging in the mouse neocortex. *Scientific Reports*, *9*(1), 13922. https://doi.org/10.1038/s41598-019-50445-0

Nusser, Z., Lujan, R., Laube, G., Roberts, J. D. B., Molnar, E., & Somogyi, P. (1998). Cell Type and Pathway Dependence of Synaptic AMPA Receptor Number and Variability in the Hippocampus. *Neuron*, *21*(3), 545–559. https://doi.org/10.1016/S0896-6273(00)80565-6

O'Keefe, J., & Dostrovsky, J. (1971). The hippocampus as a spatial map. Preliminary evidence from unit activity in the freely-moving rat. *Brain Research*, *34*(1), 171–175. https://doi.org/10.1016/0006-8993(71)90358-1

Opazo, P., Labrecque, S., Tigaret, C. M., Frouin, A., Wiseman, P. W., De Koninck, P., & Choquet, D. (2010). CaMKII Triggers the Diffusional Trapping of Surface AMPARs through Phosphorylation of Stargazin. *Neuron*, *67*(2), 239–252. https://doi.org/10.1016/j.neuron.2010.06.007

Ostroff, L. E., Fiala, J. C., Allwardt, B., & Harris, K. M. (2002). Polyribosomes Redistribute from Dendritic Shafts into Spines with Enlarged Synapses during LTP in Developing Rat Hippocampal Slices. *Neuron*, *35*(3), 535–545. https://doi.org/10.1016/S0896-6273(02)00785-7

Otmakhov, N., Tao-Cheng, J.-H., Carpenter, S., Asrican, B., Dosemeci, A., Reese, T. S., & Lisman, J. (2004). Persistent accumulation of calcium/calmodulin-dependent protein kinase II in dendritic spines after induction of NMDA receptor-dependent chemical long-term potentiation. *The Journal of Neuroscience: The Official Journal of the Society for Neuroscience*, *24*(42), 9324–9331. https://doi.org/10.1523/JNEUROSCI.2350-04.2004

Patel, H., & Zamani, R. (2021). The role of PKMζ in the maintenance of long-term memory: A review. *Reviews in the Neurosciences*, *32*(5), 481–494. https://doi.org/10.1515/revneuro-2020-0105

Paulin, J. J. W., Haslehurst, P., Fellows, A. D., Liu, W., Jackson, J. D., Joel, Z., Cummings, D. M., & Edwards, F. A. (2016). Large and Small Dendritic Spines Serve Different Interacting Functions in Hippocampal Synaptic Plasticity and Homeostasis. *Neural Plasticity*, *2016*, 6170509. https://doi.org/10.1155/2016/6170509

Perez, J. D., Fusco, C. M., & Schuman, E. M. (2021). A Functional Dissection of the mRNA and Locally Synthesized Protein Population in Neuronal Dendrites and Axons. *Annual Review of Genetics*, *55*(Volume 55, 2021), 183–207. https://doi.org/10.1146/annurev-genet-030321-054851

Pettit, D. L., Perlman, S., & Malinow, R. (1994). Potentiated transmission and prevention of further LTP by increased CaMKII activity in postsynaptic hippocampal slice neurons. *Science (New York, N.Y.)*, *266*(5192), 1881–1885. https://doi.org/10.1126/science.7997883

Pi, H. J., Otmakhov, N., El Gaamouch, F., Lemelin, D., De Koninck, P., & Lisman, J. (2010). CaMKII control of spine size and synaptic strength: Role of phosphorylation states and nonenzymatic action. *Proceedings of the National Academy of Sciences*, *107*(32), 14437–14442. https://doi.org/10.1073/pnas.1009268107

Pologruto, T. A., Sabatini, B. L., & Svoboda, K. (2003). ScanImage: Flexible software for operating laser scanning microscopes. *BioMedical Engineering OnLine*, *2*(1), 13. https://doi.org/10.1186/1475-925X-2-13

Porstmann, B., Porstmann, T., Nugel, E., & Evers, U. (1985). Which of the commonly used marker enzymes gives the best results in colorimetric and fluorimetric enzyme immunoassays: Horseradish peroxidase, alkaline phosphatase or beta-galactosidase? *Journal of Immunological Methods*, *79*(1), 27–37. https://doi.org/10.1016/0022-1759(85)90388-6

Pramio, D. T., Vieceli, F. M., Varella-Branco, E., Goes, C. P., Kobayashi, G. S., da Silva Pelegrina, D. V., de Moraes, B. C., El Allam, A., De Kumar, B., Jara, G., Farfel, J. M., Bennett, D. A., Kundu, S., Viapiano, M. S., Reis, E. M., de Oliveira, P. S. L., dos Santos e Passos-Bueno, M. R., Rothlin, C. V., Ghosh, S., & Schechtman, D. (2023). DNA methylation of the promoter region at the CREB1 binding site is a mechanism for the epigenetic regulation of brain-specific PKMζ. *Biochimica et Biophysica Acta (BBA) - Gene Regulatory Mechanisms*, *1866*(1), 194909. https://doi.org/10.1016/j.bbagrm.2023.194909

Raineteau, O., Rietschin, L., Gradwohl, G., Guillemot, F., & Gähwiler, B. H. (2004). Neurogenesis in hippocampal slice cultures. *Molecular and Cellular Neuroscience*, *26*(2), 241–250. https://doi.org/10.1016/j.mcn.2004.01.003

Ramachandran, B., Ahmed, S., & Dean, C. (2015). Long-term depression is differentially expressed in distinct lamina of hippocampal CA1 dendrites. *Frontiers in Cellular Neuroscience*, *9*. https://doi.org/10.3389/fncel.2015.00023

Ranck, J. B. (1973). Studies on single neurons in dorsal hippocampal formation and septum in unrestrained rats: Part I. Behavioral correlates and firing repertoires. *Experimental Neurology*, *41*(2), 462–531. https://doi.org/10.1016/0014-4886(73)90290-2

Rellos, P., Pike, A. C. W., Niesen, F. H., Salah, E., Lee, W. H., Delft, F. von, & Knapp, S. (2010). Structure of the CaMKIIδ/Calmodulin Complex Reveals the Molecular Mechanism of CaMKII Kinase Activation. *PLOS Biology*, *8*(7), e1000426. https://doi.org/10.1371/journal.pbio.1000426

Rey, S., Marra, V., Smith, C., & Staras, K. (2020). Nanoscale Remodeling of Functional Synaptic Vesicle Pools in Hebbian Plasticity. *Cell Reports*, *30*(6), 2006-2017.e3. https://doi.org/10.1016/j.celrep.2020.01.051

Reyes Gaido, O. E., Pavlaki, N., Granger, J. M., Mesubi, O. O., Liu, B., Lin, B. L., Long, A., Walker, D., Mayourian, J., Schole, K. L., Terrillion, C. E., Nkashama, L. J., Hulsurkar, M. M., Dorn, L. E., Ferrero, K. M., Huganir, R. L., Müller, F. U., Wehrens, X. H. T., Liu, J. O., … Anderson, M. E. (2023). An improved reporter identifies ruxolitinib as a potent and cardioprotective CaMKII inhibitor. *Science Translational Medicine*, *15*(701), eabq7839. https://doi.org/10.1126/scitranslmed.abq7839

Rezazadeh, S., Claydon, T. W., & Fedida, D. (2006). KN-93 (2-[N-(2-hydroxyethyl)]-N-(4-methoxybenzenesulfonyl)]amino-N-(4-chlorocinnamyl)-N-methylbenzylamine), a calcium/calmodulin-dependent protein kinase II inhibitor, is a direct extracellular blocker of voltage-gated potassium channels. *The Journal of Pharmacology and Experimental Therapeutics*, *317*(1), 292–299. https://doi.org/10.1124/jpet.105.097618

Rimbault, C., Breillat, C., Compans, B., Toulmé, E., Vicente, F. N., Fernandez-Monreal, M., Mascalchi, P., Genuer, C., Puente-Muñoz, V., Gauthereau, I., Hosy, E., Claverol, S., Giannone, G., Chamma, I., Mackereth, C. D., Poujol, C., Choquet, D., & Sainlos, M. (2024). Engineering paralog-specific PSD-95 recombinant binders as minimally interfering multimodal probes for advanced imaging techniques. *eLife*, *13*, e69620. https://doi.org/10.7554/eLife.69620

Sacktor, T. C. (2008). PKMzeta, LTP maintenance, and the dynamic molecular biology of memory storage. *Progress in Brain Research*, *169*, 27–40. https://doi.org/10.1016/S0079-6123(07)00002-7

Sacktor, T. C., & Fenton, A. A. (2018). What does LTP tell us about the roles of CaMKII and PKMζ in memory? *Molecular Brain*, *11*(1), 77. https://doi.org/10.1186/s13041-018-0420-5

Sadeh, N., Verbitsky, S., Dudai, Y., & Segal, M. (2015). Zeta Inhibitory Peptide, a Candidate Inhibitor of Protein Kinase M , Is Excitotoxic to Cultured Hippocampal Neurons. *Journal of Neuroscience*, *35*(36), 12404–12411. https://doi.org/10.1523/JNEUROSCI.0976-15.2015

Samavat, M., Bartol, T. M., Bromer, C., Bowden, J. B., Hubbard, D. D., Hanka, D. C., Kuwajima, M., Mendenhall, J. M., Parker, P. H., Abraham, W. C., Harris, K. M., & Sejnowski, T. J. (2022). *Regional and LTP-Dependent Variation of Synaptic Information Storage Capacity in Rat Hippocampus* [Preprint]. Neuroscience. https://doi.org/10.1101/2022.08.29.505464

Samavat, M., Bartol, T. M., Harris, K. M., & Sejnowski, T. J. (2024). Synaptic Information Storage Capacity Measured With Information Theory. *Neural Computation*, *36*(5), 781–802. https://doi.org/10.1162/neco_a_01659

Sando, R., Bushong, E., Zhu, Y., Huang, M., Considine, C., Phan, S., Ju, S., Uytiepo, M., Ellisman, M., & Maximov, A. (2017). Assembly of Excitatory Synapses in the Absence of Glutamatergic Neurotransmission. *Neuron*, *94*(2), 312-321.e3. https://doi.org/10.1016/j.neuron.2017.03.047

Sanhueza, M., Fernandez-Villalobos, G., Stein, I. S., Kasumova, G., Zhang, P., Bayer, K. U., Otmakhov, N., Hell, J. W., & Lisman, J. (2011). Role of the CaMKII/NMDA Receptor Complex in the Maintenance of Synaptic Strength. *Journal of Neuroscience*, *31*(25), 9170–9178. https://doi.org/10.1523/JNEUROSCI.1250-11.2011

Sanhueza, M., McIntyre, C. C., & Lisman, J. E. (2007). Reversal of synaptic memory by Ca2+/calmodulin-dependent protein kinase II inhibitor. *The Journal of Neuroscience: The Official Journal of the Society for Neuroscience*, *27*(19), 5190–5199. https://doi.org/10.1523/JNEUROSCI.5049-06.2007

Santini, E., Huynh, T. N., & Klann, E. (2014). Mechanisms of Translation Control Underlying Long-lasting Synaptic Plasticity and the Consolidation of Long-term Memory. *Progress in Molecular Biology and Translational Science*, *122*, 131–167. https://doi.org/10.1016/B978-0-12-420170-5.00005-2

Schoenenberger, P., Gerosa, D., & Oertner, T. G. (2009). Temporal Control of Immediate Early Gene Induction by Light. *PLOS ONE*, *4*(12), e8185. https://doi.org/10.1371/journal.pone.0008185

Schwartzkroin, P. A., & Wester, K. (1975). Long-lasting facilitation of a synaptic potential following tetanization in the*in vitro* hippocampal slice. *Brain Research*, *89*(1), 107–119. https://doi.org/10.1016/0006-8993(75)90138-9

Scoville, W. B., & Milner, B. (1957). LOSS OF RECENT MEMORY AFTER BILATERAL HIPPOCAMPAL LESIONS. *Journal of Neurology, Neurosurgery, and Psychiatry*, *20*(1), 11–21.

Semon, R. W. (1921). *The mneme*. G. Allen & Unwin ltd.

Shannon, C. E. (1948). A mathematical theory of communication. *The Bell System Technical Journal*, *27*(3), 379–423. The Bell System Technical Journal. https://doi.org/10.1002/j.1538-7305.1948.tb01338.x

Shatz, C. J. (1992, September 1). *The Developing Brain*. Scientific American. https://www.scientificamerican.com/article/the-developing-brain/

Shcherbakova, D. M., Hink, M. A., Joosen, L., Gadella, T. W. J., & Verkhusha, V. V. (2012). An Orange Fluorescent Protein with a Large Stokes Shift for Single-Excitation Multicolor FCCS and FRET Imaging. *Journal of the American Chemical Society*, *134*(18), 7913–7923. https://doi.org/10.1021/ja3018972

Shen, K., & Meyer, T. (1999). Dynamic Control of CaMKII Translocation and Localization in Hippocampal Neurons by NMDA Receptor Stimulation. *Science*, *284*(5411), 162–167. https://doi.org/10.1126/science.284.5411.162

Sheng, M., & Hoogenraad, C. C. (2007). The postsynaptic architecture of excitatory synapses: A more quantitative view. *Annual Review of Biochemistry*, *76*, 823–847. https://doi.org/10.1146/annurev.biochem.76.060805.160029

Shibata, A. C. E., Ueda, H. H., Eto, K., Onda, M., Sato, A., Ohba, T., Nabekura, J., & Murakoshi, H. (2021). Photoactivatable CaMKII induces synaptic plasticity in single synapses. *Nature Communications*, *12*(1), Article 1. https://doi.org/10.1038/s41467-021-21025-6

Shin, M. E., Parra-Bueno, P., & Yasuda, R. (2024). *Formation of long-term memory without short-term memory by CaMKII inhibition* (p. 2024.01.28.577644). bioRxiv. https://doi.org/10.1101/2024.01.28.577644

Shirke, A. M., & Malinow, R. (1997). Mechanisms of potentiation by calcium-calmodulin kinase II of postsynaptic sensitivity in rat hippocampal CA1 neurons. *Journal of Neurophysiology*, *78*(5), 2682–2692. https://doi.org/10.1152/jn.1997.78.5.2682

Shu, X., Lev-Ram, V., Deerinck, T. J., Qi, Y., Ramko, E. B., Davidson, M. W., Jin, Y., Ellisman, M. H., & Tsien, R. Y. (2011). A Genetically Encoded Tag for Correlated Light and Electron Microscopy of Intact Cells, Tissues, and Organisms. *PLOS Biology*, *9*(4), e1001041. https://doi.org/10.1371/journal.pbio.1001041

Siegelbaum, S. A., & Kandel, E. R. (1991). Learning-related synaptic plasticity: LTP and LTD. *Current Opinion in Neurobiology*, *1*(1), 113–120. https://doi.org/10.1016/0959-4388(91)90018-3

Sigmund, F., Berezin, O., Beliakova, S., Magerl, B., Drawitsch, M., Piovesan, A., Gonçalves, F., Bodea, S.-V., Winkler, S., Bousraou, Z., Grosshauser, M., Samara, E., Pujol-Martí, J., Schädler, S., So, C., Irsen, S., Walch, A., Kofler, F., Piraud, M., … Westmeyer, G. G. (2023). Genetically encoded barcodes for correlative volume electron microscopy. *Nature Biotechnology*, 1–12. https://doi.org/10.1038/s41587-023-01713-y

Sigmund, F., Pettinger, S., Kube, M., Schneider, F., Schifferer, M., Schneider, S., Efremova, M. V., Pujol-Martí, J., Aichler, M., Walch, A., Misgeld, T., Dietz, H., & Westmeyer, G. G. (2019). Iron-Sequestering Nanocompartments as Multiplexed Electron Microscopy Gene Reporters. *ACS Nano*, *13*(7), 8114–8123. https://doi.org/10.1021/acsnano.9b03140

Silva, A. J., Paylor, R., Wehner, J. M., & Tonegawa, S. (1992). Impaired spatial learning in alpha-calcium-calmodulin kinase II mutant mice. *Science (New York, N.Y.)*, *257*(5067), 206–211. https://doi.org/10.1126/science.1321493

Śliwińska, M. A., Cały, A., Borczyk, M., Ziółkowska, M., Skonieczna, E., Chilimoniuk, M., Bernaś, T., Giese, K. P., & Radwanska, K. (2020). Long-term Memory Upscales Volume of Postsynaptic Densities in the Process that Requires Autophosphorylation of αCaMKII. *Cerebral Cortex*, *30*(4), 2573–2585. https://doi.org/10.1093/cercor/bhz261

Smedler, E., Louhivuori, L., Romanov, R. A., Masini, D., Dehnisch Ellström, I., Wang, C., Caramia, M., West, Z., Zhang, S., Rebellato, P., Malmersjö, S., Brusini, I., Kanatani, S., Fisone, G., Harkany, T., & Uhlén, P.

(2022). Disrupted Cacna1c gene expression perturbs spontaneous Ca2+ activity causing abnormal brain development and increased anxiety. *Proceedings of the National Academy of Sciences of the United States of America*, *119*(7), e2108768119. https://doi.org/10.1073/pnas.2108768119

Sobczyk, A., Scheuss, V., & Svoboda, K. (2005). NMDA receptor subunit-dependent [Ca2+] signaling in individual hippocampal dendritic spines. *The Journal of Neuroscience: The Official Journal of the Society for Neuroscience*, *25*(26), 6037–6046. https://doi.org/10.1523/JNEUROSCI.1221-05.2005

Softky, W. R., & Koch, C. (1993). The highly irregular firing of cortical cells is inconsistent with temporal integration of random EPSPs. *The Journal of Neuroscience: The Official Journal of the Society for Neuroscience*, *13*(1), 334–350. https://doi.org/10.1523/JNEUROSCI.13-01-00334.1993

Sonomura, T., Furuta, T., Nakatani, I., Yamamoto, Y., Unzai, T., Matsuda, W., Iwai, H., Yamanaka, A., Uemura, M., & Kaneko, T. (2013). Correlative analysis of immunoreactivity in confocal laser-scanning microscopy and scanning electron microscopy with focused ion beam milling. *Frontiers in Neural Circuits*, *7*. https://doi.org/10.3389/fncir.2013.00026

Spacek, J., & Harris, K. M. (1997). Three-dimensional organization of smooth endoplasmic reticulum in hippocampal CA1 dendrites and dendritic spines of the immature and mature rat. *The Journal of Neuroscience: The Official Journal of the Society for Neuroscience*, *17*(1), 190–203. https://doi.org/10.1523/JNEUROSCI.17-01-00190.1997

Spruston, N. (2008). Pyramidal neurons: Dendritic structure and synaptic integration. *Nature Reviews Neuroscience*, *9*(3), Article 3. https://doi.org/10.1038/nrn2286

Stein, V., House, D. R. C., Bredt, D. S., & Nicoll, R. A. (2003). Postsynaptic Density-95 Mimics and Occludes Hippocampal Long-Term Potentiation and Enhances Long-Term Depression. *Journal of Neuroscience*, *23*(13), 5503–5506. https://doi.org/10.1523/JNEUROSCI.23-13-05503.2003

Stepanyants, A., Hof, P. R., & Chklovskii, D. B. (2002). Geometry and structural plasticity of synaptic connectivity. *Neuron*, *34*(2), 275–288. https://doi.org/10.1016/s0896-6273(02)00652-9

Stoppini, L., Buchs, P.-A., & Muller, D. (1991). A simple method for organotypic cultures of nervous tissue. *Journal of Neuroscience Methods*, *37*(2), 173–182. https://doi.org/10.1016/0165-0270(91)90128-M

Sumi, M., Kiuchi, K., Ishikawa, T., Ishii, A., Hagiwara, M., Nagatsu, T., & Hidaka, H. (1991). The newly synthesized selective Ca2+calmodulin<math><mtext>Ca</mtext><msup><mi></mi><mn>2+</mn></msup><mtext>calmodulin</mtext></math> dependent protein kinase II inhibitor KN-93 reduces dopamine contents in PC12h cells. *Biochemical and Biophysical Research Communications*, *181*(3), 968–975. https://doi.org/10.1016/0006-291X(91)92031-E

Sun, Y., Smirnov, M., Kamasawa, N., & Yasuda, R. (2021). Rapid Ultrastructural Changes in the PSD and Surrounding Membrane after Induction of Structural LTP in Single Dendritic Spines. *The Journal of Neuroscience*, *41*(33), 7003–7014. https://doi.org/10.1523/JNEUROSCI.1964-20.2021

Sutton, M. A., & Schuman, E. M. (2006). Dendritic Protein Synthesis, Synaptic Plasticity, and Memory. *Cell*, *127*(1), 49–58. https://doi.org/10.1016/j.cell.2006.09.014

Sweatt, J. D. (2004). Mitogen-activated protein kinases in synaptic plasticity and memory. *Current Opinion in Neurobiology*, *14*(3), 311–317. https://doi.org/10.1016/j.conb.2004.04.001

Tada, T., & Sheng, M. (2006). Molecular mechanisms of dendritic spine morphogenesis. *Current Opinion in Neurobiology*, *16*(1), 95–101. https://doi.org/10.1016/j.conb.2005.12.001

Takahashi, N., Kitamura, K., Matsuo, N., Mayford, M., Kano, M., Matsuki, N., & Ikegaya, Y. (2012). Locally Synchronized Synaptic Inputs. *Science*, *335*(6066), 353–356. https://doi.org/10.1126/science.1210362

Takao, K., Okamoto, K.-I., Nakagawa, T., Neve, R. L., Nagai, T., Miyawaki, A., Hashikawa, T., Kobayashi, S., & Hayashi, Y. (2005). Visualization of synaptic Ca2+ /calmodulin-dependent protein kinase II activity in living neurons. *The Journal of Neuroscience: The Official Journal of the Society for Neuroscience*, *25*(12), 3107–3112. https://doi.org/10.1523/JNEUROSCI.0085-05.2005

Tanaka, J.-I., Horiike, Y., Matsuzaki, M., Miyazaki, T., Ellis-Davies, G. C. R., & Kasai, H. (2008). Protein synthesis and neurotrophin-dependent structural plasticity of single dendritic spines. *Science (New York, N.Y.)*, *319*(5870), 1683–1687. https://doi.org/10.1126/science.1152864

Tao, W., Lee, J., Chen, X., Díaz-Alonso, J., Zhou, J., Pleasure, S., & Nicoll, R. A. (2021a). Synaptic memory requires CaMKII. *eLife*, *10*, e60360. https://doi.org/10.7554/eLife.60360

Tao, W., Lee, J., Chen, X., Díaz-Alonso, J., Zhou, J., Pleasure, S., & Nicoll, R. A. (2021b). Synaptic memory requires CaMKII. *eLife*, *10*, e60360. https://doi.org/10.7554/eLife.60360

Tazerart, S., Mitchell, D. E., Miranda-Rottmann, S., & Araya, R. (2020). A spike-timing-dependent plasticity rule for dendritic spines. *Nature Communications*, *11*(1), 4276. https://doi.org/10.1038/s41467-020-17861-7

Thomas, G. M., & Huganir, R. L. (2004). MAPK cascade signalling and synaptic plasticity. *Nature Reviews Neuroscience*, *5*(3), 173–183. https://doi.org/10.1038/nrn1346

Thomas, M. J., Moody, T. D., Makhinson, M., & O'Dell, T. J. (1996). Activity-Dependent β-Adrenergic Modulation of Low Frequency Stimulation Induced LTP in the Hippocampal CA1 Region. *Neuron*, *17*(3), 475–482. https://doi.org/10.1016/S0896-6273(00)80179-8

Tokumitsu, H., Chijiwa, T., Hagiwara, M., Mizutani, A., Terasawa, M., & Hidaka, H. (1990). KN-62, 1-[N,O-bis(5-isoquinolinesulfonyl)-N-methyl-L-tyrosyl]-4-phenylpiperazi ne, a specific inhibitor of Ca2+/calmodulin-dependent protein kinase II. *Journal of Biological Chemistry*, *265*(8), 4315–4320. https://doi.org/10.1016/S0021-9258(19)39565-1

Toni, N., Buchs, P.-A., Nikonenko, I., Bron, C. R., & Muller, D. (1999). LTP promotes formation of multiple spine synapses between a single axon terminal and a dendrite. *Nature*, *402*(6760), 421–425. https://doi.org/10.1038/46574

Toni, N., Buchs, P.-A., Nikonenko, I., Povilaitite, P., Parisi, L., & Muller, D. (2001). Remodeling of Synaptic Membranes after Induction of Long-Term Potentiation. *Journal of Neuroscience*, *21*(16), 6245–6251. https://doi.org/10.1523/JNEUROSCI.21-16-06245.2001

Tønnesen, J., Katona, G., Rózsa, B., & Nägerl, U. V. (2014). Spine neck plasticity regulates compartmentalization of synapses. *Nature Neuroscience*, *17*(5), 678–685. https://doi.org/10.1038/nn.3682

Tullis, J. E., Larsen, M. E., Rumian, N. L., Freund, R. K., Boxer, E. E., Brown, C. N., Coultrap, S. J., Schulman, H., Aoto, J., Dell'Acqua, M. L., & Bayer, K. U. (2023). LTP induction by structural rather than enzymatic functions of CaMKII. *Nature*, *621*(7977), Article 7977. https://doi.org/10.1038/s41586-023-06465-y

Turrigiano, G. (2012). Homeostatic Synaptic Plasticity: Local and Global Mechanisms for Stabilizing Neuronal Function. *Cold Spring Harbor Perspectives in Biology*, *4*(1), a005736. https://doi.org/10.1101/cshperspect.a005736

Ueda, H. H., Nagasawa, Y., Sato, A., Onda, M., & Murakoshi, H. (2022). Chronic neuronal excitation leads to dual metaplasticity in the signaling for structural long-term potentiation. *Cell Reports*, *38*(1), 110153. https://doi.org/10.1016/j.celrep.2021.110153

Van Harreveld, A., & Fifkova, E. (1975). Swelling of dendritic spines in the fascia dentata after stimulation of the perforant fibers as a mechanism of post-tetanic potentiation. *Experimental Neurology*, *49*(3), 736–749. https://doi.org/10.1016/0014-4886(75)90055-2

Wang, L., Wang, N., Zhang, W., Cheng, X., Yan, Z., Shao, G., Wang, X., Wang, R., & Fu, C. (2022). Therapeutic peptides: Current applications and future directions. *Signal Transduction and Targeted Therapy*, *7*(1), 1–27. https://doi.org/10.1038/s41392-022-00904-4

Weigert, M., Schmidt, U., Haase, R., Sugawara, K., & Myers, G. (2020). Star-convex Polyhedra for 3D Object Detection and Segmentation in Microscopy. *2020 IEEE Winter Conference on Applications of Computer Vision (WACV)*, 3655–3662. https://doi.org/10.1109/WACV45572.2020.9093435

Whitlock, J. R., Heynen, A. J., Shuler, M. G., & Bear, M. F. (2006). Learning induces long-term potentiation in the hippocampus. *Science (New York, N.Y.)*, *313*(5790), 1093–1097. https://doi.org/10.1126/science.1128134

Wiegert, J. S., Gee, C. E., & Oertner, T. G. (2017). Single-Cell Electroporation of Neurons. *Cold Spring Harbor Protocols*, *2017*(2), pdb.prot094904. https://doi.org/10.1101/pdb.prot094904

Wiegert, J. S., Pulin, M., Gee, C. E., & Oertner, T. G. (2018). The fate of hippocampal synapses depends on the sequence of plasticity-inducing events. *eLife*, *7*, e39151. https://doi.org/10.7554/eLife.39151

Willig, K. I., Wegner, W., Müller, A., Clavet-Fournier, V., & Steffens, H. (2021). Multi-label in vivo STED microscopy by parallelized switching of reversibly switchable fluorescent proteins. *Cell Reports*, *35*(9), 109192. https://doi.org/10.1016/j.celrep.2021.109192

Wilson, D. E., Whitney, D. E., Scholl, B., & Fitzpatrick, D. (2016). Orientation selectivity and the functional clustering of synaptic inputs in primary visual cortex. *Nature Neuroscience*, *19*(8), 1003–1009. https://doi.org/10.1038/nn.4323

Winnubst, J., Cheyne, J. E., Niculescu, D., & Lohmann, C. (2015). Spontaneous Activity Drives Local Synaptic Plasticity In Vivo. *Neuron*, *87*(2), 399–410. https://doi.org/10.1016/j.neuron.2015.06.029

Wittenberg, G. M., & Wang, S. S.-H. (2006). Malleability of spike-timing-dependent plasticity at the CA3-CA1 synapse. *The Journal of Neuroscience: The Official Journal of the Society for Neuroscience*, *26*(24), 6610–6617. https://doi.org/10.1523/JNEUROSCI.5388-05.2006

Witter, M. P., Kleven, H., & Kobro Flatmoen, A. (2017). Comparative Contemplations on the Hippocampus. *Brain, Behavior and Evolution*, *90*(1), 15–24. https://doi.org/10.1159/000475703

Wolff, C., Tinevez, J.-Y., Pietzsch, T., Stamataki, E., Harich, B., Guignard, L., Preibisch, S., Shorte, S., Keller, P. J., Tomancak, P., & Pavlopoulos, A. (2018). Multi-view light-sheet imaging and tracking with the MaMuT

software reveals the cell lineage of a direct developing arthropod limb. *eLife*, *7*, e34410. https://doi.org/10.7554/eLife.34410

Woods, G. F., Oh, W. C., Boudewyn, L. C., Mikula, S. K., & Zito, K. (2011). Loss of PSD-95 Enrichment Is Not a Prerequisite for Spine Retraction. *Journal of Neuroscience*, *31*(34), 12129–12138. https://doi.org/10.1523/JNEUROSCI.6662-10.2011

Wu, Y., Gao, Z., Chen, B., Koval, O. M., Singh, M. V., Guan, X., Hund, T. J., Kutschke, W., Sarma, S., Grumbach, I. M., Wehrens, X. H. T., Mohler, P. J., Song, L.-S., & Anderson, M. E. (2009). Calmodulin kinase II is required for fight or flight sinoatrial node physiology. *Proceedings of the National Academy of Sciences*, *106*(14), 5972–5977. https://doi.org/10.1073/pnas.0806422106

Xiao, K., Li, Y., Chitwood, R. A., & Magee, J. C. (2023). A critical role for CaMKII in behavioral timescale synaptic plasticity in hippocampal CA1 pyramidal neurons. *Science Advances*, *9*(36), eadi3088. https://doi.org/10.1126/sciadv.adi3088

Yamagata, Y., Kobayashi, S., Umeda, T., Inoue, A., Sakagami, H., Fukaya, M., Watanabe, M., Hatanaka, N., Totsuka, M., Yagi, T., Obata, K., Imoto, K., Yanagawa, Y., Manabe, T., & Okabe, S. (2009). Kinase-dead knock-in mouse reveals an essential role of kinase activity of Ca2+/calmodulin-dependent protein kinase IIalpha in dendritic spine enlargement, long-term potentiation, and learning. *The Journal of Neuroscience: The Official Journal of the Society for Neuroscience*, *29*(23), 7607–7618. https://doi.org/10.1523/JNEUROSCI.0707-09.2009

Yang, G., Pan, F., & Gan, W.-B. (2009). Stably maintained dendritic spines are associated with lifelong memories. *Nature*, *462*(7275), 920–924. https://doi.org/10.1038/nature08577

Yang, S. N., Tang, Y. G., & Zucker, R. S. (1999). Selective induction of LTP and LTD by postsynaptic [Ca2+]i elevation. *Journal of Neurophysiology*, *81*(2), 781–787. https://doi.org/10.1152/jn.1999.81.2.781

Yasuda, R. (2017). Biophysics of Biochemical Signaling in Dendritic Spines: Implications in Synaptic Plasticity. *Biophysical Journal*, *113*(10), 2152–2159. https://doi.org/10.1016/j.bpj.2017.07.029

Zakharenko, S. S., Patterson, S. L., Dragatsis, I., Zeitlin, S. O., Siegelbaum, S. A., Kandel, E. R., & Morozov, A. (2003). Presynaptic BDNF required for a presynaptic but not postsynaptic component of LTP at hippocampal CA1-CA3 synapses. *Neuron*, *39*(6), 975–990. https://doi.org/10.1016/s0896-6273(03)00543-9

Zakharova, G. S., Uporov, I. V., & Tishkov, V. I. (2011). Horseradish peroxidase: Modulation of properties by chemical modification of protein and heme. *Biochemistry. Biokhimiia*, *76*(13), 1391–1401. https://doi.org/10.1134/S0006297911130037

Zhang, L. I., Tao, H. W., Holt, C. E., Harris, W. A., & Poo, M. (1998). A critical window for cooperation and competition among developing retinotectal synapses. *Nature*, *395*(6697), 37–44. https://doi.org/10.1038/25665

Zhang, Q., Lee, W.-C. A., Paul, D. L., & Ginty, D. D. (2019). Multiplexed peroxidase-based electron microscopy labeling enables simultaneous visualization of multiple cell types. *Nature Neuroscience*, *22*(5), Article 5. https://doi.org/10.1038/s41593-019-0358-7

Zhang, Y.-P., Holbro, N., & Oertner, T. G. (2008). Optical induction of plasticity at single synapses reveals input-specific accumulation of alphaCaMKII. *Proceedings of the National Academy of Sciences of the United States of America*, *105*(33), 12039–12044. https://doi.org/10.1073/pnas.0802940105

Zhou, Q., Homma, K. J., & Poo, M. (2004). Shrinkage of Dendritic Spines Associated with Long-Term Depression of Hippocampal Synapses. *Neuron*, *44*(5), 749–757. https://doi.org/10.1016/j.neuron.2004.11.011

Zhou, Y., Takahashi, E., Li, W., Halt, A., Wiltgen, B., Ehninger, D., Li, G.-D., Hell, J. W., Kennedy, M. B., & Silva, A. J. (2007). Interactions between the NR2B receptor and CaMKII modulate synaptic plasticity and spatial learning. *The Journal of Neuroscience: The Official Journal of the Society for Neuroscience*, *27*(50), 13843–13853. https://doi.org/10.1523/JNEUROSCI.4486-07.2007

List of Figures

List of Tables

Plasmids in this PhD project

All the plasmids listed below were modified by Iris Ohmert for this PhD project, illustrated as: (backbone) promoter. sequence.

1. (OpAAV) hSyn. SYP-HRP-IRES-Cre
2. (pAAV) CamKIIP. dAPEX2-IRES-Cre
3. (pAAV) hSyn. DIO-FHS-paCAMKII

Sources of all the plasmids used in this PhD projects:

CheRiff-eGFP (Addgene #51697) was a gift from Adam Cohen, mKate2-N (Evrogen #FP182) was a gift from Evrogen, mEGFP-P2A-paAIP2 (Addgene #91718) was a gift from Ryohei Yasuda, FHS-paCaMKII-WPRE3, and FHS-paCaMKII (SD)-WPRE3 was a gift from Hideji Murakoshi (Shibata et al., 2021), Xph20-eGFP-CCR5TC (Addgene #135530) was a gift from Matthieu Sainlos, LSSmOrange (Agggene #37129) was a gift from Vladislav Verkhusha, dAPEX2 was a gift from David Ginty, Syn-ChrimsonR-tdT (Addgene #59171) was a gift from Edward Boyden, SYP-HRP (Addgene #117185) was a gift from David Ginty, pAAV-hSyn-DIO-ChrimsonR-mRuby2-ST (Addgene #105448) was a gift from Hillel Adesnik.

Codes produced or used in this PhD project

The codes listed below were written by myself.

1. oSTDP pairing pattern analyser (MATLAB R2022b): for assessment of acute pairing experiment.

Example outputs: Fig. 20

Available at: https://github.com/ruiwang1127/ephys4oSTDP.git

2. chronic imaging data arranger (MATLAB R2022b): for tiding up of chronic imaging data.

Example outputs: Fig. 39 to Fig.45

Available at: https://github.com/ruiwang1127/Spine-analysis.git

3. chronic imaging data analyzers (MATLAB R2022b): a pack of scripts that analyze the arranged raw data, created by 'chronic imaging data arranger', including: probability distribution analyzer (e.g. Fig.40 and Table.5), CV_Size_Slope plot (e.g. Fig.42), size effect analyzer (e.g. Fig.43), entropy calculator (e.g Fig.44).

Available at: https://github.com/ruiwang1127/Spine-analysis.git

The codes listed below were written previously in ISN, and was used in this PhD project.

1. online analysis (works under MATLAB R2009b to MATLAB R2016b): for monitor patch clamp experiment quality online.

Author: Daniel Udwari

2. Average traces (works under MATLAB R2019b): for analysing voltage clamp EPSPs automatically (example: Fig. 16).

Author: Brenna C. Fearey, modified by Margarita Anisimova

3.Data Logger (MATLAB R2023b): for monitoring laser fluctuation and imaging chamber temperature while doing chronic imaging.

Author: Thomas Oertner

3. Chronic imaging deep (Python 3.9): for detecting spines chronically imaged use deep-learning method, including pre-steps for detection, described in 2.8.1.

Author: Christian Schulze

4. SpotFi (Napari): meaning 'Spot Finder', for imaging annotation and StarDist model training, which is needed for 'Chronic imaging deep'.

Author: Christian Schulze

Abbreviations

2PLSM	two-photon laser scanning microscopy
AAV	adeno-associated viruse
ACSF	artificial cerebrospinal fluid
AMPA	α-amino-3-hydroxy-5-methyl-4-isoxazolepropionic acid
APEX2	enhanced ascorbate peroxidases2
APs	action potentials
APX	ascorbate peroxidases
ATP	adenosine triphosphate
bAP	back-propagation action potential
BDNF	brain-derived neurotrophic factor
CA1-3	Cornu Ammonis region 1-3
CaM	calmodulin
CAMKAPs	CaMKII-associated proteins
CaMKII	Ca2+/calmodulin-dependent protein kinase kinase 2
CaMKIV	Ca2+/calmodulin-dependent protein kinase ktype IV
cAMP	cyclic adenosine monophosphate
CaN	calcineurin
CLEM	correlative light and electron microscopy
CV	the coefficient of variation
DAB	3,3'-Diaminobenzidine
dAPEX2	dimeric APEX2
DG	dentate gyrus
DIV	days in vitro
EC	entorhinal cortex
EM	electron microscopy
EPSC	excitatory postsynaptic potential
EPSP	excitatory postsynaptic potential
ERK	extracellular signal–regulated kinase
early tLTD	early phase of timing-dependent long-term depression
early tLTP	early phase of timing-dependent long-term potentiation
FIB-SEM	focused ion beam scanning electron microscopy
FITC	fluorescein
FLIM	fluorescence lifetime imaging
FRET	fluorescence resonance energy transfer
GA	glutaraldehyde
GC	granule cells
GFP	green fluorescent protein
HRP	horseradish peroxidase
IEG	immediate early gene
IQR	Interquartile range
IR	infrared illumination
ISN	Institute of Synaptic Neuroscience
LED	light-emitting diodes lamps
LJP	liquid-junction potential
LM	light microscopy
LOV	light-oxygen-voltage domain
LSM	laser scanning microscopy
LSS	large stokes shift
LTD	long-term depression
LTP	long-term potentiation
late tLTD	late phase of timing-dependent long-term depression
late tLTP	late phase of timing-dependent long-term potentiation
MEM	minimal essential medium
miniSOG	mini singlet oxygen generator
MIP	maximum intensity projection
NMDA	N-methyl-D-aspartate
NMS	non-maximum suppression
NTs	non-transfected pyramidal neurons
oSTDP	Optogenetically induced spike timing dependent plasticity
PBS	Phosphate buffered solution
PFA	polymeric formaldehyde

PKA	protein kinase A
PKC	protein kinase C
PKMζ	protein kinase M-ζ
PMTs	photomultiplier tubes
PNs	pyramidal neurons
PP1	protein phosphatase 1
PSD	postsynaptic density
R_{in}	input resistance
R_m	Membrane resistance
ROI	region-of-interest
Rs	Series resistance
SC	Schaffer collateral
Scr-ZIP	the scrambled zeta-inhibitor-pipette
SEM	scanning electron microscopy
SER	smooth endoplasmic reticulum
sLTP/LTD	structural LTP /LTD
STDP	spike timing-dependent plasticity
s-vEM	SEM-based vEM
TBS	theta-burst stimulation
TEM	transmission Electron Microscopy
TFs	transfected pyramidal neurons
tLTD	timing-dependent long-term depression
tLTP	timing-dependent long-term potentiation
TMS	transcranial magnetic stimulation
TTX	tetrodotoxin
t-vEM	tEM-based vEM
UKE	University Medical Center Hamburg-Eppendorf
vEM	volume electron microscopy
Vm	Membrane potential
ZIP	the zeta-inhibitor-pipette

Contributions

Thomas Oertner and Christine Gee supervised this PhD project.

Iris Ohmert performed plasmid cloning.

Iris Ohmert and Jan Schröder prepared slice cultures and culture medium.

Ingke Braren produced the AAVs.

Paul J. Lamothe-Molina, Andreas Franzelin, Yuan ZHEN and Oana Constantin prepared immunohistochemistry solutions for the lab.

Thomas Oertner designed and built all of the self-made hardware (Fig. 16, 18, 19).

Christian Schulze developed PSD detection software.

Michaela Schweizer collected electron tomography images.

Emanuela Szpotowicz performed the OsO_4 staining, embedding and sectioning for electron tomography.

Julia Kaiser annotated electron tomography datasets.

Thomas Oertner created Fig. 19; Thomas Oertner and Christine Gee edited Fig. 65.

Oana Constantin and Christine Gee proof-read the draft.

Acknowledgements

First and foremost, I would like to thank my supervisors, Thomas Oertner and Christine Gee, for offering me the opportunity to do my PhD in your lab. I have grown into a scientist over these years under your supervision, learning from your knowledge, guidance, as well as passion, rigor, and high standards for science. I really like live imaging and patching, skills I developed here thanks to your mentorship. I am also deeply thankful for the encouragement and financial support that made it possible for me to complete my PhD and present my work at conferences.

I would like to thank Christian Schulze for his support in developing the software for image acquisition and analysis. I greatly appreciate the discussions with Christian on image analysis, from which I learned a great deal. I would also like to thank Michaela Schweizer for her support on the EM project. I would like to express my gratitude to Iris Ohmert, Jan Schröder, and Sabine Graf from our lab, as well as Emanuela Szpotowicz and Chudamani Raithore from the EM facility for their technical support. A special thank goes to Iris for cloning all the sequences I requested. I also want to thank Tim Marwedel and Heike Pehlke for their administrative support. I want to thank Chris and Oana for proofreading my dissertation. Thanks for your patience and all the valuable comments. Honestly, putting everything together and writing the dissertation was much harder than I imagined, and you made it possible. I also want to thank Oana for all your help: the discussions, advice, and everything else. I truly appreciate it.

During my PhD, one of the earliest challenges I faced was COVID-19. Many people helped me navigate that difficult period. I would like to send special thanks to those who supported me during the early stages. Thanks, Margo, for showing me everything when I first joined. Thanks, Céline, for your friendship and valuable suggestions when I started my PhD. I worked pretty hard to analyze the data from different perspectives, and it was a lot of fun. Thanks, Wei, for your friendship, for the dinners, and for the time we shared together. Trust me, I won't settle. I also want to thank Tim Fieblinger for the idea of trying the Cre/loxP system for EM labeling. It took longer than expected, but it works.

I also would like to thank all the lab mates for creating a friendly and creative environment: Céline and Mauro, Brenna, Margo, Laura, Alberto, Paul, Tim, Margarida, Andreas, Della, Oana, Marie B and Marie W, Kristina, Carolina, Charlotte, Kelsey and Julia.

Last but not least, I want to thank my family and friends. I have always received unwavering support from my parents. I know there is always somewhere I can go to rest. Sometimes I feel like I will never be as good as my mom—brave, calm, and kind—but I will keep trying. I also want to thank my grandma. I'm not a little girl anymore, but I still draw strength from the old days when I lived with you as a little girl.

I want to conclude this journey with a few lines from one of my favourite writers: "我很渺小，无论做了什么，都是同样的渺小。但是只要我还在走动，就超越了死亡。现在我是诗人。虽然没发表过一行诗，但是正因为如此，我更伟大。" ——王小波《三十而立》

Eidesstattliche Versicherung:

Hiermit versichere ich an Eides statt, die vorliegende Dissertationsschrift selbst verfasst und keine anderen als die angegebenen Hilfsmittel und Quellen benutzt zu haben.

Sofern im Zuge der Erstellung der vorliegenden Dissertationsschrift generative Künstliche Intelligenz (gKI) basierte elektronische Hilfsmittel verwendet wurden, versichere ich, dass meine eigene Leistung im Vordergrund stand und dass eine vollständige Dokumentation aller verwendeten Hilfsmittel gemäß der Guten wissenschaftlichen Praxis vorliegt. Ich trage die Verantwortung für eventuell durch die gKI generierte fehlerhafte oder verzerrte Inhalte, fehlerhafte Referenzen, Verstöße gegen das Datenschutz- und Urheberrecht oder Plagiate.

Affidavit:

I hereby declare and affirm that this doctoral dissertation is my own work and that I have not used any aids and sources other than those indicated.

If electronic resources based on generative artificial intelligence (gAI) were used in the course of writing this dissertation, I confirm that my own work was the main and value-adding contribution and that complete documentation of all resources used is available in accordance with good scientific practice. I am responsible for any erroneous or distorted content, incorrect references, violations of data protection and copyright law or plagiarism that may have been generated by the gAI.

Hamburg, den 17/12/2024 Unterschrift Rui Wang 王睿